RECEIVED
LAWRENCE
RADIATION LABORATORY

LIBRARY AND
DOCUMENTS SECTION

LBL-104

c.1

KINETICS OF THE REACTION OF PYROLYTIC GRAPHITE WITH MOLECULAR OXYGEN STUDIED BY MODULATED MOLECULAR BEAM MASS SPECTROMETRY

Richard Harold Jones
(Ph. D. Thesis)

November 1971

AEC Contract No. W-7405-eng-48

For Reference

Not to be taken from this room

LBL-104

c.1

DISCLAIMER

This document was prepared as an account of work sponsored by the United States Government. While this document is believed to contain correct information, neither the United States Government nor any agency thereof, nor the Regents of the University of California, nor any of their employees, makes any warranty, express or implied, or assumes any legal responsibility for the accuracy, completeness, or usefulness of any information, apparatus, product, or process disclosed, or represents that its use would not infringe privately owned rights. Reference herein to any specific commercial product, process, or service by its trade name, trademark, manufacturer, or otherwise, does not necessarily constitute or imply its endorsement, recommendation, or favoring by the United States Government or any agency thereof, or the Regents of the University of California. The views and opinions of authors expressed herein do not necessarily state or reflect those of the United States Government or any agency thereof or the Regents of the University of California.

0 0 0 0 3 6 0 3 3 2 0

KINETICS OF THE REACTION OF PYROLYTIC GRAPHITE WITH MOLECULAR OXYGEN STUDIED BY MODULATED MOLECULAR BEAM MASS SPECTROMETRY

Contents

Abstract vii

List of Abbreviations ix

I. Introduction 1

A. Statement of the Problem 1

B. Graphite Structure and Properties 2

C. Oxidation of Graphite 6

D. Molecular Beam Techniques 16

II. Response of Modulated Molecular Beam System to Different Reaction Mechanisms 19

A. General Features 19

B. Adsorption-Desorption 25

C. Molecular Transit Effects 29

D. Series Processes 30

E. Solution-Diffusion 32

1. Semi-Infinite Medium 32

2. Finite Medium Without Loss at Rear Wall 35

3. Finite Medium With Loss at Rear Wall 35

F. Surface Diffusion 36

G. Branch Processes 39

H. Experimental Philosophy 42

III. Experimental 44

A. Description of the Apparatus 44

1. General Features 44

2. Vacuum System 52

3. Gas Inlet System 55

4. Beam Source 57

5. Beam Modulation and Reference Signal 59

6. Target Preparation, Mounting, Heating, and Temperature Measurement 63

7. Mechanical Alignment 67

8. Detection System 69

B. Beam Properties 74

C. Summary of Experimental Parameters, Basic Operating Proceedure, and Data Handling 88

D. Reagent Purity 95

E. Experimental Program 99

IV. Basal Plane Reaction 102

A. Data Acquisition and Preliminary Interpretation . . . 102

B. Reaction Model--CO Production 116

C. Comparison with Experiment--Determination of Kinetic Parameters 122

D. Interpretation 126

E. Further Proof--Waveform Analysis 131

F. CO_2 Reaction 136

G. Reaction of Annealed Graphite 140

V. Prism Plane Reaction 142

A. Data Presentation and Interpretation 142

B. Multi-Branch Reaction Mechanism 154

C. Double-Diffusion Model 159

D. Room Temperature Reaction 171

E. Mixed Isotope Reaction 173

F. Annealed Prism Plane Pyrolytic Graphite 179

0 0 0 0 3 6 0 5 3 2 1

VI. Quasi-Equilibrium Analysis 182

VII. Conclusion 186

Acknowledgment 189

Appendix I 190

Appendix II 192

References 194

0 0 0 0 3 6 0 3 3 2 2

KINETICS OF THE REACTION OF PYROLYTIC GRAPHITE WITH MOLECULAR OXYGEN STUDIED BY MODULATED MOLECULAR BEAM MASS SPECTROMETRY

Richard Harold Jones

Inorganic Materials Research Division, Lawrence Berkeley Laboratory
and Department of Nuclear Engineering, College of Engineering;
University of California, Berkeley, California

ABSTRACT

The kinetics of pyroytic graphite oxidation were studied using an experimental system in which a molecular beam of oxygen is directed at a heated graphite target maintained in high vacuum. Gaseous reaction products desorbing from the graphite were monitored by a quadrupole mass spectrometer. The molecular beam was modulated and AC phase lock detection was employed to enhance the signal-to-noise ratio. By the AC detection technique, one determines not only the reaction product signal amplitude but also the reaction phase lag which is directly related to the duration of some reaction process (i.e. it represents a surface residence time). Reaction probabilities of $2x10^{-5}$ or greater could be detected.

The reactivity of both the basal and prismatic (edge) planes of pyrolytic graphite was measured. The graphite targets were heated from the rear by electron bombardment. Basal plane targets were heated to 1800°K. Prism plane targets, with their higher heat conductivity normal to the surface, could be heated to 2700°K. The effective oxygen beam pressure at the target ranged between $5x10^{-6}$ and $2x10^{-4}$ torr. The oxygen beam temperature could be controlled independent of the target temperature from room temperature to 1200°K. The beam modulation frequency could be varied from 2 to 1500 Hz thereby providing a selective probe of reaction processes with different characteristic times.

Oxidation of the basal plane producing CO was found to proceed via two branches. Molecular oxygen dissociates on the surface forming one bound CO and one mobile adsorbed O atom. The adsorbed atomic oxygen migrates about the surface until it finds a suitable carbon atom with which it reacts.

Oxidation of the prism plane producing CO was found to be affected by diffusion of surface species into the bulk graphite. This diffusion process acts as a flywheel which smooths the AC signal thereby strongly demodulating the amplitude and producing a phase lag independent of all experimental conditions.

Samples of pyrolytic graphite were tested in the as-deposited condition and after annealing at 3000°C. Annealed basal surfaces were found to be quite unreactive. The annealed prism plane target was less prone to diffusion loss of reacting species and exhibited a higher reactivity than had been observed for as deposited samples. The high apparent reactivity of the annealed prism plane specimen is a consequence of the AC detection method which discriminates against processes delayed for times on the order of a modulation period.

Oxidation of pyrolytic graphite was observed to proceed at room temperature. This rather unexpected phenomena is ascribed to the unusually clean surface conditions which are maintained in the high vacuum environment.

LIST OF ABBREVIATIONS

a	distance per jump
a	general signal amplitude
A_j	signal amplitude
A	pre-exponential for rate constant, k
A_d	pre-exponential for rate constant, k_d
$A_{d_1}^{R}$	amplitude correction (reactant), transit from chopper to target
$A_{d_2}^{R,P}$	amplitude correction (reactant or product), transit from target to detector
A_Z	amplitude correction, complex impedance
$\bar{c}$	mean molecular speed
C	cosine intergral of time varying surface concentration
C	general concentration (volumetric)
C_1	concentration in renucleation region, grain boundary
C_2	concentration in grain
C_s	source conductance
C_{d_1}	net amplitude correction, transit chopper to target
C_{d_2}	net amplitude correction, transit target to detector
C_Z	net amplitude correction, complex impedance
d_t	see Fig. 24.
d_{ch}	see Fig. 24.
d_c	see Fig. 24.
d_t	see Fig. 24.
D	general diffusion coefficient
D_1	diffusion coefficient in renucleation region (grain boundary)
D_2	diffusion coefficient in grain
D_v	volume diffusion coefficient

D_s	surface diffusion coefficient
e	base of natural logarithm
E	general activation energy
E_d	activation energy for desorption
E_1	activation energy for the first of a series or branch process
f	modulation frequency (Hz)
g(t)	beam modulation gating function
g_1	first Fourier component amplitude of g(t)
G	capture rate of atoms by an active site
H	solubility constant
ΔH	enthalpy change
I_o	beam intensity at target (molecs/cm^2-sec)
j	$\sqrt{-1}$
J(0)	centerline beam intensity (molecs/ster-sec)
k	general rate constant
k	rate constant for surface migration
k	rate constant for desorption
k_d	rate constant for desorption
k_1	rate constant for the first of a series or branch process
k^+	rate constant for generation of active sites
k^-	rate constant for site deactivation
K	Clausing factor
K	equilibrium constant
K_{S*}	equilibrium constant for active site concentration
ℓ	leak rate
ℓ	thickness of finite medium
ℓ	separation of active sites

ln	natural logarithm
L	channel length
L	general beam flight path
m	molecular mass
m_i	mass, species i
M_R	molecular weight of reactant
M_P	molecular weight of product
n	general surface concentration
n_P	general surface concentration of product
n_1^*	first Fourier coefficient of n (possibly complex)
n_A	surface concentration on A sites
n_B	surface concentration on B sites
n_j	number of jumps per encounter (surface migration)
N	number of channels
N	number of renucleation regions per unit length
N_{S*}	surface concentration of active sites
p_{eq}	equivalent pressure
p_i	partial pressure, species i
p_L^*	"critical pressure", mean free path = channel length
p_o	chamber pressure
p_s	source driving pressure
p_s^o	initial source pressure
P	branching ratio (P_1 first branch)
r	radial coordinate (cylindrical coordinates)
R	gas constant
R_i	desorption rate, species i
$\overline{r^2}$	mean square displacement (surface migration)
r_{cl}	see Fig. 24.

r_{c2}	see Fig. 24.
S_o	pumping speed
ΔS	entropy change
s_R	mass spectrometer signal due to reactant
s_P	mass spectrometer signal due to product
$\mathcal{S}_R$	first Fourier component amplitude of s_R
$\mathcal{S}_P$	first Fourier component amplitude of s_P
$\mathcal{S}$	first Fourier component "density" signal
S	first Fourier component "flux" signal, $S = \mathcal{S}\sqrt{T}$
$\mathcal{S}$	sine integral of time varying surface concentration
t	time
T	absolute temperature
T_R	temperature of reactant
T_P	temperature of product
T_S	surface temperature
T_B	beam temperature
V_r	reservior volume
x	coordinate into bulk
X	transit parameter
y	coordinate into grain
Z_i	gas impingement rate, species i
α	most probable molecular speed
β	general instrumental constant
β_R	instrumental constant for reactants
β_P	instrumental constant for products
Γ	surface migration jump frequency (sec^{-1})
δ	fraction of B sites which regenerate A sites
δ	width of "grain boundary" renucleation region

Δ	width of developed surface at mouth of grain boundary
Δ	slope of Arrhenius plot
ε	apparent reaction probability
ε_ι	apparent reaction probability of small fraction ι of product
$\tilde{\varepsilon}$	approximate apparent reaction probability
ζ_i	equilibration coefficient (Sticking probability), species i
η	sticking probability
η_o	bare surface sticking probability
η_ι	sticking probability resulting in the fraction ι of product
ι	small fraction of product
κ	"bimolecular" site annealing rate constant
θ	beam impingement angle (45°)
σ	molecular cross section
σ	site cross section
ϕ	reaction phase lag, signal phase
ϕ_1	reaction phase lag for the first of a series of processes
ϕ_d	reaction phase lag for the desorption process
ϕ_{mech}	mechanical phase shift
$\phi^{R,P}_{meas}$	measured (reactant or product) phase lag
$\phi^{R}_{d_1}$	transit phase lag, chopper to target
$\phi^{R,P}_{d_2}$	transit phase lag, target to detector (reactant or product)
ϕ_Z	complex impedance phase lag
$\Delta\phi_{d_1}$	net phase correction, transit chopper to target
$\Delta\phi_{d_2}$	net phase correction, transit target to detector
$\Delta\phi_Z$	net phase correction, complex impedance
χ	peaking factor
ω	modulation frequency (rad/sec)

I. INTRODUCTION

A. Statement of the Problem

The reaction of carbons and various gases, including oxygen, has been the subject of experimental investigation for many years, particularly by fuel research laboratories. As with most heterogeneous chemical studies, the early work lacked a good understanding, or at least characterization, of the solid. Two crystalline forms of carbon, diamond and graphite, occur in nature and have been used in reaction studies to provide a characterizable material.

Graphite has a structure consisting of widely spaced layers of tight hexagonal meshes of carbon atoms. (A more complete description is found in the section I-B.) The anisotropy of graphite is exhibited notably in a much lower thermal conductivity perpendicular to the layer planes than parallel to the layer planes. Atoms bound in the central region of the mesh planes are expected to be much less chemically reactive than atoms loosely bound at the edges. A synthetic material known as pyrolytic graphite exhibits the anisotropic properties to a greater extent than conventional polycrystalline graphite. Pyrolytic graphite is deposited as a layer of basal planes by cracking a gas such as ethane on a suitable substrate heated to high temperature.

Due to its favorable neutron moderating and structural properties, carbon has been an important material in the nuclear energy field, having been employed in the first reactor at Chicago. More recently, the search for improved nuclear fuel packages has led to consideration of uranium carbide pellets which could be compatibly clad in pyrolytic graphite as an aid to retaining fission products.

In the case of nuclear fuel pellets, the inherent thermal insulation

of the coating is detrimental. However, specific application of this reduced heat conductivity may be made in fabricating reentry shields for aerospace vehicles or in high temperature terrestrial insulation problems requiring structural rigidity.

Effective engineering design requires some knowledge of life expectancy of materials used. In the nuclear and aerospace applications cited, this implies an understanding of the rate of burn up of the pyrolytic graphite sheath, either by reaction with oxygen impurity in the reactor coolant or oxygen in the earth's atmosphere. The oxidation of pyrolytic graphite at temperatures up to 2700°K at fairly low oxygen pressures, ca. 10^{-5} torr (10^{-8} atmosphere) has been investigated in this work.

B. Graphite Structure and Properties

The crystallography of graphite is illustrated in Fig. 1 as a lamellar structure of hexagonal mesh planes separated by 3.35 Å. The hexagonal grid spacing is 1.42 Å and plane stacking follows ABAB.... A stacking sequence ABCA... known as rhombohedral graphite may be produced from hexagonal graphite by mechanical work.[1] The base of the graphite unit cell is drawn by heavy lines in Fig. 2. Two plane designations are in use; a three-cipher using axes x1,x2 and z, and a convenient symmetrical four-cipher based on x1, x2, x3 and z. The basal or layer planes are denoted (001) or (0001), while the two types of edge or prismatic planes known descriptively as the "zig-zag" and "armchair" faces are denoted (110) and $(1\bar{1}0)$; or $(10\bar{1}0)$ and $(11\bar{2}0)$[2].

Bonding within the plane is regarded as a resonance among the plane atoms similar to the resonance in benzene rings as represented in Fig. 3a. A small fraction of preferred electron distribution (quinod structure) similar to the options in Fig. 3b, 3c is also tenable since it would

0 0 0 0 3 6 0 5 3 2 7

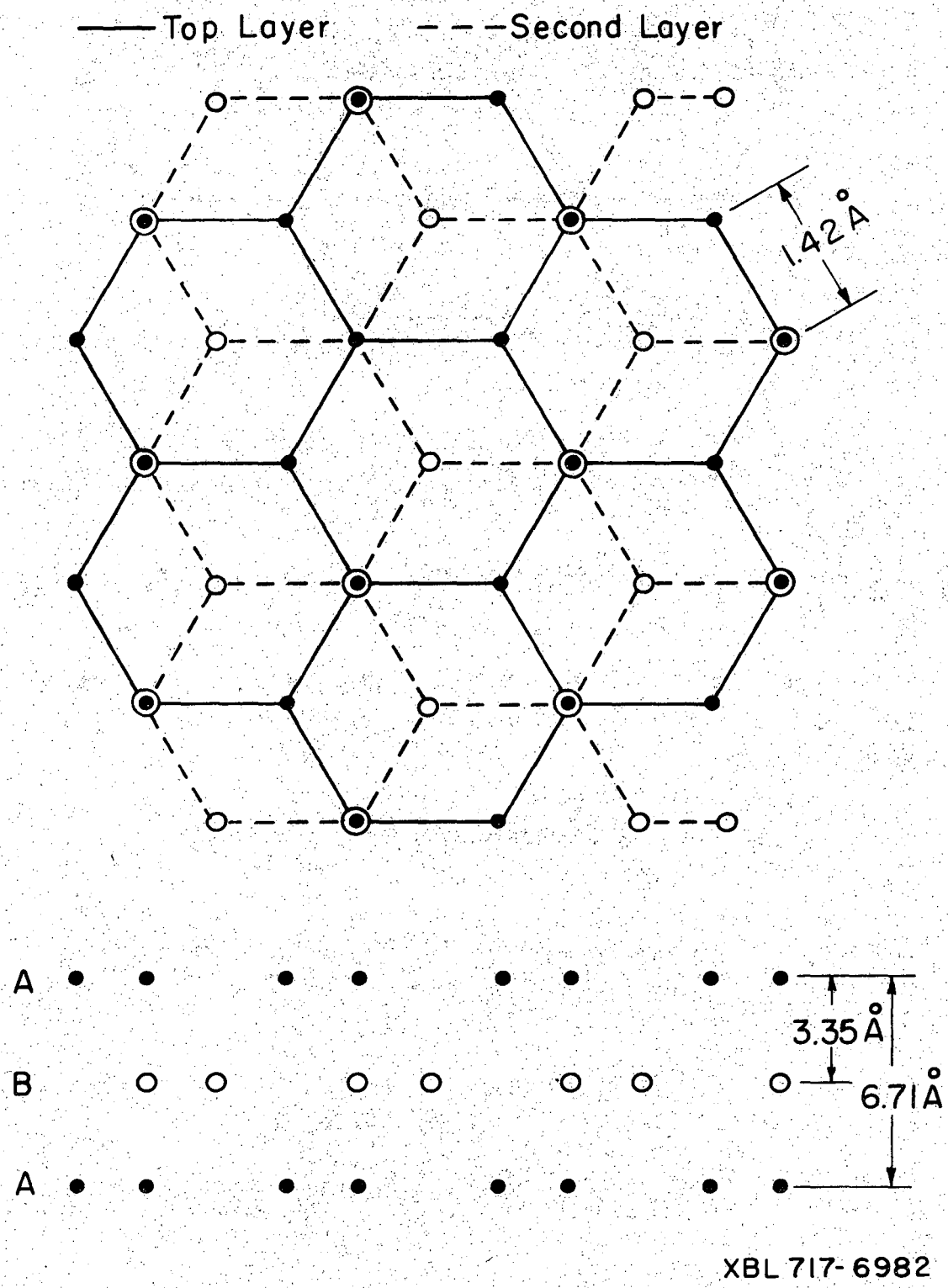

Fig. 1 Graphite structure.

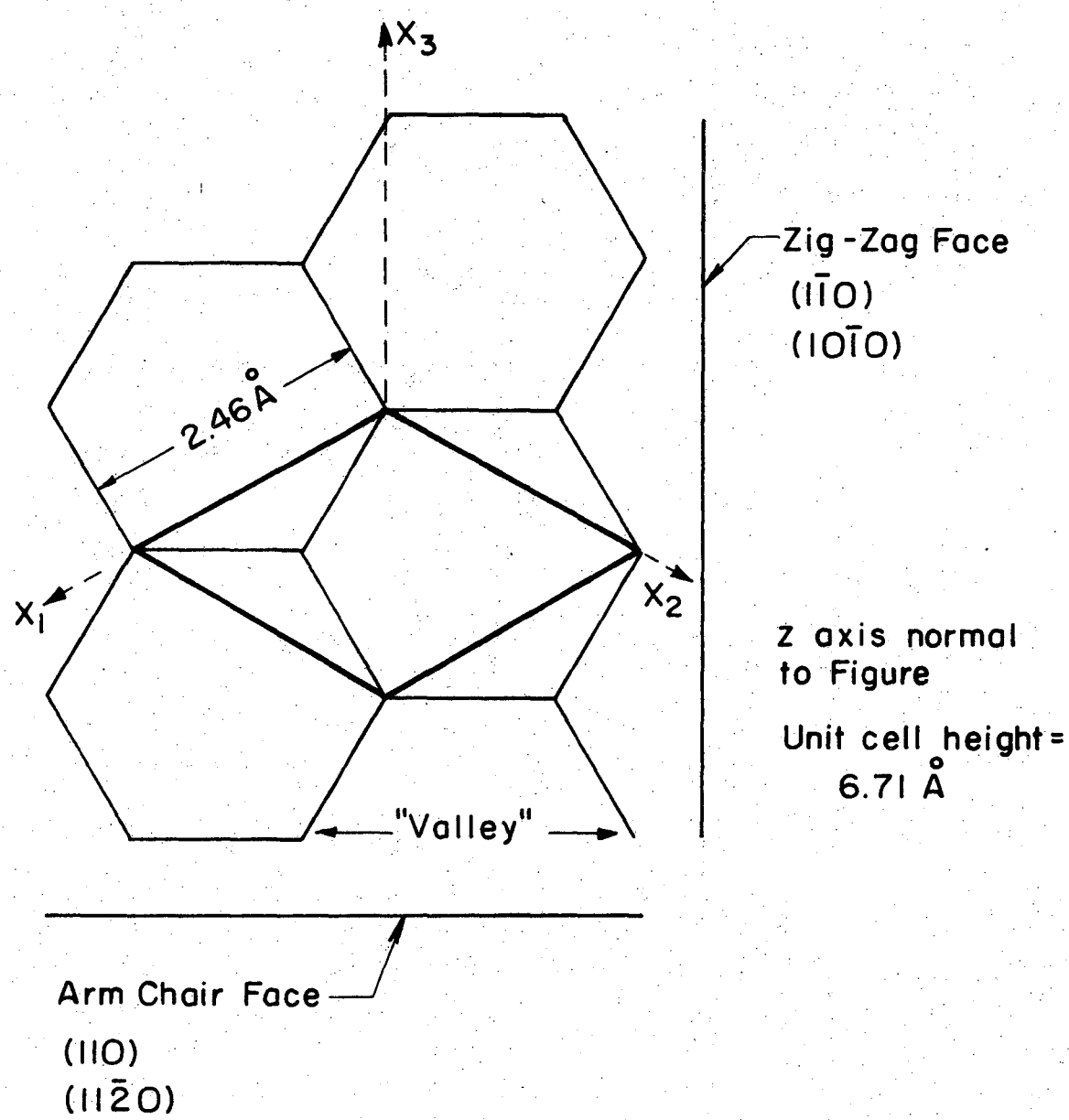

Fig. 2 Base of graphite unit cell.

0 0 0 0 3 6 0 5 3 2 8

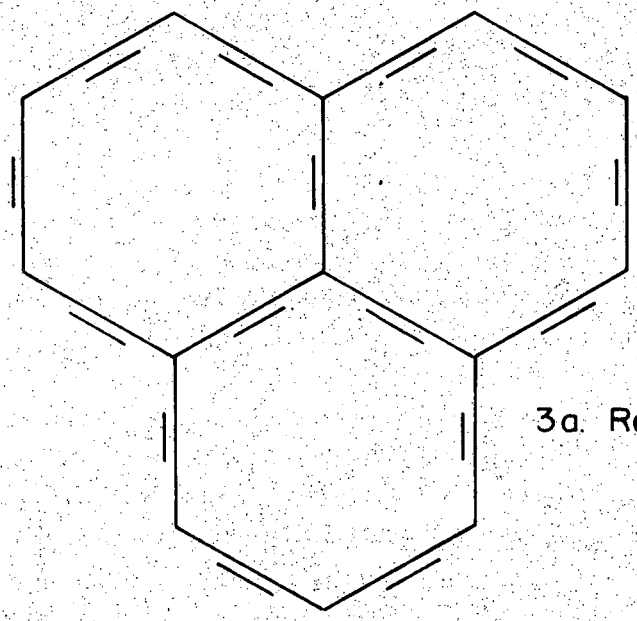

3a. Resonance Bonding

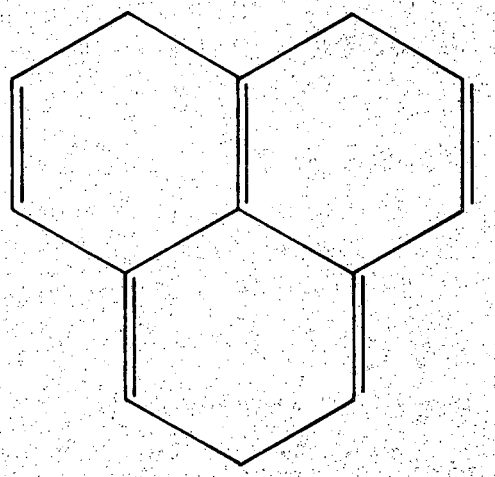

3b.

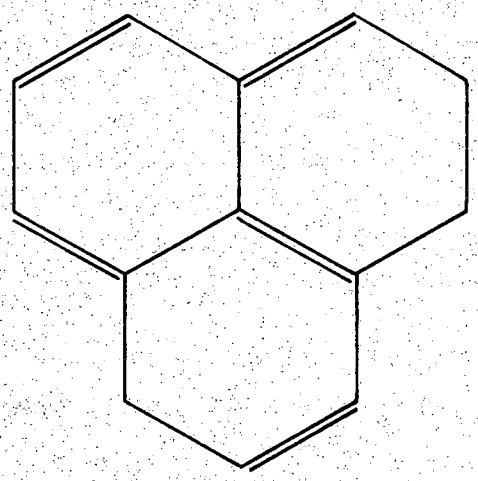

3c.

Quinod Bond Distributions

XBL 717-6984

Fig. 3 Chemical binding in graphite.

permit somewhat tighter stacking of the planes.[3]

Pyrolytic graphite[4] grows as cones from nucleation sites on the deposition substrate. As the layers accumulate, additional cones may be born. Typically as-grown pyrolytic graphite is less dense (2.0 gr-cm^{-3}) than natural graphite crystals (2.26 gr-cm^{-3}) and the interplanar spacing is about 3.45 Å rather than 3.35 Å. Heat treatment at about 3000°C shrinks the (c-axis) interlayer spacing to about 3.35 Å in individual crystalites. A 2% increase in a-axis dimension due to heat treatment is ascribed to straightening "kinked" layer planes. Not all crystalites are oriented parallel to the substrate but deviations from order are typically about 0.1%. More seriously, the crystalites (cones) assume random orientations with respect to rotation about the c-axis.

The anisotropy of pyrolytic graphite is exemplified by its thermal conductivity which is similar to iron parallel to the basal planes, but is about 100 times smaller (comparable to alumina brick) perpendicular to the basal planes.

C. Oxidation of Graphite

Not only has every common form of carbon been the subject of oxidation studies, but such work has been carried out both as "pure science" studies and as engineering design studies measuring erosion of devices fabricated from the carbon of interest. Only the former, more fundamental, work will be reviewed here.

Early work by Strickland-Constable[5] (1944) used filaments resistively heated to 1200-2300°K and burned in an oxygen background of 20-500 millitorr. The filaments were of carbonized extruded cellulose pyrocoated by cracking a mixture of hydrogen and ethane. CO from the reaction was catalytically oxidized (Pt) to CO_2 which was trapped. The remaining O_2

was then measured by a McLeod gauge as were the CO_2 fractions of different origin upon desorption. The principal reaction product was found to be CO. The CO/CO_2 ratio was always greater than 7 and varied inversely with temperature. CO was found to be a primary product, not formed by secondary reduction of CO_2. Conversely, the small amounts of CO_2 produced did not permit a determination of its origin; CO_2 could be produced by secondary oxidation of CO. One major problem arose due to the filament mounting. With the filament and a parallel support constituting a hair-pin configuration, a glow discharge was frequently observed between segments at different potential. When the glow discharge effects could be avoided, the reaction was found to obey first order kinetics with a maximum in rate at about 1500°K, falling to a plateau from 1900-2300°K. The rate was found to exhibit hysteresis such that on proceeding from a lower to a higher temperature a new rate lower than the steady rate is obtained. Reciprocally, on reducing temperature, the initial rate was found to be higher than the steady rate. Such hysteresis was explained as due to an inhibiting surface cover which was removable at high temperatures. Duval[6] also using a hot filament technique obtained similar results but a reverse hysteresis. A particularly good description of this hysteresis effect is provided by Boulangier et al.[7] in relation to a similar reaction.

Criticizing the results of Strickland-Constable,[5] Meyer[8] shows that the former, due to lack of a flow technique, was unable to prevent multiple collisions with the hot filament. Also it is indicated that inadequate coating of the filament could result in reactions in crevices tending toward an equilibrium CO/CO_2 ratio of the Boudouard reaction rather than a ratio due to a primary reaction. Furthermore, reaction in cracks could take place with preheated oxygen gas. In contrast to

Strickland-Constable,[5] Meyer[8] finds the reaction to be first order from 1000-1500°K while from 1800-2500°K a zero order reaction is observed. The CO/CO_2 ratio was nearly unity and was independent of temperature and pressure. No maxima in the rate was observed, rather the results indicated a positive temperature coefficient characterized by an activation energy of 25 kcal. $mole^{-1}$ from 1000-1500°K and an activation energy of 90 kcal. $mole^{-1}$ from 1800-2500°K. The zero order dependence at high temperatures is ascribed to evaporation of reaction product as being the rate limiting step.

In 1950, Strickland-Constable[9] surveyed some of the existing data for the oxidation of carbon by N_2O, CO_2, and H_2O as well as O_2. All systems reported showed a relatively flat temperature dependence from 1500°K onward. Since some of the work reported was done on charcoal, the objection to possible crevice reactions raised by Meyer[8] is significant. The reactions at high temperature were found to be first order while at reduced temperatures zero order behavior was observed. Due to low sensitivity at low temperatures, it was suggested that this effect be reinvestigated. Also questioned was the applicability of the results to systems where the reacting gas might be more nearly heated to the temperature of the carbon.

In later work Strickland-Constable et al.[10,11] directed a 0.2 atmosphere jet of oxygen at a heated carbon bar and photographed projected shadows of the erosion profile. Some of this work was done on bulk pyrolytic graphite. The first report[10] covered temperatures from 1300-2300°K and the data were shown to fit a theory of Blyholder, Binford and Eyring[12] which concerns oxidation on two types of sites, A and B, dominated at low temperatures by the more reactive A sites which represent a fraction, x, of the surface. At higher temperatures the A sites

rearrange to form less reactive B sites reducing the oxidation rate, while at still higher temperatures the oxidation rate increases with increase in the B site reactivity. (1) The coverage of A sites is determined as a balance between the oxidation of bare A sites $\propto (1-\theta_A)x$ and the desorption of CO from covered A sites $\propto \theta_A x$. The rate of reaction on A sites is, $v_A = k_A px/(1 + k_z p)$. (2) A sites are created when B sites are oxidized and desorb CO. The rate of B site oxidation is, $v_B = k_B\, p\, (1-x)$. (3) A sites are thermally transformed to B sites at a rate, $k_T\, x$. Processes (2) and (3) determine the steady state value of x. The total rate of oxidation is the sum of rates (1) and (2).

The following parameter values were chosen[10] to fit the data: (g-atom carbon/cm^2 - sec, p in atmospheres)

$$k_A = 20 \exp -30000/RT,$$
$$k_B = 4.46\text{x}10^{-3} \exp -15200/RT,$$
$$k_T = 1.51\text{x}10^{5} \exp -97000/RT,$$
$$k_z = 21.3 \exp +4100/RT.$$

The theory involves four rate constants (8 adjustable parameters) and would be expected to reproduce some range of observations. It was encouraging that when the measurements were extended to 2700°K[11] the same kinetic parameters continued to produce a good fit. The oxidation rate peaks at 2300°K and decreases on further heating. Since the rate obtained with pyrolytic graphite was substantially less than measured on more porous reactor graphite, mass transfer effects were assumed to be negligible for the pyrolytic graphite measurements.

Oxidation in a gas flow system was done by Horton[13] using pyrolytic graphite samples in the form of basal plane wafers. Reaction rate of the basal plane was measured in terms of weight loss of carbon and the

relative rates on basal and edge planes were noted by geometrical measurements. The reaction (900-1800°K) was found to be one-half order with an activation energy of 37 kcal. $mole^{-1}$. A mechanism consisting of rapid adsorption of oxygen with rate limiting desorption of CO or CO_2 was suggested.

Pyrolytic graphite for aerospace applications has been studied by Rosner and Allendorf[14]. They used a gas flow system and optically monitored the ablation of a filament of tungsten coated with pyrolytic graphite. Comparisons were made with isotropic graphite and oxidations of both graphites using atomic and molecular oxygen were made. For pyrolytic graphite and molecular oxygen the study covered 1300-2000°K at a typical O_2 pressure of 30 millitorr. The reaction was found to be nearly first order and exhibited a maxima at 1900°K. In comparison with isotropic graphite, the pyrolytic graphite was found to be much less reactive with molecular oxygen. However, with atomic oxygen both types of graphite were found to react rapidly.

With the interest in working on a simply characterized specimen, oxidation has been studied using naturally occuring graphite single crystals. The crystals, while too small for burning to yield gross dimensional changes, are ideal for microscopic examination (electron and optical) of the basal plane. Perhaps best known in this area is the work of Hennig[15,16,17] who found that the edge planes oxidized at least 20 times faster than the basal planes and that the rate varied as the square root(or lower power) of the oxygen pressure. The etch pits on the basal planes were found to be hexagonal bounded by "vertical" $(11\bar{2}0)$ faces. A "two competing sites" model was proposed to rationalize the results. Both these sites span the "valley" of a $(11\bar{2}0)$ or armchair

face (Fig. 2). The more reactive oxide B spans one oxygen atom across this diametral gap, while the less reactive A oxide has one oxygen atom on each side. The rate determining step is the interaction of an O_2 with B to form volatile products.

Electron microscope studies lend themselves well to topographical studies of oxidation. The effect of lattice defects on reactivity [17] was measured showing increased reactivity due to screw dislocations, Frenkel defects, and quenched defects. Twin boundaries were less effective in promoting reaction. Particularly lucid discussions of the results obtained by optical microscopy are provided by Thomas[18,19] and Thomas and Hughes[20]. Their studies with 10 torr oxygen at 1100-1200°K determined fairly large activation energies for recession in $\langle 10\bar{1}0 \rangle$ and $\langle 11\bar{2}0 \rangle$ directions (66 and 62 kcal. mole^{-1} respectively). The reaction was found to be of half order or less.

Modification of graphite reactivity by impurity catalysts has been studied. Harker[21] used cocoanut charcoal in a flow system to study the effects of alkali metals on the reaction with oxygen. An "ignition temperature" change was used as a measure of catalysis. The enhanced reactivity found was attributed to attack of the surface by free metal. Heintz and Parker[22] studied the effects of large impurity concentrations (0.1 mole%) of 42 transition metals mixed in powdered graphite. The reactions as carried out were first order in oxygen pressure from 900-1100°K. Two characteristics were noted. Those metals with 5 or 10 electrons in their (n-1)d orbitals do not π bond readily and are active catalysts. Also, metal oxides of high vapor pressure are catalysts. A similar conclusion was made by Amariglio and Duval[23] who also found high volatility of the oxide to be related to significant acceleration of

graphite oxidation. Metals exhibiting two degrees of oxidation under combustion conditions are most effective and it is proposed that the metal oxide furnishes a "reactive" oxygen to the graphite.

Roscoe[24] studied catalytic effects of boron and molybdenum on oxidation of natural graphite crystals and concluded that the catalyst acts on existing active sites.

Hering et al.[25] indentified oxidation etch pits in graphite with the presence of sodium impurities by autoradiography.

The surface oxide states previously invoked to explain oxidation results have been subject to more direct study. Tonge[26] used infrared techniques to investigate the oxide exchange reaction, $C_f + CO_2 \rightleftharpoons C(O) + CO$, where C_f are free carbon sites and C(O) are surface oxide sites. It was found that a "clean" surface may be prepared by treatment with carbon monoxide. Menster and Ergun[27] studied the oxide exchange reaction by using carbon-14 as a tracer. The activation energy for forward and reverse reactions were found to be 53 and 36 kcal. $mole^{-1}$ respectively.

By wet chemistry Puri[28] studied adsorption of water and methanol on a variety of carbons, from sugar charcoal to Spheron 6, which had been reacted previously in oxygen. The heat of immersion of carbon in water was found to be a function of the oxide released as CO_2 rather than a function of total oxide.

By subjecting carbon to oxidation and successive degassing, Bonnetain, Duval and Letort[29] found a close relation between the production rates of CO and CO_2. They concluded that the simplest model accounting for these effects would be based on a complex surface oxide state. They further note that the CO_2 is desorbed irreversibly in contrast to the CO which was found to inhibit desorption if accumulated in the gas background.

Adsorption experiments by Hart et al.[30] in the temperature range from 25-400°C revealed two levels of adsorption. The low temperature adsorbed state gave way to the higher state at 280°C for a sample previously receiving 14.4% burn-off. For higher burn-off samples (15.2%) the threshold moved from 280°C to 210°C at the expense of the low temperature state. Dissociative immobile adsorption was assumed and was verified by experiments on a kinetic isotope effect using O_2^{18-18}. It was suggested that different types of adsorption sites may be associated with the various carbon-carbon distances in graphite.

Laine et al.[31] reacted oxygen with graphitized carbon, Spheron 6, and monitored the course of the reaction mass spectrometrically. From a material balance, a buildup of adsorbed oxygen (surface oxide) was determined. After combustion the surface oxide was then desorbed and found to be removed largely as CO. Outgassing experiments yielded the total active surface area. Due to change in the available surface area with coverage, the reaction was found to deviate from first order. This study was continued by Lussow et al.[32] to the temperature range from 570 to 950°K. Oxygen chemisorption was found to increase rapidly above 670°K indicating two types of active sites. As oxygen reacts with the carbon, first order behavior occurs when a saturation surface oxide complex has been built up. Under low coverages, the most reactive type of site dominates. Analysis of the rate constant for oxygen consumption measured under these conditions suggests that an oxygen molecule forms a mobile adsorption complex precursor which dissociates to form two mobile atomic oxygen surface complexes. This conclusion, in contrast to that of Hart[30], suggests that different types of sites, dominating in various temperature ranges, may have fundamentaly different behavior.

Using heavy oxygen (O_2^{18-18}) as a tracer, Walker et al.[33,34] have studied Graphon oxidation at temperatures ca. 600°C and pressures less than 100 millitorr. Gaseous reaction species were analyzed with a mass spectrometer.

Since adsorbed oxygen had been found to desorb from the surface complex in increasing amounts with increasing temperature, it was asked if the oxygen complex which first went onto the Graphon surface was the most strongly held and consequently the last to be desorbed as CO or CO_2. A Graphon sample at 280°C was given a partial surface coverage using O_2^{16-16} then an additional adsorption was made with O_2^{18-18}. Upon desorbing the surface complex, the fraction of O^{18} in each gaseous species was found to be invariant with desorption temperature indicating that the time of formation had little effect on the temperature of removal.[33-34]

A very careful study of alternate reactions leading to CO_2 production was done using O^{18} tagged reactants.[33,34] Although encumbered by a tendency toward isotopic exchange among product CO_2 gas molecules, the experiments clearly showed that CO_2 was a primary reaction product with an equilibrium distribution of CO_2^{16-16}, CO_2^{16-18}, and CO_2^{18-18}, although a non-equilibrium reagent O_2 mixture was used. The results suggest that O_2 dissociates to form a mobile surface oxide complex preceeding CO_2 formation and desorption.[33,34]

Using graphon preoxidized in O_2, the desorption of surface oxide was studied by Bansal et al.[35] and Phillips et al.[36] The surface oxides were desorbed as CO and CO_2 while heating the sample slowly (3°C/min.) from 500-1000°C. The surface oxide is fairly stable up to its formation temperature but desorbs beyond it. Also, oxides formed at higher temperatures are less stable than those formed at lower temperatures. Graphs of cumulative CO evolution vs. temperature reveal several breaks in the

slope of the curve suggesting CO evolution from a few distinct types of sites. The cummulative CO_2 evolution vs. temperature curve passes through a maximum due to secondary reaction of CO_2 with graphon. It is proposed that the secondary reaction proceeds on highly reactive "nascent" sites formed by desorbing the oxide.

Walker et al.[37] measured the thermoelectric power of graphite containing chemisorbed oxygen. From their results they conclude that chemisorption ties up p_z electrons in the surface oxide complex. They conclude further that the oxygen chemisorption is first order with rate independent of surface coverage and that the activated complex of chemisorption is immobile.

A study of the graphite basal plane structure and possible chemisorption using low-energy electron diffraction (LEED) was done by Lander and Morrison[38]. They found that the diffraction pattern from the surface mimicked that of the bulk and showed no change when various gases, including O_2, were available for chemisorption. They conclude that O_2 does not chemisorb in monolayer quantities, for pressures up to 10^{-4} torr, in times of tens of minutes, from room temperature upwards. Their results are well represented by a one-dimensional analysis which supports the picture that each layer is very tightly bound but is only loosely coupled to neighboring planes.

A more detailed LEED oxidation study by Gérard[39] also failed to show the presence of surface oxide modification of the basal plane diffraction pattern. In addition to the six-spot symmetry expected from the hexagonal mesh of graphite, two types of three-spot patterns were found. These were designated as Δ and ∇ patterns, and represent the effects of two alternate basal surface stackings, AB or BA. They alternately oxidized and examined the graphite. The three-spot pattern was found to alternate

between Δ and ∇ as A and B planes were sequentially gasified. This seems to strengthen the microscopic observations that broad shallow etch pits were produced and that reaction along the layers is much faster than reaction normal to the layers. With reaction taking place at the pit edges, surface oxide could be expected to be formed and desorbed only at these boundaries which constitute a negligible fraction of basal plane projected area since the etch pits were found by Hennig[15] to have "vertical" sides. Consequently, a clean basal surface would be observed in the LEED studies.

As the ultimate effort to study carbon oxidation on a clean, well defined, non-porous surface, Evans and Phaal[40] measured the kinetics of oxygen reacting with diamond. In the temperature range 650-750°C an activation energy of 55 kcal. mole^{-1} was measured. At higher temperatures, 850-1000°C, a black carbon film had formed and the activation energy had dropped to 37 kcal. mole^{-1}. Although very very thin, this carbon film dramatically affects the oxidation kinetics. One might do well to question other "chemical rates" for diffusion control through nearly negligible thin films.

D. Modulated Beam Technique

In this work the kinetics of pyrolytic graphite oxidation were studied using an experimental system in which a molecular beam of oxygen is directed at a heated graphite target. Gaseous reaction products are monitored by a quadrupole mass spectrometer.

In this basic form, independent control is obtained over gas impingement rate, gas temperature, and target temperature. Furthermore, selective study of a particular crystallographic face is afforded and impingement direction is defined. Since the beam gas is in free flight from the

beam source to the target, reaction with atomic beams can be studied. Similarly, since the gaseous products travel directly from the target to the mass spectrometer, free radicals and other unstable product species may be detected, and appearance potential measurements of reaction products may be made to determine their electronic states. Of particular importance is the uninhibited supply of reactants to the surface unperturbed by diffusion layer effects.

A principal disadvantage to molecular beam studies is the small reaction product signal in a relatively high noise background. By modulating the reactant beam and applying some form of phase-lock detection, the weak signal may be extracted from the noise. In this way one obtains not only the magnitude of the product signal but also the phase angle (phase lag) of the product signal relative to the modulated reactant beam. This phase lag is related to gas phase transit times and a reaction delay or surface residence time. Such a direct measurement of surface residence time provides a particularly sensitive test of proposed reaction mechanisms.

This work represents the second generation of modulated molecular beam heterogeneous reaction studies in our laboratory. Previously, Krakowski and Olander[41] studied the dissociation of hydrogen on tantalum. Pioneering efforts by other groups include (although not exclusively); the work of Brackman and Fite[42] on the interaction of hydrogen with cooled copper, the work of Smith and Fite[43] and McKinley[44] on the nickel-chlorine system, the work of Anderson and Boudart[45] on germanium oxidation, the study of N_2O dissociation on Tungsten by Muschlitz et al.,[46] and the study of chlorination of germanium and silicon by Madix and Schwarz[47].

Applications of molecular beam techniques to reaction studies have been reviewed by Merrill[48] who predicts considerable sophistication (complication) in future experimental systems.

II. RESPONSE OF MODULATED MOLECULAR BEAM SYSTEM TO DIFFERENT REACTION MECHANISMS

A. General Features

The use of a modulated molecular beam to study reaction kinetics is essentially an "integral"[49] technique which requires that the system response for various reaction mechanisms be computed and then compared with experimental data. This inductive search for the correct reaction mechanism may be greatly simplified if the general behavior of certain classes of mechanisms is understood.

A typical modulated beam reactive scattering system is shown in Fig. 4. The molecular beam leaves the source tube, is modulated by the beam chopper, and travels through the first collimator toward the target. Scattered beam molecules or desorbed product species pass through the second collimator and through the density sensitive ionizer of the quadrupole mass spectrometer. A fraction 10^{-4} of the molecules are ionized, extracted, and sent through the quadrupole mass filter where they strike the first dynode of an electron multiplier. The electron multiplier output goes to a phase-lock detector.

Various devices for phase-lock detection may be employed but the following theoretical development assumes the use of a lock-in amplifier. A lock-in amplifier passes the input signal (of frequency ω rad/sec) through a narrow band amplifier then rectifies the signal in a synchronous demodulator which operates at the same frequency ω. The demodulator is synchronized to a reference signal which is generally chosen to match the modulation performed by the beam chopper. A variable phase shifter is provided to adjust the phase of the demodulation relative to the reference signal. Lock-in processing amounts to multiplying the input

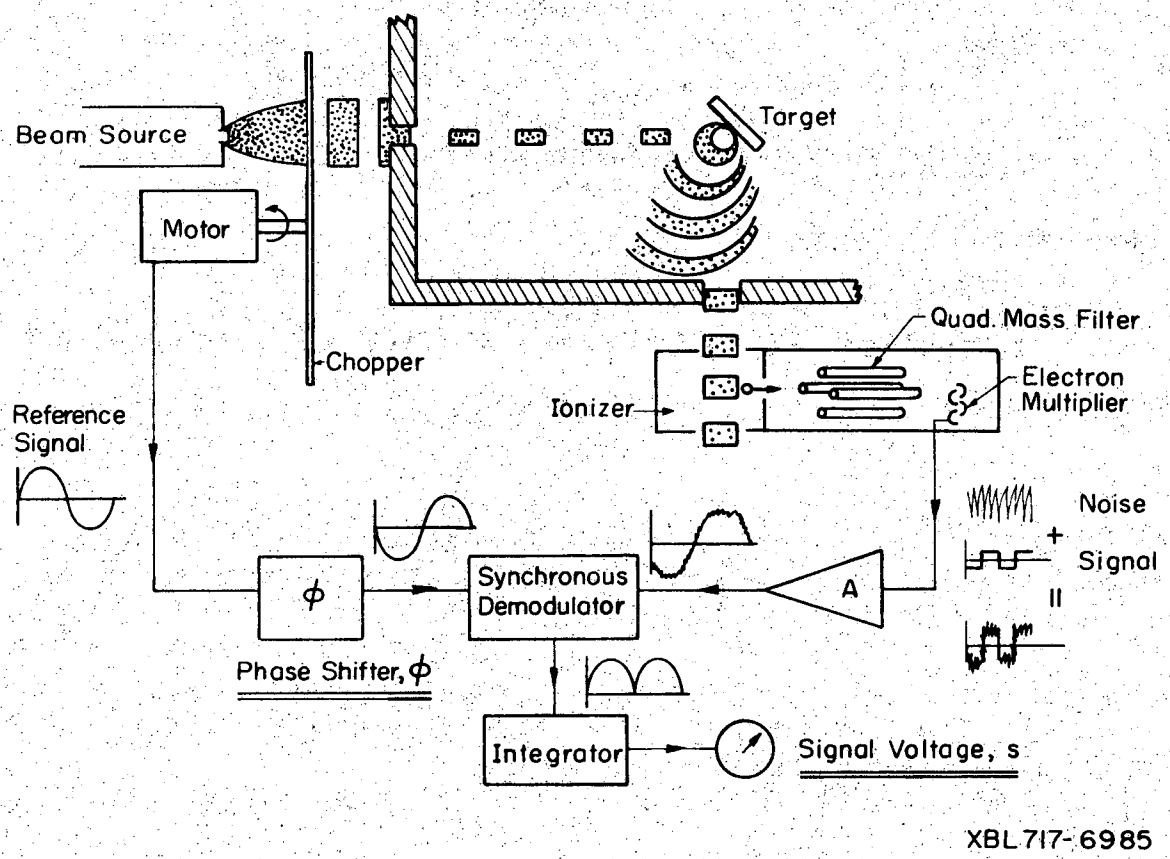

Fig. 4 Typical modulated beam reactive scattering experiment.

signal by $\sin(\omega t + \phi)$ and averaging the result, thereby obtaining essentially the fundamental Fourier coefficient of the input waveform with respect to $\sin(\omega t + \phi)$. Typically, the phase angle ϕ is adjusted to maximize this coefficient (call it $\mathcal{A}$) and one identifies ϕ as the phase lag, (relative to the reference signal), of the input signal of amplitude $\mathcal{A}$.

In order to analyse a proposed reaction mechanism, one writes a surface mass balance with a modulated feed of reactants. Olander[50] evaluated the product emission for representative reactions having (i) first and second order processes, (ii) fast and slow desorption, (iii) desorption and solution-diffusion, and (iv) desorption and surface migration. He obtained the complete solution considering a square chopped beam, solving the surface balances during beam-on and beam-off periods, and using a cyclic steady state boundary condition. The resulting complete solution was then partially expanded as a Fourier series in which the <u>amplitude</u> and <u>phase</u> of the <u>fundamental</u> component represent the signal amplitude and phase measured by a lock-in detector. For any <u>non-linear process</u>, this is the proper approach, eg., to obtain the complete solution and then to extract the fundamental Fourier component of the result.

Although non-linear surface processes are quite common and important (eg., bimolecular recombination) the following discussion will be devoted to linear processes which provide ample complication or "structure"[51] to the amplitude and phase data. For a linear surface process, we may apply the principle of superposition and not only simplify the analysis but also avoid any unnecessary work. That is, since we plan to extract <u>only</u> the fundamental Fourier component by lock-in detection, and

since in a linear system each component behaves independently, then we need only evaluate the system response to the fundamental component of the modulated molecular beam (any DC component, background, or higher harmonics may be ignored). Instead of evaluating the response to a square, trapezoidal or other complex wave; only the response to a simple sinusoid need be calculated.

We need the response to the fundamental component of the modulated reactant flux as $A \sin(\omega t - \phi)$ where the reaction phase lag (due to residence time) is explicitly noted as ϕ. Only the amplitude, A, and phase, ϕ, are given by the lock-in amplifier, and these may be conveniently determined by calculating a response $A\, e^{-j\phi}\, e^{j\omega t} = A^*\, e^{j\omega t}$ to a driving function $e^{j\omega t}$.[†,52]

For the simple case of diffuse scattering of the modulated reactant beam from the surface, the mass spectrometer signal due to the scattered reactant is,

$$s_R(t) = \frac{\beta_R\, I_o}{\sqrt{T_R}}\, g(t) \qquad (1)$$

where the beam with a strength I_o at the surface has been modulated by a function g(t). β_R is an instrumental constant accounting for the collimation geometry and the mass spectrometer efficiency. Since the mass spectrometer responds to the density of molecules in its ionizer, the scattered flux has been converted to a density equivalent by dividing by

---

[†] $A\sin(\omega t - \phi)$ may be expressed after Euler in complex form as $A[\exp j(\omega t - \phi) - \exp -j(\omega t - \phi)]/2j = A^*/2j \exp j\omega t - A^{*+}/2j \exp -j\omega t$, where $A^* = A \exp -j\phi$ is a complex amplitude and A^{*+} is its complex conjugate. Since the conjugate solution is obtained for the conjugate driving function, we need only calculate the response $A^* \exp j\omega t$ to a driving function $\exp j\omega t$.

the mean speed as represented by the square root of the absolute temperature of the molecules scattered into the ionizer.[53]

The lock-in detector sees this signal $s_R(t)$ as

$$S_R\, e^{j\omega t} = \frac{\beta_R\, I_o}{\sqrt{T_R}}\, g_1\, e^{j\omega t} \quad , \tag{2}$$

where g_1 is the first Fourier coefficient of $g(t)$, and the lock-in detector measures a signal magnitude S_R at zero phase (no reaction delay).†

Reaction products in this linear analysis desorb at a rate proportional to the density $n_P(t)$ of product on the surface with a first order rate constant k_d. The mass spectrometer signal due to desorbed product is,

$$s_P(t) = \frac{\beta_P\, k_d}{\sqrt{T_P}}\, n_P(t) \quad . \tag{3}$$

The lock-in detector sees this signal $s_P(t)$ as

$$S_P{}^*\, e^{j\omega t} = \frac{\beta_P\, k_d}{\sqrt{T_P}}\, n_1\, e^{j(\omega t - \phi)} \tag{4}$$

where n_1 is the first Fourier coefficient of $n_P(t)$ and the phase lag of product desorption ϕ is specifically noted. The lock-in detector measures a signal magnitude $|S_P{}^*|$ at a phase setting ϕ.

Numerical evaluation of β is difficult and subject to change due to aging of the electron multiplier, etc. It is convenient to use the ratio of product to reactant signals,

---

†Actually the lock-in amplifier measures the rms value of the first Fourier component not its amplitude but this scale factor may be incorporated in β.

$$\frac{S_{P*}}{S_R} = \sqrt{\frac{T_R}{T_P}}\left[\frac{k_d\ n_1}{I_o\ g_1}\right]e^{-j\phi} = \sqrt{\frac{T_R}{T_P}}\ \varepsilon\ e^{-j\phi} \quad , \tag{5}$$

where ε is the apparent reaction probability and ϕ is the reaction phase lag. In practice, the measured density signals S are immediately corrected by the square root of temperature to give flux signals,[53]

$$S = S\sqrt{T} \quad , \tag{6}$$

therefore we have,

$$\frac{S^*_P}{S_R} = \varepsilon\ e^{-j\phi} = \left[\frac{k_d\ n_1}{I_o\ g_1}\right] e^{-j\phi} \quad . \tag{7}$$

The apparent reaction probability, ε = desorption flux/impingement flux, is a convenient ratio and becomes the true reaction probability in the limit of zero frequency. It is remarkably easy to operate at a low reaction probability $\leq 10^{-2}$ such that the desorbed product signal S^*_p represents $k_d\ n_1\ e^{-j\phi}$ and the scattered reactant signal S_R represents $I_o g_1$ on the same basis without needing to correct for consummed reactant.

The instrumental constants, β_R, β_P, have been assumed equal although different species are involved. How good is this approximation?

Product desorption is assumed to be diffuse although some small correction to this may be in order.[54] Also, it is assumed that the primary beam is scattered diffusely from the room temperature target. This is an excellent approximation since very "perfect" surfaces are required to obtain significant specular reflection.[55] Consequently, equivalent fractions of scattered reactant or emitted product flux enter the solid angle subtended by the mass spectrometer ionizer.

The mass spectrometer response to a particular species is a

complicated function of the operating conditions of the spectrometer and the atomic properties of the mass species. Fortunately, the species of interest in this work (CO^{28}, O_2^{32}, CO_2^{44}) are not vastly different in molecular weight. The ionizer controls are tuned to maximize the signal at a particular mass number (say mass 32). Since this maximum is quite broad, re-tuning the ionizer on a different mass peak (say mass 28 or 44) provides only a 10% increase in signal.

Variations of resolution over the mass range (which is an inherent feature of the quadrupole mass spectrometer) may alter the sensitivity at each mass number. We neglect this effect. Calibration with a known gas mixture would be required for more precise studies than those reported here.

We may now begin to study different reaction mechanisms. To evaluate a particular <u>linear</u> reaction mechanism we assume a driving function $g_1 e^{j\omega t}$ of reactant and a surface density response $n^* e^{j\omega t}$ of product species.†

B. Adsorption-Desorption

As an example consider the case of simple adsorption-dissociation-desorption from a beam of intensity I_o with a sticking probability η and a desorption rate constant k_d,

$$A_2(g) + 2S \xrightarrow{\eta I_o} 2\,(SA)_a \xrightarrow{k_d} 2S + 2A(g) \quad . \tag{8}$$

We write a surface mass balance on the number of adsorbed A atoms, n, as

---

†(n^* is complex of the form $n_1 e^{-j\phi}$)

$$\frac{dn}{dt} = 2\eta I_o\, g(t) - k_d\, n \quad , \tag{9}$$

where $I_o g(t)$ is the modulated reactant flux. Substituting for $g(t)$ and n our driving function and trial solution, we obtain

$$j\omega n^* e^{j\omega t} = 2\eta I_o g_1 e^{j\omega t} - k_d n^* e^{j\omega t} \tag{10}$$

and solving for n^* we have

$$n^* = \frac{2\eta I_o}{k_d + j\omega} \quad . \tag{11}$$

The desorption rate of adsorbed A is, of course, $k_d n^* e^{j\omega t}$ or neglecting the time dependence,

$$k_d\, n^* = \frac{2\eta I_o g_1 e^{-j \tan^{-1}(\omega/k_d)}}{\sqrt{1 + (\omega/k_d)^2}} = \varepsilon\, I_o g_1 e^{-j\phi} \tag{12}$$

where ε is the apparent reaction probability and ϕ is the reaction phase lag.

$$\varepsilon = \frac{2\eta}{\sqrt{1 + (\omega/k_d)^2}} \tag{13}$$

and

$$\phi = \tan^{-1}(\omega/k_d) \quad . \tag{14}$$

We see here the importance of providing a variable chopping frequency ω. If the parameter ω may be adjusted to produce a variation in ε and ϕ, then the desorption rate constant k_d and the sticking probability η may be easily determined. More important, the frequency spectra

of ε and ϕ provide sensitive checks on the proposed reaction mechanism. In the present case we have a simple linear variation of tan ϕ with ω of slope $1/k_d$. Similarly, this reaction mechanism predicts a linear variation of $1/\varepsilon^2$ with ω^2 exhibiting a slope $(2\eta k_d)^{-2}$. Returning to equation 12 we may note that the product emission rate may be represented as a reaction product vector of amplitude ε and phase angle ϕ. For this example, the product vector locus as frequency is increased is a semicircle as sketched in Fig. 5. The apparent reaction probability decreases from the steady state or true DC value, and the phase lag ϕ increases from 0° to 90° as ω increases (for $\omega \sim k_d$).

It is common practice to make an Arrhenius plot of reaction kinetic data. When a straight line is fitted to the data, the slope equals 1/R (R the gas constant) times the activation energy for the controlling kinetic step. If we plot the natural logarithm of the apparent reaction probability ε as a function of reciprocal temperature, what does this slope represent?

For simple desorption with ε given by Eq. (13), the Arrhenius slope, $\Delta = \partial \ln \varepsilon/\partial(1/T)$ is[51,56]

$$\Delta = -\frac{E_d}{R}\,\frac{\omega^2}{k_d^{\,2} + \omega^2} \quad . \tag{15}$$

Under steady state conditions, the rate of surface dissociation is determinded only by the sticking probability (constant) --- all reactants that stick are desorbed as atoms. The modulated beam experiment permits investigation of the desorption rate constant k_d when $\omega \sim k_d$. At high frequencies ($\omega \gg k_d$) the slope of the Arrhenius plot is $-E_d/R$.

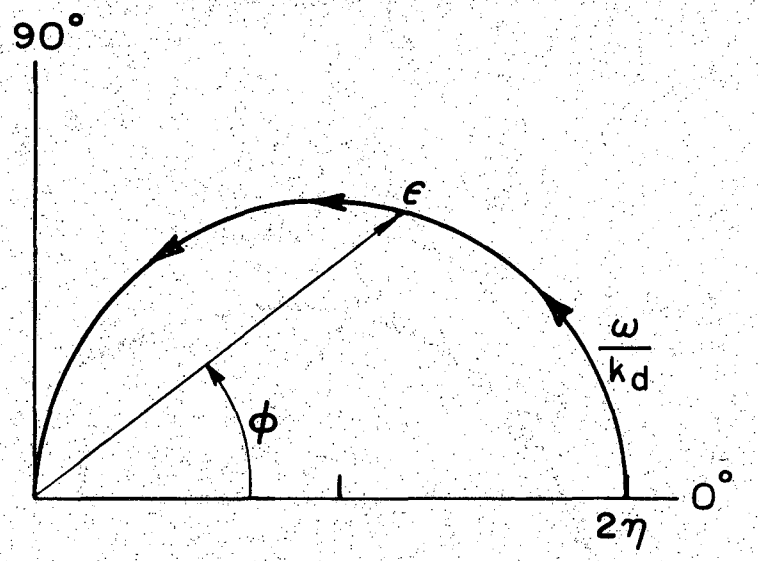

5a. Single Process

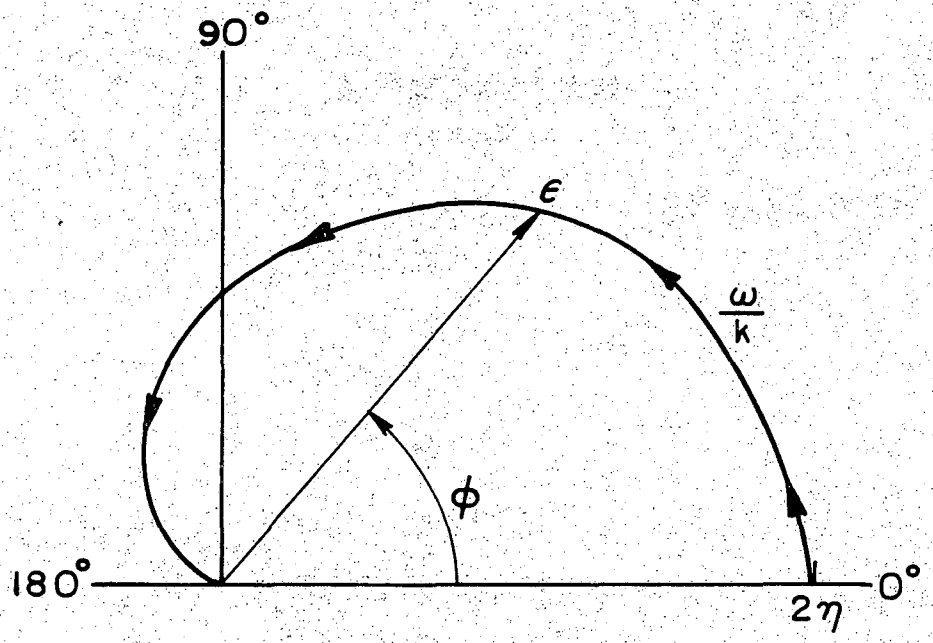

5b. Series Process
$k_d = k_1 = k$

XBL717-6986

C. Molecular Transit Effects

Up to this point, the analysis has considered the chopped beam at the surface at zero phase and the detector responding to emitted products just as they leave the surface. Actually, the reactants travel some distance from the chopper to the target. Due to finite molecular velocities (ca. 4×10^4 cm/sec), a molecule traveling 4 cm requires 10^{-4} seconds and this delay represents 36° phase lag at 1000 Hz. Furthermore, since the beam contains a spectrum (Maxwellian) of velocities, the chopped wave shape varies as the beam packet travels to the target since the faster molecules will flow into the trough left by the preceeding packet and the slower molecules will fall back into the trough from their packet. In this manner, the wave amplitude is decreased and the effect is called dispersion demodulation attenuation.

The dispersion attenuation and phase shift for Maxwellian molecular beams have been computed and tabulated[57] for different beam properties (ie., flux or density). For the beam path from the chopper to the target, it is the corrected beam flux which we require. The attenuation due to transit may be used to scale up the measured amplitude and the transit phase lag may be subtracted from the total measured phase lag. Similarly, transit from the target to the mass spectrometer ionizer modifies the total response. In this case, however, a correction based on scattered (emitted) number density is required since the ionization process is density sensitive.[53,58]

The magnitude of these corrections depends on the modulation frequency ω, the path length L, and the gas temperature T as reflected in the most probable speed $\alpha = \sqrt{(2kT/m)}$. The dispersion amplitude attenuation and phase shift are tabulated in terms of a parameter $X = \omega L/\alpha$.[57]

In reaction kinetic studies where transit effects must be corrected for, it is desirable to have short beam paths. However, transit demodulation measurements over long paths may be used to determine the speed spectrum of a molecular beam.[59]

The application of these corrections to reactions involving only linear processes is straight forward, but the loss of system sensitivity due to transit demodulation and, even worse, $1/r^2$ dilution of intensity should be considered in experiment design. For non-linear reactions, however, the particular shape of the beam wave striking the target is important. Consequently, a short chopper-to-target distance is desirable to retain a "simple" square chopped reactant feed. After solving the non-linear problem and obtaining the first Fourier coefficient, the usual corrections may be applied to the transit from the target to the detector.

D. Series Processes

As a second example consider the simple series process,

$$A_2(g) + 2S \xrightarrow{\eta I_o} 2(SA)_a \xrightarrow{k_1} 2(SA)_a^+ \xrightarrow{k_d} 2S + 2A(g) \quad , \qquad (16)$$

where adsorbed $(SA)_a$ goes to a desorption precursor state $(SA)_a^+$ by a step described by a first order rate constant k_1. The surface balances for $(SA)_a$ and $(SA)_a^+$ may be written as,

$$\text{for } (SA)_a: \quad \frac{dn}{dt} = 2\eta I_o \, g(t) - k_1 \, n \qquad (17a)$$

$$\text{for } (SA)_a^+: \quad \frac{dn'}{dt} = k_1 \, n - k_d \, n'. \qquad (17b)$$

Substituting trial solutions $n^* \, e^{j\omega t}$ and $n^{*\prime} \, e^{j\omega t}$ for n and n', the response to an excitation $g(t) = g_1 e^{j\omega t}$ may be written as,

$$k_d n^{*\prime} = \frac{2\eta I_o g_1}{(1 + j\omega/k_d)(1 + j\omega/k_1)} = \varepsilon\, I_o g_1 e^{-j\phi}$$

$$= \frac{2\eta I_o g_1\, e^{-j\tan^{-1}(\omega/k_d)}\, e^{-j\tan^{-1}(\omega/k_1)}}{\sqrt{(1 + \omega^2/k_d^2)}\sqrt{(1 + \omega^2/k_1^2)}} \quad . \qquad (18)$$

from which we see,

$$\varepsilon = \frac{2\eta}{\sqrt{(1 + \omega^2/k_d^2)}\sqrt{(1 + \omega^2/k_1^2)}} \qquad (19)$$

and

$$\phi = \tan^{-1}(\omega/k_d) + \tan^{-1}(\omega/k_1) = \phi_d + \phi_1 \quad . \qquad (20)$$

If one of the rates is very fast, the slow process becomes rate determining and the behavior of ε or ϕ reduces to that of equation 13 or 14 respectively.

A graphical representation for arbitrary k_1, k_d requires a family of curves, however for $k_1 = k_d$ the reaction vector locus is illustrated in Fig. 5b. Again the apparent reaction probability is a monotonically decreasing function of ω (for $\omega \sim k_d$) and the phase lag ϕ increases with ω but may now approach 180°.

As in the case of simple desorption, the DC rate is determined solely by the constant sticking probability. For the modulated beam experiment the Arrhenius slope Δ is given by,[56]

$$\Delta = \frac{-E_d}{R}\frac{\omega^2}{k_d^2 + \omega^2} - \frac{E_1}{R}\frac{\omega^2}{k_1^2 + \omega^2} \qquad (21)$$

The modulation frequency ω may possibly be adjusted to separate the

effects of different rate constants and thereby permit their evaluation.

Each additional series process will simply contribute its additional phase lag and introduce further amplitude reduction as a multiplier $\sqrt{1 + \omega^2/k^2}$.

E. Solution-Diffusion

Rate limiting steps controlled by the diffusion of some chemical species are common and represent another class of mechanisms.

1. Semi-infinite medium

Let us first consider a model in which dissociatively adsorbed gas may diffuse into (and out of) the bulk before desorption.

$$A_2 + 2S \xrightarrow{\eta I_o} 2(SA)_a \xrightarrow{k_d} 2\,A(g) + 2S \quad . \tag{22}$$

$$2(SA)_a \rightleftarrows \text{Bulk}$$

Solution (H solubility)
Diffusion (D_v bulk diffusion coef.)

Denoting the surface concentration by n(t) and the bulk concentration by C(x,t), these quantities are related at the surface by,

$$C(0,t) = H\,n(t) \quad , \tag{23}$$

where H is a constant solubility coefficient.

A surface balance on n may be written as,

$$\frac{d\,n(t)}{dt} = 2\eta I_o\,g(t) - k_d\,n(t) + D_v\left(\frac{\partial C}{\partial x}\right)_{x=0} \tag{24}$$

which serves as a boundary condition to the bulk diffusion equation,

$$\frac{\partial\,C(x,t)}{\partial t} = D_v\,\frac{\partial^2\,C(x,t)}{\partial x^2} \quad . \tag{25}$$

A response $C(x,t) = \xi(x)\,e^{j\omega t}$ is assumed to an excitation g(t) =

$g_1 e^{j\omega t}$ and Eq. (25) is solved subject to Eq. (24) and requiring a finite concentration at large x (semi-infinite medium boundary condition).

The emission rate of product A is given by,

$$k_d\, n(t) = \frac{k_d}{H}\, C(0,t) \quad , \tag{26}$$

and the apparent reaction probability vector

$$\varepsilon\, e^{-j\phi} = \frac{2\eta}{[(1 + j(\omega/k_d)] + H\sqrt{\frac{D_v}{k_d}}\sqrt{\frac{\omega}{k_d}}\left(\frac{1+j}{\sqrt{2}}\right)} \quad . \tag{27}$$

Eq. (27) differs from the simple desorption example by the second term in the denominator, and may be separated into its polar components as:

$$\varepsilon = \frac{2\eta k_d}{\sqrt{\left(k_d + H\sqrt{\frac{D_v\omega}{2}}\right)^2 + \left(\omega + H\sqrt{\frac{D_v\omega}{2}}\right)^2}} \tag{28}$$

$$\tan\phi = \left(\frac{\omega + H\sqrt{\frac{D_v\omega}{2}}}{k_d + H\sqrt{\frac{D_v\omega}{2}}}\right) \tag{29}$$

For strong solution-diffusion control ($H\sqrt{D_v\omega/2}$ large compared to ω and k_d) a <u>constant</u> 45° phase shift is obtained and the apparent reaction probability, ε, varies as $\omega^{-1/2}$.† Of course, under these conditions the apparent reaction probability is already very much less than 2η. At very high frequencies the diffusion control diminishes and the phase angle approaches 90° as for simple desorption. A magnified polar diagram of

---

†The frequency dependence of ε for simple desorption is ω^{-1} for $\omega >> k_d$.

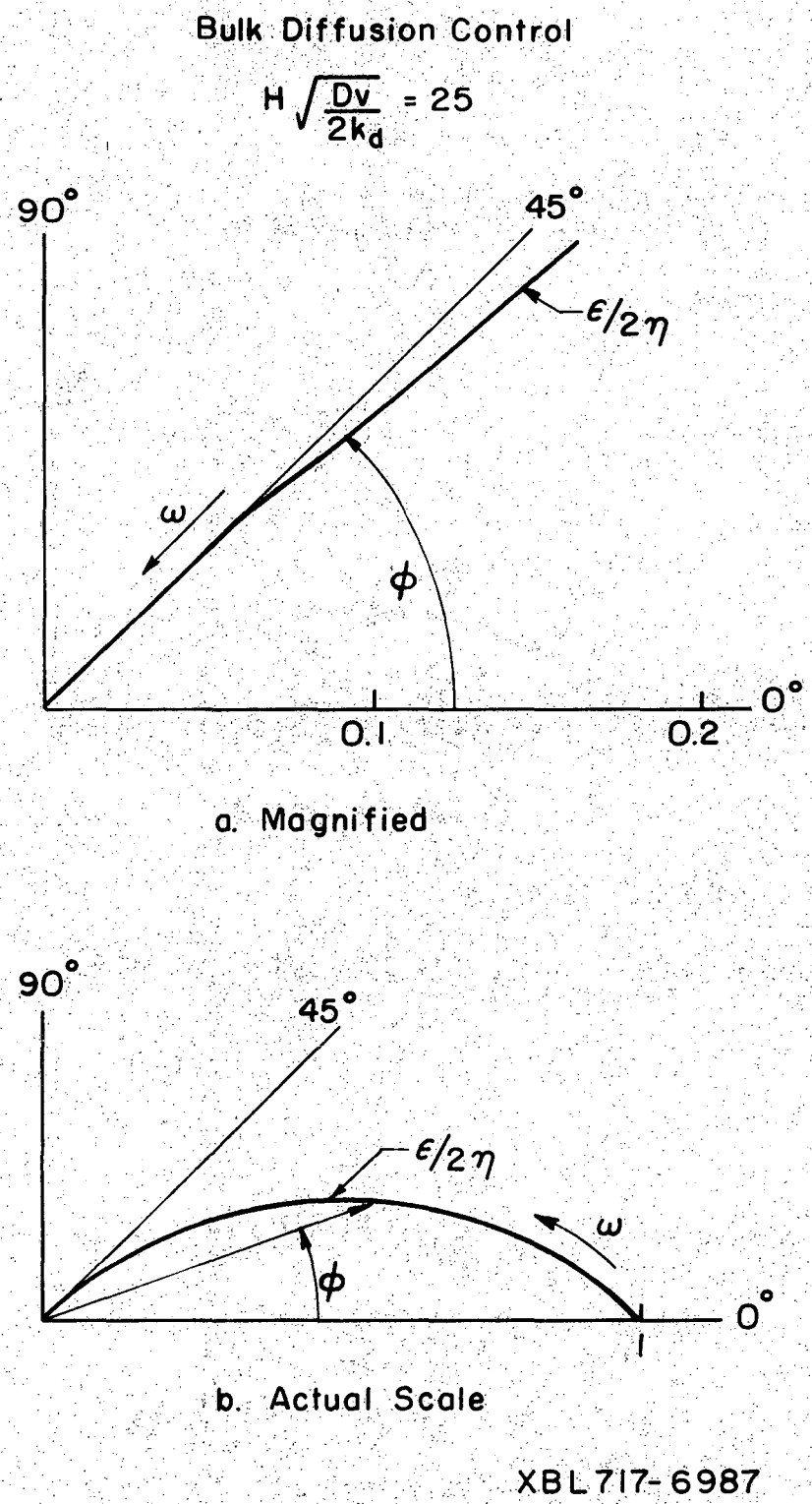

Fig. 6 Bulk diffusion controlled reaction vector locus.

this behavior is shown in Fig. 6a and the complete locus is shown in Fig. 6b for perspective.

2. <u>For a finite medium with no loss at the rear wall</u>, a boundary condition at the rear wall, $x = \ell$, may be written as

$$\left(\frac{\partial C(x,t)}{\partial x}\right)_{x=\ell} = 0 \quad . \tag{30}$$

This serves to multiply the second term in the denominator of Eq. (29) by $\tanh\left(\sqrt{j\omega/D_v}\,\ell\right)$. In the limit $\ell \to 0$ we obtain an impenetrable front surface and Eq. (12). For $\ell \to \infty$, Eq. (27) is recovered.

3. <u>For a finite medium of thickness ℓ, loss of atoms from the rear face gives a new boundary condition at $x = \ell$:</u>

$$\frac{1}{H}\left(\frac{\partial C}{\partial t}\right)_{x=\ell} = -k/H\ C(\ell,t) - D_v\left(\frac{\partial C}{\partial x}\right)_{x=\ell} \tag{31}$$

This changes the hyperbolic tangent correction term to

$$\tanh\left[\sqrt{\frac{j\omega}{D_v}}\,\ell - 1/2\ \ln\left\{\frac{\sqrt{j\omega D_v} - 1/H\ (k + j\omega)}{\sqrt{j\omega D_v} + 1/H\ (k + j\omega)}\right\}\right] \tag{32}$$

Large solubility (H large) permits the bulk to absorb the pulsing of the reactant flux so that loss through the rear face is negligible and we recover example E-2.

The interesting feature of a reaction dominated by solution - diffusion control when studied by the modulated beam technique is the 45° phase lag which is insensitive to the modulation frequency ω. It is significant that solution - diffusion control is not represented by a "characteristic time" for which the tangent of phase lag would increase with ω. Rather, the solid acts as a "flywheel" adjusting to the

modulation period, and delaying the effect of pulsing the reactant feed. Similar effects are observed in cyclic heat transfer.[60]

F. Surface Diffusion

Two mechanisms involving surface diffusion are possible.

In one case, an atom with a desorption life time of $1/k_d$ simultaneously migrates over the surface. Providing that the adsorbed atom does not wander off the edge of the target surface or otherwise out of view of the mass spectrometer detector, this surface diffusion process does not affect the response of the system; however, a more venturesome surface diffusion would provide loss of signal due to geometrical dilution.[50] This "radial spreading" problem, which was important in the H_2 - Ta study of Krakowski and Olander[41] is not considered here.

A model in which an adsorbed atom must diffuse to an active site before it is desorbed is the second case of interest. Here we have a series process of surface diffusion and desorption. We seek to represent the surface diffusion step by a phenomenolgical first order rate constant.

Consider an adatom A which diffuses on the surface to encounter an active surface atom S* with which it reacts to form adsorbed product $(SA)_{ads}$. This process may be represented as,

$$A + S^* \xrightarrow{k} (SA)_{ads} \quad . \tag{33}$$

How may we interpret this rate constant k?

1. Assume that the concentration of available S* sites is controled by thermal processes only --- <u>independent</u> of adsorbed gas concentration. Then,

$$N_{S^*} = k^+/k^- = K_{S^*} \quad , \tag{34}$$

where K_{S*} is an equilibrium constant to describe S* site concentration, N_{S*}.

Because of this rapid production and annealing of S* sites, the rate cannot be described by conventional surface diffusion of adsorbed A toward fixed S* sites. Rather, S* sites are seen as popping up and annealing out all around the surface, and occasionally appearing close enough to an atom of A to cause reaction.

The rate constant for reaction with S* sites, k, may be interpreted as follows:

The surface sees a flux of S* sites at the rate

$$k^{+} \text{ (S* sites/ cm}^{2} \text{ - sec)} \quad .$$

These survive for a mean time of $1/k^{-}$ before annealing. During this time each mobile A negotiates a mean square displacement in two dimensions which is given by the Einstein relation as,

$$\overline{r^2} = 4\ D_s\ (1/k^{-}) \quad ,$$

where D_s is the surface diffusion coefficient. Taking $\overline{r^2}$ as a cross section for the interaction of an A atom with a S* site, the rate is;

$$k\ A = k^{+}\ (4\ D_s\ /\ k^{-})\ A \quad ,$$

and by Eq. (34),

$$k = 4\ D_s\ N_{S*} \quad . \tag{35}$$

2. In analysis of fission gas bubble nucleation,[61] one considers the number of jumps made by a gas atom before it joins another. For a gas atom jumping by steps of length a in a lattice of spacing a in which

there is a concentration N of other gas atoms which may be encountered from z possible adjacent sites, the probability of an encounter in a given jump is $zN/(1/a^2)$ (which is z times the fraction of total sites which are occupied by gas atoms). The average number of jumps per encounter is n_j, the reciprocal of this probability of encounter.

By this analysis the rate of encounter of A with S* sites may be written in terms of the jump frequency Γ as,

$$k = \Gamma/n_j = z\ 4\ D_s\ N_{S*} \quad . \tag{36}$$

where the definition,

$$D_s = \Gamma a^2/4 \tag{37}$$

has been used.

3. The first order rate constant, k, may also be taken as the reciprocal of the mean time for A to diffuse the distance ℓ between neighboring S* ($\ell^2 \approx 1/N_{S*}$).[62] Using the Einstein relation for a two-dimensional random walk we have;

$$k = \frac{1}{\ell^2/4\ D_s} = 4\ D_s\ N_{S*} \quad . \tag{38}$$

4. If the S* sites are stationary and act as large enough sinks to establish a steady concentration gradient, steady state macroscopic diffusion theory may be applied.

The total surface area is divided into independent circular cells of radius, $R = 1/\sqrt{\pi N_{S*}}$, centered on the S* sites, which have an effective radius, r_S. The rate of capture of adsorbed atoms by active sites, G, is related to the phenomenological rate constant, k, by,

$$G = k\ \bar{n} \tag{39}$$

where $\bar{n}$ is the average concentration of adsorbed atoms in the circular cell (to be determined by diffusion theory).

Fick's law for surface diffusion (characterized by a surface diffusion coefficient D_s) in cylindrical coordinates is,

$$D_s \frac{1}{r} \frac{d}{dr}\left(r \frac{dn}{dr}\right) = -G \quad . \tag{40}$$

Since the active site S* is a perfect sink for adsorbed atoms, the boundary condition at $r = r_s$ is $n(r_s) = 0$. The independent cells do not have any flux of atoms between them therefore, $(dn/dr)_{r=R} = 0$.

Equation (40) is solved subject to the boundary conditions at r_s and R to yield n(r) which is then averaged over the annulus to give $\bar{n}$. The phenomenological rate constant is then identified by inserting the result into Eq. (39). This procedure yields:

$$k = \left[\frac{2\pi}{\ln(R/r_s)}\right] D_s \, N_{S*} \quad . \tag{41}$$

Equations (35), (36), (38), and (41) all indicate that the first order rate constant describing migration of reactant to active sites on the surface is proportional to the product of the surface diffusion coefficient of the migrating atom (D_s) and the density of active sites (N_{S*}). The constant of proportionality differs from one derivation to another but appears to be between one and ten.

G. Branch Processes

Some reactions may yield the same products by means of different paths. These reactions are particularly interesting if the reactions along different paths proceed at different rates.

Consider for example a two branch process in which dissociated A

enters branch 1 with probability P_1 or enters branch 2 with probability P_2, $(P_1 + P_2 = 1)$. The desorption rate constants, k_1 and k_2, respectively, are assumed to be different. The process may be represented by:

$$A_2 \xrightarrow{\eta I_o} 2\,(A)_{ads} \begin{cases} \xrightarrow{P_1} (SA)^1_{ads} \xrightarrow{k_1} S + A(g) \\ \xrightarrow{P_2} (SA)^2_{ads} \xrightarrow{k_2} S + A(g) \end{cases} \tag{42}$$

Other steps more complicated than simple adsorption could be incorporated into a branch path, and more than two branches are possible.

Branch processes may arise if different types of surface sites participate in significant proportions in the reaction but at different rates.

The apparent reaction vector for the reaction sequence represented by Eq. (42) is,

$$\varepsilon\, e^{-j\phi} = \frac{2\eta P_1}{1 + j(\omega/k_1)} + \frac{2\eta P_2}{1 + j(\omega/k_2)} \quad . \tag{43}$$

Plots of the apparent reaction vector locus as frequency is varied are useful for analyzing branch processes. For $k_1 = k_2 = k_d$, the paths are indistinguishable and Eq. (43) reduces to Eq. (12) so the apparent reaction vector locus is a semicircle as in Fig. 5a. At the other extreme, for $k_2 \gg k_1$, the second process acts at full strength while the slow first process runs its course then the second process undergoes its demodulation thereby tracing out two semicircles. For $P_1 = P_2 = 0.5$, the apparent reaction vector loci for various ratios, k_2/k_1, are plotted in Fig. 7a. It is seen that increasing the separation of the k's deepens the dip in the curve and that a clear distinction between single or

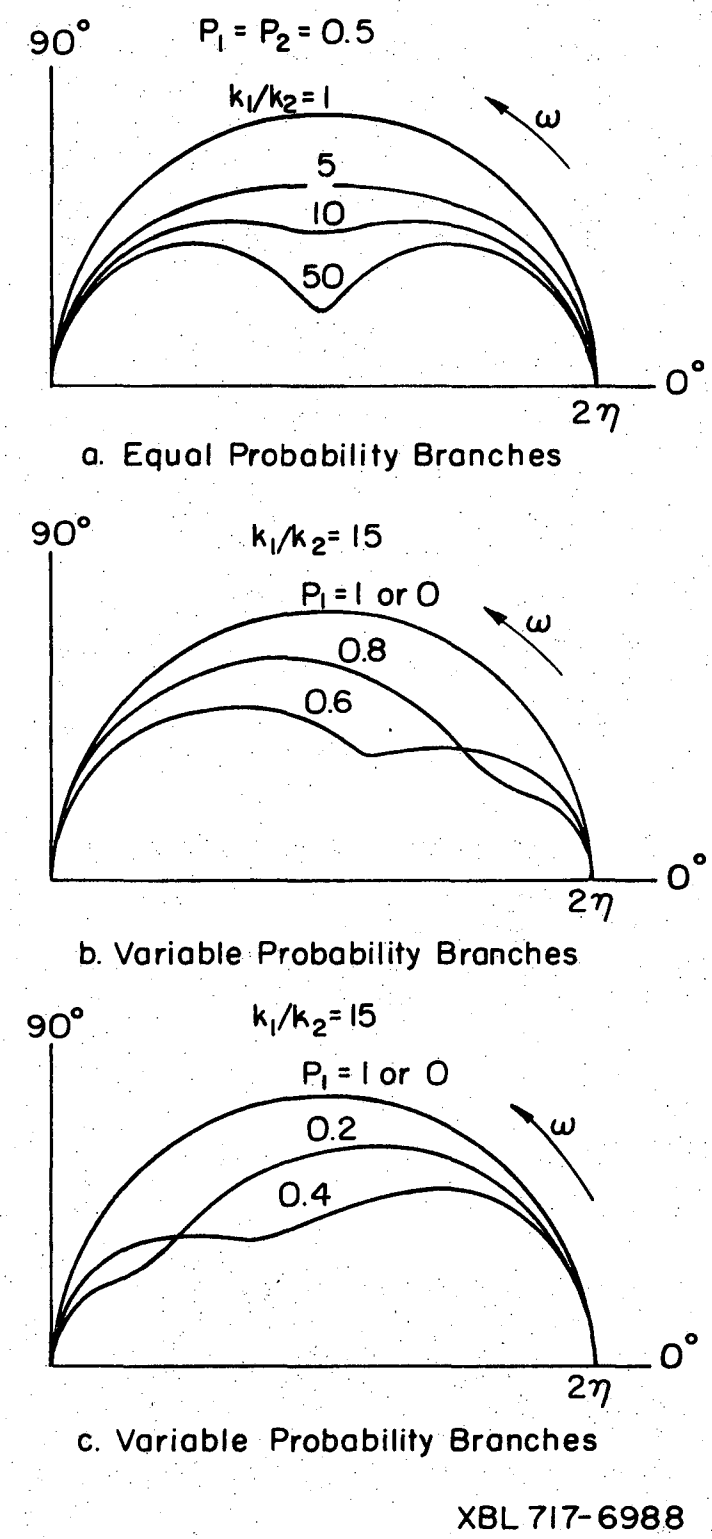

Fig. 7 Branch process reaction vector locus.

branch processes requires a rate constant ratio of 5 or greater.

By adjusting the P's and k's (and adding additional branches if necessary), the theory may be tailored to give a satisfactory match to virtually any linear reaction process. Figures 7b, 7c illustrate the effect of juggling the P's.

H. Experimental Philosophy

The reaction mechanisms reviewed in this chapter are not all-inclusive, and other schemes may represent a given reaction more closely. The best reaction model is one that encompasses all reliable data with the fewest adjustable parameters of physical significance.

The specific rate of a first order chemical reaction depends on the particular reaction mechanism and the values of the controlling rate constants. It is the aim of reaction kinetic studies to ascertain the reaction mechanism and to evaluate the rate constants of the elementary steps which constitute the overall process.

Non-linear reactions show a dependence of the reaction probability on the reactant pressure as well as on temperature. This extra complication, although not insurmountable, requires a more tedious analysis as suggested earlier and will be illustrated for some of the data in this work.

Primary experimental variables in a modulated molecular beam chemical kinetic study are the reactant gas beam intensity I_o, the target temperature T_s, the modulation frequency ω, (rad/sec) and the beam temperature T_B. Data obtained from an experiment are the apparent reaction probability ε, and the reaction phase lag ϕ. Basically, one expects to determine: (1) the reaction order by varying I_o, (2) the activation energy(s), E_a, by varying T_s, and (3) the value of the rate constant(s),

k, and therefore the pre-expontential A by variation of ω. In the low frequency limit (if experimentally accessible) the sticking probability η could be determined. Typically, adjustment of the modulation frequency, ω, does not effect a clean separation of different kinetic steps. Nevertheless, an organized investigation of a reaction can produce the desired information. The beam temperature T_B may be varied to determine if the rate is a function of the state of the reactant gas.

Preliminary experiments should be done first to determine if the experiment is sufficiently sensitive over a range of temperature, pressure, and modulation frequency to give useful data. Next a convenient temperature and frequency are chosen and the reactant gas pressure is varied to determine reaction order.[†] Reaction order determinations should eventually be made at several temperatures and frequencies.[††]

With the reaction order determined the pressure and temperature are set and the frequency ω is varied to obtain data for a reaction vector locus plot. Characteristic features such as the number of humps, their relative sizes and their separation are considered to determine the complexity and type of the reaction mechanism to fit to the data. For linear processes, the "frequency scan" data will determine the rate constants and branching ratios at any temperature and pressure. Rate constants determined by frequency scans at different temperatures may be plotted Arrhenius fashion to obtain the activation energy(s) E_a.

[†] A square modulated beam has no second or other even harmonics, but nonlinear surface processes would generate even harmonics. Measurement of the even harmonic content of a reaction product signal could be used to verify first order behavior but the sensitivity of this determination is probably quite low.

[††] The third, fifth and higher harmonics (odd, of the square wave) could be used with linear reactions as a means of extending the frequency range of observation. However, the beam intensity of these higher harmonics is reduced from that of the fundamental by factors of 1/3, 1/5, ... respectively.

III EXPERIMENTAL

A. Description of Apparatus

1. General Features

Although a great many experimental parameters might be adjusted to probe all the intricacies of a heterogeneous reaction, the experimental complexities introduced with each variable generally reduce over-all system sensitivity. In order that gas-solid systems with reaction probabilities in the range of 10^{-4} to 10^{-5} might be studied, a system emphasizing sensitivity (or large signal-to-noise ratio) was developed. To this end the system was designed (1) to be compact, to minimize $1/r^2$ beam spreading losses, and (2) to use differential pumping to provide maximum isolation of chopped beam and reaction product signal (except when due to interaction of the reactant beam with the target surface).

The beam transport portion is shown in Fig. 8 with the general vacuum system labeled to assist identification of features in the equipment photographs, Figs. 9, 10, and 11. Unlike typical apparatus for molecular beam scattering studies there is no provision for variation of the angle of beam incidence or the angle of reaction product observation. Both directions are fixed at 45° to the surface normal and are coplanar. There is also no provision for mechanical velocity selection of beam molecules which is typically accomplished by a series of rotating toothed discs in the beam path. Incorporation of angular variation and velocity selection generally results in a bulkier system with much greater $1/r^2$ dilution of the beam as well as a cluttered vacuum tank with reduced local pumping speed just where good pumping is desired. There has been,

0 0 0 0 3 6 0 5 3 4 8

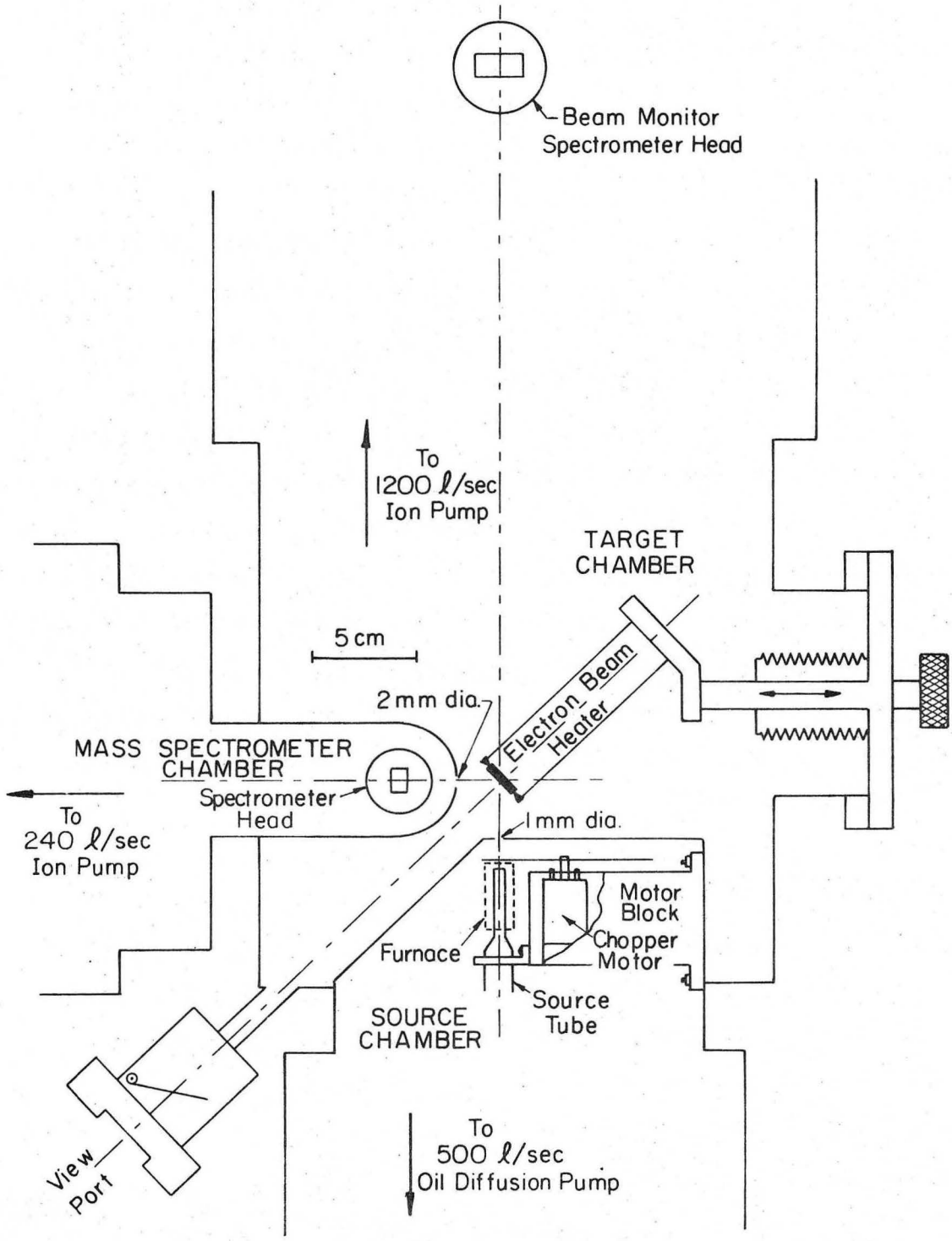

XBL 717-6989

Fig. 8 Beam transport geometry (plan view).

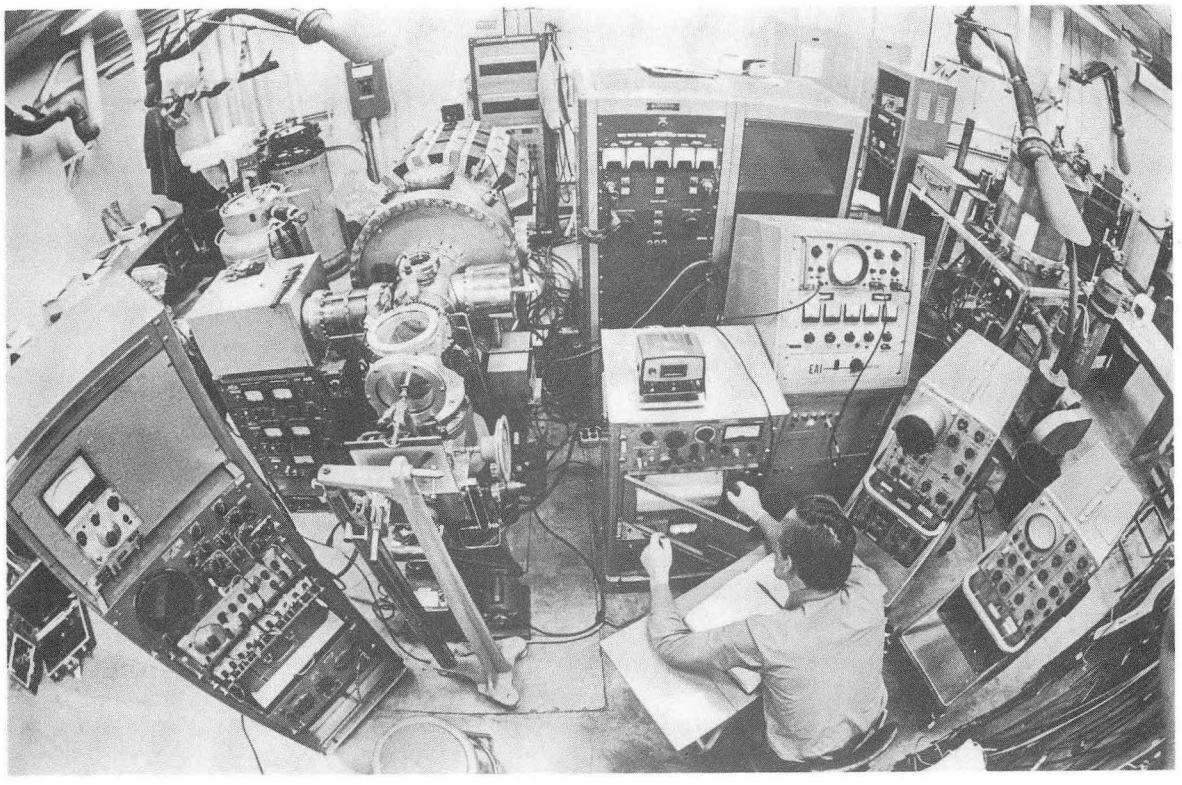

XBB 715-2247

Fig. 9 Equipment layout as seen through "fish eye" lens.

0 0 0 0 3 6 0 0 3 4 9

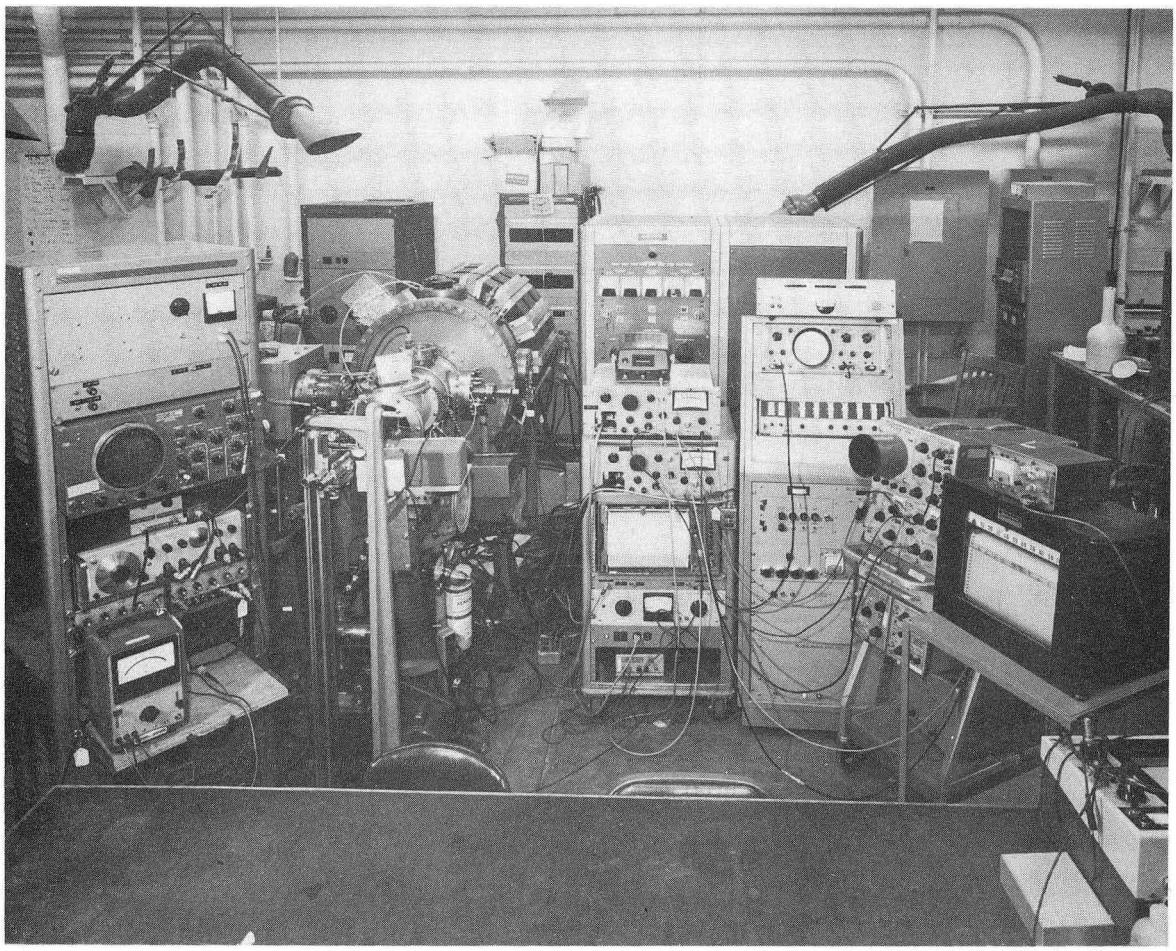

XBB 715-2150

Fig. 10 Equipment layout--operating area. Major components from left to right are: Modulation electronics, vacuum system, signal processing electronics, and quadrupole mass spectrometer controls backed by the 10Kw electron beam heater power supply.

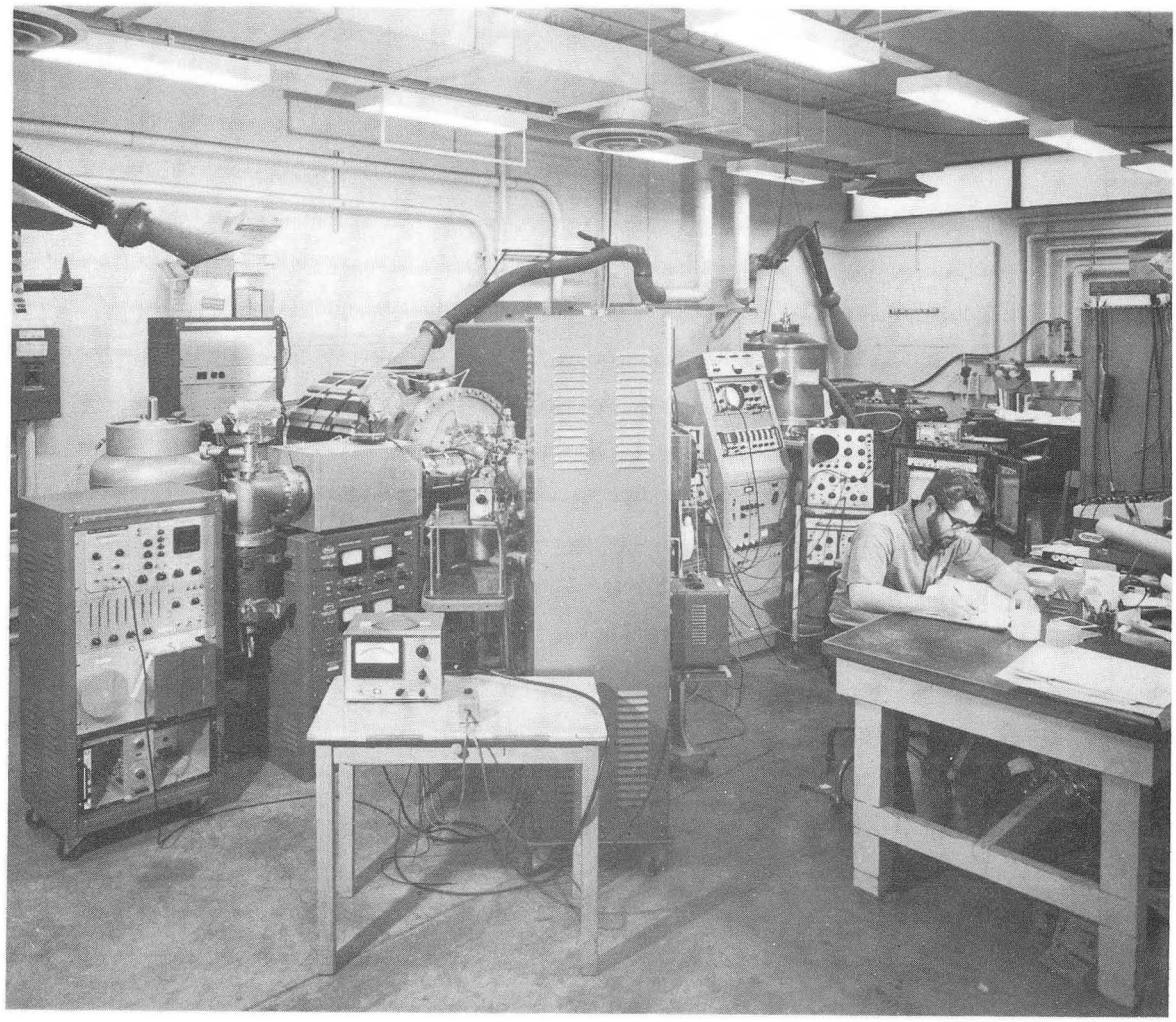

XBB 715-2155

Fig. 11 Equipment layout--looking toward pyrometer viewport. At the left is the CAT unit for waveform measurements followed by 3 ion gauge controllers and topped by the 240 liter/sec ion pump.

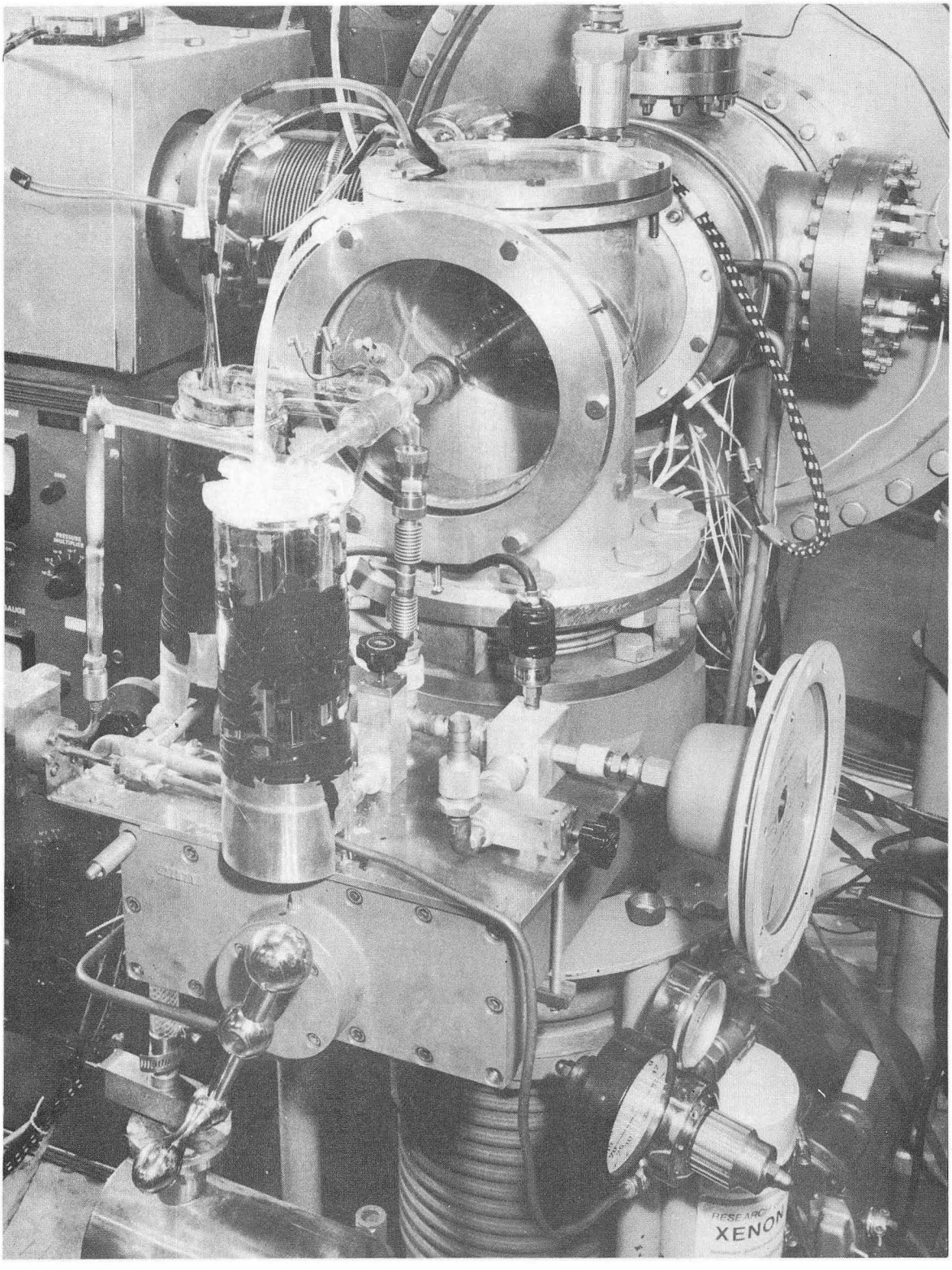

XBB 715-2154

Fig. 12 Gas inlet system and source chamber.

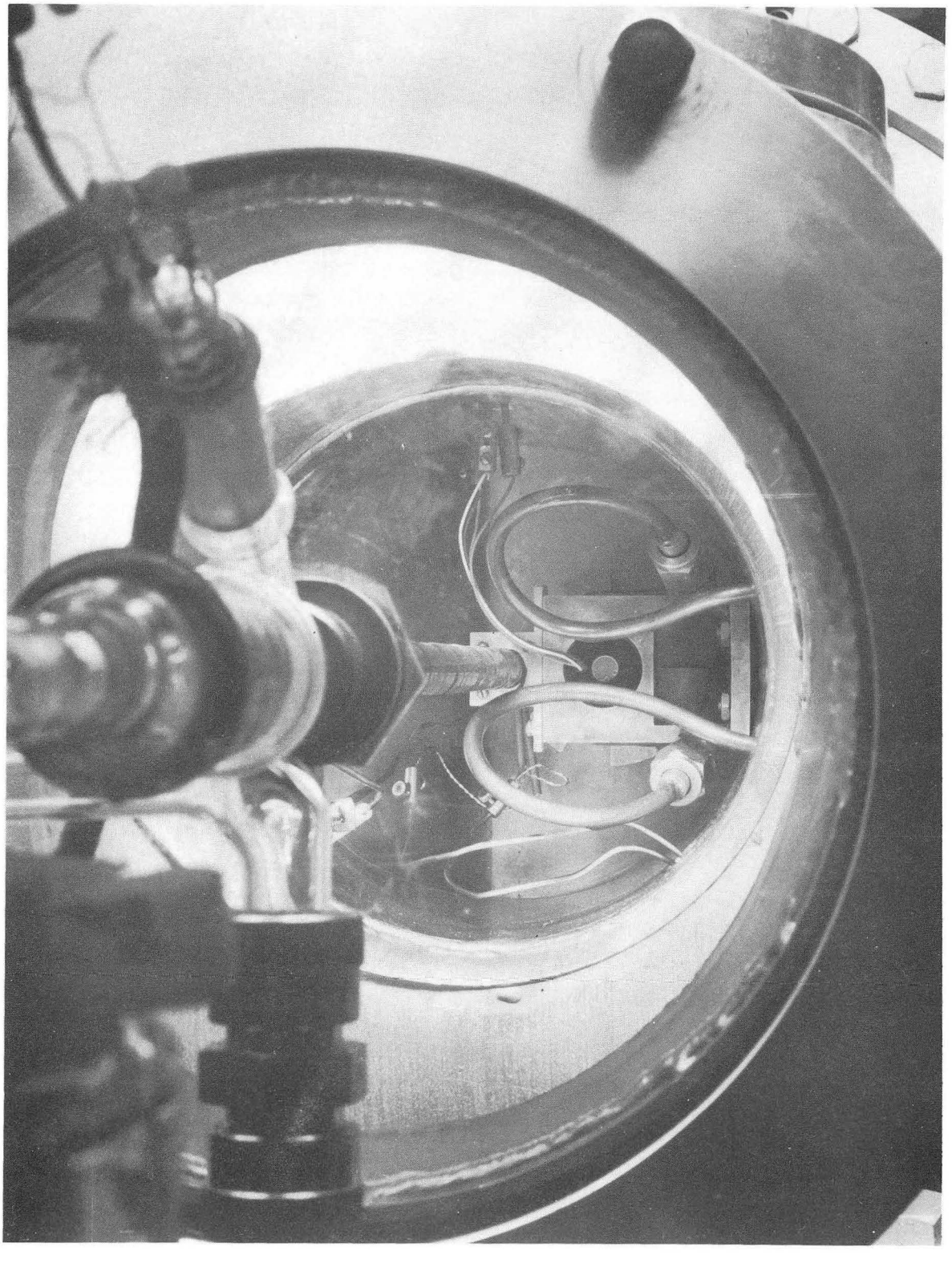

XBB 715-2153

Fig. 13 Interior of source chamber.

0 0 0 0 3 6 0 5 3 5 1

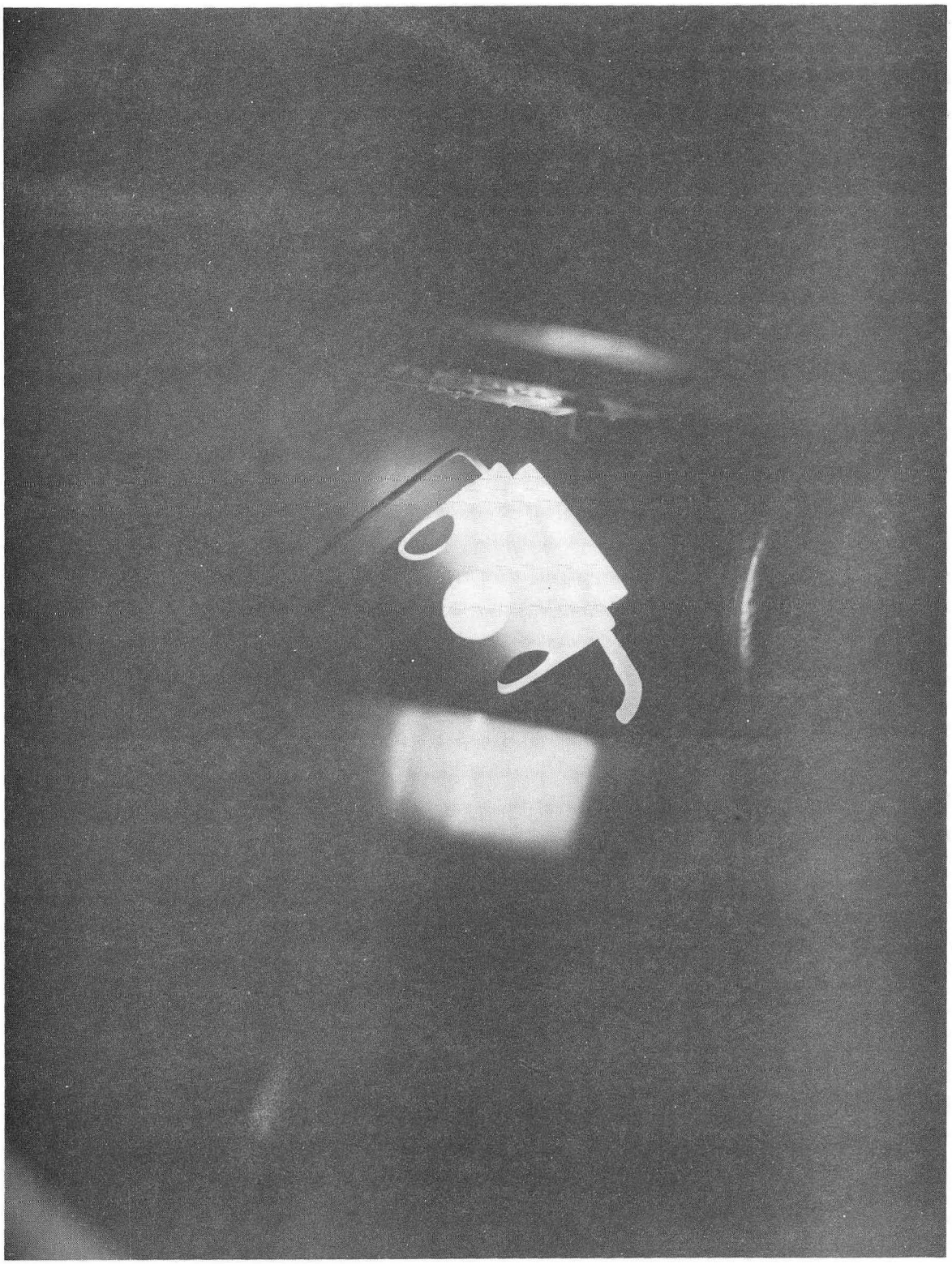

XBB 715-2151

Fig. 14 Interior of target chamber illuminated by a hot target. The beam enters from above through a hole in the dimpled foil heat shield.

however, an attempt to develop such a system.[63]

Information on the condition of the target surface and possible chemisorption of reactant or background gases could possibly be obtained by low-energy electron diffraction (LEED) or Auger electron spectroscopy,[63,64] but no extra space for the LEED optics and detection screen has been provided. Furthermore, the high heat loads from the hot target could damage the LEED or Auger detection screen if one had been crowded into the vacuum system. LEED has been used successfully in chemisorption studies under milder environmental conditions.[64]

2. Vacuum System

Figure 8 illustrates the modular system design--flange mounted components are inserted like fingers into a glove. Many individual components may be dismounted for adjustment or repair without disturbing adjacent parts. The system consists of three vacuum chambers: (1) the beam source chamber, (2) the target chamber, and (3) the mass spectrometer detector chamber.

The beam source exhausts into the source chamber which is fabricated as a cross from 7-inch diameter aluminum pipe (Figs. 9, 10, 12, 13). The source tube enters through a glass plate capping one horizontal arm and the beam is extracted through a collimating orifice in the center of the opposite arm. The top arm is covered by a large glass view port, and the bottom arm leads to the vacuum pump. This chamber is evacuated by a NRC 500 liter/second, 6-inch oil diffusion pump with liquid nitrogen baffle and gate valve. A Welch #1397 mechanical pump with dry trap is used to rough the system or back the diffusion pump. Within the source chamber are the chopper motor, a beam heater, and a source bake heater. Electrical connections for these devices and cooling water for the motor are

introduced through Cajon "O" ring compression fittings placed around the periphery of the arm containing the beam source tip. Pressure measurement is by a type RG-75 "Bayard-Alpert" gauge using a Veeco RG-31X ionization gauge controller. The gauge tube is also mounted in a Cajon fitting near the beam source tip. Typical operating pressures of less than 1×10^{-4} torr are obtained in this "O" ring sealed chamber when the strongest beam is generated.

The target is enclosed in a 304 stainless steel chamber pumped by an Ultek 1200 liter/second ion pump (Fig. 8). The beam enters through a 1 millimeter diameter collimating orifice and travels along the axis of this large pump. Two tungsten foil radiation heat shields are placed in the target chamber on the wall between the hot target and the beam chopper to protect the chopper motor (Fig. 14). A secondary quadrupole mass spectrometer head (Electronics Associates Inc.) is positioned in the target chamber on the beam flight path to permit monitoring the primary beam composition when the target is retracted. A small view port with a sapphire window looks directly at the target face for temperature measurement by an optical or infrared pyrometer. Another view port at the rear of the 1200 liter/second ion pump, on the beam axis, is used for system alignment. Two larger viewports are provided for inspection of target chamber contents: one (4-inch dia.) above the target holder, and one (6-inch dia.) beside the beam monitor spectrometer head. Clean roughing of the target chamber and large ion pump may be accomplished by two cycles of a single Ultek sorption pump connected through a viton "O" ring sealed valve at the rear of the ion pump. Pressure is measured in the target chamber by another RG-75 ionization gauge tube using a second RG-31X controller. This copper gasket sealed chamber attains a

base pressure of $1x10^{-9}$ torr and operates at about $3x10^{-8}$ torr under normal beam load.

The mass spectrometer head for reaction product detection is installed through an adjustable bellows in its own separately pumped vacuum chamber. The ionizer is positioned so that it receives molecules scattered perpendicular to the primary beam (Fig. 8).

Molecules entering the mass spectrometer chamber may pass freely through the spectrometer ionizer (if not ionized) and travel through a 6-inch length of stainless steel bellows, an open mesh shield screen, and a 240 liter/second Varian ion pump. The outboard end of the Varian ion pump is terminated in an elbow which connects a Varian sublimation pump and its piggy-back single element ion pump. A glass view port is provided in the side of the elbow on line with the scattered beam direction for alignment purposes. Roughing of this mass spectrometer chamber is accomplished only through the 2 mm diameter collimating orifice in the wall between the spectrometer and target chambers. Tubulation in the mass spectrometer chamber is nominal 6-inch 304 stainless steel. The pressure in this chamber is also monitored by a RG-75 ionization gauge tube using a Varian 971-0003 controller. Operating pressure in this all metal chamber is typically $4x10^{-10}$ torr with full molecular beam load.

Both the target and spectrometer chambers receive a bake-out on every pump down from atmosphere. The 1200 liter/second Ultek pump has internal heaters, and the 240 liter/second Varian ion pump uses an external heat shroud. Baking is done for 8 hours at 200°C without removing the pump magnets. Appendages are baked by heat tapes. The sublimation pump is easily baked by stopping its cooling water.

3. Gas Inlet System

Molecular oxygen is taken from the gas cylinder and a Matheson #3500 stainless steel regulator through stainless steel tubing to a Granville Phillips "variable leak" valve. The controlled gas flow then enters an all glass (Pyrex and fuzed silica) concourse (Figs. 12, 13, 15). First the gas passes along two tungsten wire electrodes between which an electrical discharge was maintained in early experiments to help purify the oxygen.†

Beyond the electrode section the gas passes through a coiled Pyrex cold trap section containing glass beads. The gas then flows down a long thin quartz delivery tube up to the source tip. In some applications, (using dissociated oxygen) it is desirable to "fast" flow the gas by the source tip to minimize recombination. For operation in this mode, the excess gas is removed by a channel coaxial to the delivery tube. This exhaust channel is also protected by a bead-filled coiled cold trap. Source tube pressure is measured, at this down-stream position after the second cold trap, by a Wallace Tiernan gauge (0.1 - 20 torr) or a thermocouple gauge both of which were calibrated against a traped McLeod gauge. The source tube is evacuated by a Welch #1402 mechanical pump with dry trap connected down stream of the second cold trap. Throttling

---

†Nitrogen (mass 28) is a typical contaminant in reagent oxygen and unfortunately has the same mass number as an important product species, carbon monoxide, in the reaction system studied. It was expected that the electrical discharge would form oxides of the nitrogen which could be cold trapped. An AC arc was struck between the 5 mm spaced tungsten electrodes by a power supply having a peak voltage of 1200 volts but resistively limited to a maximum average current of 200 milliamperes. Glow discharge purification was partially successful --- the mass 28 contaminate could be reduced to about 2×10^{-5}; however, a quanity of very high purity oxygen was acquired (Air Reduction Co., Rare Gas Purification Division, Riverton, N. J.) which needed no further purification by this means.

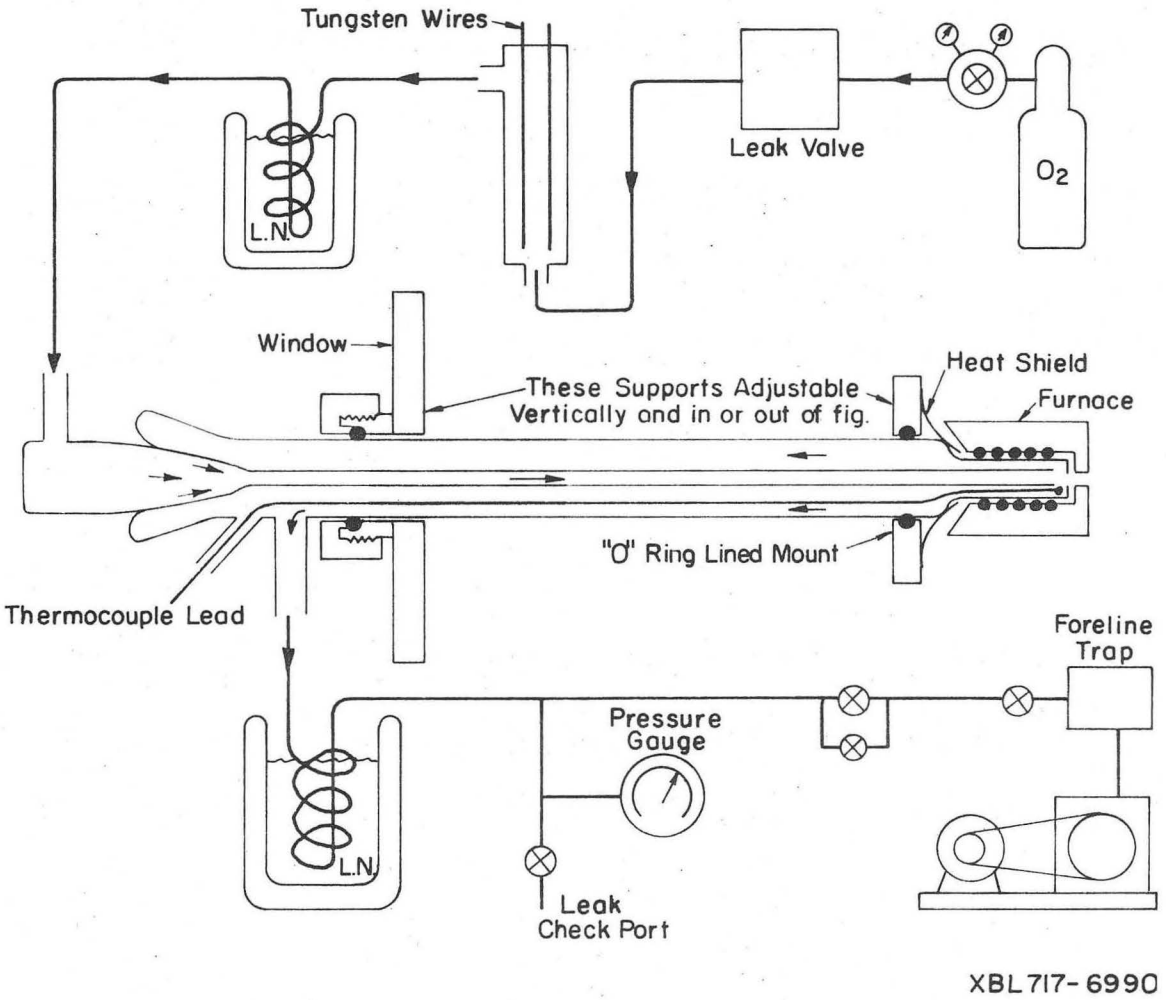

Fig. 15 Gas inlet system: Gas inlet schematic, cutaway of the beam source, source tube evacuation schematic. All glass construction between cold traps.

valves permit controlling the degree of pumping to adjust source pressure under flow conditions.

Automatic liquid nitrogen level control is provided for these two cold traps and the liquid nitrogen baffle on the source chamber diffusion pump. A device which detects when the level is low then delivers liquid nitrogen for a fixed time period works best. Other systems which detect high and low liquid levels give erratic performance unless very clever shielding is provided to prevent splashing cold liquid on the thermal sensor during filling.

4. Beam Source

The beam source chosen for this work consists of an array of ~70 small 0.05 mm diameter capillaries formed in a 0.3 mm thick quartz membrane by electron beam milling† (Fig. 16). The membrane closes off a 4 cm length of 6 mm quartz tube which is joined to a 30 cm length of 12 mm quartz tubing (Fig. 15). The small gas delivery tube lays inside this larger source tube assembly and extends to within 5 mm of the membrane closure. Non-metalic construction was used to permit use of atomic oxygen and quartz was favored to allow the source to be heated to generate a high temperature beam. A small furnace that slips over the narrow source tip consists of a boron nitride liner which is threaded internally to hold a platinum heating coil. The furnace liner is enclosed by tungsten foil heat shields and a stainless steel can except for a small hole for the beam to pass through. Beam source temperature is measured by a Pt, Pt-Rh 10% thermocouple (chosen for its inertness)

---

†Electron beam milling was done by TRI-D Corporation, 7 Johnson Avenue, Plainville, Conn. 06062. The molecular beam forming qualities of this source have been investigated in reference (70).

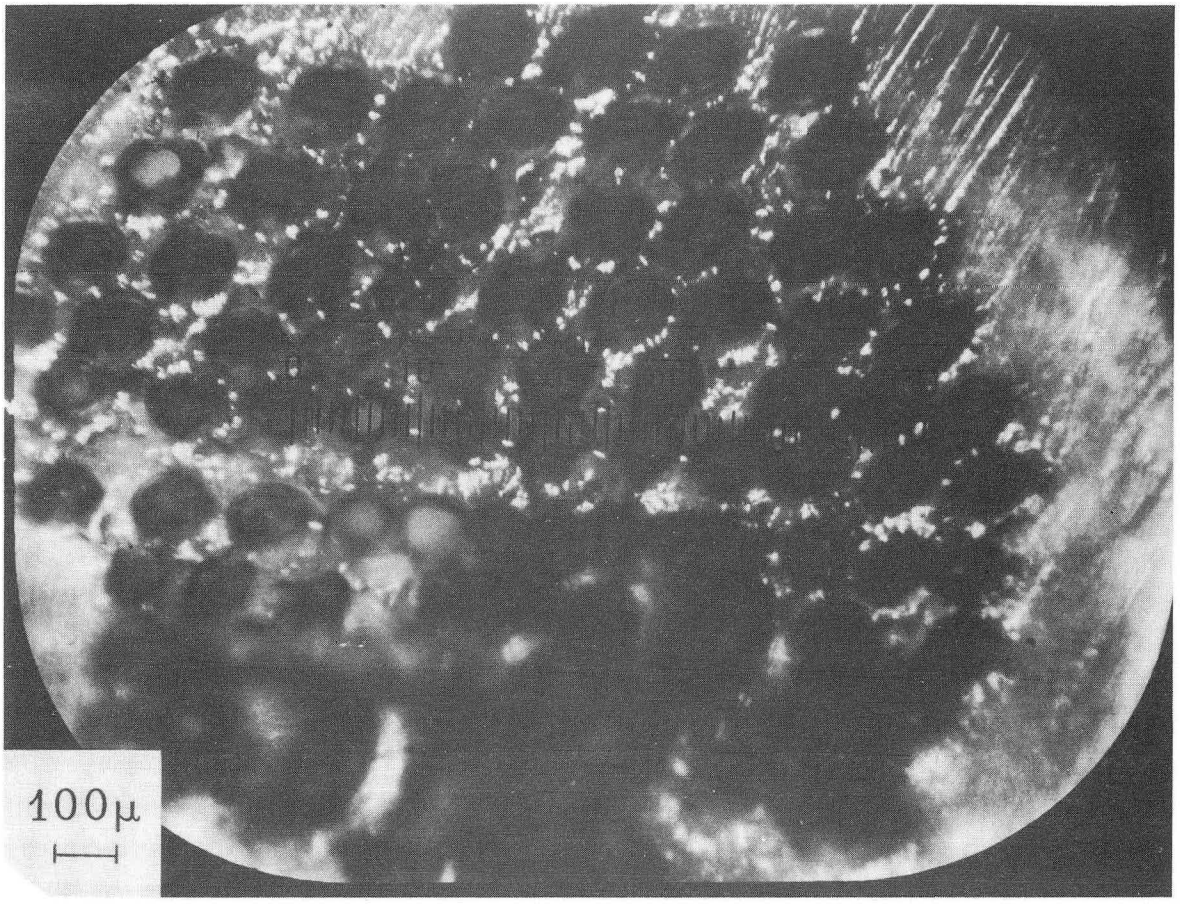

XBB 6811-7098

Fig. 16 Quartz membrane source (50×).

0 0 0 0 3 6 0 3 5 5

inside the source tube at the tip. The thermocouple leads are insulated in drawn quartz capilaries and the leads exit through black wax seals 35 cm away from the source tip. Thermocouple output voltage is measured by a Leeds and Northrup #8687 potentiometer or a Hewlett Packard 412A millivoltmeter. An Electronics Research Associates TR 32-8 regulated power supply (4-32 volts @ 8 amps max.) has been used to heat the source tube to a cautious 950°C.

The source tube is centered on the horizontal axis of the 7-inch aluminum cross previously described, and enters through a Cajon "O" ring fitting in a glass window on one arm of the cross, Figs. (12, 13, 15). The nose of the source tube is held in an "O" ring lined sleeve about the 12 mm tubing. Both mounting points are adjustable for aiming the beam. The glass window may be slid around on its "O" ring seal before being clamped in place. The front mount may be adjusted vertically using slotted holes or it may be moved sideways by compensating shims. This aiming motion may be compared to the technique used with a billiard cue.

A flexible collar of radially slotted tungsten foil protects the front "O" ring from damage by the beam heater.

A nichrome ribbon wrapped around the 30 cm length of source tube provides for its bake-out.

5. Beam Modulation and Reference Signal

In this apparatus the beam was chopped by a rotating slotted disc driven by a synchronous motor which is mounted in a water cooled brass block in the source chamber near the collimator (Figs. 8, 13). This motor mounting block also holds the front source tube mount. A Globe #SC-53A 111-2, 2 phase, 6 pole motor was used with a 3-inch diameter symmetrically cut 6-blade chopper to provide a beam chopped at twice the

frequency of the power driving the motor. Separation of modulation rate from the motor power frequency eliminates this source of interference. The chopper disc was tested for static balance by suspending it at its hub on a conical pivot. An imbalance equivalent to 1 milligram on the edge could be detected and adjustment was made by grinding the face of heavy blades.

In similar applications, the motor is powered by an audio oscillator through a power amplifier. The two phases of power necessary are obtained by using a phasing capacitor in series with one winding. This phase shifting approach is awkward for a wide frequency range of operation since quite an assortment of fairly large (~1 mfd.) capacitors must be switched in as speed is varied. Also, different drive is supplied to the windings at extremes of the frequency range, resulting in pulsing rotation and requiring excessive power dissipation to maintain motion. A capacitive load is presented to the amplifier and non-sinusoidal driving voltages are common. Considerable improvement is obtained by feeding each motor winding from a separate power amplifier, the phase shift for one winding being obtained before power amplification. This arrangement presents a properly phased sinusoidal driving voltage to each winding and just sufficient drive power may be used to obtain smooth rotation.

Motor power was supplied by two Dynakit Mark III 60 watt amplifiers driven by a Hewlett Packard 203A audio oscillator which conveniently provides two individually attenuated outputs with adjustable phase angle between them. A Dumont 304-AR oscilloscope was connected to the motor windings to display the 90° Lissajous circle pattern which served to indicate phasing errors or overloads. With this arrangement the motor (designed to operate at 8000 rpm) was used as received without change of

lubricants from 20-15,000 rpm. Bardeen Bartemp bearings have been tried but were not found to be any better than those supplied with the motor.

A reference signal synchronized to the beam chopping is typically obtained by using a light and photocell placed on opposite sides of the chopper blade. Our compact design precluded this method. Instead, the chopper is viewed under a synchronized stroboscope flash. By adjusting the delay of the strobe sync signal, the chopper blade may be observed at a particular reference "position" coincident with this synchronizing pulse which is then used for the reference signal. This strobe technique also provides for inspection of the rotating motion since pulsing rotation is seen as flutter. A slow precessing motion is also sometimes observed. Both these anomalies may be corrected by adjusting the drive power (if the motor bearings are sound).

A signal from the motor drive oscillator is used to synchronize the strobe. Since the chopping rate is twice the motor driving frequency, the rate of this synchronizing signal from the motor drive oscillator must be doubled to provide a proper sync and reference signal. This is accomplished with a full wave bridge rectifier fed through a good quality audio frequency isolating transformer from a square wave output on the model 203A oscillator.[59] This derived chopping rate pulse train synchronizes two series connected Data Pulse 101 pulse generators which provide the required adjustable delay for the strobe reference synchronizing pulse.

At the highest chopping rate (1500 Hz) the strobe light (General Radio 1531-AB) would be forced to operate at a considerably higher rate than its design intended (25000 rpm or 417 Hz). Exceeding the design duty cycle was found to diminish the flash tube life and result in erratic firing. The effective strobing rate was therefore reduced by dividing

the reference pulse rate with up to two series connected flip-flops providing division by 4, 2, or 1. The level changes of the flip-flop output were differentiated and these trigger pulses were then amplified and used to trigger the strobe. The strobe flash was not significantly delayed by this extra electronic processing of its trigger pulse.

The rotating chopper wheel was viewed under strobe flash by a 25 power cathetometer and the pulse generator delay was adjusted to "position" a blade edge at a reference mark scribed on the vacuum chamber wall. This cathetometer magnification was sufficient to set the reference to better than 0.2° of modulation phase angle.

Ideally, the reference "position" mark would correspond to where the chopper is half open to the beam. Under these conditions the beam comes on at zero phase angle. Generally, however, there is a mechanical phase shift due to particular mounting positions of collimator and chopper axes with respect to the reference mark. This shift from "absolute zero of phase" may be determined by extrapolating phase data, (from a simple process like beam transit) to its zero frequency ("zero absolute phase") value.[59] In order to obtain absolute phase values, this pre-shift of phase is determined and subtracted from measured phase data.

Fast rise times of the beam modulation envelope may be obtained with (1) narrow beam and wide chopper blades (and gaps) or (2) wide beam scanned by a narrow gap. A round beam symmetrically modulated (without sweeping an arc) by a chopper with gap or blade dimension equal to the beam diameter gives a sinusoidal variation of beam intensity. This same sinusoidal rise and fall occurs during the opening and closing times when small round beams are modulated by wide choppers. A measured wave shape of the reflected oxygen beam is shown in Fig. 42 and illustrates

the nearly square beam modulation profile obtained for this work. A beam which is well described by on and off intensities only is easiest to use to evaluate non-linear reaction mechanisms.

6. Target Preparation, Mounting and Heating

Pyrolytic graphite targets are prepared from discs 15 mm in diameter and 5 mm thick cut from bulk pyrolytic graphite. The discs were supplied by Union Carbide in two configurations with the basal plane parallel or perpendicular to the disc face. Target details are shown in Fig. 17.

The pyrolytic graphite targets are heated from the rear by electron bombardment. Figure 18 shows the target holder - electron beam heater assembled on a linear motion feedthrough and 6-inch vacuum flange. A coaxial electron beam heater assembly of tantalum with alumina insulation is used to hold a flat spiral or "pancake wound" tungsten filament 3 mm behind the target. The filament is heated resistively and biased to high potential by a 10 kilowatt Temescal Metalurgical Corp. EBH-10M-3 power supply. The target is mounted in the end of the tantalum outer tube and is at ground potential (Fig. 14).

The highly anisotropic thermal conductivity of pyrolytic graphite presents a great obstacle to achieving proper heating of the target face. The thermal conductivity normal to the basal planes (c direction) is 100 times less than along the basal planes (a direction). Heating a target with a basal plane face from the rear is quite difficult because appreciable heat is lost by radiation from the front face, and the rear face of the target must be heated excessively in order to raise the front face to the desired temperature. This problem was solved by removing material from the rear center of the target leaving a thin front face at the end of a thin sleeve. Back-to-front conduction was increased by this modification which permitted temperatures of 1800°K to be reached.

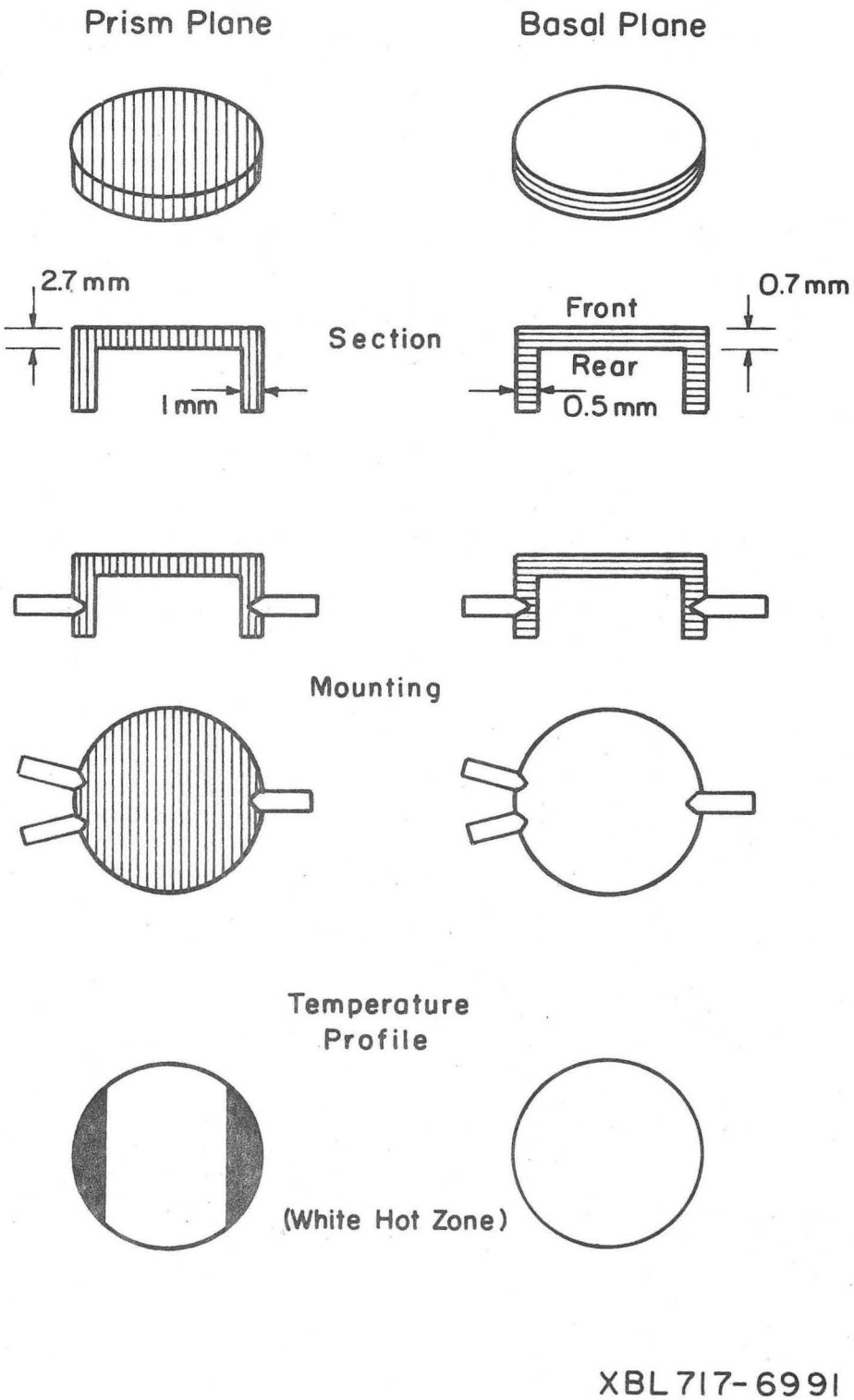

Fig. 17 Target details.

0 0 0 0 3 6 0 5 3 5 8

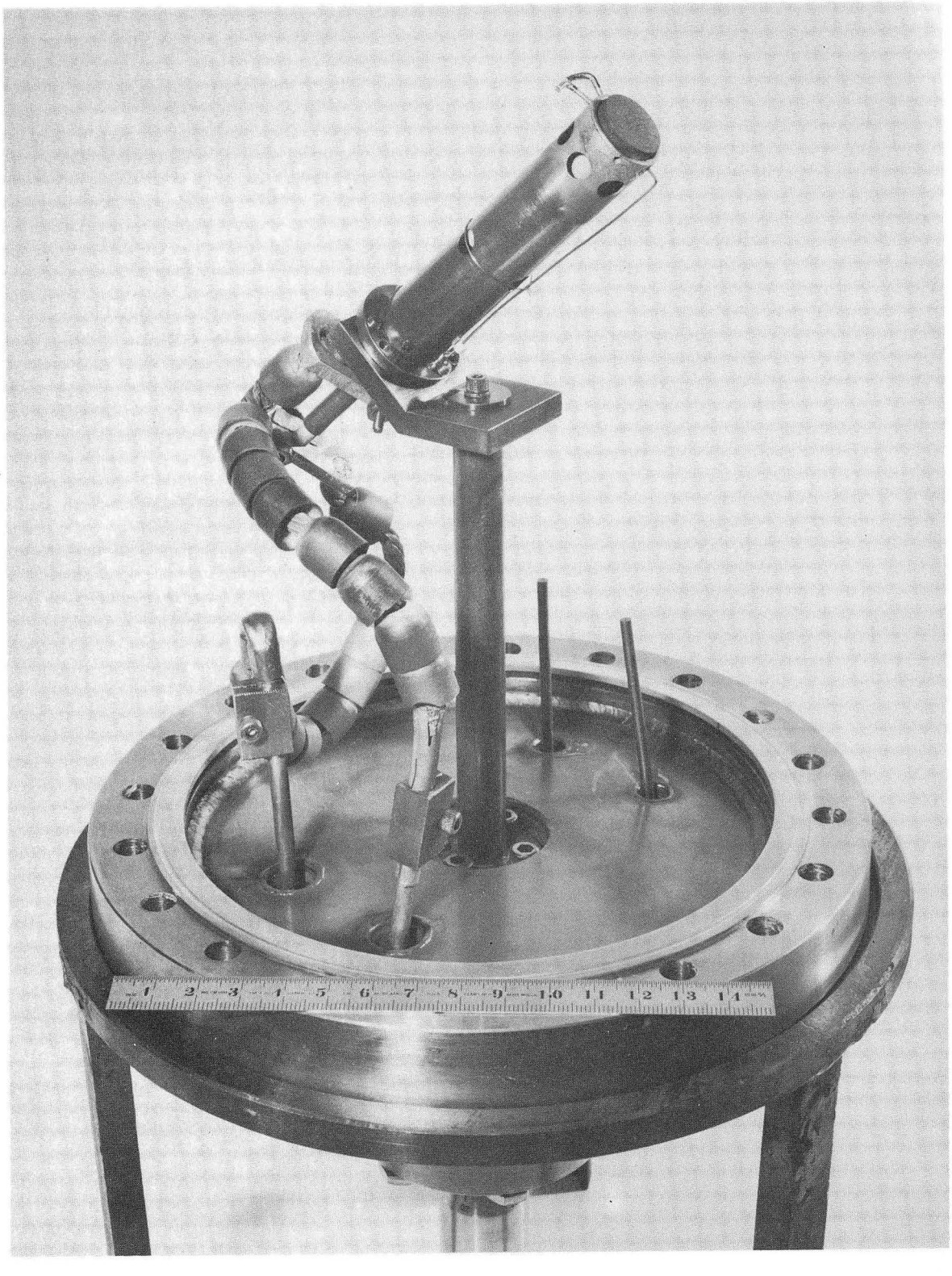

XBB 715-2152

Fig. 18 Target holder--electron beam heater.

Targets having prismatic plane faces (c axis parallel to the surface) presented a different problem. Heat was conducted easily from the rear to the front face but radial heat loss to mounting points was not uniform and gave a temperature band across the sample perpendicular to the "c" direction. The prism plane targets are also thinned in the center from the rear, and by fastening the target at the extreme basal layer edges a reasonably uniform hot zone (band) is obtained. Two fixed set screw points positioned close together on one side and a long tungsten spring loaded pointer engaging a shallow hole on the opposite side hold the target. The mounting points contact the target down on the thin sleeve section to minimize conduction heat loss from the target face. This mounting is also used for basal plane targets.

Target temperature is measured by optical or infrared pyrometers. The emissivity of the pyrolytic graphite was taken as 0.76 independent of the crystallographic face or the temperature.[4,66] The target face is viewed at normal incidence through a sapphire window having 87% transmission at the 0.65 micron wavelength of the optical pyrometer detector, and 92% transmission at the 2.0 and 2.6 micron wavelength of the infrared pyrometer. Fogging of the window by graphite vaporized at high temperatures was found to be considerable and a shutter was arranged to minimize this. The shutter, an iron flap, was placed in the vacuum chamber just behind the window. An electromagnet could be switched on to lift the flap and allow a temperature measurement then the flap would be quickly dropped. Two pyrometers were used: an Ircon 300C infrared pyrometer for temperatures up to 1700°C (although the instrument is calibrated to

2800°C), or a Leeds and Northrup disappearing filament type from about 800°C to the highest temperature studied (2200°C).

This Leeds and Northrup pyrometer has the usual series connection of the filament, current adjusting rheostat, batteries and a suppressed scale (50 - 100 ma) current meter calibrated in degrees centigrade. In conventional operation, the batteries are connected, then the rheostat is adjusted to illuminate the filament to viewing brightness, the temperature scale is read, and, finally, the rheostat is turned down before disconnecting the battery. Such extra use of the rheostat could be avoided by simply making or breaking the battery connections under illumination current. The thermal shock to the filament, however, is considerable, as are the meter excursions particularly on disconnect. Safe, convenient operation was provided by (1) connecting a large capacitor (50,000 mfd.) in parallel with the series connected rheostat, meter, and filament; and (2) adding a push-button switch and resistor in series with the battery. The turn-off time is determined by the rheostat and filament resistance in conjunction with the necessarily large capacitor. The turn-on time is set by the resistor which also limits the surge current drawn from the battery. With this modification a temperature is read simply by pushing the button and adjusting (if necessary) the filament current. When the measurement is complete, the button is simply released and the filament cools gently as the meter point falls slowly.

7. Mechanical Alignment

The molecular beam is to intersect the line of flight through the spectrometer at the center of the target face (Fig. 8). This alignment is achieved in several steps.

During fabrication, after the beam entrance collimator had been

drilled, a gas laser beam was shown through the hole. A drill was prepared for the second collimator with the spindle parallel to the desired line of flight through the spectrometer head. The drill position was then translated to where it was centered in the laser beam at the hump on the curved spectrometer enclosure and the collimator hole in the curved wall between the target and mass spectrometer chambers was drilled.

Later, aligning the source tube mounts was done using the adjustments previously described so that the gas laser beam would pass along the source centerline and through the first collimator. A dummy brass source tube was used with various end plugs providing holes of different resolution. After this alignment, the dummy source tube could be replaced by the real source tube which is transparent and would also pass the laser beam.

The target was then aligned with the laser beam coming through the first collimator. The target holder mounting flange is rotatable about a horizontal axis and since the target is mounted off-axis this provides for raising or lowering the target (at the expense of a slight change in the impingement angle). The target heater mounting bracket provides a nominal 45° angle to the beam and the spectrometer flight paths. Translation by the linear motion feedthrough varies the position of beam intersection with the target such that this intersection may fall on the line through the spectrometer ionizer. The target vacuum flange is rotated so that the light spot, as seen through the direct view pyrometer port, is centered vertically on the target. The linear motion feedthrough is then adjusted to center the light spot horizontally so that it may be seen by looking through the elbow view port, mass spectrometer chamber, and second collimator.

The product detector mass spectrometer head is adjusted by jack

screws on its bellows to center the ionizer about this scattered laser beam. Fine adjustment of these jack screws is done later to peak the mass signal with a beam on. Also, the target linear motion feedthrough is adjusted with a beam on to peak the signal. This adjustment primarily varies the angle at which the scattered molecules enter the ionizer. Unless the response is peaked in this way, when the chopping frequency is increased an unusually rapid attenuation of a reflected beam is observed.

The primary beam monitor spectrometer in the target chamber is also adjusted to center the laser light from the beam source in its ionizer. A trial and error approach must be used since no external control of position is provided.

8. Detection System

Quadrupole mass spectrometers were used to provide compact mass selective detectors. An early model Electronics Associates Inc. quadrupole head and ionizer was used for the less stringent task of monitoring the primary beam composition. This head was positioned along the beam flight line and was exposed to the beam when the target was retracted by its linear motion feedthrough. For the more difficult task of reaction product detection a modern Granville Phillips "Spectrascan" head was used. Both heads were powered (alternately) by a single EAI Quad 250 electronics package. An improved ionizer-controller was developed around Kepco PAT power modules and one Kepco JQE 6-10 supply. This new ionizer controller forms an attractive package monitored by General Electric edgewise panel meters and using 10-turn adjustments of operating voltages and currents. To avoid errors in re-tuning the center mass control when observing different species, a Power Designs 5005R power

supply was connected to the spectrometer center mass circuit and provided with switch selected 10-turn programing resistors that could be set and locked to a particular mass (28, 32, 44).

The modulated signal current from the spectrometer head is dropped across a 1.11 megohm resistance and represents a voltage which is processed in analog form by a Princeton Applied Research Corp. HR-8 lock-in amplifier. Due to stray and cable capacitance, the voltage response lags the current excitation and a phase shift and amplitude attenuation of the electrical signal occurs. A circuit model of the important components was formulated[59] considering the total stray and cable capacity (about 60 mmfd. as measured by a Tektronix 130, L-C meter) in parallel with the 1.11 megohm load resistor across the input of the lock-in amplifier's type A preamplifier. A series connection of 0.1 mfd. capacitor and 10 megohm resistor in shunt with the input circuit reflects the 10 megohm AC input impedance of the lock-in preamplifier. At 1000 Hz. this complex input impedance (essentially 1.0 megohm and 60 pf.) represents a 25° phase shift and 10% amplitude attentuation. Data taken at different frequencies were corrected, using circuit model calculations, for the perturbation introduced by this complex impedance.

Besides minimizing the complex impedance correction, the 1.11 megohm load resistor provides a necessary DC load for the last dynode of the electron multiplier. Without this DC return path, the potential of the last dynode will float up toward that of the next to the last dynode and the amplification decreases markedly.

There are three means of signal processing,

(1) Determination of the complete wave shape,

(2) Digital counting techniques,

(3) Lock-in detection.

Phase sensitive devices/techniques such as waveform eductor or computer of average transients (CAT) give the complete wave shape. Only the fundamental frequency component (given directly by a lock-in amplifier) is required for comparison to linear reaction models. Although the complete waveform could be compared to reaction models, correcting wave shape for complex impedance effects would be quite difficult. The wave could be Fourier analyzed and the corrections applied to each component. Of course, the corrections to the higher harmonics are larger.

Digital (pulse counting) techniques are ideal in principle because equal weighting is given each ion pulse and pulse height discrimination techniques may be used to filter certain noise levels. In particular, an annoying microphonic pickup from motor vibration suggested use of some pulse processing technique to mask this low frequency signal compared to fast-rising ion pulses. The microphonic problem was traced to some loose connections in the quadrupole head. Simply tightening the screws restored normal operation. This was important because pulse techniques are not quite compatible with the present experiment.

In applying the pulse counting technique, ion pulses are counted during quarter cycles then sums and differences are formed in order to evaluate an amplitude and phase representation of the waveform.[65] This technique is best suited to weak signals (low count rates). The highest count rates to be handled with negligible counter dead time are about 10^5 and after passing through an electron multiplier with a gain of 10^5 this gives a current of about 0.01 microampere or 10 millivolts across 1 megohm. This maximum counting rate is about a factor of 50 too slow for the signals of scattered reactant beam that we encounter. Additionally, careful isolation and shielding of the 5 Mhz R. F. quadrupole power

is necessary to avoid counting this huge background.

Phase lock processing by means of a lock-in amplifier was chosen for data taking in this experiment. The input signal is brought to the type A preamplifier of the lock-in amplifier through a small relay which can switch the signal to an oscilloscope (Hewlett Packard 130C) for observing the mass spectrum during preliminary tuning. The type A preamplifier is operated in the differential mode (A-B) with the signal connected to input A and input B grounded. The signal channel is operated with a Q of 10.

The lock-in amplifier reference channel is operated in the "automatic mode" driven by negative pulses from the reference strobe pulse train before applying the strobe-saving pulse rate division. Reference tuning (main tuning) is done, using a dual beam oscilloscope (Tektronix 551 with type B and D plug-ins), to match the negative trigger pulse and the zero crossing of the calibrator signal which is derived from the reference channel of the lock-in. Signal channel tuning (fine tuning) is done to peak the response to the calibrator signal which is connected to the preamplifier input whenever the electron multiplier output is switched to the Hewlett Packard 130C oscilloscope.

In one method of operation the lock-in amplifier is frequency tuned to the signal of interest then the phase control is adjusted to peak the signal. The lock-in output is then proportional to the signal amplitude and the phase setting corresponds to the phase angle of the signal. This phase adjusting method is relatively insensitive because one is tuning for a maximum at the relatively flat peak of a sine curve. A more sensitive adjustment is obtained by adjusting the phase control for null (operating on the slopped zero crossing of a sine curve) then

shifting the phase setting by 90° to achieve the phase angle of maximum signal and to read the signal strength. This method has been employed in some of this work.

An even better approach is to use a lock-in amplifier which concurrently displays the magnitude of the signal at two phase settings separated by 90°. One output is set to give the component of input signal in phase with the reference signal, S_0. The other output is set to give the component of input signal shifted 90° in phase from the reference signal, S_{90}. From these two rectangular components, the peak magnitude and phase angle of the signal may be easily computed.

$$S = \sqrt{S_0^{\,2} + S_{90}^{\,2}}$$

$$\phi = \tan^{-1}\left(\frac{S_{90}}{S_0}\right)$$

The Princepton Applied Research HR-8 lock-in with its new #127 two-phase accessory may be used. Although slightly less convenient, (twice as much tuning is required) two lock-ins may be connected in parallel at the electron multiplier with one lock-in operated at 90° with respect to the other. This two phase method using two available HR-8s has been used in our experiments.

The output signal(s) is integrated by the 12 db/octave filter in the lock-in amplifier using a suitable time constant (1 to 100 sec.) to obtain a reasonably steady reading. Very steady signals are read on the lock-in amplifier's panel meter or on a Digitec Z 200-B digital voltmeter. Signals exhibiting more fluctuation are recorded on a Honeywell 153x27 or Varian G-40 strip chart recorder and the average trace height (example in Fig. 27) is tabulated as the magnitude (or 0° or 90° component) of the

signal. Delegating some of the necessary smoothing to the chart recording ensures that a sufficiently short electrical filtering time-constant may be used in order that slowly changing reaction conditions or instrument drifts will not be ignored.

An interesting method of recording "two phase" data employs an X - Y recorder (Houston Instruments) the pen tracing the history of the reaction vector. A time base may be added to this type of chart by applying clocked pulses to the pen lift mechanism.

It would be advantageous if a small computer could be added to the two-phase measurement scheme to calculate "on line" the signal amplitude and phase values which would be recorded on the strip chart.

B. Beam Properties

This section relates the properties of the molecular beam source, the source driving pressure, and the source temperature to the impingement rate of beam molecules with the solid surface.

The ideal beam source emits in a central cone of very small angle. Such a source would pass a substantial portion of its efflux through the source collimator with very little remaining to be scavenged by the source chamber pump. Early beams were generated by effusion orifices with broad isotropic or cosine emission patterns. They possessed, however, a Maxwellian speed distribution which was attractive because it could be characterized by its temperature.[67] Beams generated by skimming the central portion of the mach disc from a hydrodynamic jet are, by comparison, enormously strong but have a relatively high speed and are nearly monoenergetic.[68] Such characteristics are, nevertheless, useful in some studies.[69]

One knows that the total effusive flow through an orifice is larger

than the effusive flow through a channel of the same diameter--the channel conductance being reduced by wall collisions.[67] If the pressure is such that the center of the channel is transparent to molecules, that is if no intermolecular collisions occur, the centerline flux for both the orifice and channel are the same. Consequently, the channel gives a more directed or peaked efflux which may be more efficiently utilized. To capitalize on this increased efficiency the source pressure cannot simply be increased for that would affect the centerline transparency. Instead, in order to fully utilize the source chamber pumping additional channels are used and there results a multichannel source. An extensive investigation of the flow characteristics of channel sources has been undertaken in this laboratory (70, 71, 72, 73, 59) including, in particular, evaluation of the beam source used in this work. What follows is an application of the results of that study which is reviewed in reference 74.

Although theoretical expressions of centerline intensity[75] and total leak rate[76] exist for channel sources, the direct experimental verification of the former requires a difficult absolute calibration. Furthermore, fabrication of multichannel sources seldom results in perfectly cylindrical channels with accurately determinable dimensions. However, experimental determination of the total leak rate is trivial and measurement of the angular emission pattern is fairly easy.

The total leak rate ℓ may be related to the source pressure p_s (torr) by,

$$\ell = \frac{p_s}{RT} C_s \text{ , molecules/sec} \tag{44}$$

where R is the gas constant (1.015×10^{-22} lit-torr/molec - °K), T is the absolute temperature and C_s is the source conductance. For N uniform

channels of radius a, and Clausing factor K; C_s is given by,

$$C_s = K\ 3.51\text{x}10^{22}\ RT\ N\pi a^2\ /\ \sqrt{MT}\ ,\ \text{lit/sec} \qquad (45)$$

If the source is fed from a reservoir of volume V_r at an initial pressure p_s^o, the pressure decay with time t (sec) is

$$p_s/p_s^o = \exp -(C_s/V_r)t \quad . \qquad (46)$$

For the quartz multichannel source a reservoir V_r = 24 liters produced the room temperature leak down curve of Fig. 19 using helium.

From Eqs. (44) and (45) it is seen that at constant leak rate (as provided by a fixed setting of the "leak valve"), the pressure will adjust to the source temperature as

$$p_s \propto \sqrt{T} \qquad (47)$$

Using oxygen gas this relationship was verified as shown in Fig. 20.

The total leak rate as a function of source pressure at various source temperatures for oxygen gas was calculated from Eq. (44) using Eq. (45) to correct the conductance measured with helium by the rato of the square root of the molecular mass,

$$C_s(O_2)/C_s(He) = \sqrt{M_{He}/M_{O_2}} = 0.354 \quad .$$

The result is displayed in Fig. 21.

Angular emission patterns were measured, again using helium, by sampling the efflux in the plane of the source axis with a rotatable probe connected to a commercial leak detector.[77] A representative distribution for the source is shown in Fig. 22. No absolute measure of

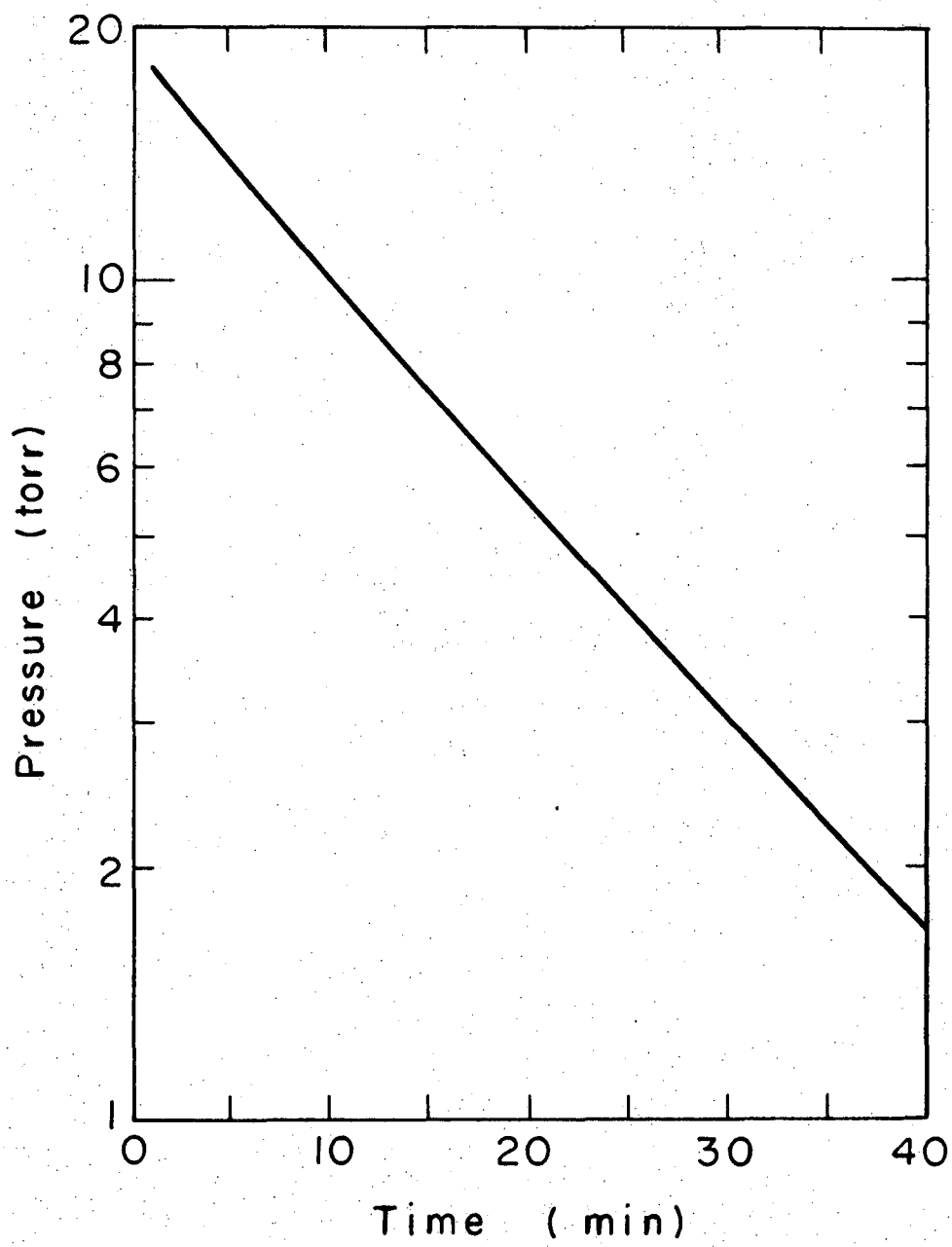

XBL6811-7181

Fig. 19 Beam source helium leak down.

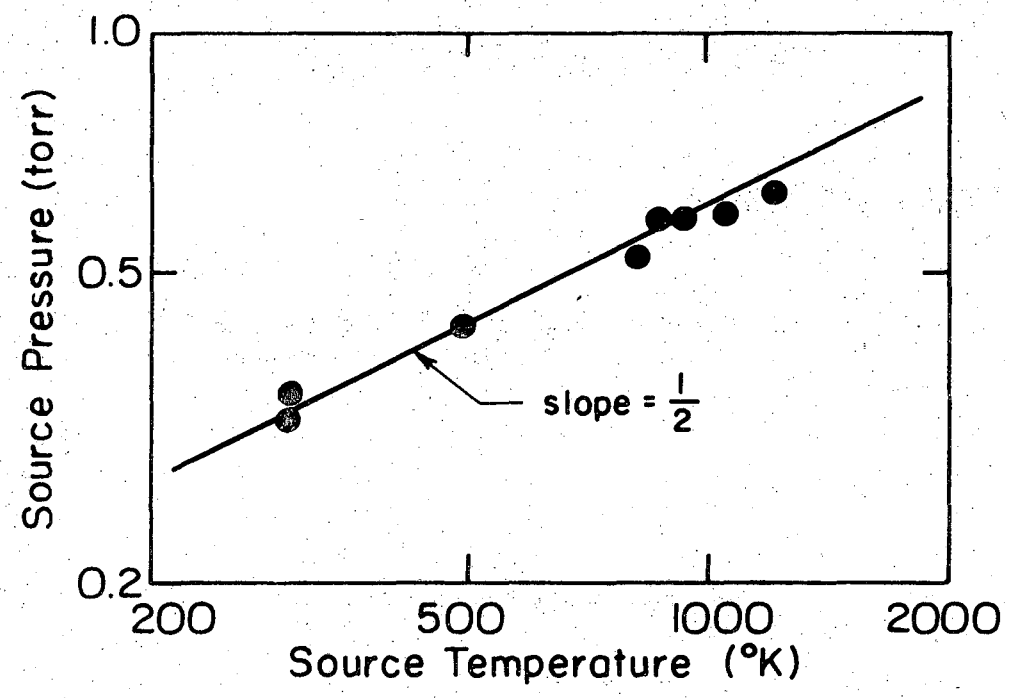

XBL717-6992

Fig. 20 Pressure vs temperature relationship for constant leak rate.

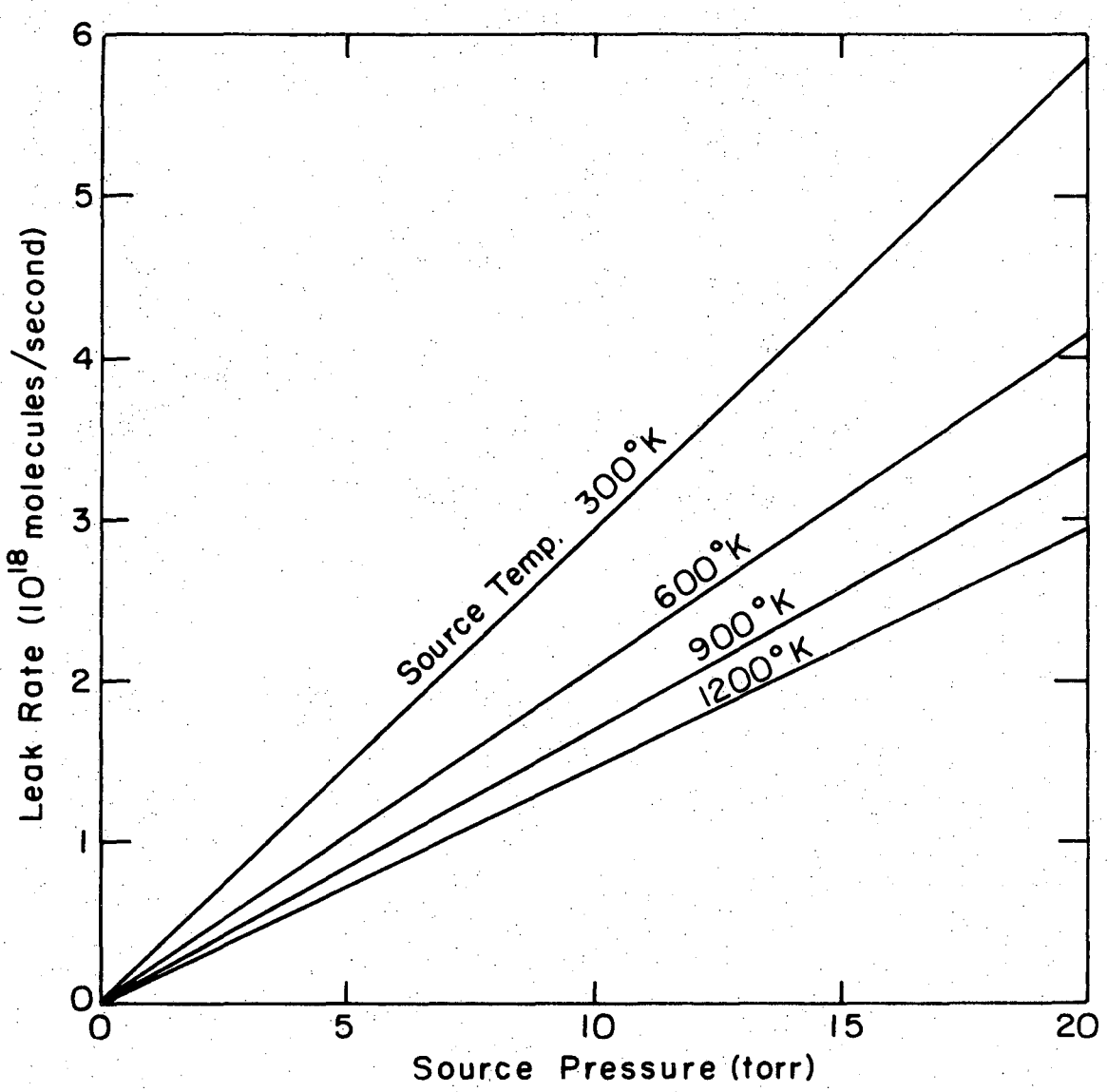

XBL 717-6993

Fig. 21 Leak rate as a function of source driving pressure for various source temperatures.

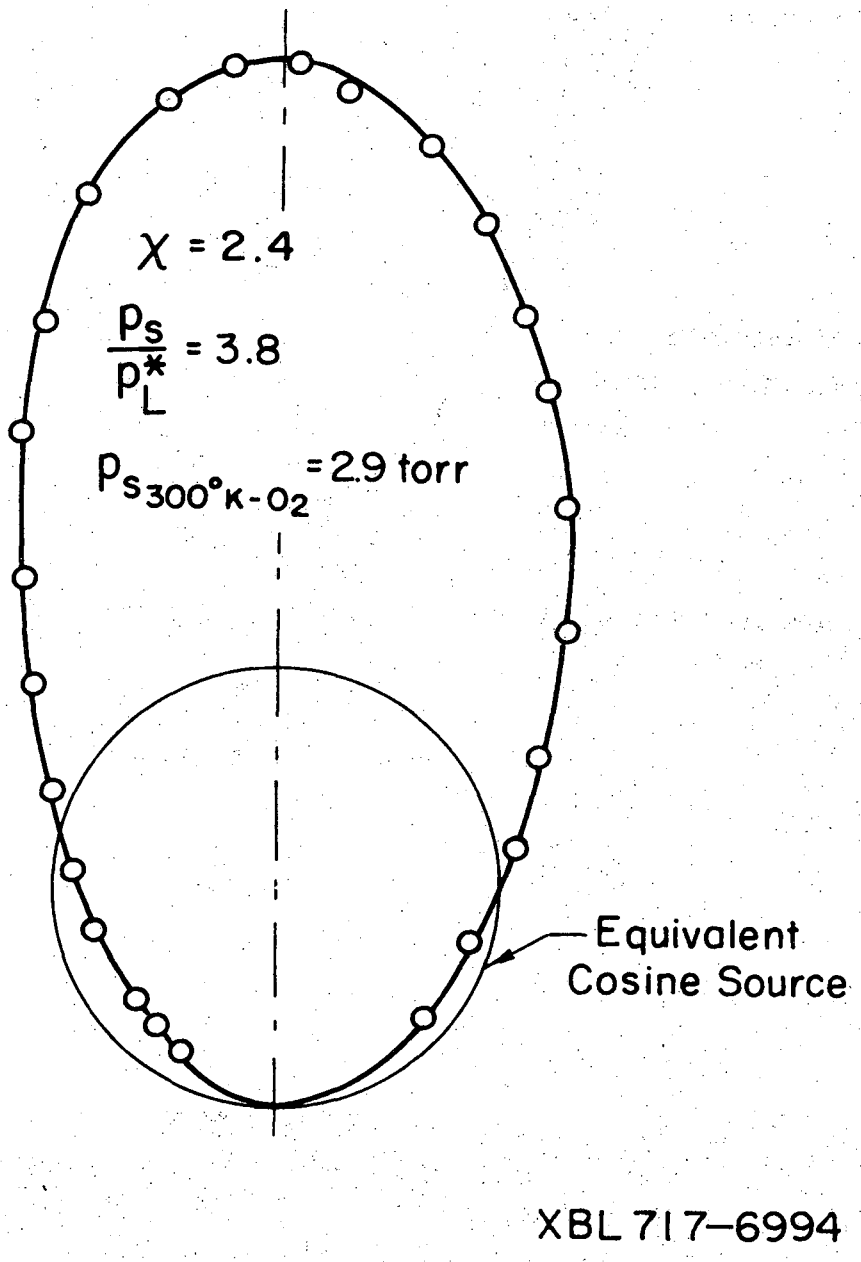

Fig. 22 Angular emission pattern for 2.9 torr oxygen (measured using helium).

intensity need be obtained in this way, because the integral of efflux in all directions is proportional to the total leak rate previously determined which may be used to scale the figure. The objective of a multichannel source is to increase the centerline emission for a given leak rate. The circle on Fig. 22 represents an orifice (cosine) emission pattern of the same total leak rate and the improvement obtained is evident. (More highly peaked emissions may be obtained from other sources but they are considerably more difficult to align and the gain in intensity is less than previously anticipated.[71])

Theoretical development leading to the Clausing factor K in Eq. (45) requires collision free flow as the molecules rattle down the channel.[67] More specifically, this requires that the mean free path be on the order of or greater than the channel diameter. In order to obtain the maximum peaking factor from a channel source, a molecule traveling parallel to the source axis must pass through the entire channel without suffering a collision. This more stringent condition requires that the mean free path be greater than the channel length. In most cases of practical application, the source pressure is generally such as to trade-off a small loss in peaking for a higher total efflux to fully utilize the source chamber pumping. Theory has been developed to predict the variation with source pressure of the peaking factor χ defined as,

$$\chi = \left.\frac{\text{centerline intensity of channel source}}{\text{centerline intensity of orifice}}\right|_{\ell} \qquad (48)$$

where the subscript ℓ indicates that both be operated at the same total leak rate. The various predictions will not be developed here but may be found in references (70, 75, 78). Some values for this source measured using helium are shown with two best theoretical predictions in

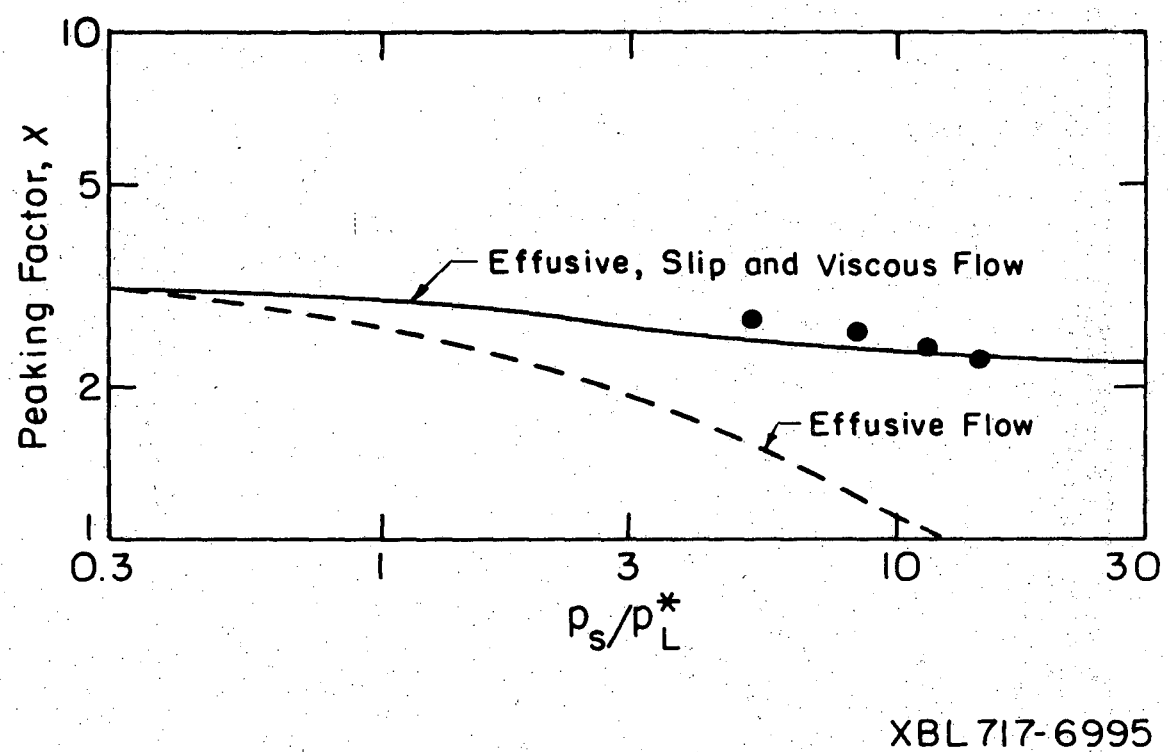

Fig. 23 Peaking factor as a function of reduced source pressure p_s/p_L^*.

Fig. 23. Simple theory predicts the variation of χ/χ max as a function only of the reduced pressure variable p_s/p_L^* where p_L^* is the source pressure for which the mean free path is equal to the channel length L,

$$p_L^* = kT/(\sqrt{2}\,\pi\,\sigma^2\,L),\ \text{torr} \quad , \tag{49}$$

where k is Boltzmann's constant, T is the absolute source temperature, and σ is the molecular collision diameter. At 300°K for the quartz multi-channel source (L = 0.030 cm) using molecular oxygen $\sigma = 2.98\text{x}10^{-8}$ cm; $p_L^* = 0.26$ torr.

The beam intensity may now be evaluated. For a given pressure and temperature the development leading to Fig. 21 gives the leak rate, ℓ. For an ideal orifice the centerline intensity J(0) is related to the total leak rate by $J(0) = \ell/\pi$ and the channel peaking factor gives us χ better or,

$$J(0)_{\text{channel}} = \frac{\chi\ell}{\pi}\ ,\ \text{molec/sec-ster} \tag{50}$$

The geometry of beam collimation is shown in Fig. 24. Considering the beam to originate at a point, the flux at the target position is

$$I_o = \frac{\chi\ell}{\pi}\quad \pi\left(\frac{r_{cl}}{d_c}\right)^2 \quad \frac{1}{\pi}\left(\frac{d_c}{r_{cl}\ d_t}\right)^2 \frac{\text{molec}}{\text{cm}^2\text{-sec}} \tag{51}$$

for d_t in cm. The collimation is seen to only define the target area on which the beam strikes --- it does not affect the beam intensity. The point source approximation is found to be satisfactory in this situation.[71] One may note in Fig. 24 that the beam strikes the target obliquely spreading the beam flux over an area of target larger than the

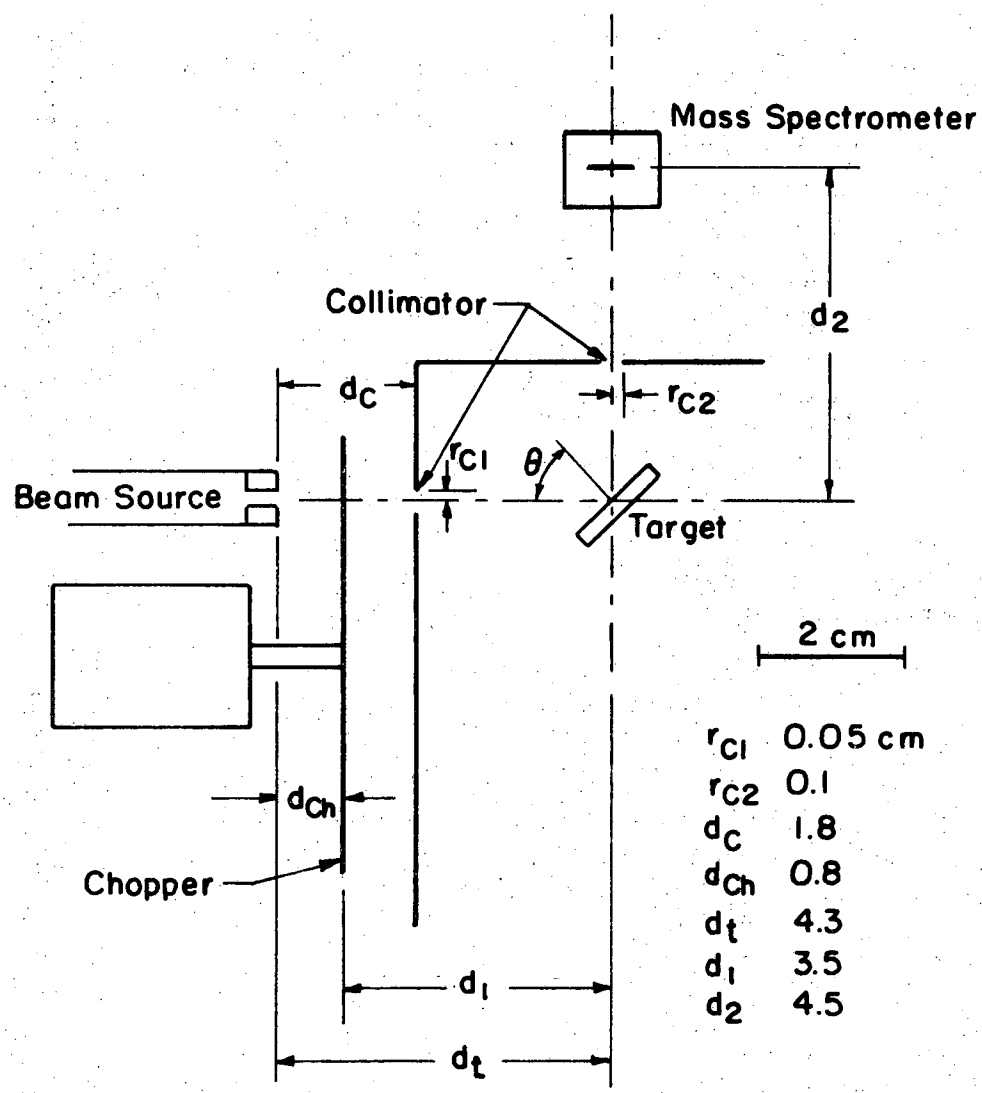

XBL 717-6996

Fig. 24 Beam collimation geometry.

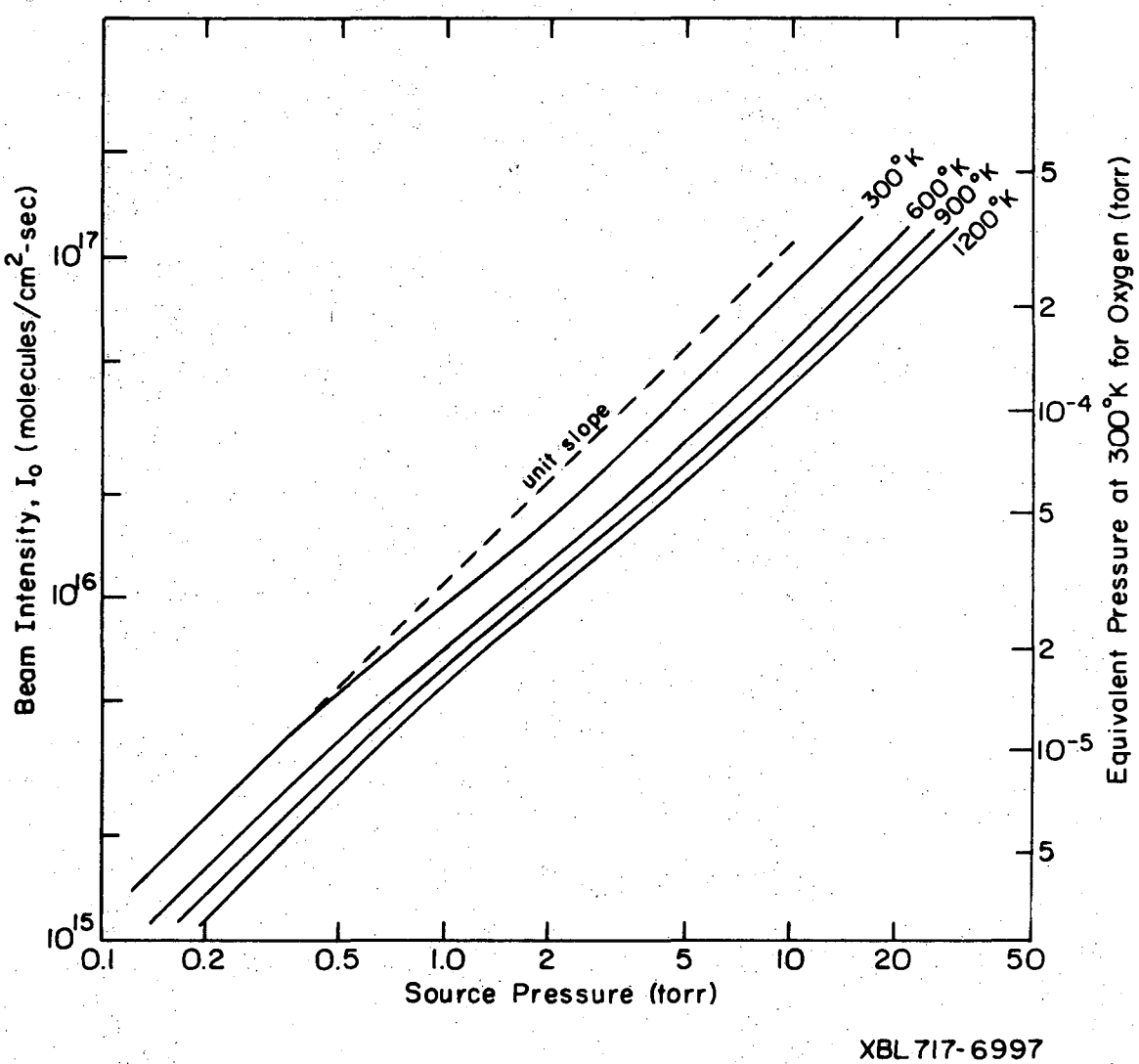

Fig. 25 Beam intensity on the target, I_o, as a function of source driving pressure.

beam cross section. This reduces the effective intensity by the cosine of the impingment angle θ.

Neglecting variation in σ with temperature, Fig 25 shows the variation of beam intensity on the target, I_o, with source pressure p_s for four source temperatures. The deviation from unit slope and linearity is due to the non-linear variation of χ with pressure taken from the upper curve of Fig. 23

Equivalent pressure is sometimes† a convenient concept used to relate beam experiments to more conventional investigations. It is the pressure for which a target bathed in the gas at beam temperature receives the same collision flux as from the beam, ie., $I_o = n\bar{c}/4 = p_{eq}\bar{c}/4kT_B$ or in convenient terms,

$$p_{eq} = \sqrt{M\ T_B}\ I_o/\ 3.51\text{x}10^{22},\ \text{torr}, \tag{52}$$

M is the molecular mass (amu) and T_B is the source-(beam) temperature (°K). The right hand ordinate of Fig. 25 gives the equivalent pressure for the 300°K curve (only). If the peaking factor χ were independent of pressure, Eqs. (44, 45, 51, 52) show that the equivalent beam pressure would be simply proportional to the source pressure, and independent of source (beam) temperature.

A new question comes to view: Does the beam possess the same temperature as the source, or may it be described by any <u>temperature</u> which implies a Maxwellian speed distribution? For a long single channel

---

†Since pressure is rate of change of momentum per unit area, a heated beam gives a higher equivalent pressure than a cooled beam of the same impingement rate. The equivalent pressure concept applied to beams at different temperatures may be misleading.

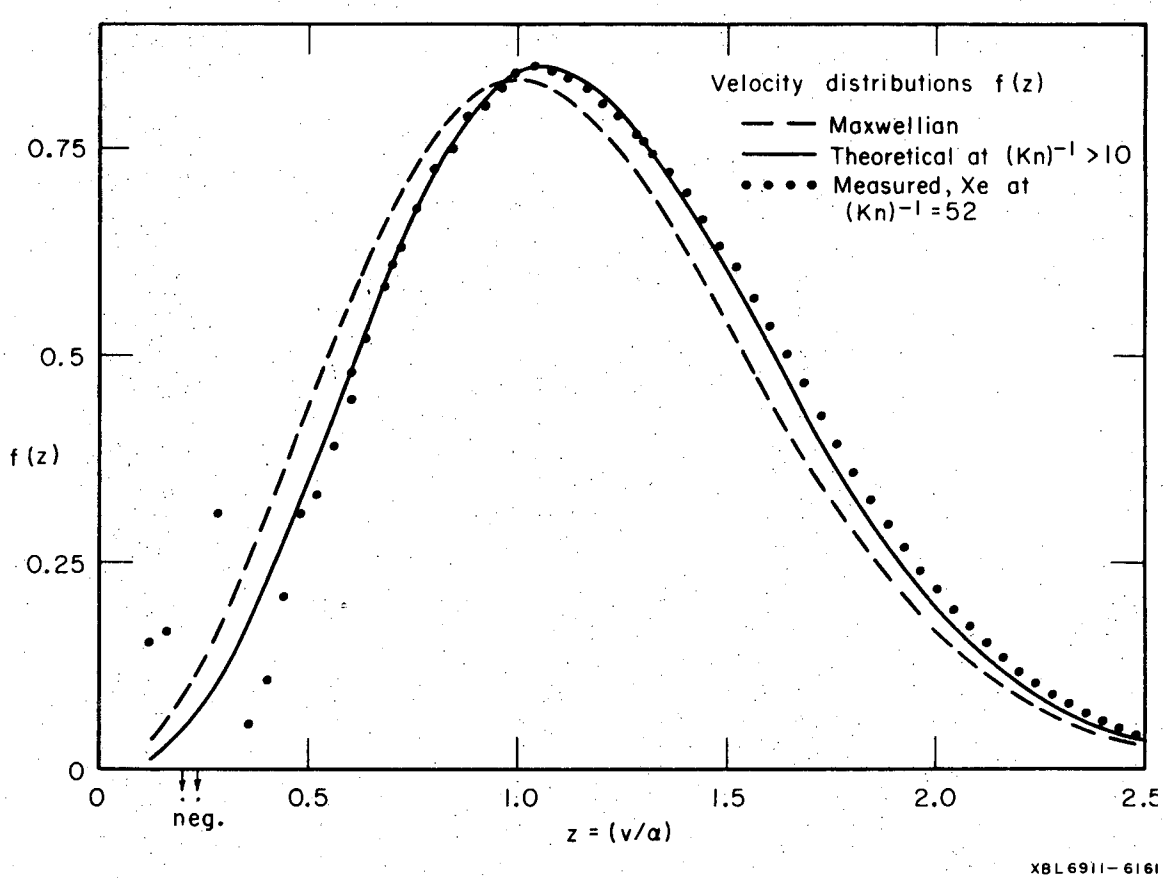

Fig. 26 Maxwellian and theoretical hardened molecular speed distributions, f(z), as a function of reduced speed $v/\sqrt{2kT/M}$.

operated at pressures below which slip or viscous flow becomes significant, it has been shown theoretically[73] that only a small deviation from a Maxwellian spectrum is expected which may be expressed as a 5 1/2% increase in average energy. Available data seem to confirm this prediction. Figure 26 shows equilibrium and hardened spectra with experimental data.[59] A temperature would still be a reasonable parameter for such a beam. The quartz multichannel source used in this work has a substantial centerline flux due to slip and viscous effects (for beam pressures frequently used) as shown by the peaking factor in Fig. 23. No experimental determination of the velocity spectrum has been made but it will be assumed that there is no significant perturbation and even the anticipated 5 1/2% energy enhancement will be ignored.

C. Summary of Experimental Parameters, Basic Operating Proceedure, and Data Handling

With the present system, the target is maintained in a vacuum of ca. 10^{-8} torr. The maximum attainable temperature is limited only by vaporization of material from the rear of the target with consequent reduction in structural integrity and the risk of dropping the target from its holder.

The equivalent beam pressure at the target has a maximum value of ca. 10^{-4} torr (intensity $\sim 10^{17}$ molecules/cm^2 - sec) limited by the source chamber pumping speed. Beam pressure may be reduced 3 orders of magnitude before encountering serious background contamination either in the target chamber or in the source chamber.

Modulation frequency using the 6 blade chopper disc may be varied from 2 to 1500 Hz.

The beam is typically maintained at room temperature but may be heated to 950°C.

No variation in impingement or observation angle is provided --- both are 45° to the surface normal and are coplanar.

The mass spectrometer settings are "peaked" for each species observed. Typical ionizer settings are:

Filament Current	2.4 amps
Filament Voltage	2.0 volts
Emission Current	1.0 milliampere
Electron Extractor Current	0.1 milliampere
Extractor Voltage	50 volts
Ion Energy	15 volts
Focus Voltage	150 volts
Electron Energy	65 volts.

The mass spectrometer is operated in the low mass range, 0-100 AMU, with the resolution at mass 28 adjusted to just touch the valley between mass peaks to the base line (i.e., "unit resolution"). Voltage to the 14 stage electron multiplier is adjusted from 2.5 to 3.0 kilovolts to provide the best signal-to-noise ratio.

The detection system is capable of resolving a modulated signal that is 10^{-3} below a "steady" background at the same mass setting. Background signals may be true background species or demodulated reaction product in the mass spectrometer chamber. In this apparatus signal measurements have been extended down to 200 nanovolts for weak reactions. Measurements at these low levels typically require 2 hours to acquire a satisfactory chart recording.

Although the effect of the beam temperature has been examined briefly, the primary experimental variables were the beam intensity I_o (determined by the source pressure), the target temperature T_S, and the modulation frequency ω. The experimental goal was to determine for all points in the three dimensional space (I_o, T_S, ω) the apparent reaction

probability ε, and the reaction phase lag ϕ. Three blocks of data were obtained by holding each of two parameters constant and varying the third. This longer approach provides an overabundance of data but guarantees the most reliable information on the effect of varying each parameter. Any two blocks of experimental data would, in principal, determind the third block of data, but since each setting of a parameter (particularly the target temperature T_S) is not conveniently duplicated, considerable interpolation of data from two blocks would be necessary to determine the partial derivative of ε and ϕ with respect to the parameter which was not explicitly scanned.

All ion pumps are operated continuously as are the inlet system cold traps. Between runs the source chamber is kept evacuated by the mechanical roughing pump. A day of experimenting begins by filling the liquid nitrogen cold baffle and warming the diffusion pump. The chopping motor is brought up to a convenient speed and gas is admitted to the beam source to establish the desired source pressure. The mass spectrometer filament is heated and with the target still at room temperature, the signal and phase of the scattered oxygen beam is measured. The signal at mass settings 28 (CO), and 44 (CO_2) are also measured to check system noise levels and/or purity. The desired target temperature is then established and reaction measurements are begun.

As has been indicated in sections II A, II C, and III A-8, the raw data (the signal amplitude and phase) of all species (reactants and products) are corrected to remove the effect of the density sensitive ionizer and to remove the amplitude attenuation and phase lag due to molecular transit and the integrating effect of the complex impedance.

The measured phase lag for any species is the sum of phase lags from several steps. Initially, the chopped beam has a mechanical phase shift (independent of frequency), ϕ_{mech}, due to the relative position of the beam axis, the chopper axis, and the reference mark (section II A-5). The beam is delayed in transit from the chopper to the target yielding a phase lag, ϕ_{d_1}, (section II C, and Fig. 24). Interaction with the target introduces the reaction phase lag, ϕ, and transit of desorbed product or scattered reactant from the target to the mass spectrometer adds a second transit phase lag, ϕ_{d_2}. The transformation of the mass spectrometer output current to a voltage signal at the lock-in amplifier adds a complex impedance phase lag, ϕ_Z, which has been calculated previously.[59] The measured phase lags for scattered reactant (R) and desorbed product (P) are given by:

$$\phi^R_{meas} = \phi_{mech} + \phi^R_{d1} + \phi^R_{d2} + \phi_Z \tag{53}$$

$$\phi^P_{meas} = \phi_{mech} + \phi^R_{d1} + \phi + \phi^P_{d2} + \phi_Z \quad . \tag{54}$$

Scattered reactant and desorbed product are both fed by the primary reactant beam therefore, a reactant transit phase lag from the chopper to the target, ϕ^R_{d1}, occurs for both species as does the constant mechanical phase shift. The complex impedance phase lag, ϕ_Z, affects each species equally for measurements at a common frequency. Reaction phase lag, ϕ, is absent for simple scattering of the reactant beam.

Systematic perturbations also affect the measured signal amplitudes. Besides $1/r^2$ attenuation, collimation, and other effects grouped in the instrumental constant β (section II A) the AC signal amplitudes are subject to transit demodulation attenuation and are reduced by the integration of the complex impedance. The measured amplitudes of

scattered reactant and desorbed product may be related by demodulation factors ($A \leq 1$) to the amplitudes calculated for reaction models (S_R, $|S_P^*|$):

$$S^R_{meas} = \frac{S_R}{\sqrt{T}} A^R_{d1} A^R_{d2} A_Z \tag{55}$$

$$S^P_{meas} = \frac{|S_P^*|}{\sqrt{T}} A^R_{d1} A^P_{d2} A_Z \quad . \tag{56}$$

The density sensitive response of the mass spectrometer detector has been included as the square root of the temperature of the species when it enters the ionizer. The complex impedance amplitude attenuation factor, A_Z, is a function of the modulation frequency, ω, but is independent of the molecular species and has been calculated previously.[59] A transit demodulation of the amplitude of the primary beam affects the signals of both scattered reactant and desorbed product.

The transit demodulation factors, A_{d_1}, A_{d_2}, and the transit phase lags, ϕ_{d_1}, ϕ_{d_2}, are tabulated[57] as functions of the parameter $X = \omega L/\alpha$ where $\alpha = \sqrt{2kT/M}$; T is the temperature (°K), M is the molecular mass, ω is the modulation frequency (rad/sec), and L is the flight path length. Several beam properties may be subject to a transit demodulation perturbation. We are concerned with the correction to beam <u>flux</u> over the path from the chopper to the target (path d_1), and the correction to beam <u>density</u> over the path from the target to the detector (path d_2). All parameters in X are easily assigned except perhaps the temperature T. For a room temperature beam scattered from a room temperature target a temperature assignment of 300°K has been made for the paths to and from the target. For a beam of temperature T_B incident on the target, T_B is used over the path from the chopper to the target. Reaction

products are assumed to desorb after equilibration with the target surface and are assigned the target temperature, T_S, for the path from the target to the detector. A reactant beam of temperature T_B impinging on a target at temperature T_S ($T_S \neq T_B$) is scattered with a temperature T^* which is determined by T_B, T_S, and a parameter called the thermal accomodation coefficient, which is not generally known. Fortunately, the reaction measurements may be referred to the signal from a room temperature primary beam (300°K) scattered (with the same temperature, 300°K) from a room temperature target.

Data from every series of measurements are corrected using Eqs. (53), (54), (55), and (56) to obtain the <u>reaction phase lag, ϕ</u>, and the reactant amplitude S_R and the product amplitude $|S_P^*|$ from which the <u>apparent reaction probability</u>, $\varepsilon = |S_P^*| / S_R$, is calculated.

The reaction phase lag is calculated by subtracting the measured reactant phase lag from the measured product phase lag in order that only small differences in the phase corrections between reactant and product signals need be considered. The mechanical phase shift cancels exactly and we obtain the reaction phase lag as,

$$\phi = \left(\phi^P_{meas} - \phi^R_{meas}\right) - \Delta\phi_{d_1} - \Delta\phi_{d_2} - \Delta\phi_Z \quad . \tag{57}$$

The net phase corrections are:

$$\Delta\phi_{d_1} = \phi_{d_1}(M_R, \omega, T_B) - \phi_{d_1}(M_R, \omega', 300°K) \tag{58a}$$

$$\Delta\phi_{d_2} = \phi_{d_2}(M_P, \omega, T_S) - \phi_{d_2}(M_R, \omega', 300°K) \tag{58b}$$

$$\Delta\phi_Z = \phi_Z(\omega) - \phi_Z(\omega') \tag{58c}$$

The parameters which determine each correction are explicitly noted. M_R, M_P are the masses of the reactant and product species. Reaction studies using a beam with temperature $T_B \neq$ room temperature (300°K) are considered as is the possibility that the modulation frequency, ω, at which product measurements are performed differs from the modulation frequency, ω', at which the scattered reactant "calibration" was measured.

An approximate apparent reaction probability $\tilde{\varepsilon}$ is determined by dividing $S^P_{meas}\sqrt{T_S}$ by $S^R_{meas}\sqrt{300}$,

$$\tilde{\varepsilon} = \frac{S^P_{meas}\sqrt{T_S}}{S^R_{meas}\sqrt{300}} \quad . \tag{59}$$

$\tilde{\varepsilon}$ is corrected to give the apparent reaction probability, $\varepsilon = |S^*_P|/S_R$, by multiplying by the <u>ratios of nearly equal</u> amplitude correction factors arising from transit demodulation and the complex impedance. The correction factors are:

$$C_{d_1} = \frac{A_{d_1}(M_R, \omega', 300°K)}{A_{d_1}(M_R, \omega, T_B)} \tag{60a}$$

$$C_{d_2} = \frac{A_{d_2}(M_R, \omega', 300°K)}{A_{d_2}(M_P, \omega, T_S)} \tag{60b}$$

$$C_Z = \frac{A_Z(\omega')}{A_Z(\omega)} \quad , \tag{60c}$$

and the apparent reaction probability is given by,

$$\varepsilon = \tilde{\varepsilon}\ C_{d_1}\ C_{d_2}\ C_Z \quad . \tag{61}$$

A set of reaction probability vector data is composed of reaction product amplitudes and phases and one or more "calibration" measurements (amplitude and phase) of room temperature reactant scattered from a room temperature target. Under certain conditions, some correction terms may be identical for reactants and products, and their effect may be totally neglected. For example, if all measurements of a set are performed at the same frequency, the complex impedance effects cancel. If the primary beam temperature is the same for all measurements of a set (ie., T_B is room temperature) and the modulation frequency is constant, then there is no net correction for beam transit from the chopper to the target (path d_1). At low frequencies (and for species, temperatures, and distances in this work) all corrections are small and consequently their differences are negligible. Simplified correction procedures were employed whenever possible.*

D. Reagent Purity

Impurities in the reagents in any chemical system are always a matter of concern, particulary when new physical information is sought by an experiment. In this section the purity of the pyrolytic graphite targets and the oxygen beam will be discussed.

The oxygen gas used in this study was quite pure but had the following contaminants as reported in the analysis tagged to the bottle by the supplier.

---

*The transit time of the ionized molecules in the mass spectrometer detector contributes additional phase delay (but no amplitude attenuation). This relatively small phase correction (discussed in Appendix II) was not applied to the data obtained in this work.

Species	Parts per million
N_2	4
CO_2	2.5
CO	0
H_2	0
He	0
Ne	0
Kr	4
Xe	1
Hydrocarbons	0

Although the purity of the beam was examined by retracting the target and using the beam monitor spectrometer, the contaminant levels listed above are roughly an order of magnitude below the resolution of the beam analysis spectrometer system (even using a modulated beam). Only a major (but unimportant) contaminant like krypton (which occurs at a mass number having a negligible background pressure) could be detected. The concentration of krypton was found to be in agreement with the supplier's analysis.

Delivering pure gas to the beam source is not, however, the total answer to achieving a pure flux of reactant at the surface. Two additional contributions must be considered: 1) the flux from background gas in the target chamber, and 2) the background "beam" driven by the source chamber background pressure through the first collimator. Of course, the major background species in either the source chamber or the target chamber is likely to be the same species as the beam gas, but the molecules (atoms) which do not come directly from the beam source may be of an entirely different nature with respect to temperature, electronic state, modulation, etc. In fact, for a non-linear

surface process the non-modulated DC background directly affects the reaction rate --- even the rate measured by the modulated beam technique! Consequently, a system parameter, the beam to background ratio must be considered. This is best handled using the equivalent pressure concept.

The equivalent pressure of the primary beam was determined in section III B as a function of source driving pressure. Operating conditions (pumping speeds, and gas loads) determine the pressures in the source chamber and the target chamber. The pressure in the target chamber may be compared directly, but we must calculate the equivalent pressure of a background beam effusing from the source chamber through the first collimator onto the target.

The equations have already been presented. Using Eqs. (44), (45, (K = 1, N = 1)) and (50) we obtain, in terms of the source chamber pressure, the centerline intensity of the emission from the collimating orifice. This intensity is diminished by "$1/r^2$" as the "beam" travels to the target, and we obtain the equivalent background pressure as simply,

$$P_{eq} = \frac{r_{c1}^2}{\left(d_t - d_c\right)^2} P_{\text{source chamber}} \tag{62}$$

$$= 4\text{x}10^{-4} P_{\text{source chamber}}.$$

Operating pressures are tabulated along with the equivalent pressures calculated at the target and the beam to background ratio.

(all pressures in torr) *Hot Target	Beam Off (Base Press.)	Average Beam	Maximum Beam
Beam Source Press.	10^{-4}	4	15
Source Chamber Press.	$2x10^{-7}$	$8x10^{-5}$	$2x10^{-4}$
Target Chamber Press.	$2x10^{-9}$	$4x10^{-8}$*	$2x10^{-7}$*
Mass Spec. Ch. Press.	$8x10^{-10}$	$2x10^{-9}$	$3x10^{-9}$
Equiv. Press. at Target			
Molec. Beam	---	$8x10^{-5}$	$3x10^{-4}$
Source Ch. Bkg.	$8x10^{-11}$	$3x10^{-8}$	$8x10^{-8}$
Beam/Background Ratio	---	1000	1000

An enviable beam to background ratio is obtained with this apparatus.

Pressures in all chambers rise significantly above base pressure when a beam is generated demonstrating that excessive pumping speed has not beem provided. Each pump must work to maintain the low pressure.

Chamber pressure p_o is related to the leak rate into the chamber ℓ and the pumping speed S_o by,

$$\ell = 3.24 \times 10^{19}\ p_o\ S_o \text{ (molecules/lit-torr).} \quad (T = 300°K) \tag{63}$$

It would be interesting to compare the leak rate, calculated from the pump speed and the observed pressure rise, to the total leak rate calculated as the beam and background effusion loads. At a source driving pressure of 4 torr, the target chamber pressure rises $4x10^{-8}$ torr. With the 1200 liters/second rated pumping speed, Eq. (63) implies a total flux of $1.6x10^{15}$ molecules/second into the target chamber. The collimated molecular beam falls on $4x10^{-2}cm^2$ of target surface with an intensity of $3.3x10^{16}$ molecules/cm^2 - sec, corresponding to a beam load into the target chamber of $1.3x10^{15}$ molecules/second. The effusion load from the source chamber background is $0.2x10^{15}$ molecules/second

(with a cosine distribution) calculated from Eqs. (44), (45), (K=1, N=1)). The total beam plus background load is 1.5×10^{15} molecules/second, in agreement with the value calculated from the pressure rise in the target chamber.

Purity of the unreacted pyrolytic graphite was investigated by neutron activation analysis looking for long lived species and tungsten, in particular. A sample of tungsten was also activated for calibration. The atomic concentration of tungsten was found to be less than 5 parts per billion and the total metalic impurity content is estimated to be less than 1 part per million (atomic).

Impurity determination by X-ray fluorescence analysis failed to reveal any impurities in the graphite but the sensitivity of this technique is only about 10 parts per million.

E. Experimental Program

In this work several pyrolytic graphite targets were subject to oxidation studies. The following summary indicates the course that the investigation followed.

One may recall that the target is mounted with its face in a vertical plane and that the molecular beam comes in horizontally impinging on the target at a 45° angle. Two possible mounting configurations for prism (edge) plane samples were used --- either with the laminations running horizontally or vertically. With the laminations horizontal the molecular beam may probe directly into the gaps between layers, but with the laminations vertical the direct view into the gaps between layers may be shadowed by the ridges of laminations.

The first sample was a prism plane specimen (for which we might expect good reactivity) mounted with the layers horizontal. Reaction

with molecular oxygen was measured up to the highest target temperatures used in this work (2700°K), and showed that the experimental system would perform as expected. Erosion of the rear of the target was found to be rapid at these high temperatures so when the second target was installed (in the same configuration) more modest temperatures were used (up to 2400°K). The greater part of prism plane data was obtained on this second target.

The prism plane reaction was found to be first order but exhibited a hysteresis in reaction probability upon cycling the temperature. Furthermore, the reaction phase lag stubbornly refused to approach zero at low frequencies as predicted by simple reaction models. After many months of reaction studies, the sample began to exhibit a substantial reaction (formation of CO) at room temperature. It was thought that catalytically active tungsten might have diffused through the target from the rear face where it is deposited by vaporizing the electron beam heater filament. The sample was removed from the vacuum system. It had developed a crack, through the center, parallel to the basal layers. Possibly, the crack may have exposed highly reactive atoms. At least, the crack would permit easy migration of tungsten to the front face. Electron micrographs were taken, then the sample was tested by X-ray fluorescence on the front and near faces. Finally a sample was scraped from the front face for neutron activation analysis which revealed tungsten present at 6 parts per million (atomic).

The investigation then split into two paths --- a review of previously postulated reaction mechanisms and an assault on basal plane reaction data.

Study of the basal plane reaction was restricted to temperatures under 1800°K and only one sample was used. The reaction was found to

be non-linear, thus providing a great challenge for model fitting. Some annealed pyrolytic graphite had been obtained and a basal plane sample of this material was studied but no reaction could be measured.

A new prism plane sample was then installed with the laminations vertical and its reactivity was determined. The sample was then rotated to the configuration with the laminations horizontal, and the reactivity was again determined. No appreciable difference in reactivity was found --- any shadowing effect was nil.

The "standard" (cracked) prism plane specimen was then reinstalled (after the face had been scraped of any tungsten to obtain a sample for activation analysis). A two week burn off at moderate temperature, with the beam on, removed any disturbed material from the surface. After reconditioning no substantial room temperature reaction was observed. On this resurrected sample, the reaction mechanism forming CO_2 was investigated using a mixture of O_2^{16-16} --- O_2^{18-18}.

Finally the reactivity of an annealed prism plane sample was measured.

On various samples throughout the experimental period, the oxygen gas was replaced by various inert gases (helium, neon, argon, krypton, xenon) to measure their thermal accomodation coefficient. One would try to determine the temperature of the scattered beam by measuring the phase lag due to transit from the target to the mass spectrometer. This apparatus provides only marginal resolution for these measurements due to the short flight path (d_2 = 4.5 cm). The results have no bearing on this work and will not be discussed. It is the use of extraneous gases in a beam striking the heated graphite targets which is specifically being indicated although no effect on the graphite reactivity is expected.

IV. BASAL PLANE REACTION

A. Data Acquisition and Preliminary Interpretation

The front face of basal plane samples were prepared for reaction studies by a mechanical polishing sequence ending with 1 micron diamond abrasive and Alumet polishing lubricant. Samples were washed with water and methyl alcohol prior to mounting in the target holder. Once installed, a sample is degassed while the system is pumped down and baked at 200°C for 8 hours. Finally the sample is heated to around 1300°K and subjected to an oxygen beam of about $3x10^{16}$ molecules/cm^2-sec ($\sim 10^{-4}$ torr) in order to burn off any disturbed surface material and obtain a "reproducible" surface condition. The reaction rate decreases during this preoxidation which occupies about 1 week (ca. 30 hours) and is estimated to remove $2x10^{19}$ carbon atoms/cm^2 of geometrical surface or 5000 basal layers (1.5 microns).

Data on the basal plane reaction are obtained beginning with a temperature traverse for a beam of $3.4x10^{16}$ molecules/cm^2-sec modulated at 16 Hz. Figure 27 shows a typical chart recording of the CO signal for the reaction proceeding at an apparent reaction probability of $1x10^{-3}$. The apparent reaction probability for CO (the most prominent species) is plotted Arrhenius fashion in Fig. 28 and illustrates a hysteresis behavior for the temperature cycle similar to that observed by other investigators.[6,7,79]

Several runs were made to verify the existence of this hysteresis and the results are illustrated in Fig. 29.

The hysteresis is believed to arise from a competition between 1) burn off which produces an especially reactive surface, and 2) thermal annealing which deactivates the surface. Consider the following temperature history. At a given temperature the two processes above

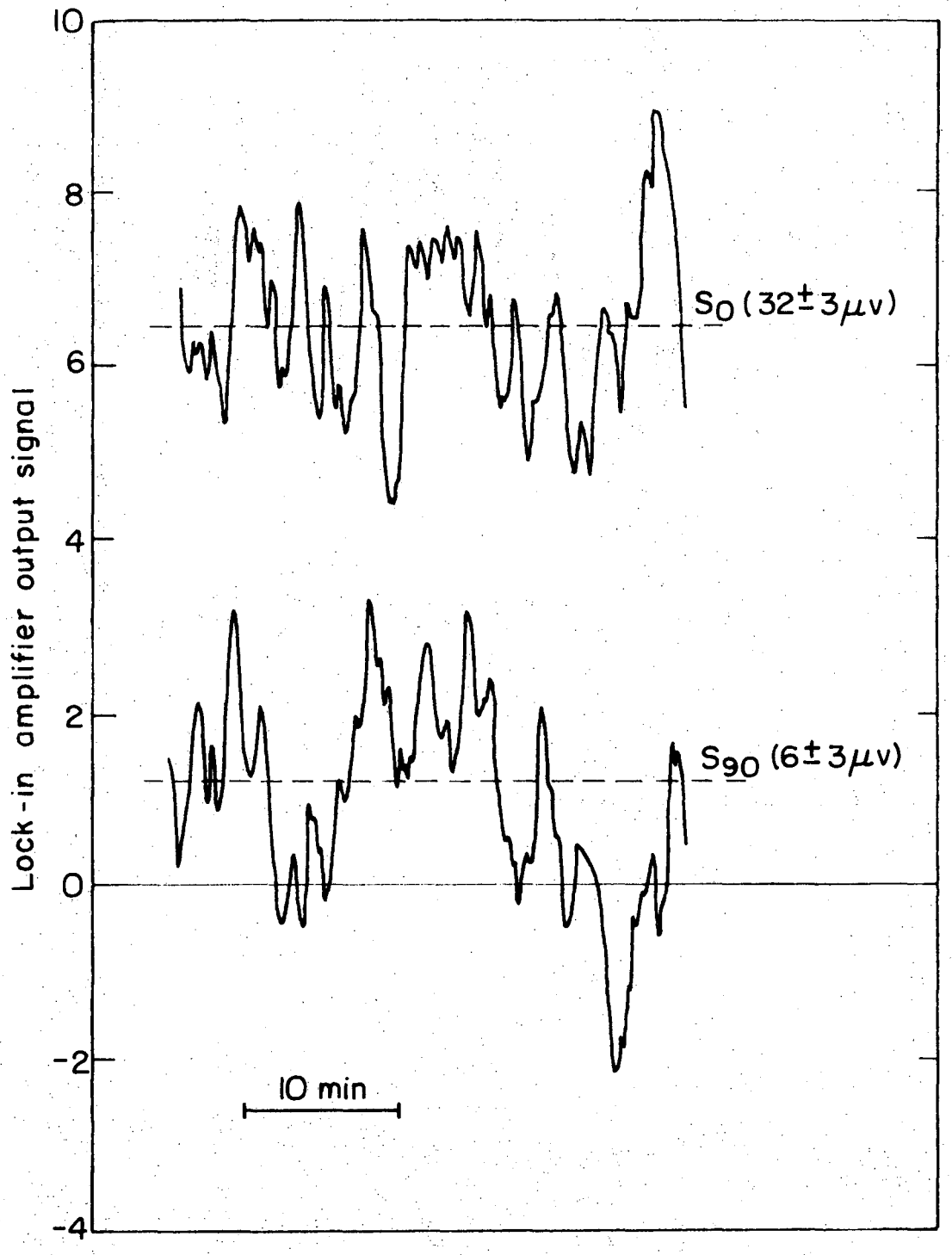

XBL 717-6999

Fig. 27 Typical CO signal at an apparent reaction probability of ~1×10^{-3}

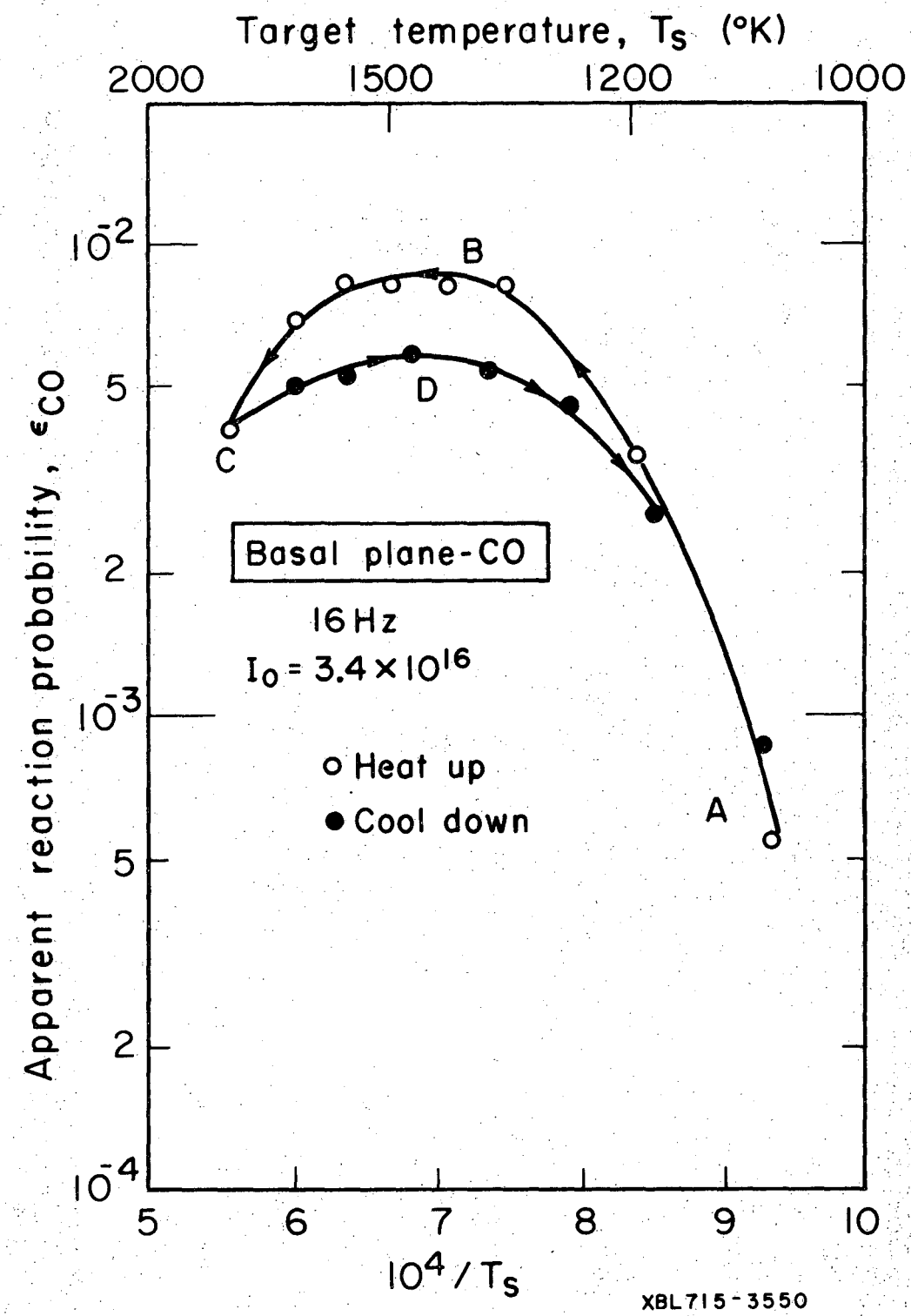

Fig. 28 Arrhenius plot of the apparent reaction probability.

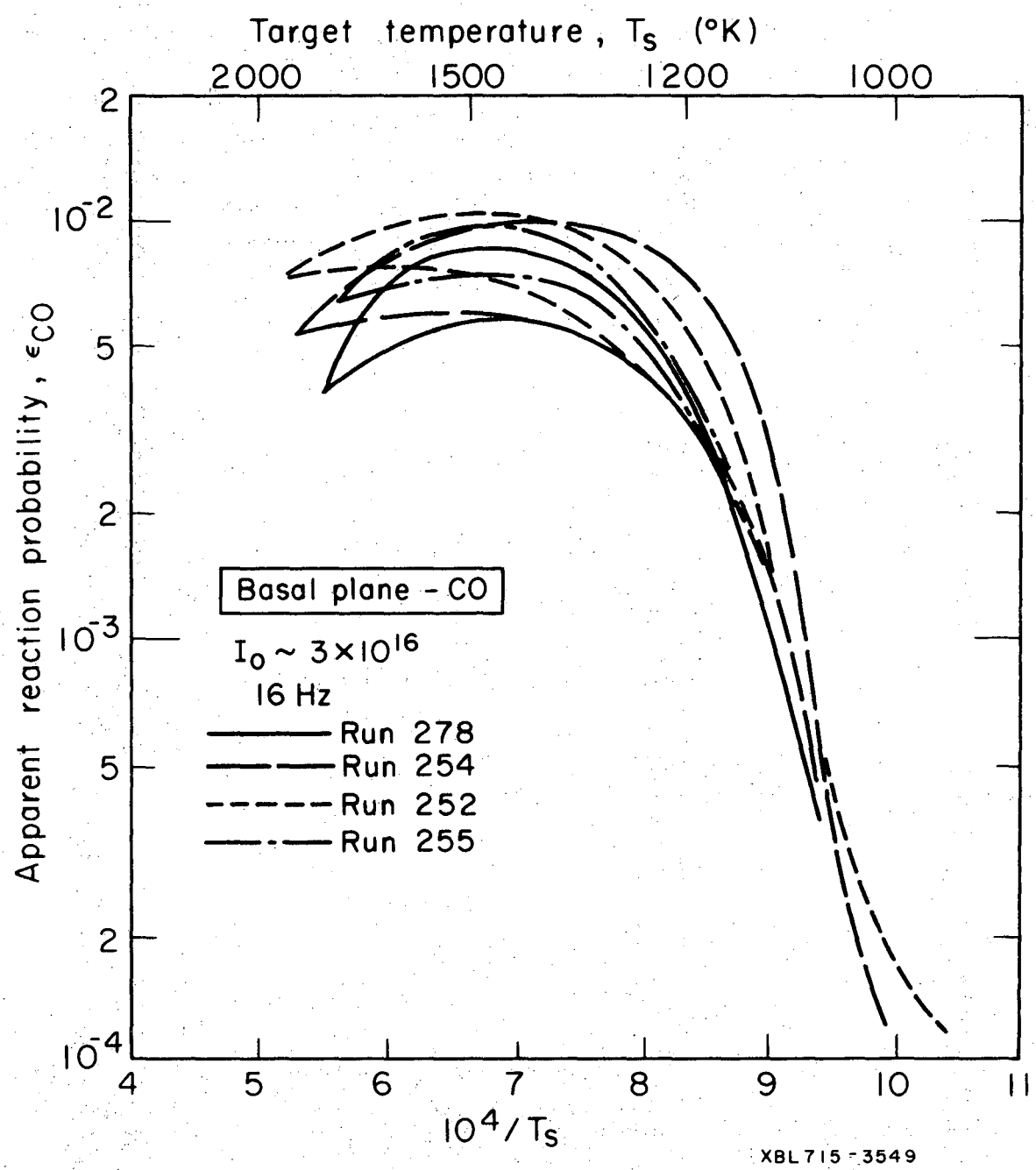

Fig. 29 Reproducibility of hysteresis cycles.

establish a certain concentration of active surface sites. When the temperature is raised, the previous concentration of active sites is in excess of the stationary value at the new temperature and thermal annealing acts only slowly to restore the balance. Consequently, the sample shows temporary "super-reactivity". Near the peak reactivity, thermal annealing mechanisms begin to destroy active sites at a rate comparable to the rate of generation by oxidation. Beyond the peak, thermal annealing exerts sufficient control to reduce the reactivity. This serves to explain the peak in the curve and the fact that the curve for increasing temperature lies above the "stationary" value.

Upon cooling down from a high temperature, the apparent reaction probability follows the lower curve in Fig. 28 which is found to be the curve of stationary state reactivity.

Due to the nature of this hysteresis, none would be observed if the temperature were scanned sufficiently slowly so that the surface activity might be able to keep in step. That the lower curve should happen to be congruent with the steady state apparent reaction probability is entirely circumstantial. Duval[6,79] and others[7] have observed hysteresis in which the reactivity was found to overshoot (undershoot) whenever the temperature was raised (lowered).

Consider bringing a sample from the temperature of peak reactivity (1450°K), where a stationary concentration of active sites has been established, to a lower temperature (say 1125°K) and holding it there with the beam on to develop the active surface. When the temperature is then quickly raised to the peak of the reactivity curve (1450°K), the initial deviation from the previous lower stationary state curve should depend on the time spent oxidizing at 1125°K. However, if the

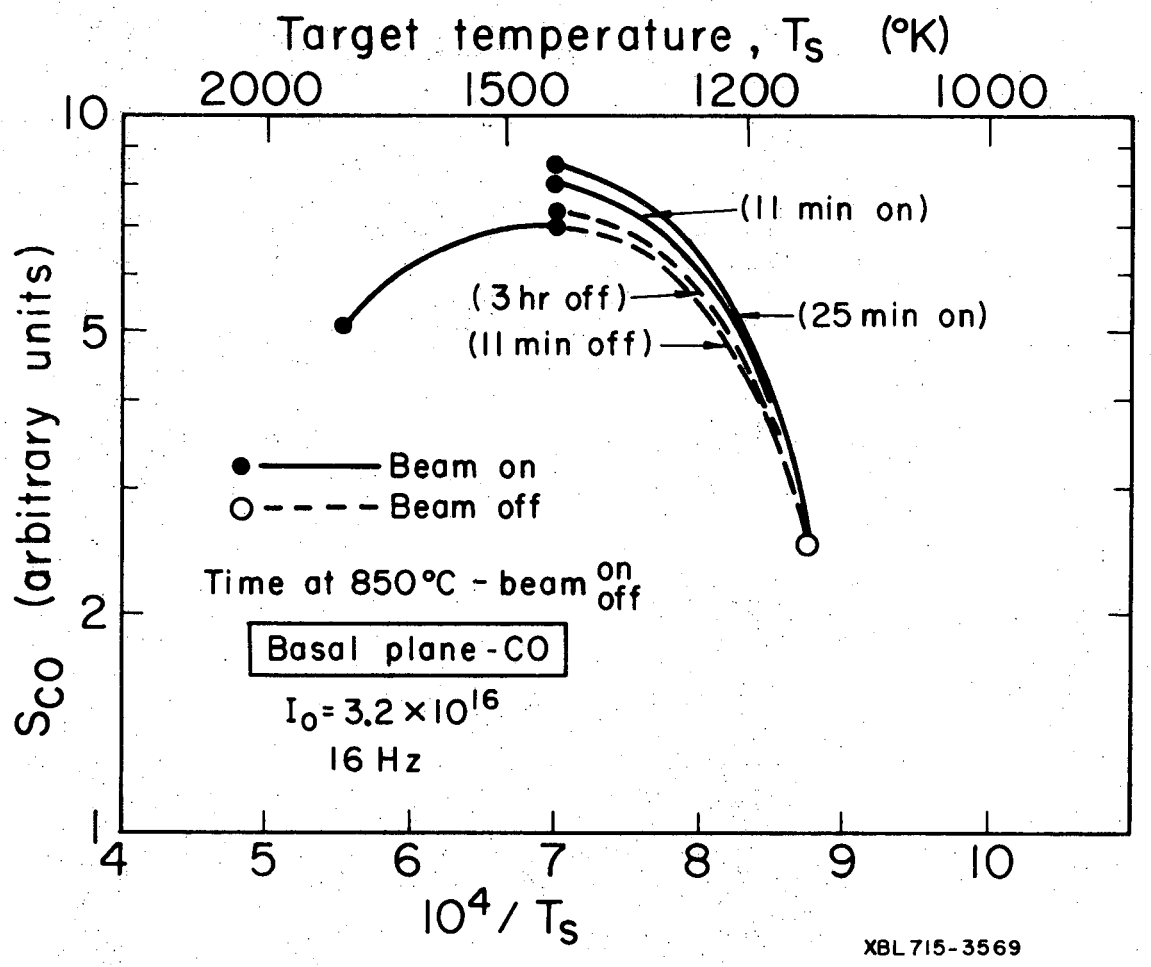

Fig. 30 Beam on--beam off cycling to show oxidative surface development.

beam were turned off while the sample is cooked at 1125°K, no surface reconstruction will take place, (no oxidation, and the thermal annealing rate is low) and, when the target is reheated to 1450°K, the apparent reaction probability (measured with the beam turned on again, of course) will still be at the stationary value. Figure 30 shows the results of such tests which support the explanation that the hysteresis depends on the oxidative generation of active sites which proceeds at low temperatures where the thermal annealing is not effective.

One may achieve a super-reactive condition on the upper curve then follow the reaction as the sample burns away and the apparent reaction probability approaches the stationary value. At 1410°K with a beam of intensity $I_o = 3.2 \times 10^{16}$ molecules/cm^2-sec modulated at 16 Hz, the approach to the lower stationary curve is shown in Fig. 31, which represents a mean life time (1/e fall period) of 40 minutes. (The primary beam intensity, I_o, is applied to the target only half the time due to the symmetrical modulation, consequently the average beam intensity for burn off calculations is $I_o/2$). In two mean life times the reaction probability has approached the lower equilibrium curve to within 13% (based on the initial difference in reaction probability between the upper and lower curves of Fig. 28). During this time 5×10^{17} atoms of carbon/cm^2 (125 basal layers) have been removed. This burn off also corresponds to the removal of 9×10^{-7} gr-atoms carbon/cm^2, and this compares well with the value of 3×10^{-7} gr-atoms/cm^2 estimated by Duval.[79]

A companion parameter to the apparent reaction probability, ε, is the reaction phase lag, ϕ. The variation of CO reaction phase lag with temperature is represented in Fig. 32 and shows <u>no</u> hysteresis as temperature is cycled.

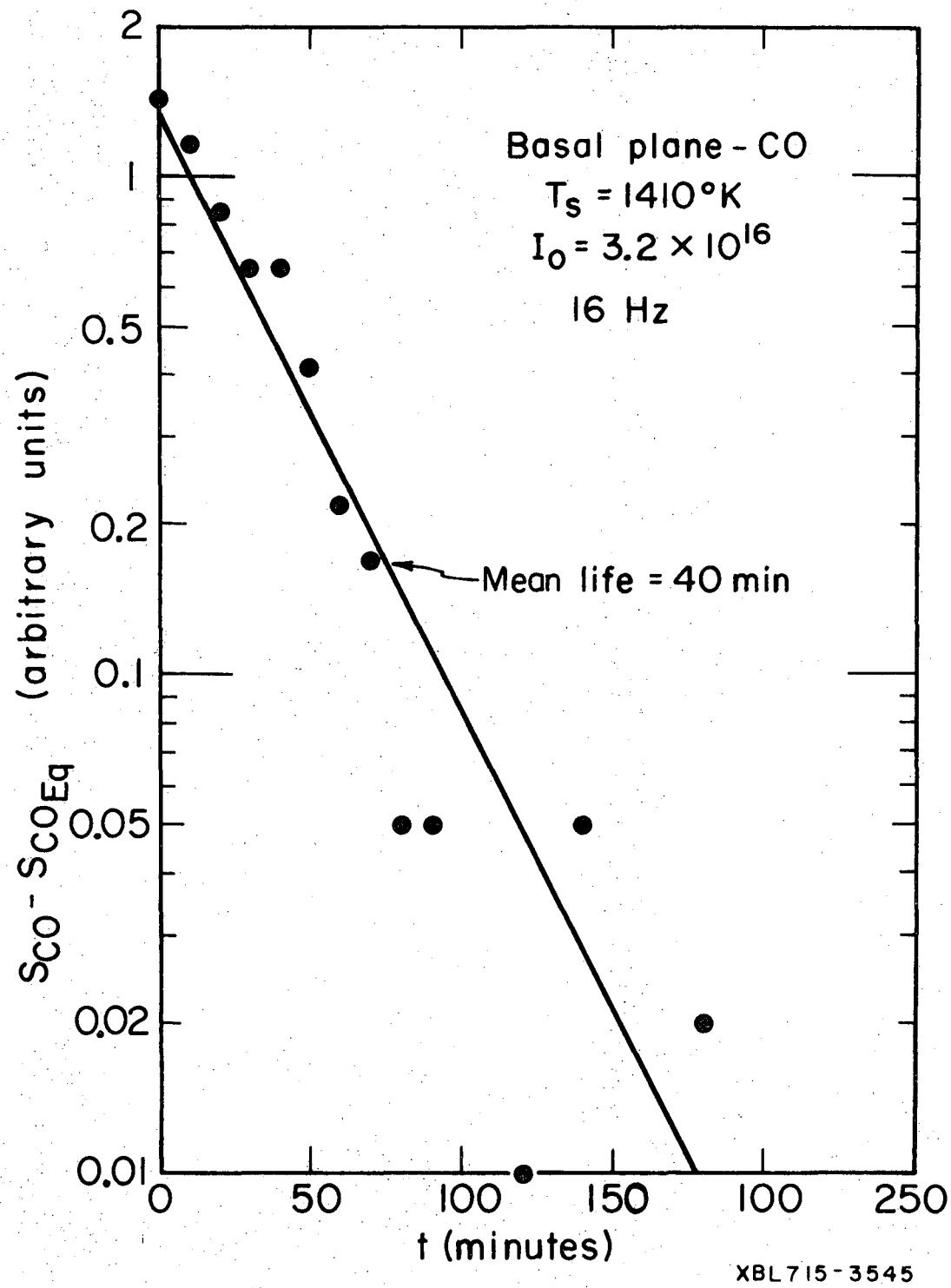

Fig. 31 Approach to equilibrium reactivity during burn off.

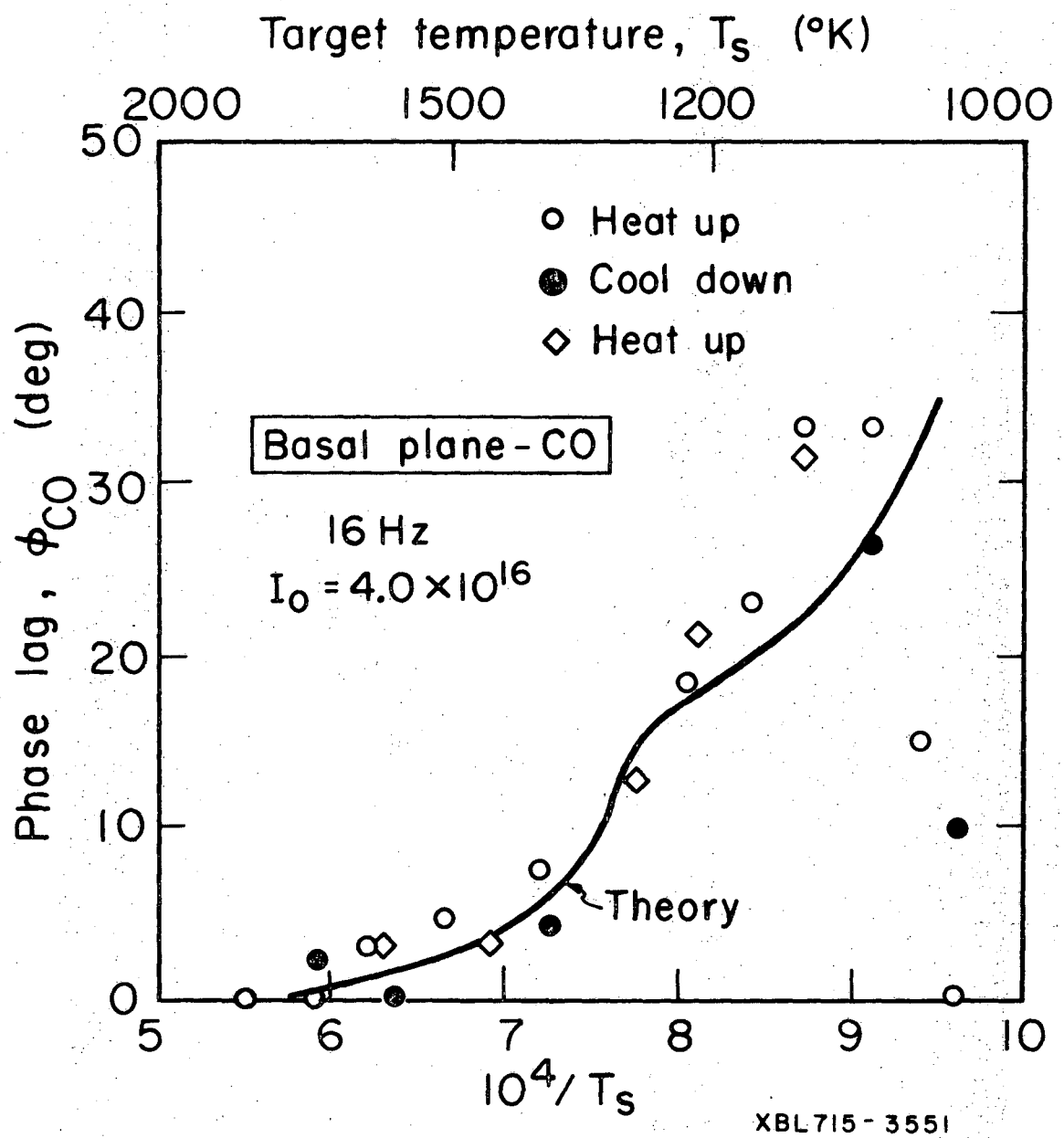

Fig. 32 Reaction phase lag vs reciprocal temperature.

0 0 0 0 3 6 0 5 3 8 1

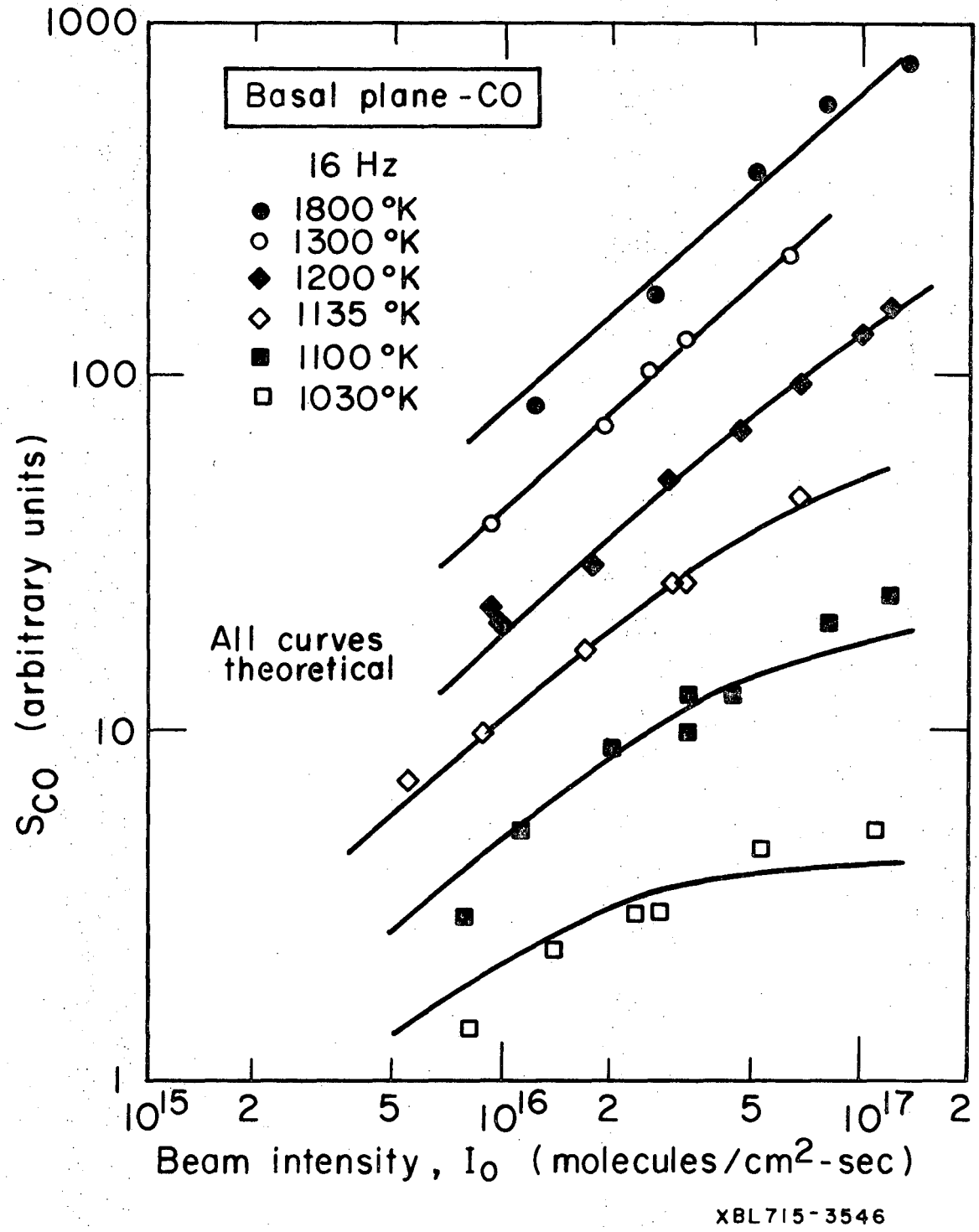

Fig. 33 Kinetic order--CO signal vs beam intensity.

The kinetic order was determined and gave the results of Fig. 33. On this figure the CO signal and oxygen beam intensity are plotted on logarithmic scales and the slope gives the effective kinetic order at each temperature. At high temperatures ($\geqslant 1200°K$) a first order reaction is observed, but as the temperature is reduced the reaction begins to follow progressively lower order kinetics. An arbitrary scale has been used for the signal amplitude and the curves have been stacked above each other proceeding to higher temperatures. If the otherwise useful apparent reaction probability, ε, had been plotted, the upper three curves would be awkwardly intertwined because ε passes through a maximum with T_S.

The reaction rate was found to be insensitive to the temperature of the incident beam as shown in Fig. 34 as an Arrhenius plot of CO signal and beam temperature, T_B. If a beam molecule made only <u>one</u> collision with the surface before reacting or being reemitted, then the chemical kinetics of this reaction is independent of the incident gas temperature. If, however, a molecule made several collisions with, for example, a roughened surface before reacting or being reemitted, then the oxygen would be <u>preheated</u> regardless of the incident beam temperature and this beam heating experiment would be inconclusive.

The capability to extract <u>kinetic</u> information by varying the modulation frequency was only partially exploited in this study. Figures 35 and 36 show the variation of ε and ϕ with frequency for one reaction temperature. A <u>two branch</u> process is suggested because of the slow variation of reaction phase with modulation frequency, $f = \omega/2\pi$ (Fig. 36). For example, the reaction phase at 50 Hz is 10° or $\tan \phi = 0.176$ and at 500 Hz for a one branch process a value of $\tan \phi = 1.76$ or $\phi = 60°$ would be expected whereas, the phase measured at 500 Hz is

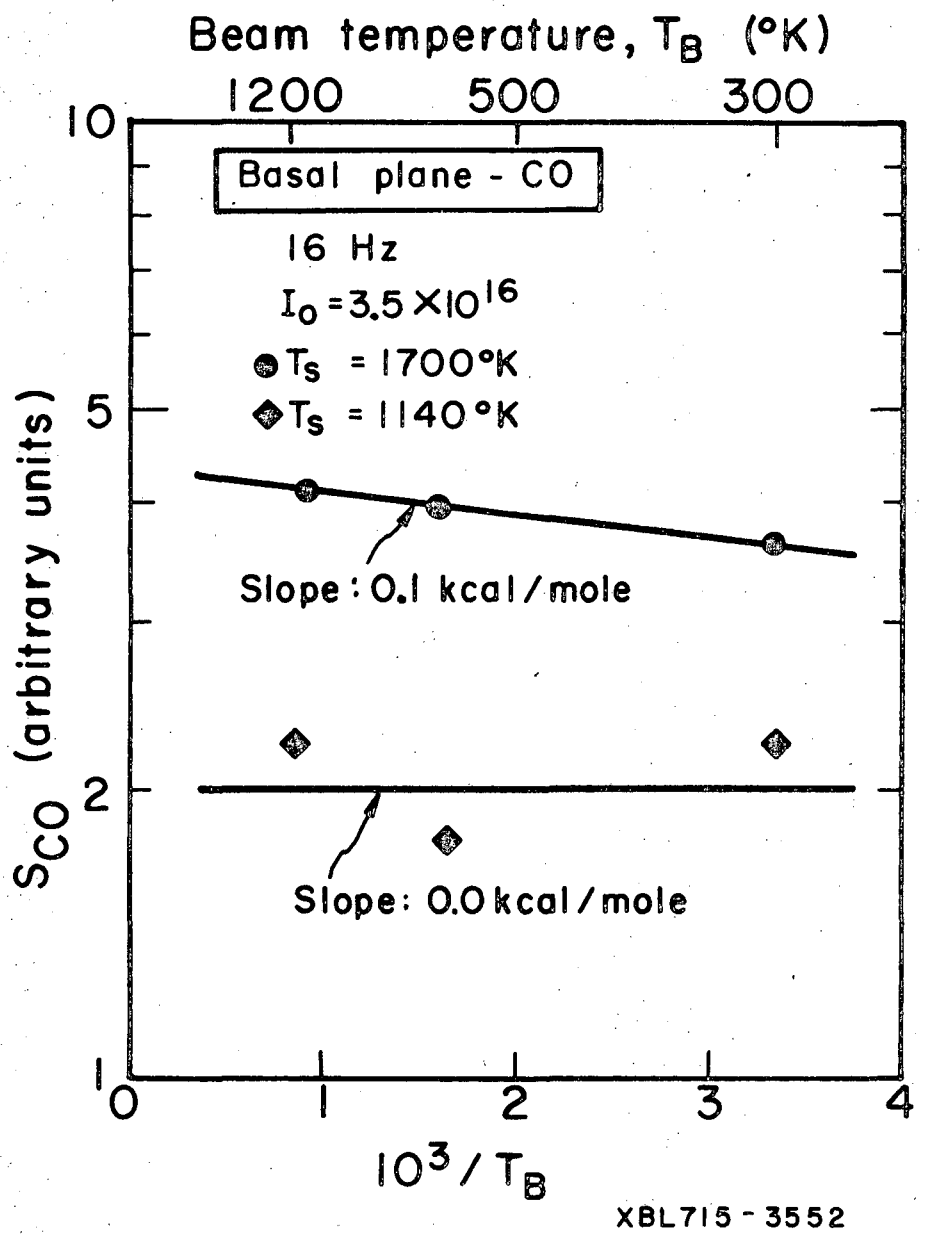

Fig. 34 Sensitivity to beam temperature.

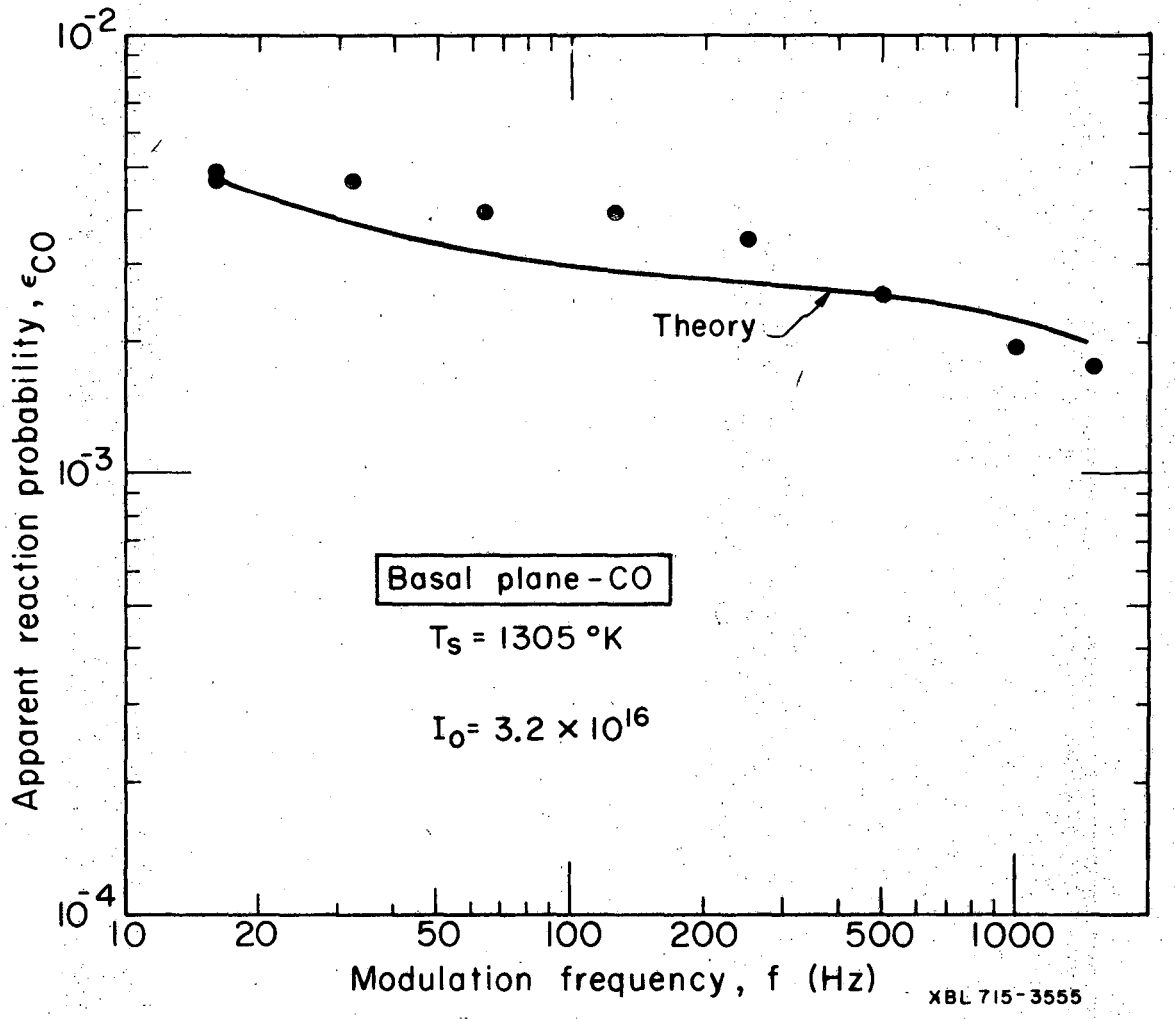

Fig. 35 Frequency scan of the apparent reaction probability ($f = \omega/2\pi$, Hz.).

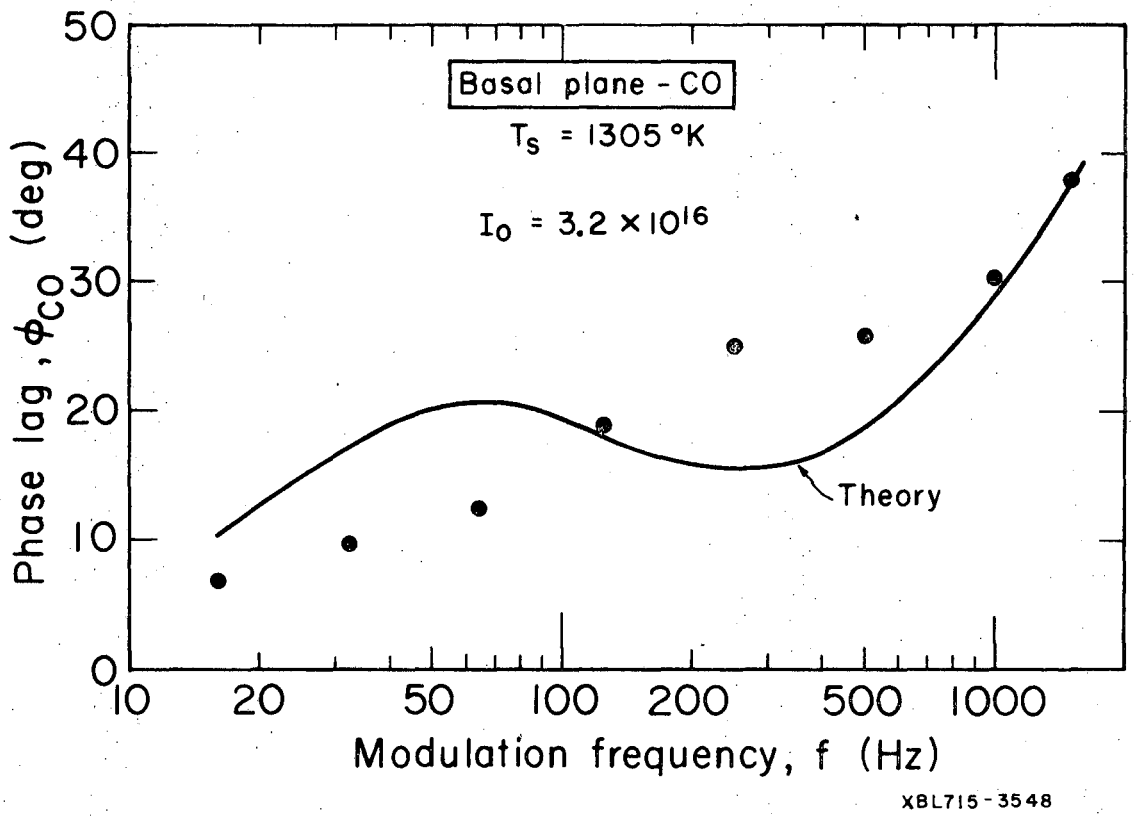

Fig. 36 Frequency scan of the reaction phase lag ($f = \omega/2\pi$, Hz.).

only 25-30°. The variation of the apparent reaction probability with frequency (Fig. 35) is a less sensitive test of a kinetic model but ε is seen to decrease with increasing modulation frequency as expected.

Only a small amount of CO_2 was produced by the reaction therefore CO_2 production does not significantly compete with CO production. Due to the small CO_2 signals only a few experiments measuring CO_2 were performed. This sparse CO_2 data will be discussed later.

B. Reaction Model-CO Production

The essential features of the reaction mechanism implied by the experimental observations have been presented in the previous section. They will be reviewed here in order to establish a basis for the proposed reaction model.

(a) The reaction appears to proceed via two branches to give CO product.

(b) Although the reaction is first order at high temperatures, at lower temperatures the kinetic order is less than one.

(c) Hysteresis in the apparent reaction probability but <u>not</u> in the reaction phase lag shows that the hysteresis does <u>not</u> occur in the rate constants for the elementary steps, k's, but rather in a parameter like the sticking coefficient, η. The hysteresis was explained as due to a lag in the reconstruction of the surface --- trying to achieve a balance between reaction roughening and thermal annealing. A variation in the fraction of reactive surface would be reflected as a change in the sticking probability.

The proposed mechanism for basal plane oxidation considers oxidation on two types of sites, A and B. An oxygen molecule from the beam chemisorbs only on an A site forming one bound CO and releasing the second O atom which migrates about the surface until it finds a B site

0 0 0 0 3 6 0 5 3 8 4

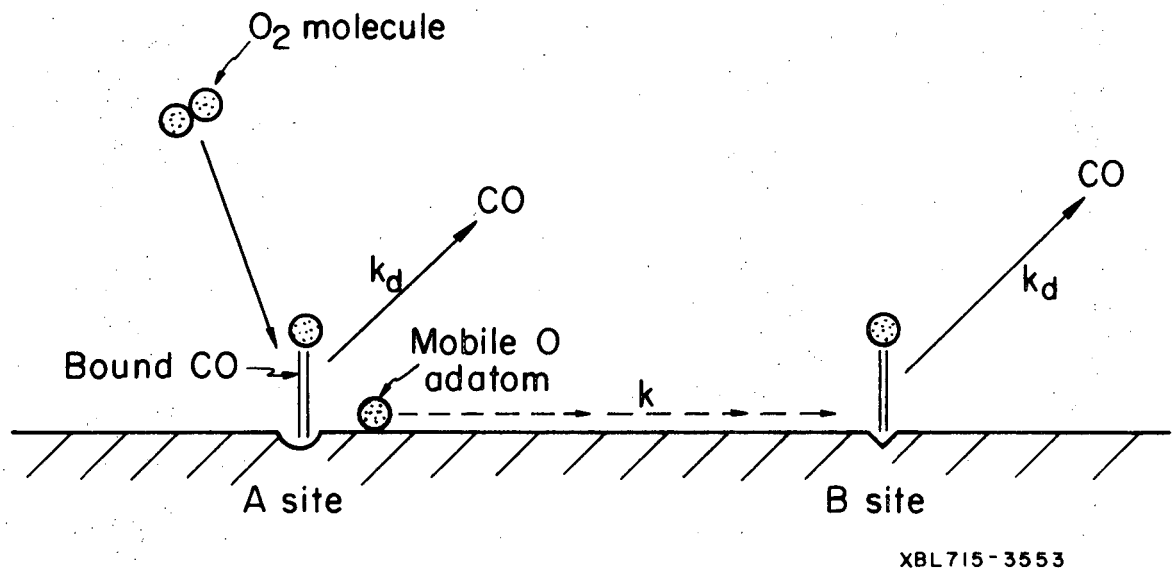

Fig. 37 Basal plane CO reaction mechanism.

where it becomes bound as CO. A pictorial representation of this mechanism is given in Fig. 37. The surface migration is described by a first order rate constant k (Section II-F). CO desorption from both A and B sites is described by the same rate constant k_d. Desorption from an A site leaves behind a bare A site in <u>each</u> case. Desorption from B sites <u>occasionally</u> uncovers a bare A site. This feature is required to provide a net oxidative generation of A sites, and is similar to the model used by Strickland-Constable.[10,11] There is a generation of new bare A sites by oxidation. A sites are deactivated thermally. The oxidative production and thermal annealing of A sites determines the concentration of A sites. Empty B sites are assumed to be always available at a concentration N_B which is not modified when migrating O atoms adsorb on B sites. The constant B site concentration may be incorporated into the surface diffusion rate constant k.

The elementary processes may be written as,

$$O_2(g) + S_A \xrightarrow{\sigma} \begin{cases} (CO)_{ads} \xrightarrow{k_d} CO(g) + S_A \\ O_{ads} + S_B \xrightarrow{k} (CO)_{ads} \xrightarrow{k_d} CO(g) + S_B \text{ (or } S_A) \end{cases} .$$

The interaction of O_2 gas with A sites is described by the A site cross section σ which is related to the bare surface sticking probability η_o through the total concentration of A sites, N_A:

$$\eta_o = \sigma N_A \tag{64}$$

Surface mass balances on O adsorbed on A sites (concentration n'), and CO adsorbed on A and B sites (concentrations n_A, n_B) may be written:

$$\frac{dn'}{dt} = \sigma I_o \, g(t) \, N_A \left(1 - \frac{n_A}{N_A}\right) - k \, n' \tag{65}$$

$$\frac{dn_A}{dt} = \sigma I_o\, g(t)\, N_A \left(1 - \frac{n_A}{N_A}\right) - k_d n_A \tag{66}$$

$$\frac{dn_B}{dt} = k\, n' - k_d\, n_B. \tag{67}$$

$I_o\, g(t)$ is the time varying beam flux whose interaction with available bare A sites is described by a cross section σ. The available A sites are reduced from the concentration of total A sites, N_A, by a coverage factor $(1 - n_A/N_A)$ because some A sites are occupied by $(CO)_{ads}$.

A surface balance on the total A site concentration N_A may be written as,

$$\frac{d\, N_A}{dt} = k^+ + \delta k n' - k^- N_A(1 - \frac{n_A}{N_A}) - \kappa[N_A(1 - \frac{n_A}{N_A})]^2 \tag{68}$$

where k^+ provides for thermal generation of A sites to guarantee some A sites to initiate the reaction and k^- is the rate constant for annealing of unoccupied A sites. The term $\delta kn'$ accounts for the bare A sites which are created when CO desorbs from a fraction δ of occupied B sites. An additional loss term like $-\kappa[N_A(1 - n_A/N_A)]^2$ is included to limit N_A to some finite concentration.[79] Equations (65), (66), (67) and (68) are coupled by N_A, n', n_A and n_B. However, the term $\delta kn'$ in Eq. (68) must be a minor perturbation because although the variation on n' occurs at a modulation rate > 1 cycle/second, the restoration (or generation) period of hysteresis is on the order of 40 minutes. The concentration of A sites may be taken as constant in Eqs. (65), (66) and (67) which will be solved to yield the stationary behavior represented by the lower curve in Fig. 28.

The coupled equation (65), (66) and (67) are <u>non-linear</u>, therefore the response to the complete modulated beam flux must be determined then the first Fourier component may be calculated to compare to the

experimental lock-in amplifier data. Fortunately, the beam profile arriving at the target is nearly square chopped. The beam is either fully <u>on</u> or fully <u>off</u>. Equations (65), (66), and (67) are each solved in a piecewise linear manner using $g(t) = 0, 1$ for half modulation cycles and the results are matched using a cyclic steady state boundary condition.[50]

When the beam is <u>off</u> ($g(t) = 0$), Eq. (66) may be solved to yield,

$$\frac{n_{A_{OFF}}}{N_A}(t) = a_{OFF}\, e^{-k_d t}. \tag{69}$$

Equation (65) is solved for $n'(t)$ which is substituted into Eq. (67) then $n_B(t)$ is found.

$$\frac{n'_{OFF}}{N_A}(t) = c_{OFF}\, e^{-kt} \tag{70}$$

$$\frac{n_{B_{OFF}}}{N_A}(t) = c_{OFF}\, \frac{k}{k_d - k}\, e^{-kt} + b_{OFF}\, e^{-k_d t} \tag{71}$$

When the beam is <u>on</u> ($g(t) = 1$), all three equations are sequentially coupled. Equation (66) is solved for $n_A(t)$ which is substituted into Eq. (65). Equation (65) is solved for $n'(t)$ which is substituted into Eq. (67). Finally, Eq. (67) is solved for $n_B(t)$. Proceeding in this manner one obtains:

$$\frac{n_{A_{ON}}}{N_A}(t) = \frac{\sigma I_o}{k_d + \sigma I_o} + a_{ON}\, e^{-(k_d + \sigma I_o)t} \tag{72}$$

$$\frac{n'_{ON}}{N_A}(t) = \frac{\sigma I_o k_d}{k(k_d + \sigma I_o)} + \frac{a_{ON}\ \sigma I_o}{(k_d + \sigma I_o - k)} e^{-(k_d + \sigma I_o)t} + c_{ON}\ e^{-kt} \quad (73)$$

$$\frac{n_{B_{ON}}}{N_A}(t) = \frac{\sigma I_o}{k_d + \sigma I_o} - \frac{a_{ON}\ k}{(k_d + \sigma I_o - k)} e^{-(k_d + \sigma I_o)t}$$

$$+ c_{ON} \frac{k}{k_d - k} e^{-kt} + b_{ON}\ e^{-k_d t} \quad (74)$$

The six constants a_{ON}, a_{OFF}, b_{ON}, b_{OFF}, c_{ON}, c_{OFF} are determined from cyclic matching conditions which for a modulation frequency ω (rad/sec) may be written as,

$$n'_{ON}(0) = n'_{OFF}(0) \quad (75a)$$

$$n'_{ON}(-\frac{\pi}{\omega}) = n'_{OFF}(\frac{\pi}{\omega}) \quad (75b)$$

$$n_{A_{ON}}(0) = n_{A_{OFF}}(0) \quad (75c)$$

$$n_{A_{ON}}(-\frac{\pi}{\omega}) = n_{A_{OFF}}(\frac{\pi}{\omega}) \quad (75d)$$

$$n_{B_{ON}}(0) = n_{B_{OFF}}(0) \quad (75e)$$

$$n_{B_{ON}}(-\frac{\pi}{\omega}) = n_{B_{OFF}}(\frac{\pi}{\omega}) \quad (75f)$$

The complete time dependence of n', n_A, n_B has been determined. The rate of CO desorption is $k_d(n_A + n_B)$ of which we need only the amplitude and phase of the first Fourier component. The first Fourier component of the modulation function $g(t)$ is $g_1 = 2/\pi$. Sine and cosine integrals S, and C are evaluated from which we calculate the apparent reaction probability, ε_{CO}, and reaction phase lag, ϕ_{CO}, by:

$$\varepsilon = \frac{k_d}{I_o}\frac{\pi}{2}\sqrt{S^2 + C^2} \tag{76}$$

$$\phi = -\tan^{-1}(C/S) \tag{77}$$

$$S = \frac{\omega}{\pi}\left\{\int_{-\pi/\omega}^{o}(n_{A_{ON}} + n_{B_{ON}})\sin(\omega t)dt + \int_{o}^{\pi/\omega}(n_{A_{OFF}} + n_{B_{OFF}})\sin(\omega t)dt\right\} \tag{78}$$

$$C = \frac{\omega}{\pi}\left\{\int_{-\pi/\omega}^{o}(n_{A_{ON}} + n_{B_{ON}})\cos(\omega t)dt + \int_{o}^{\pi/\omega}(n_{A_{OFF}} + n_{B_{OFF}})\cos(\omega t)dt\right\} \tag{79}$$

Explicit expressions for S and C are available in appendix I.

C. Comparison with Experiment --- Determination of Kinetic Parameters

Fortunately, certain simplifications may be made so that all parameters need not be determined simultaneously. In the high temperature limit, ($T_S \gtrsim 1200°K$), $n_A/N_A \ll 1$, the reaction is linear. Eqs. (66), (67) may be added together to form one equation in the total surface density of CO, $n = n_A + n_B$,

$$\frac{dn}{dt} = \sigma I_o g(t)\, N_A + k\, n' - k_d\, n \quad . \tag{80}$$

Equations (80) and (65) (neglecting n_A/N_A) are easily solved for the response to the fundamental component of the beam modulation by substituting, $g(t) = g_1\, e^{j\omega t}$, $n'(t) = n'_1{}^*\, e^{j\omega t}$, $n(t) = n_1{}^*\, e^{j\omega t}$ and proceeding as in section II to obtain,

$$\varepsilon\, e^{-j\phi} = \eta_o \frac{1}{\left(1 + j\frac{\omega}{k_d}\right)}\left[1 + \frac{1}{\left(1 + j\frac{\omega}{k}\right)}\right] \tag{81}$$

where $\eta_o = \sigma\, N_A$ is the bare surface sticking probability.

At high temperature we assume $k_d \gg \omega$. Then from Eq. (81) the reaction phase lag is given by,

$$\tan \phi = \frac{\omega/k}{2 + (\omega/k)^2} \tag{82}$$

The low frequency (16 Hz) phase lag data measured at temperatures above 1300°K were used to calculate values of k from Eq. (82). An estimated ±1° error in determining the phase was considered and the k values with error bars were plotted Arrhenius fashion in Fig. (38) from which the activation energy, E, and the pre-exponential, A, were determined.

$$k = A\, e^{-E/RT_S} \qquad A = 2.5 \times 10^7 \text{ sec}^{-1}$$

$$B = 30 \text{ kcal/mole}$$

The rate constant k is thereby determined for all temperatures. At 1305°K, the variation of reaction phase lag with frequency is used to determine the value of k_d at that <u>one</u> temperature. Using Eq. (81) (the linear limit is still valid) for various ratios k/k_d a family of curves of reaction phase vs modulation frequency may be generated (Fig. 39). The best ratio, $k/k_d = 0.02$, was chosen to match the data (Fig. 36) and determine k_d at 1305°K. Considering k_d to be of the form, $k_d = A_d\, e^{-E_d/RT_S}$, we now have one constraint on (A_d, E_d).

This is the end of the well-paved road. Parameters yet to be determined are σ and E_d (or alternately, A_d), and we must venture into the non-linear region.

For a selected value of E_d, A_d is determined, (by the condition $k/k_d = 0.02$ at 1305°K). Then with a selected value of the cross section σ, the apparent reaction probability ε and the reaction phase lag ϕ are calculated along with the variation of product amplitude S_{CO} with beam intensity I_o (order plot, Fig. 33). The parameters E_d (or A_d) and σ are adjusted to provide the best fit to all the data. The theoretical

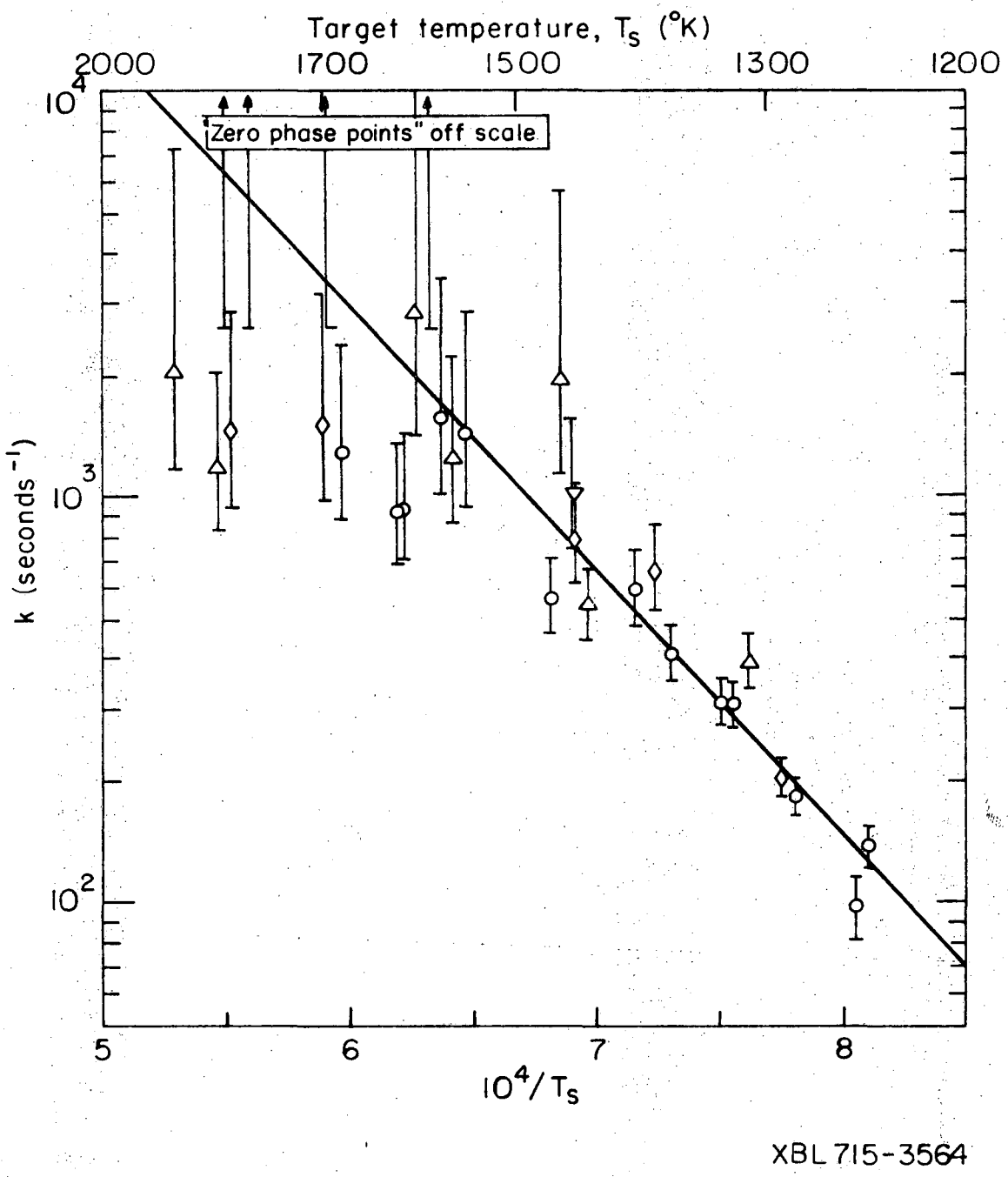

Fig. 38 Data Reduction--Arrhenius plot of the rate constant k.

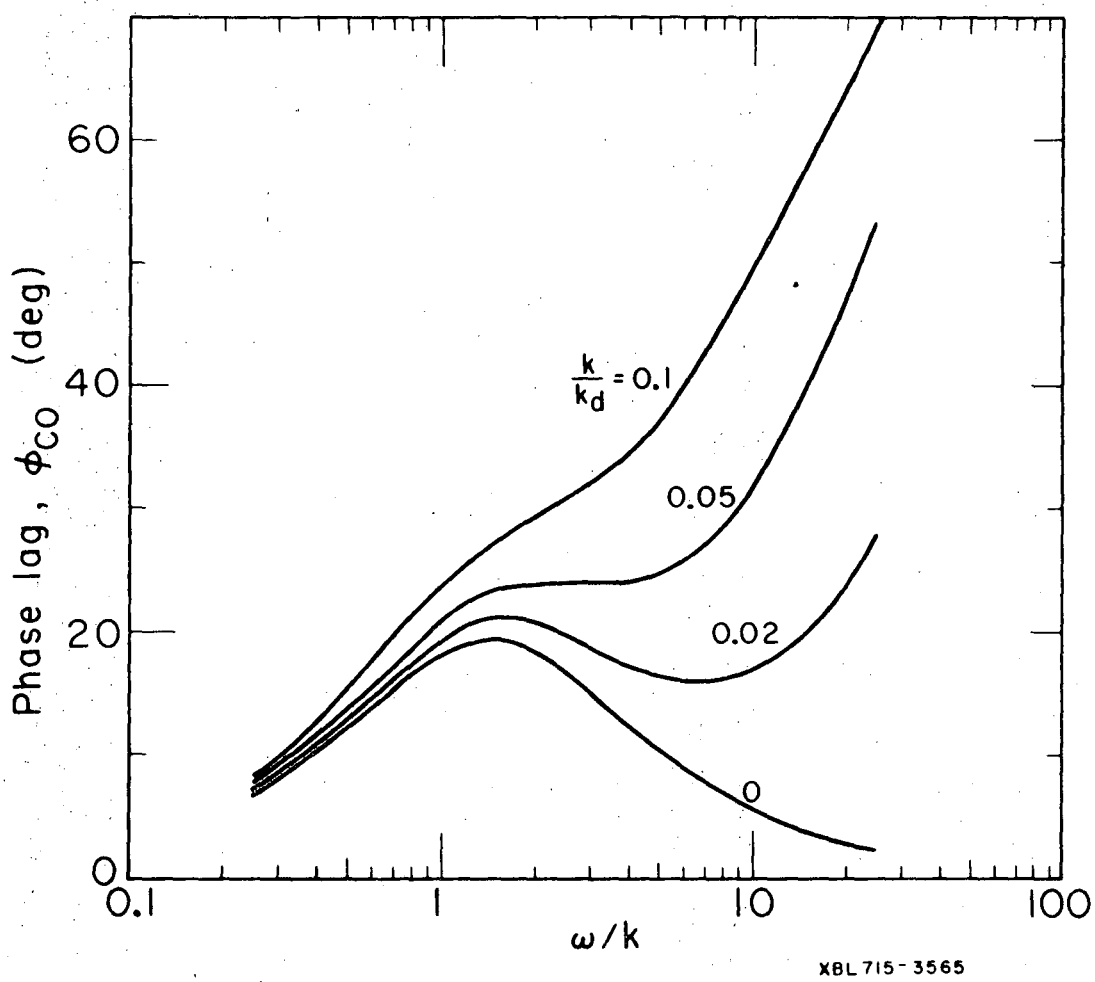

Fig. 39 Theoretical reaction phase lag vs modulation frequency for various ratios k/k_d.

variation of the apparent reaction probability ε with reciprocal temperature T_S is shown in Fig. 40 and the other comparisons of theory and experiment have already been seen (Figs. 32, 33, 35, 36). From this tedious calculation we obtain:

$$E_d = 50 \text{ kcal/mole}$$
$$A_d = 3 \times 10^{12} \text{ sec}^{-1}$$
$$\sigma = 75 \times 10^{-16} \text{ cm}^2$$

The assumption $k_d \gg \omega$ made to evaluate the parameters in k at the high temperature end of the linear limit may be checked. At 1300°K we calculate:

$$k_d = 3 \times 10^{12} \, e^{-50/(2 \times 1.3)} = 1.3 \times 10^4 \text{ sec}^{-1}$$

The modulation frequency was 16 Hz (ω = 100 radians/sec), therefore the assumption is satisfactory at 1300°K and becomes better at higher temperatures when k_d increases.

D. Interpretation

If we may assume that the maximum in reaction probability in Fig. 40 (lower curve) represents reaction on a clean surface suffering no demodulation, then we determine.

$$2 \, \eta_o = 2 \, \sigma \, N_A \approx 5 \times 10^{-3}$$

or,

$$N_A = 3 \times 10^{11} \text{ sites/cm}^2 \quad .$$

The A sites of 75 Å^2 area are equivalently 10 Å in diameter or encompass fifteen basal plane mesh hexagons. The A sites are separated by 180 Å ($1/\sqrt{N_A}$).

By the model an A site may be created by desorption of CO from a

0 0 0 0 3 6 0 3 3 8 9

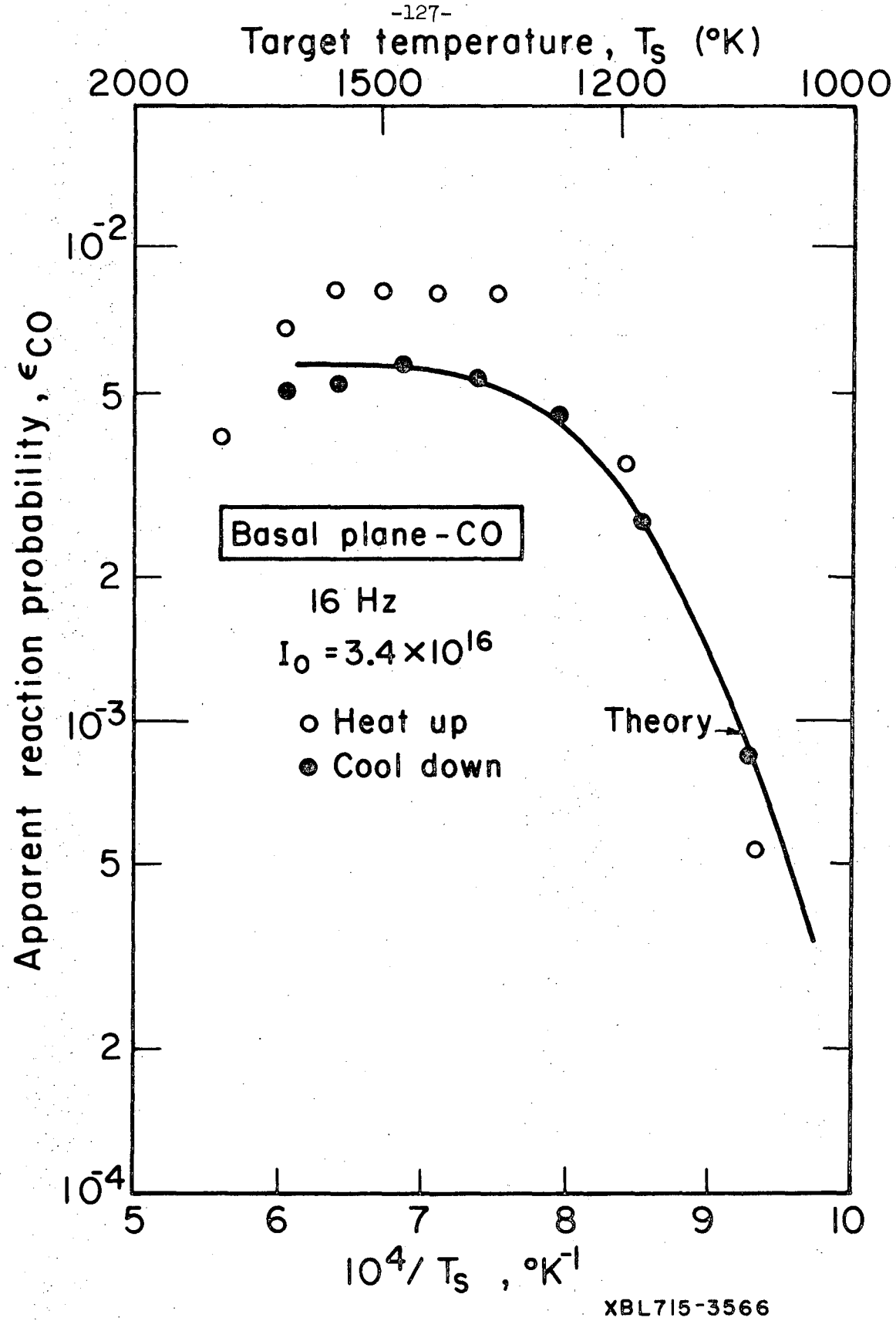

Fig. 40 Fit to theory--Arrhenius plot of the apparent reaction probability.

filled B site whereby one carbon atom is removed from the surface. A "filled" A site is returned to a reactive state when it too desorbs CO thereby removing one carbon atom from the surface. However, the A site cross section for chemisorption was determined to be 75 $Å^2$, so apparently a single basal plane vacant A site of area 2.5 $Å^2$ exerts an influence on chemisorption over an area 75 $Å^2$.

It was determined that "super-reactivity" (due to an excess concentration of A sites) encountered on the upper branch of the hysteresis curve (Fig. 28) is reduced to the stationary state reactivity if the reaction is allowed to proceed for an hour or so removing a hundred basal layers. If an A site is only the size of one or a few carbon atoms, why must so many layers be removed before normal reactivity is restored? The answer, of course, is that while annealing processes are working to remove excess A sites, all A sites are initiating gasification of the surface. Burn off at an A site simply regenerates a new A site. Additionally, burn off from a few suitable B sites will create A sites. Eventually, after many layers are gasified, the annealing processes have caught up and the reaction rate returns to normal.

Let us further consider Eq. (68). Although it is possible to obtain a <u>small</u> term, dN_A/dt, from the difference of nearly equal <u>large</u> terms, this is not likely to exist in the present case because then a small deviation in N_A would be quickly corrected. Consequently, the dominant positive and negative terms must be on the order of dN_A/dt. In order that the term $\delta kn'$ should not prompt the hysteresis to recover in a time on the order of a modulation period, it must be small compared to dN_A/dt. From the measured hysteresis recovery, we have $(dN_A/dt)/N_A = (40 \text{ minutes})^{-1} = 4 \times 10^{-4} \text{ sec}^{-1}$. At steady state with $\sigma = 75$ $Å^2$ and

a beam of 3.3×10^{16} molecules/cm^2 - sec. we obtain $kn'/N_A = 120$. Therefore, δ must be much less than 3×10^{-6} in order that the hysteresis should not be corrected in a time commensurate with a modulation period.

This very small value of δ implies that on the order of 10^6 carbon atoms (or more) will be gasified before a new A site is generated from a B site. Typical A site concentrations are on the order of 10^{11} cm^{-2} so we see that by the time 10^{17} carbon atoms/cm^2 have been removed, one entirely new generation of A sites will have been created from B sites. This value (10^{17} carbon atoms/cm^2) is on the order of the burn off level which restored normal reactivity and suggests that during the burn off, each A site generated one extra A site further prolonging the restoration process.

Although the concentration of A sites, N_A, was regarded at the outset as an explicit function of temperature and previous oxidation, only a single "typical" value of N_A was extracted from the data. Every last scrap of experimental data was used to derive the kinetic parameters, but more extensive data could have provided for a more careful consideration of the variation in N_A. Nevertheless, from the hysteresis experiments we may note that the A site concentration produced at 1125°K was only reduced by a factor of two when held at 1450°K.

The rate constant k cannot be ascribed to a simple desorption because of the low value of the pre-exponential factor ($A = 2.5 \times 10^7$ sec^{-1}). Rather, it probably represents migration of O_{ads} to B sites as discussed in section II-F. The rate constant may be related to the surface diffusion coefficient D_S and the surface concentration of B sites.

$$k = 4\, D_S\, N_B = A\, e^{-E/RT_S} \quad . \tag{83}$$

The surface diffusion coefficient D_S is activated by the energy E, and is given by,

$$D_S = 6 \frac{\Gamma a^2}{4} e^{-E/RT_S} \quad . \tag{84}$$

It is assumed that an atom diffusing on the basal plane may jump in six directions. Taking a jump frequency of $\Gamma = 10^{13}$ sec^{-1} and a jump distance, a = 2.5 Å, we obtain from the measured pre-exponential factor ($A = 2.5 \times 10^7$ sec^{-1}) the average surface concentration of B sites,

$$N_B = 7 \times 10^8 \text{ cm}^{-2} \quad ,$$

or a B site spacing of 3800 Å ($1/\sqrt{N_B}$).

The special property assigned to B sites --- that they be always available in a fixed concentration unperturbed by adsorption of O atoms or desorption of CO --- deserves further comment. Curiously, although type B sites are found in a concentration that is 400 times smaller than the concentration of A sites, the B sites do not saturate and contribute to non-linear behavior. The extraordinary properties of B sites are, perhaps, the most serious blight on this reaction model. Nevertheless, it is instructive to speculate on a physical model for such B site behavior. Empty, available B sites might be thermally generated and annealed so rapidly as to maintain a steady empty B site concentration. Alternatively, a B site could be a "macro" site encompassing many potentially reactive carbon atoms. Perhaps "macro" B sites are regions where dislocation lines terminate at the surface surrounded by many disturbed carbon atoms. If the total number of atoms in "macro" B sites were much greater than the number of A sites in a given area, the A sites could become saturated by adsorbed CO before adsorption began clogging B sites. Of course, when A sites are

saturated the filling of B sites will cease because an empty A site is required to dissociate O_2 to provide a migrating O_{ads} for a B site to capture.

The B site density, N_B, was estimated from the measured surface migration rate constant, k, and an estimated surface diffusion coefficient, D_s. B sites were regarded as lattice point locations, but with "macro" B sites which represent a larger sink the surface diffusion coefficient would be a bit larger (depending on the "macro" B site circumference) and a revised (downward) estimate of N_B would result.

Electron micrographs were obtained of the target surface before and after reaction (Fig. 41). Oxidation has certainly obliterated any preconditioning due to polishing. No "hexagonal etch pits" such as observed by Hennig[15,16,17] or Thomas[18,19,20] are apparent. In fact, the micrograph hardly looks like a flat or reaction pitted basal surface at all. It resembles more closely the micrographs of the allotrope(s) "white carbon".[66] Of course, the reaction analysis which was often presented in terms of "basal surface layers removed" is entirely independent of this colorful "unit" of reaction progress.

E. Further Proof-Waveform Analysis

Although everyone will agree that a reaction response will lag the modulated beam excitation to an extent determined by its "residence time", the conviction that a lock-in amplifier will properly process the first Fourier component of the reaction signal and allow us to extract the correct kinetic information has not found its way into all hearts. Perhaps if the kinetic parameters extracted by the lock-in could be shown to properly reconstruct the complete time dependence of the reaction signal some apprehension would vanish.

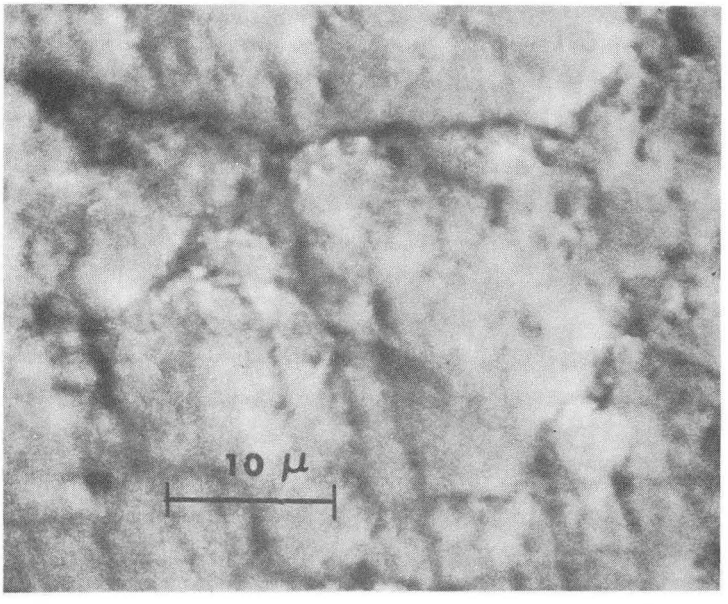

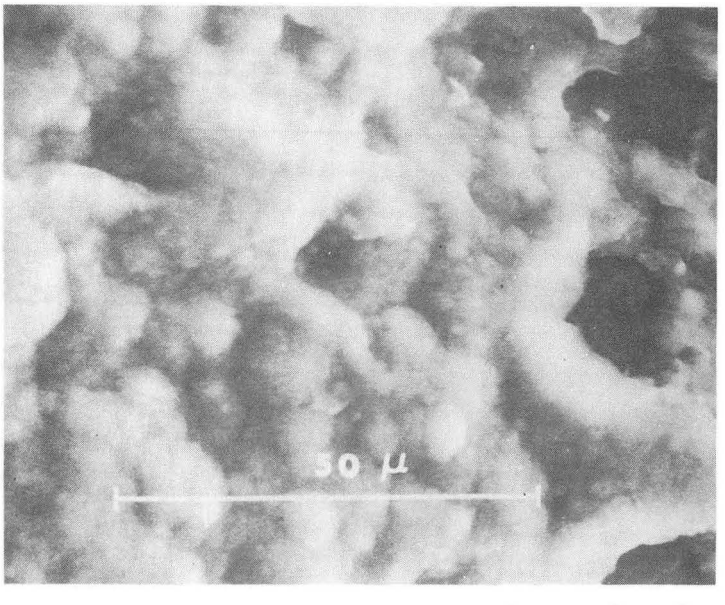

XBB 718-3769

Fig. 41 Basal Plane sample scanning electron micrographs, before and after oxidation.

0 0 0 0 3 6 0 5 3 9 2

A computer of average transients "CAT" (Technical Measurements Corp. CN-1024/202) was used to recover the weak CO signal of 1175°K reaction from the noise background. The CAT (or multiscaler) operates by repetitively scanning a noisy signal containing periodic information. A scan is initiated in synchronization with the primary modulation which stimulated the periodic signal, and the time for one scan is divided into "channels". As the channels are scanned, they sample the signal and noise and accumulate a record of the signal plus noise. Over many scan cycles the noise component in all channels will approach a common value (increasing, however, with each scan). The periodic information is inherently different in all channels and will eventually be seen to rise out of the noise. Such was the case in this work, the CAT output was a large DC noise level added to the periodic reaction signal. The CAT was connected through a Keithley 610B electrometer amplifier to the mass spectrometer and set to repetitively scan the output signal with the onset of each scan synchronized to the beam modulation. Each scan covered a little over two modulation periods and many scan cycles (40,000 sweeps) were required. Figure 42 shows the scattered reactant beam profile, and the desorbed CO reaction product signal along with two theoretical predictions of CO signal shape. It may be noted that the CO signal shape is not unusual --- it simply tries to follow the beam modulation.

The basal plane reaction model predicts that the rise and fall of the CO signal, which is proportional to $k(n_A + n_B)$, is controlled by Eqs. (69), (71), (72), and (74) which contain three exponential terms. The theoretical waveform has been superimposed on the data in Fig. 42, and the agreement is satisfactory.

It might be suggested that a single decay constant representation

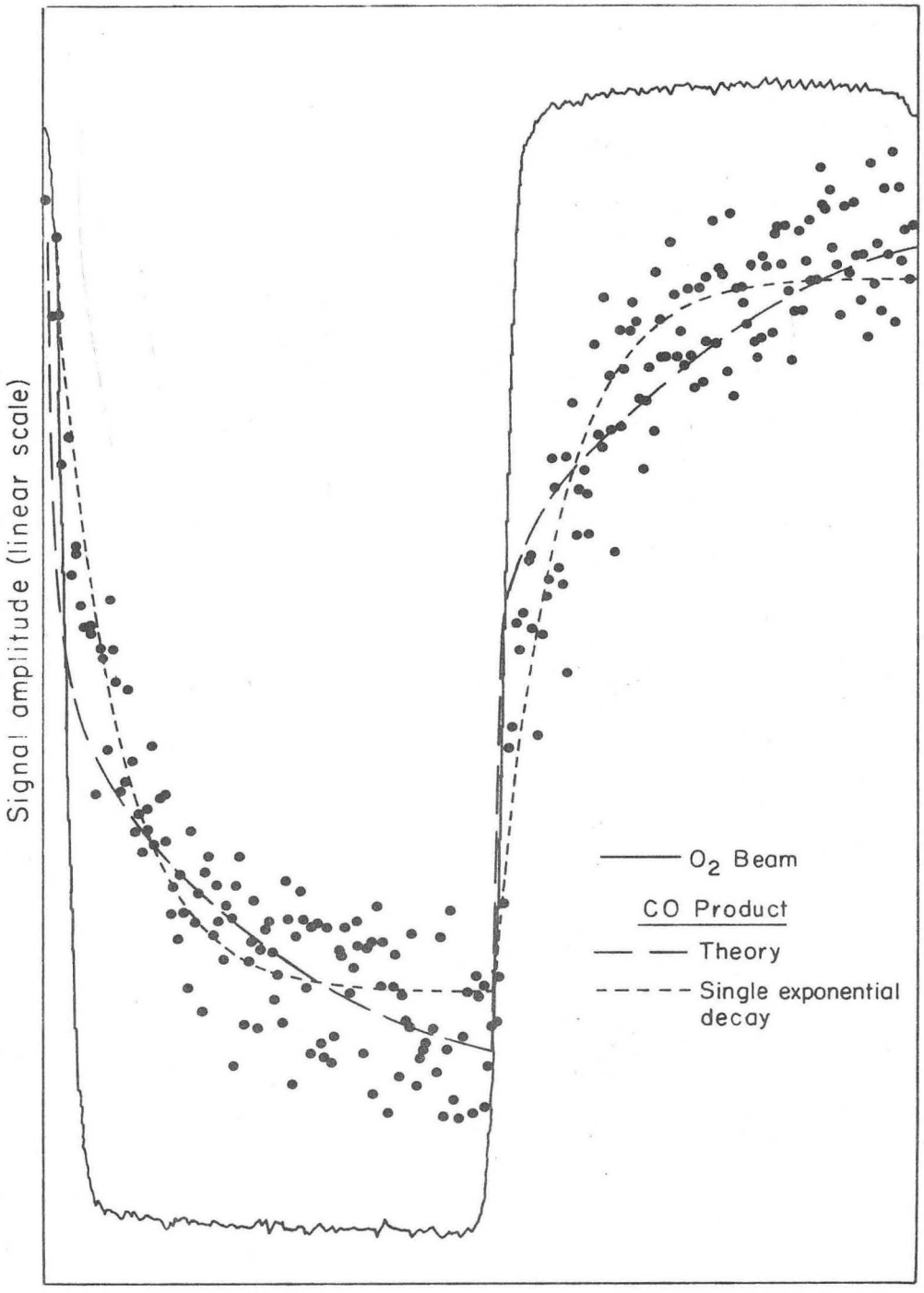

XBL719-7315

Fig. 42 CAT-extracted waveform of reactant O_2 and CO reaction product signals. Two theoretical approximations to the CO signal. Target temperature, T_S = 1175°K. Modulation frequency, f = 16Hz.

of the CO signal would mimick the wave shape sufficiently well. A best representation by a single decay waveform has been added to Fig. 42, and it appears to fit the CAT data equally well! Nevertheless, a model with a single rate constant can only satisfy part of the data.

Variation of the modulation frequency serves to selectively probe reaction steps having different characteristic times. The lock-in amplifier is usually employed to measure only the fundamental frequency component. The complete waveform (obtained using the CAT) contains additional information from the higher harmonics of the square chopped primary beam. The waveform of desorbed reaction products is determined by the modulation frequency and the rate constants or characteristic reaction times. Varying the modulation frequency reflects differently the effects of various reaction steps. Although a suitable experiment was not performed, the follow paragraph describes how a single exponential waveform would not adequately describe the reaction.

The single exponential waveform is seen to represent a compromise between the fast rise and slow rise portions of the theory waveform. If the modulation frequency were raised substantially, the slower rising exponential(s) (of the theory waveform) would be significantly compressed (not having sufficient time to rise) and the dominant characteristic would be the faster rising component. The single exponential would be refit to a new value biased toward the fast rise exponential. This readjustment of what is essentially the <u>rate constant</u> is inadmissable, because the parameters such as the target temperature which determine the rate constant have not been changed.

No attempt was made to extract the complete wave form using a much higher modulation frequency for two reasons. First, a suitable modulation frequency would be about 1000 Hz, but the fastest CAT sampling

rate is 32 micro-seconds per channel which in each sweep would spread 33 modulation cycles across the 1024 channels, providing only 15 data points per half cycle of modulation. Second, transit and complex impedance corrections would have to be applied in detail to the complete waveform considering the effect on each harmonic of which the waveform is composed. Furthermore, due to the poor signal only the proposed trial single exponential waveform is "known" as to shape, and the amplitude and phase corrections would have to be applied to each trial waveform before it was compared to the CAT data. A Fourier analysis-synthesis procedure may be circumvented in this case (section III A-8). The complex impedance and molecular transit effects could be formulated as a circuit model and a piecewise-linear solution obtained in each half period for excitation by exponential rise or fall segments.

F. CO_2 Reaction

Although the oxidation of basal plane pyrolytic graphite produced sufficient CO to enable to detailed study of this reaction, only a small quantity of CO_2 was produced. The apparent reaction probability for CO_2 production, ε_{CO_2}, was typically an order of magnitude below ε_{CO}, and the CO_2 signals were very near the lower bound of system sensitivity (Fig. 43). Each data point required a considerable observation (integration) time on the order of two hours. No frequency scans were made, in fact a low modulation frequency (16 Hz) was used to avoid excess loss of signal due to demodulation. Nevertheless, the reaction phase measured at three temperatures was found to be 25-30° (Fig. 44), which for a one step process would imply demodulation to 85-90% of the DC signal value.

0 0 0 0 3 6 0 5 3 9 4

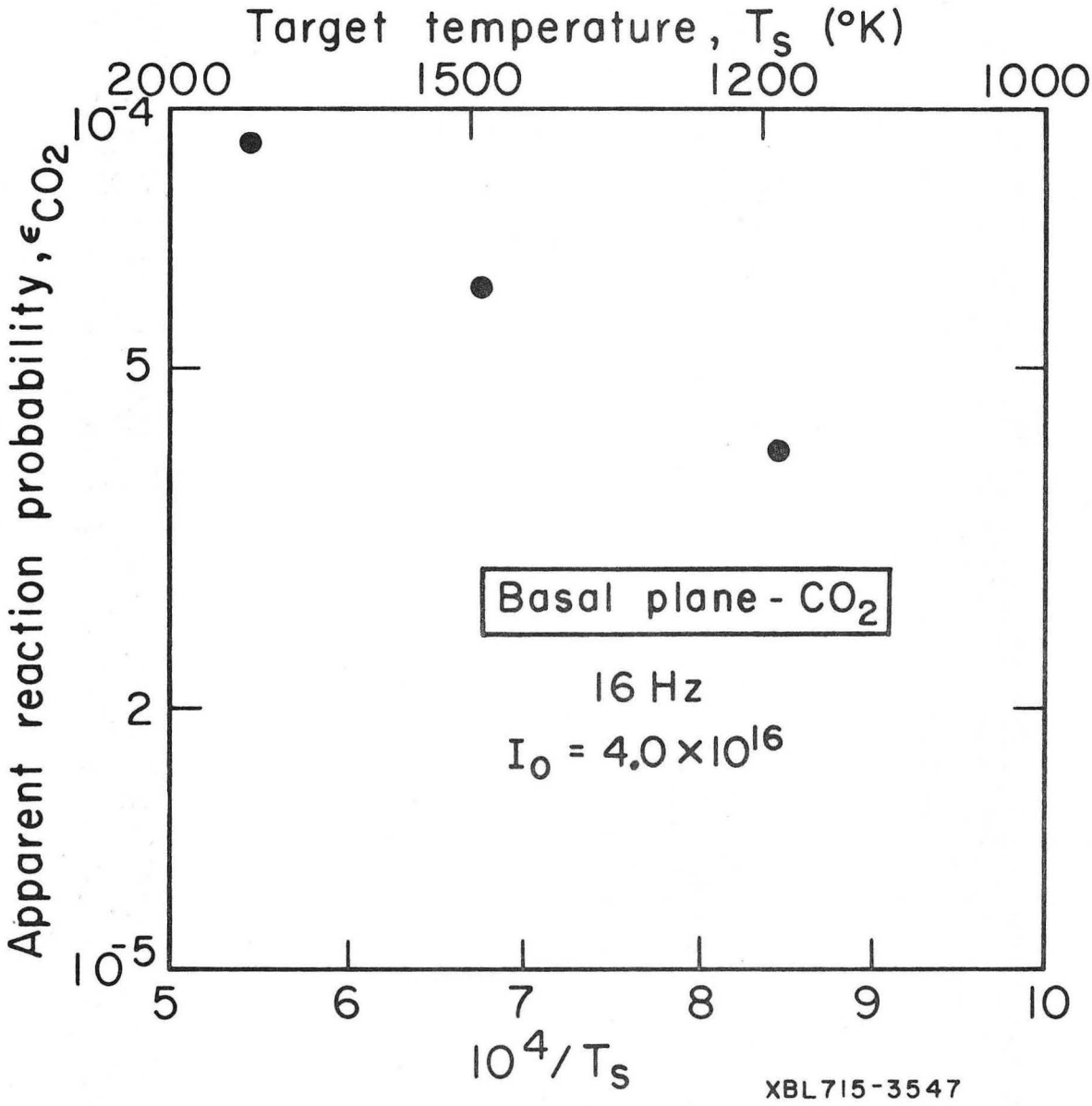

Fig. 43 Arrhenius plot of the apparent reaction probability.

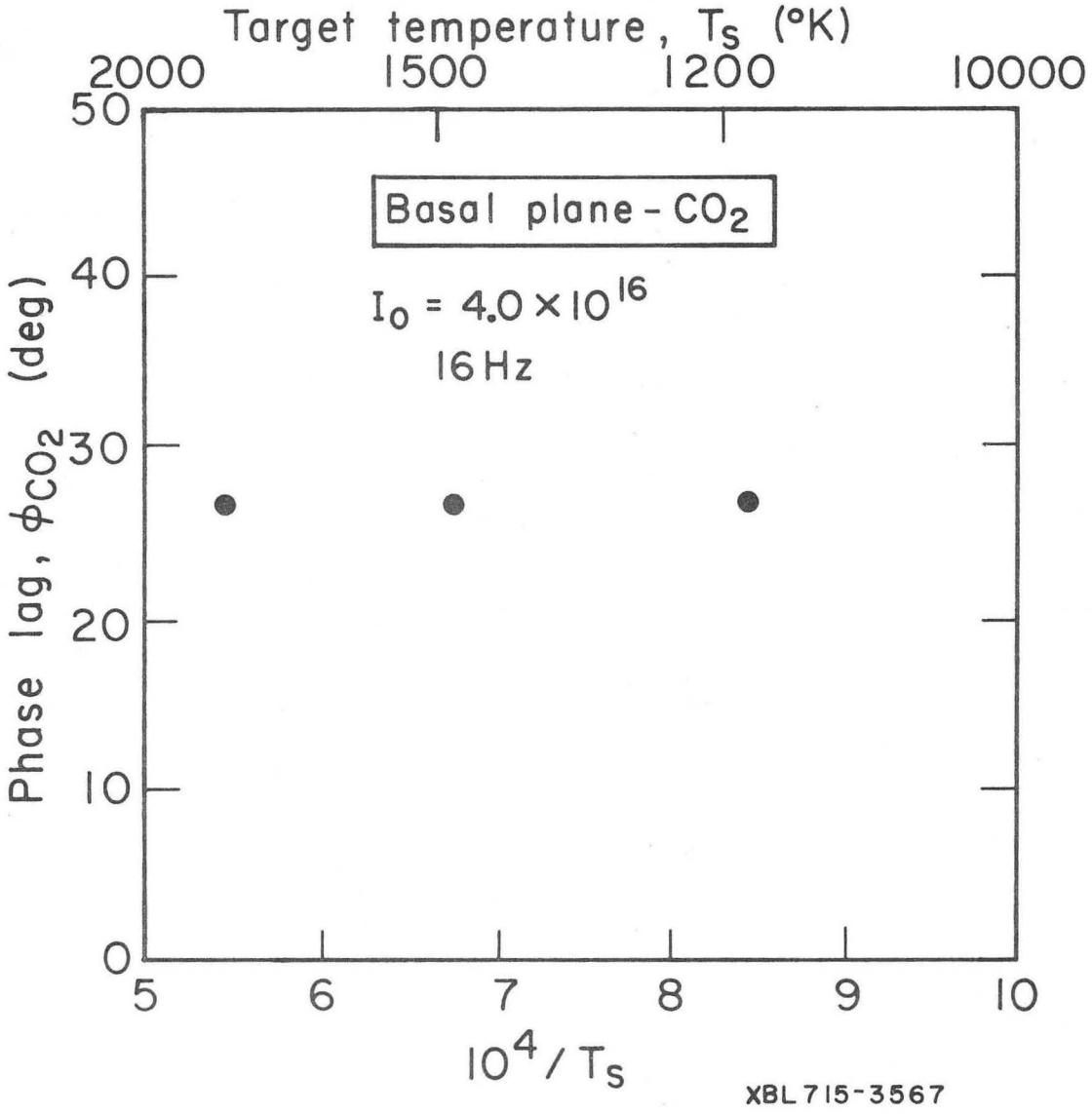

Fig. 44 Reaction phase lag vs reciprocal temperature.

0 0 0 0 3 6 0 3 3 9 5

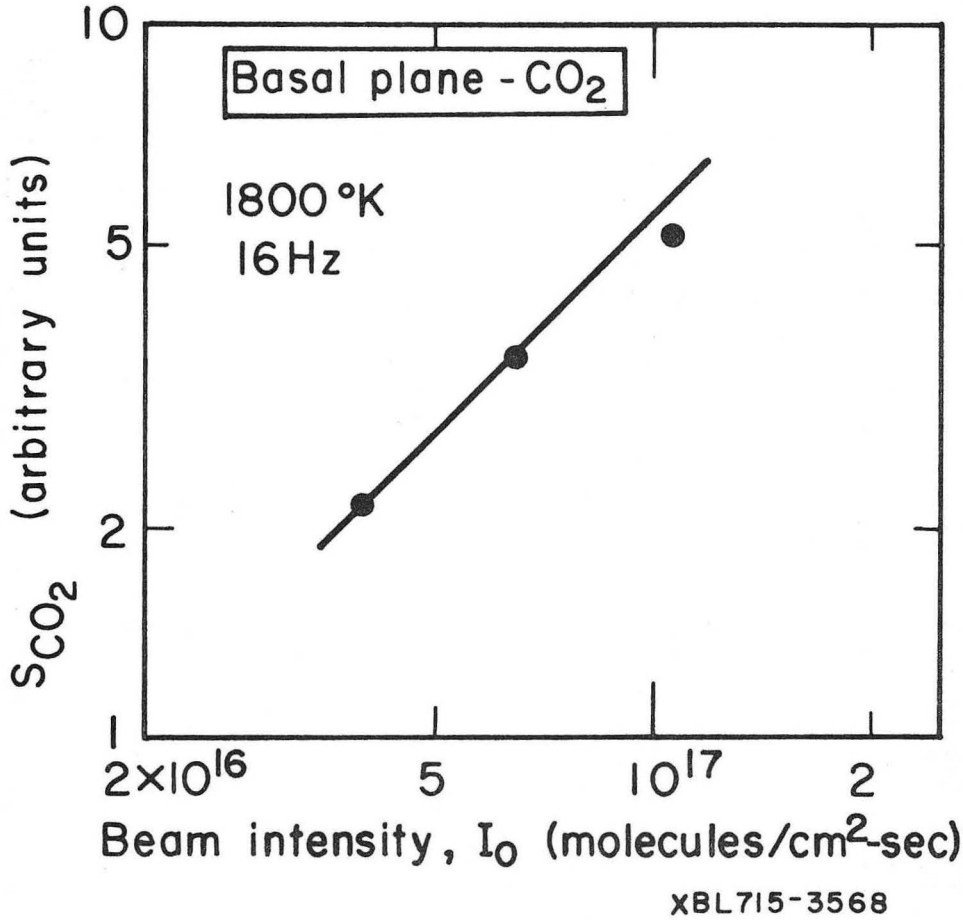

Fig. 45 Kinetic order--CO_2 signal vs beam intensity.

Although no reaction mechanism is to be postulated, if a one step process were operating, a rate constant of 200 sec^{-1} would be obtained from the phase data using Eq. 14. Continuing to pursue the consequences of a one step process, we find from Fig. 43, and Eq. (15) an activation energy for the rate constant of about 25 kcal/mole. This relatively high activation energy and the flat phase behavior in Fig. 44 are, of course, not consistent and would yield different pre-exponential factors for the three temperatures studied:

$$k = 200\ sec^{-1},\ E = 25\ kcal/mole$$

$$k = A\ e^{-E/RT_S}$$

A (sec^{-1})	T_S (°K)
6×10^6	1200
8×10^5	1500
2×10^5	1850

A process described by a rate constant with a pre-exponential of 10^6 is hardly a desorption process but more likely another surface diffusion controlled process limit.

The CO_2 reaction was found to be first order (Fig. 45).

G. Reaction of Annealed Graphite

As-depositied pyrolytic graphite on which the preceeding reaction study was made may be reduced to a more perfect (and possibly less reactive) state by annealing at high temperature. Samples of pyrolytic graphite annealed at 3000°C for over two hours (not annealed under pressure) were obtained from Union Carbide.

Using a Picker X-ray diffractometer the basal reflections were measured and found to be considerably more intense than for un-annealed

0 0 0 0 3 6 0 5 3 9 6

(as deposited) specimens. That is, while the diffraction peak could be recorded for un-annealed graphite using 1 nickel filter and an X-ray tube current of 7 milliamperes, the annealed graphite diffraction peak could only be fit on the recorder if 3 nickel filters were used and the X-ray tube current was reduced to 2 milliampers.

The reflection peaks occured at "2θ"=26.1° and 26.6° respectively for the as-deposited and annealed graphite. For copper K_α radiation this corresponds to a "c" or basal spacing of 3.41 Å and 3.36 Å respectively showing a tighter spacing in the annealed sample.

The density of the as-deposited and annealed specimens are 2.17 gr/cm^3 (96.3% theoretical) and 2.25 gr/cm^3 (99.5% theoretical) respectively.

The reaction of annealed basal plane pyrolytic graphite with molecular oxygen was <u>not</u> found definitely to proceed for temperatures up to 1850°K. The limit of system sensitivity allows us to classify the reaction probability for annealed basal surfaces as being on the order of or less than 2×10^{-5}.

V. PRISM PLANE REACTION

A. Data Presentation and Implications

Samples of pyrolytic graphite having prism plane front faces were polished with 1 micron abrasive and pre-oxidized in the same manner as the basal plane specimens. The reaction rate on freshly polished samples diminished somewhat by burning as disturbed material was removed, but later the reactivity surpassed the initial rate when the reaction etched surface had been developed. Electron micrographs were obtained of a polished specimen and a fully developed reactive surface (Fig. 46).

Carbon atoms dangling by only a few bonds at the edge of the prismatic planes are expected to be much more reactive than the atoms securely bound in the mesh of the basal planes. Consequently, the pyrolytic graphite reaction studies were commenced with a prism plane sample to "cut our teeth" on a "strong" signal. However, when the typical apparent reaction probability for producing CO from the prism plane was measured to be only 10^{-3}, the hopes for measuring a reaction on the basal plane dimmed swiftly. Not only was the prism plane reaction less "active" than had been wished, but the data which was experimentally accessible exhibited more than its share of anomalous behavior.

Both reaction products, CO and CO_2, were detectable although only one tenth as much CO_2 was produced as compared to CO. Over the range of parameters investigated, the reactions producing CO and CO_2 seemed to be very similar although the higher uncertainty due to the weaker CO_2 signals tends to obscure some of the finer details.

The reaction was found to be first order for both CO and CO_2 production as illustrated by log-log plots of signal strength vs beam intensity (Figs. 47 and 48). Although the figures only present kinetic order data for relatively high temperatures, the first order behavior

0 0 0 0 3 6 0 3 3 9 7

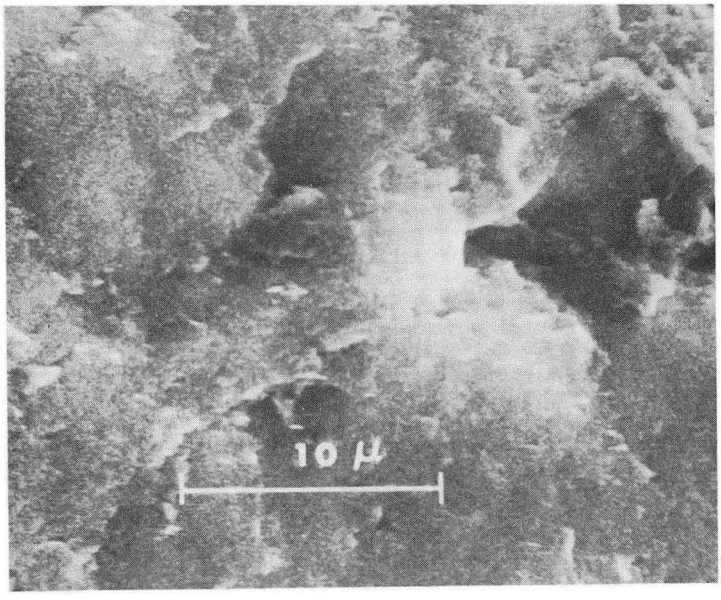

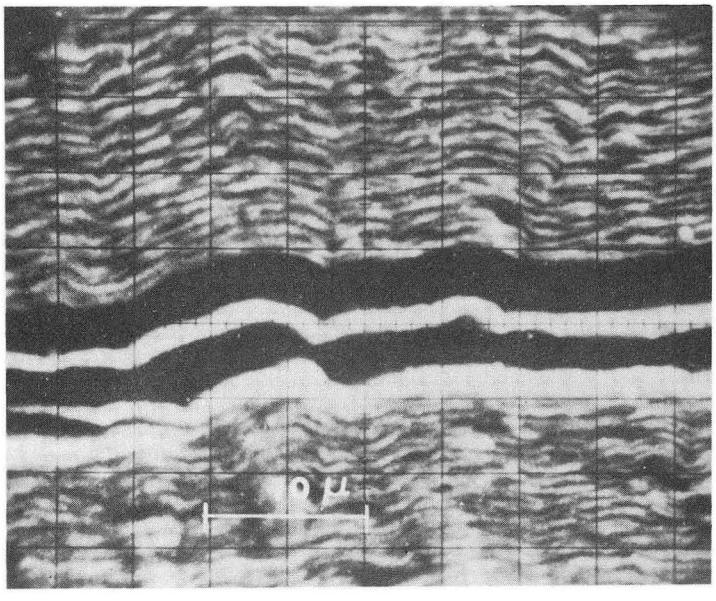

XBB 718-3770

Fig. 46 Prism plane sample scanning electron micrographs, before and after oxidation. The oxidized target has a crack (slot) across the center.

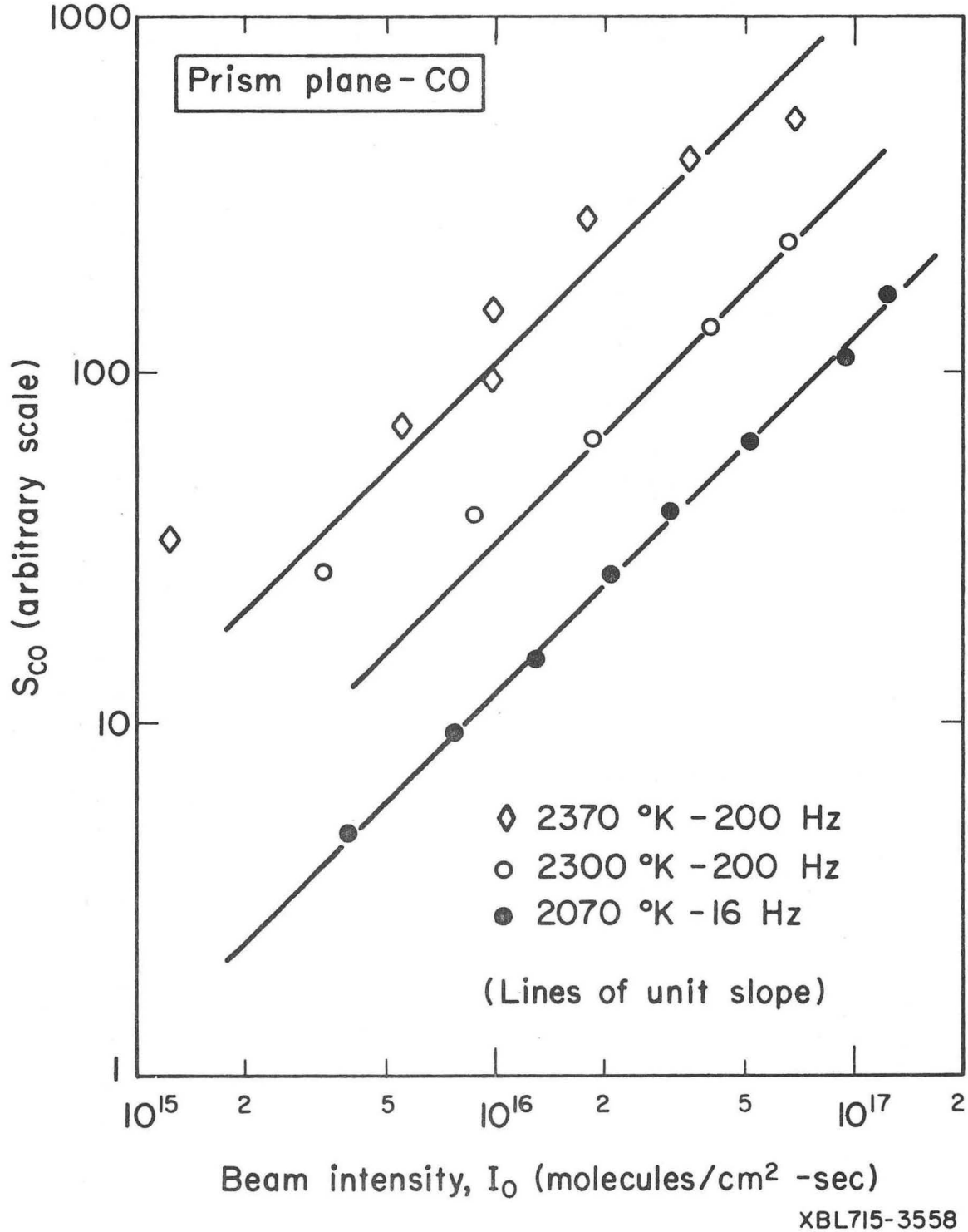

Fig. 47 Kinetic order--CO signal vs beam intensity.

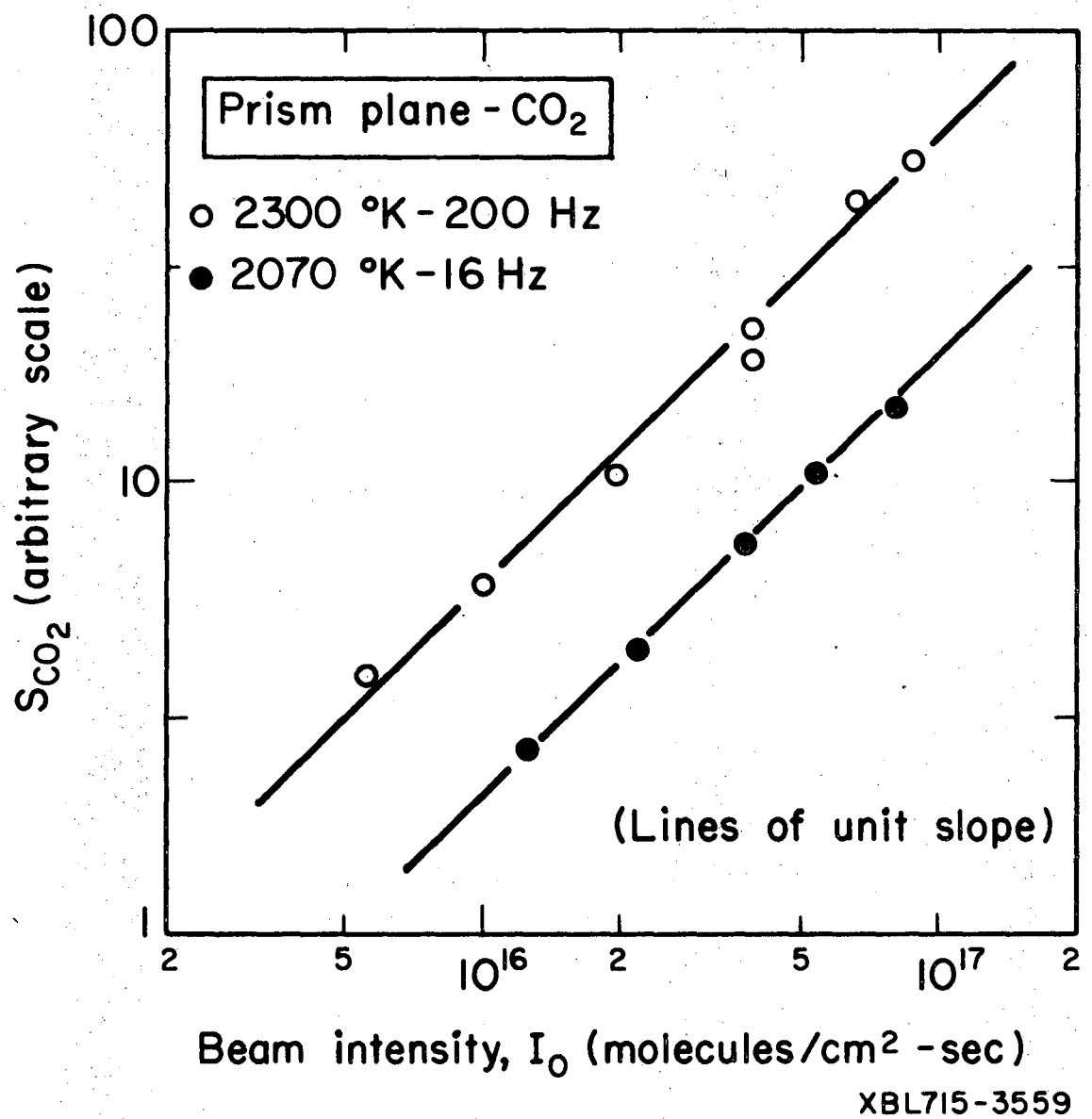

Fig. 48 Kinetic order--CO_2 signal vs beam intensity.

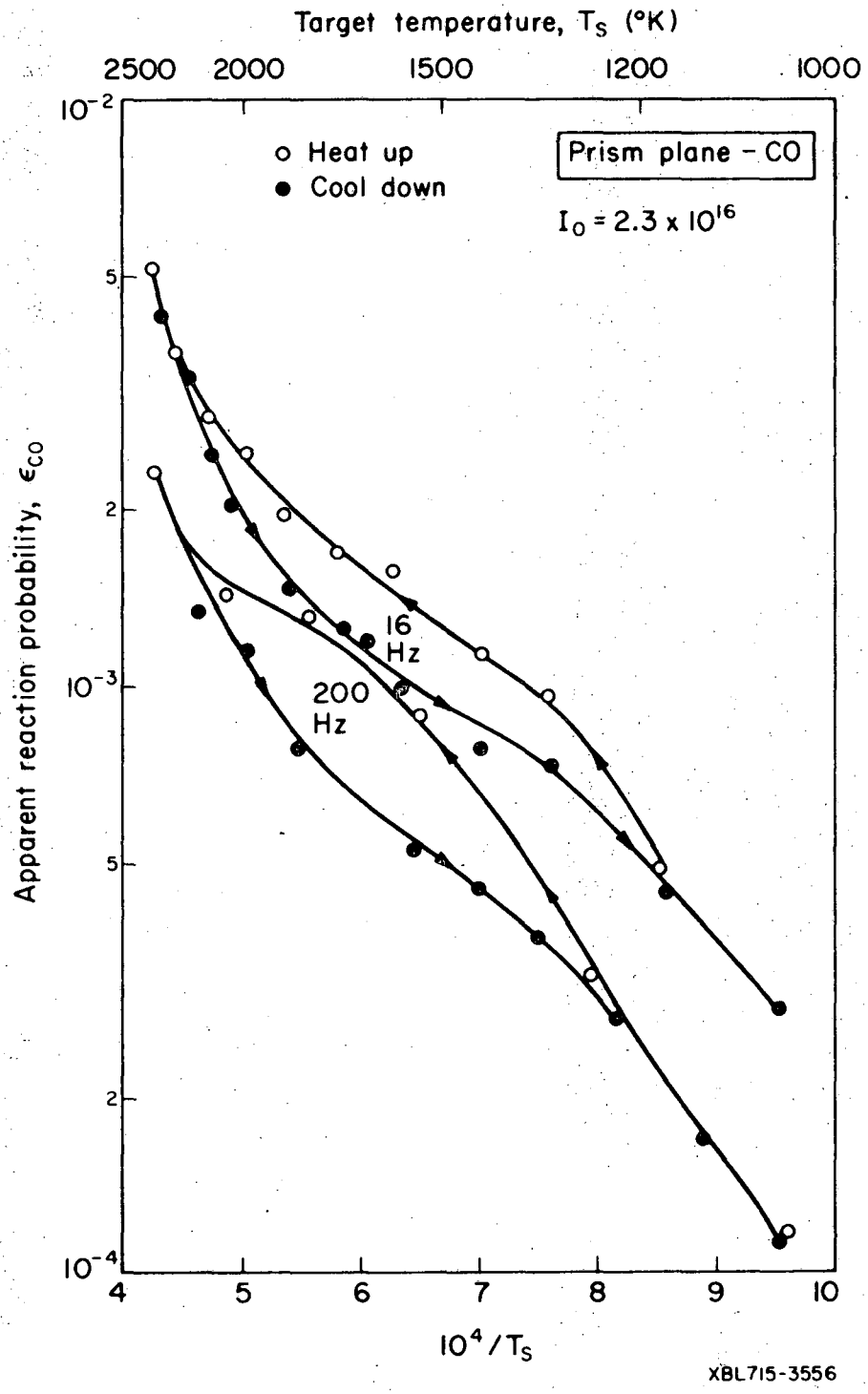

Fig. 49 Arrhenius plot of the apparent reaction probability.

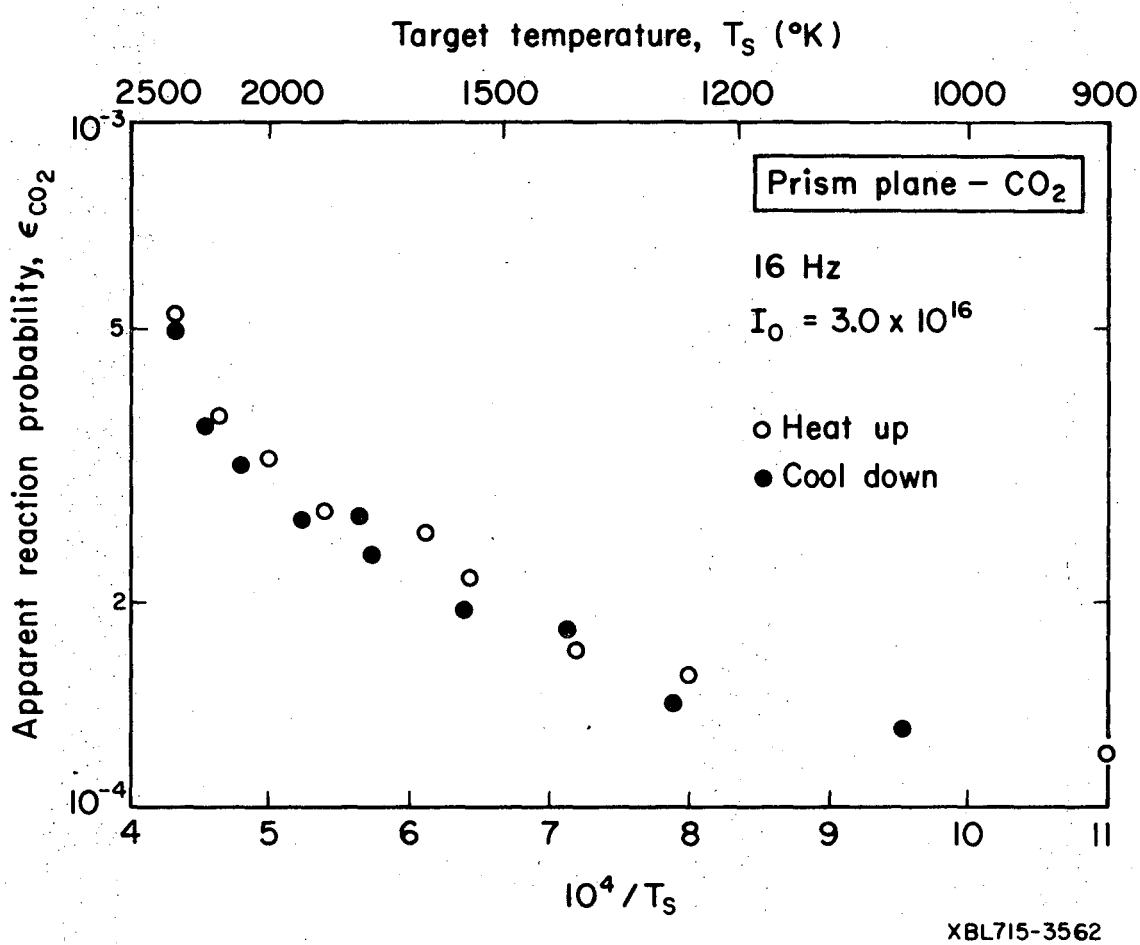

Fig. 50 Arrhenius plot of the apparent reaction probability.

was found to persist down to at least 1400°K.

The apparent reaction probability, ε, is plotted Arrhenius fashion in Figs. 49, 50, and at least in Fig. 49 some hysteresis may be noticed. This hysteresis was not so carefully investigated as the basal plane hysteresis which was measured later. However, many traverses of the hysteresis loop were made --- hoping it would disappear! It did not.

Reactivity measurements were extended up to 2700°K for the first target and a whopping 10% reactivity was observed. Evaporation of carbon from the rear of the target was very rapid and only a few measurements were obtained before the target was thinned so much that non uniform heating occurred and cracks developed. The second target from which the bulk of the data was obtained was not heated above 2400°K and lasted much longer.

Reaction phase lag data were found to be "very peculiar" (Figs. 51 and 52). Not only did the phase remain nearly invariant as temperature was changed, but what change was encountered appeared to follow a hysteresis loop. Hysteresis of ϕ and ε for CO production show the higher ε corresponding to a lower phase and vice versa. Conversely, the CO_2 production data fail to reveal a distinct hysteresis in ε, but there is possibly hysteresis in the reaction phase lag ϕ. At a relatively high temperature (2100°K) a frequency scan for the CO reaction yielded the results for ε_{CO} and ϕ_{CO} shown in Figs. 53 and 54 respectively. The apparent reaction probability is still increasing as the modulation frequency is reduced and it is suspected that, even at the lowest modulation frequency which was used in this study, the measured apparent reaction probability is significantly demodulated below the true reaction probability (typically 2η).

Particularly striking is the reaction phase lag of about 22 1/2°

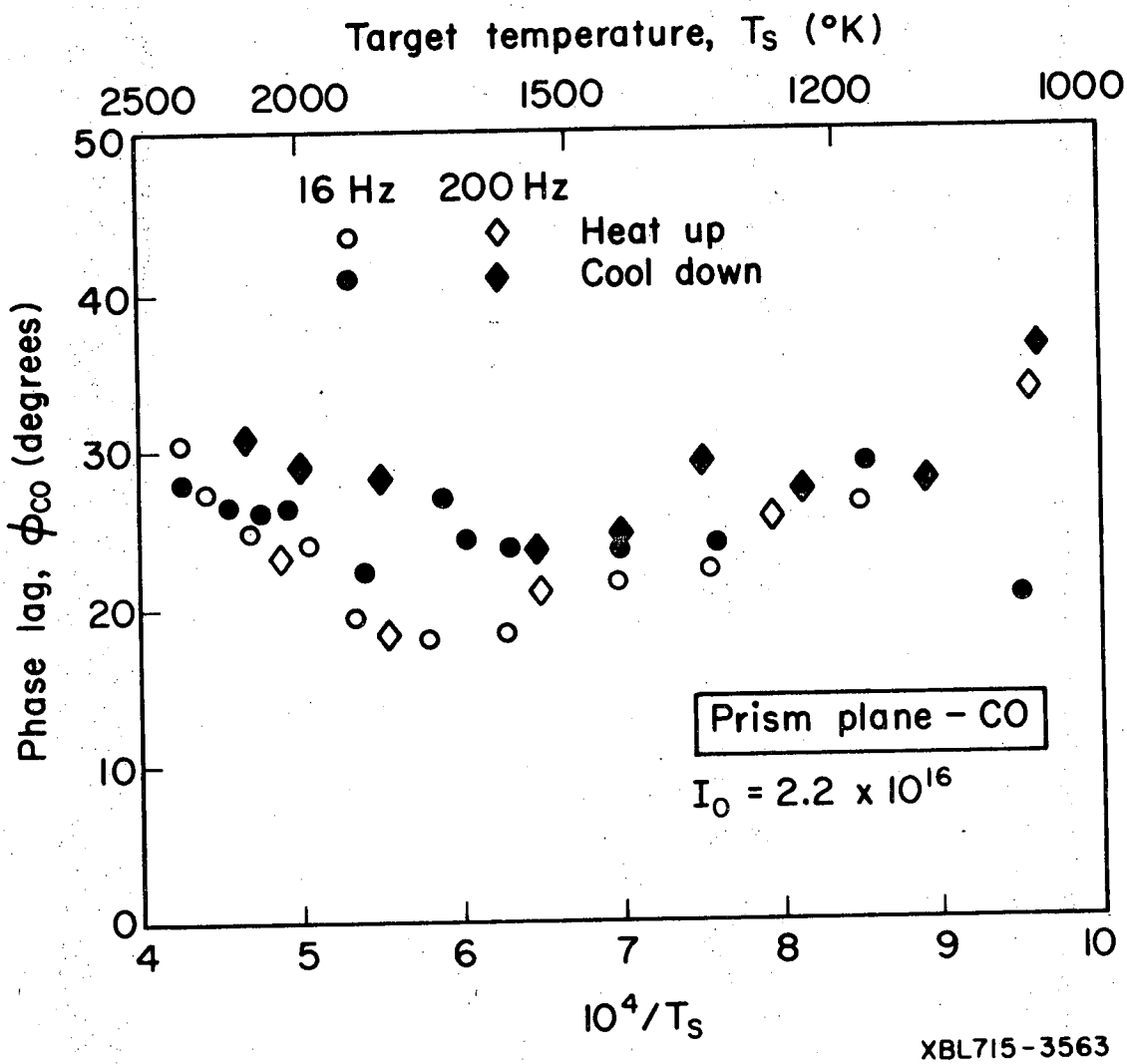

Fig. 51 Reaction phase lag vs reciprocal temperature.

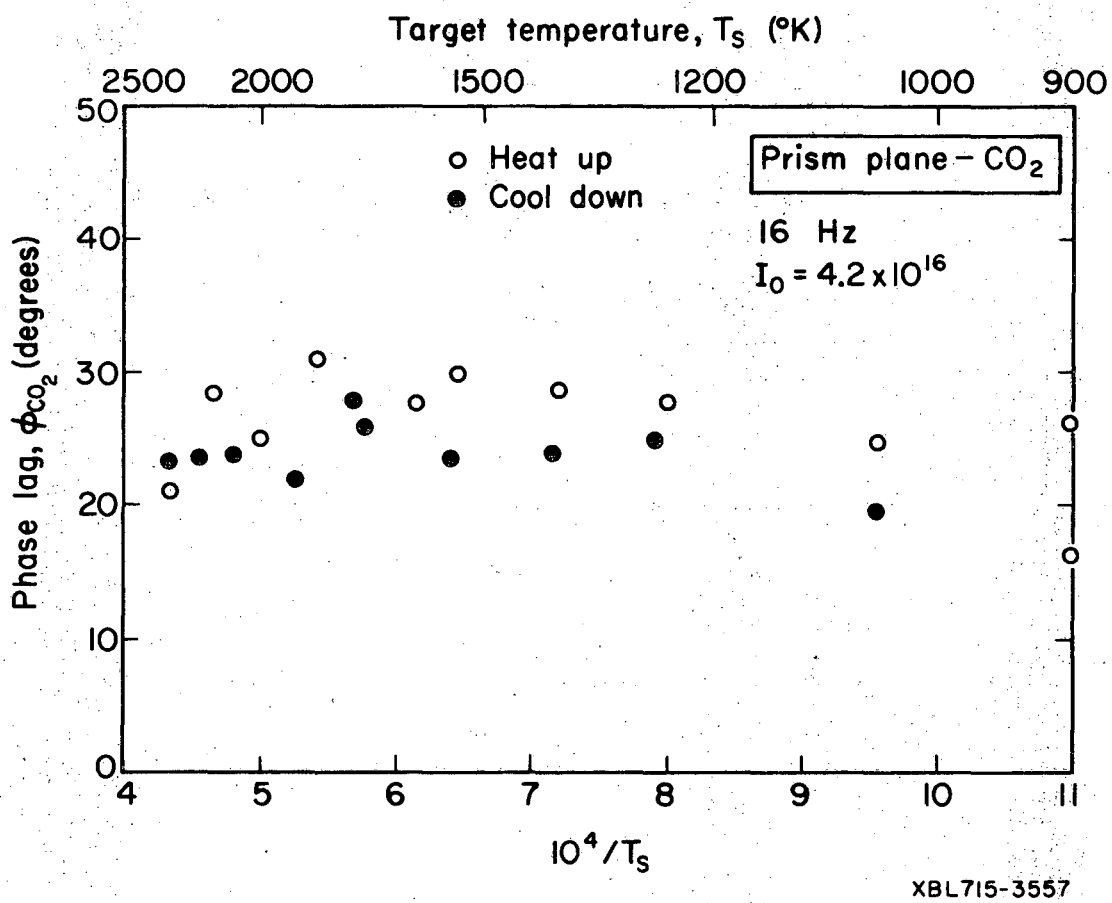

Fig. 52 Reaction phase lag vs reciprocal temperature.

0 0 0 0 3 6 0 3 4 0 1

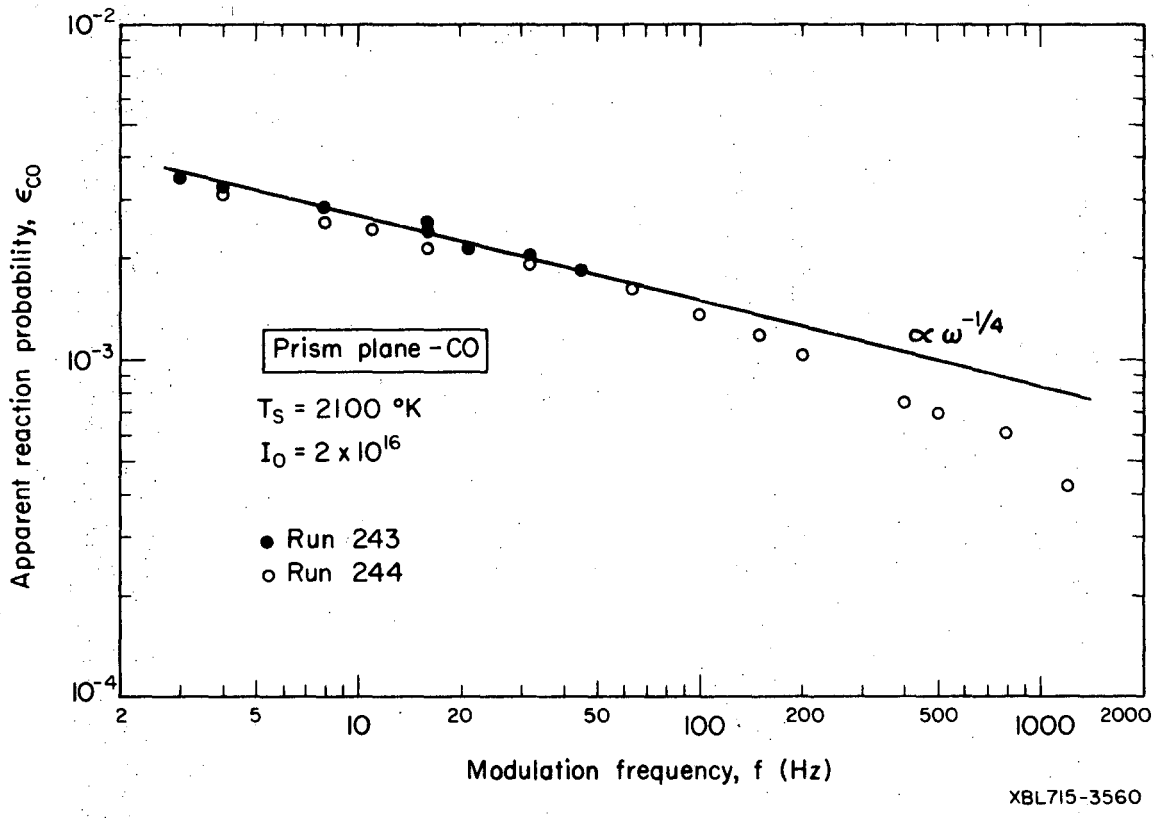

Fig. 53 Frequency scan of the apparent reaction probability.

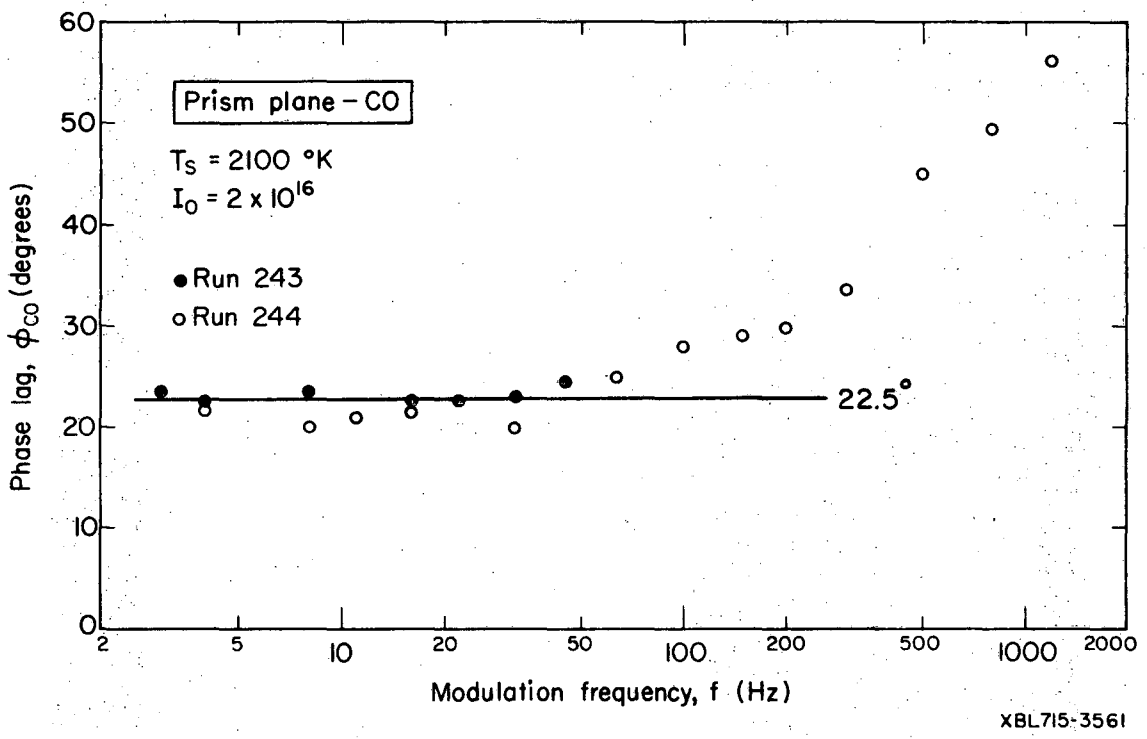

Fig. 54. Frequency scan of the reaction phase lag.

($\pi/8$ radians)--a value that remains quite constant as the modulation frequency is varied (Fig. 54). In the companion figure (Fig. 53) it may be noticed that the apparent reaction probability, ε, decreases as $\omega^{-1/4}$ over the same frequency range, and one may be reminded that the reaction was found to be first order (linear).

There is an interesting result from linear network analysis.[80] The effect of passing a sinusoid through an electrical network may be represented as multiplying the sinusoid by $e^{A + iB}$. (In the reaction notation, A corresponds to the natural logarithm of the apparent reaction probability, $\ln \varepsilon$, and B corresponds to the reaction phase lag, ϕ.) In terms of a logarithmic frequency variable $u = \ln(\omega/\omega_c)$, where ω_c is a particular frequency of interest, the relation which we require is,

$$\phi(\omega_c) = B_c = \frac{1}{\pi}\int_{-\infty}^{\infty} \frac{dA}{du} \ln(\coth |\tfrac{u}{2}|)\, du \quad . \tag{85}$$

For the case in which $dA/du = 1/4$ (ε vs ω would have a $-1/4$ slope on a log-log plot), Eq. (85) gives $B_c = \pi/8$ for all ω_c, ($\phi = 22\ 1/2°$).

This exercise provides, however, only an interesting consistency check. There are no clues as to how to synthesize a circuit (or reaction model) to provide this behavior. It is also clear that this analysis accounts only for demodulation effects, <u>changes</u> in A with frequency (or u). That is, the low frequency limit of $e^A = \varepsilon$ is a <u>constant</u> attenuation (typically 2η for the reaction models discussed previously) and is not determined from the variation of ϕ with frequency.

Two reaction models which synthesize the required frequency behavior will be considered. Unfortunately, insufficient data are available to fully exploit either model.

B. Multi-Branch Reaction Mechanism

In the general section on reaction models it was suggested that an observed reaction behavior could be conveniently modeled as arising from reaction along several "parallel" branches which give the same product (section II-G). To this end, a reaction vector locus plot was prepared (Fig. 55) which exhibits four humps suggesting a four branch process (assuming the humps are not scatter!) described by four different rate constants:

$$O_2 \xrightarrow{\eta} 2\,O_{ads} \quad \left\{ \begin{array}{lll} \xrightarrow{P_1} CO_{ads} & \xrightarrow{k_1} & CO(g) \\ \xrightarrow{P_2} CO_{ads} & \xrightarrow{k_2} & CO(g) \\ \xrightarrow{P_3} CO_{ads} & \xrightarrow{k_3} & CO(g) \\ \xrightarrow{P_4} CO_{ads} & \xrightarrow{k_4} & CO(g). \end{array} \right.$$

The reaction product vector is given by,

$$\varepsilon\, e^{-j\phi} = \frac{2\eta\, P_1}{1 + j(\omega/k_1)} + \frac{2\eta\, P_2}{1 + j(\omega/k_2)} + \frac{2\eta\, P_3}{1 + j(\omega/k_3)} + \frac{2\eta\, P_4}{1 + j(\omega/k_4)} \qquad (86)$$

By juggling the P's and k's a fit to the "normalized" curve $(\varepsilon/2\eta)e^{-j\phi}$ was obtained over the range of modulation frequency used. In general, the relative sizes of two humps depends on their relative P's and the depth of separation depends on the ratio of k's. Varying the magnitude of the k's moves the points for a given modulation frequency along the curve. The sum of the P's must be one. Parameter values determined after several trials gave the fit to the measured apparent reaction probability and phase lag as illustrated in Figs. (55), (56), and (57).

The parameters were determined as:

0 0 0 0 3 6 0 5 4 0 3

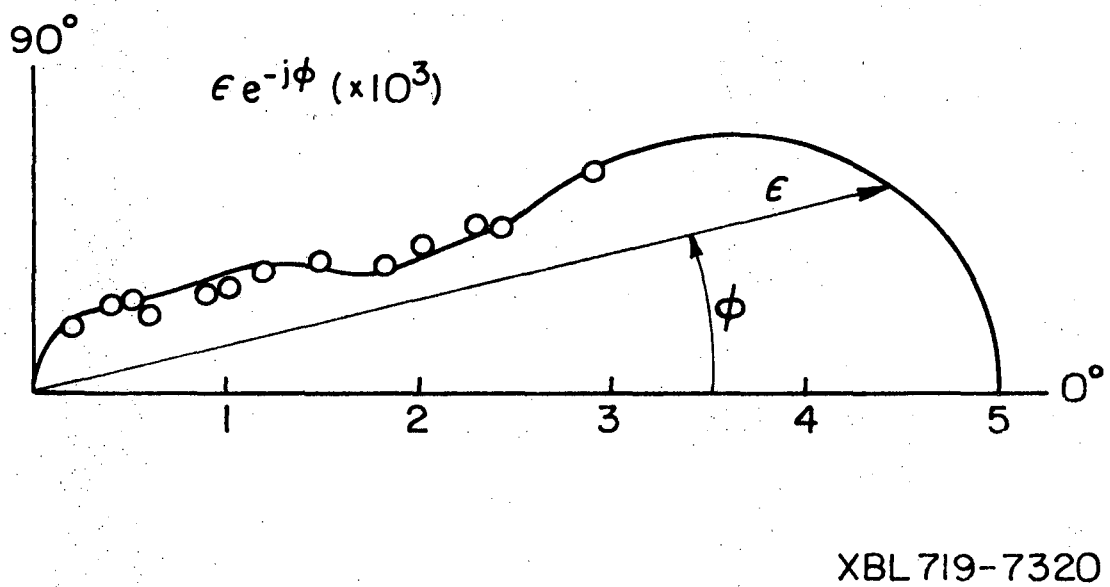

Fig. 55 Reaction product vector locus plot.

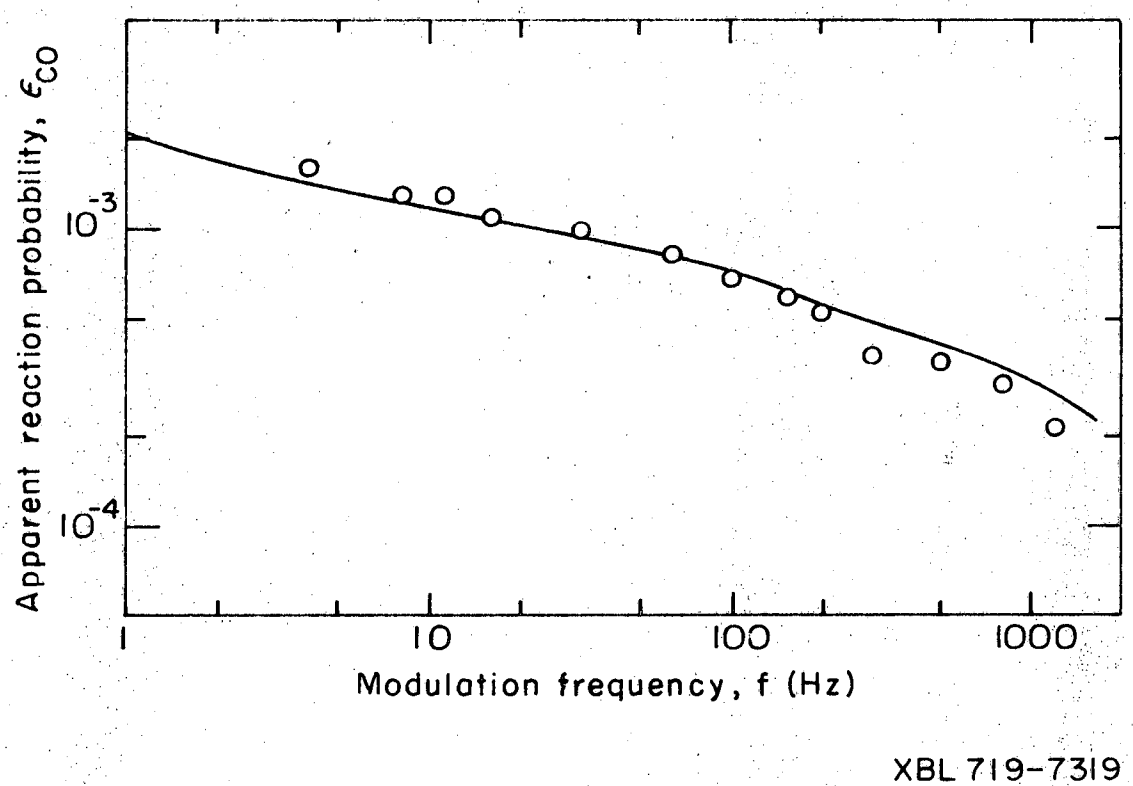

Fig. 56 Four branch fit--amplitude vs frequency.

0 0 0 0 3 6 0 3 4 0 4

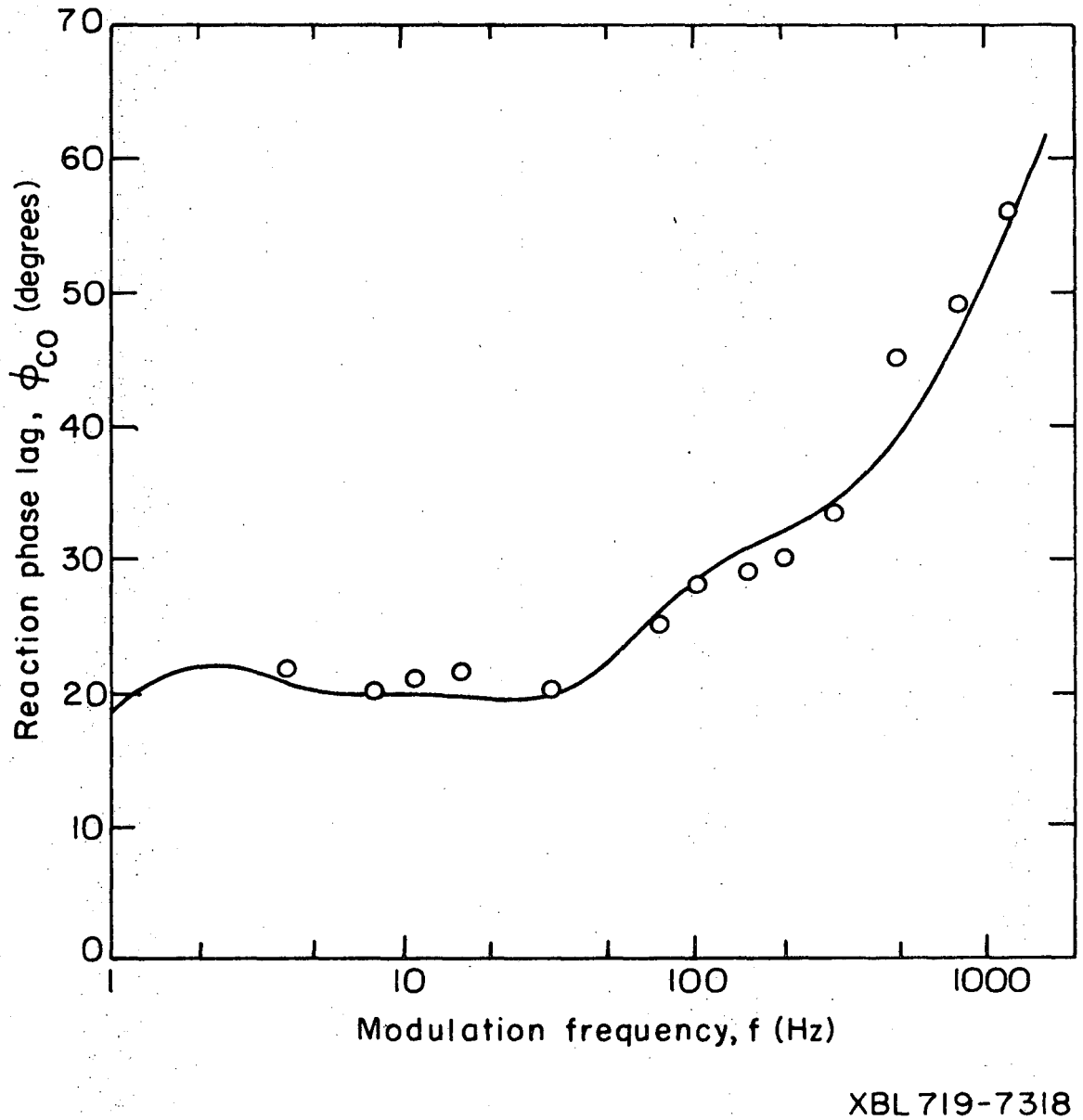

Fig. 57 Four branch fit--phase vs frequency.

P_1	0.15	k_1	1000.	(sec^{-1})
P_2	0.20	k_2	100.	
P_3	0.15	k_3	10.	
P_4	0.50	k_4	1.2	

$\eta = 2.5 \times 10^{-3}$

The sticking probability, η, was obtained by extrapolating the theoretical reaction product locus to zero frequency. Values of k are believed to be determined to within a factor of two and the P's are good to about 25%. These are values at 2100°K. It would be desirable to obtain the P's and k's from frequency scans at different temperatures. In the derivation leading to Eq. (86) the P's are assumed not to be functions of temperature (except possibly due to hysteresis). This could be checked. The rate constants (k's) determined from runs at different temperatures could be plotted Arrhenius fashion to deduce the activation energies.

This data reduction approach takes cognizance of the fact that the k's and the modulation frequency ω (or f) are conjugate time variables of the reaction system. The rate constants are determined by frequency scans then the variation of the k's with temperature is considered to determine the activation energies and pre-exponentials. This is the direct approach. Modulating the reactant beam at different rates is essentially equivalent to conventionally following the course of the reaction in time. The worth of temperature scans at constant frequency, however, should not be discounted too heavily because these measurements are the ϕ ones that will reveal hysteresis if it is present.

C. Double Diffusion Model

The most significant feature of the prism plane reaction data is the nearly constant reaction phase lag (20°-30°) which is maintained over a substantial range of temperature and modulation frequency. Constant phase behavior has been demonstrated for surface reaction in competition with ordinary bulk diffusion (Section II-E), but, alas, the value of the constant phase angle was 45°. Of course, any phase lag from 0° to 45° could be obtained by combining in the proper proportions some diffusion controlled reaction (45°) with some fast reaction (0°).

Unfortunately, although a bulk diffusion controlled process can provide a constant 45° phase lag, its apparent reaction probability varies with temperature and modulation frequency. Therefore, the proportions producing the desired (20°-30°) phase lag would not be maintained unless the fast reaction (0° phase lag) also exhibited the same variation of its apparent reaction probability with temperature and modulation frequency. The last requirement is clearly impossible for a linear reaction. Indeed, as is easily shown by Eq. (85) the required reduction of the fast reaction signal amplitude with increasing frequency (proportional to $\omega^{-1/2}$ as for diffusion control) is consistent with a phase lag of 45° not 0°. A different approach is clearly required.

A satisfactory reaction model may be formulated when we consider the anisotropic graphite layer structure and take a clue from the electron micrograph of the reacted prism plane surface (Fig. 46) which reveals reaction proceeding preferentially on the edges of certain basal layers.

Pyrolytic graphite is deposited as layers of basal planes when a gas such as ethane is cracked on a suitable substrate heated to high temperature. Nucleation occurs on many sites and growth cones rise

from the substrate. Basal layer stacking is well ordered within a single cone but differs from one cone to the next by rotation about the "c-axis". Slight disturbances during pyrolytic deposition result in renucleation with a consequent change in orientation. The less ordered renucleation-transition region between continuously deposited layers would be expected to be more reactive than the continuously deposited layers themselves. Typically, renucleation occurs after depositing 1000 basal layers [81] (0.3 micron) and the reaction etched furrows in Fig. 46 have approximately this spacing.

It is partly the less uniform renucleation-transition region which gives as-deposited pyrolytic graphite its less than theoretical density. Diffusion would be expected to proceed faster in the less crowded renucleation-transition region than between the more closely packed ordered layers. Diffusion which proceeds rapidly along grain boundaries and also dissipates into the bulk has been considered previously.[82] A reaction model controlled by this double diffusion will be shown to produce a constant reaction phase lag (22 1/2°).

Consider a prismatic face with N bands of high diffusivity renucleation regions (of average thickness δ) per unit length (measured along the "c" axis). Reaction is initiated at the edges of the renucleation regions developing an oxidized surface with a reactive region of width Δ ($\Delta \geqslant \delta$) at each high diffusivity band (Fig. 58). Adsorption of reactant from the gas phase is assumed to take place only on the reactive strips (of width Δ) with a local sticking probability η. (The average sticking probability for the whole prismatic surface is then $N\Delta\eta$.)

An interacting oxygen molecule will be assumed to be rapidly converted to adsorbed CO. (A more reasonable sequence of simple steps

0 0 0 0 3 6 0 3 4 0 6

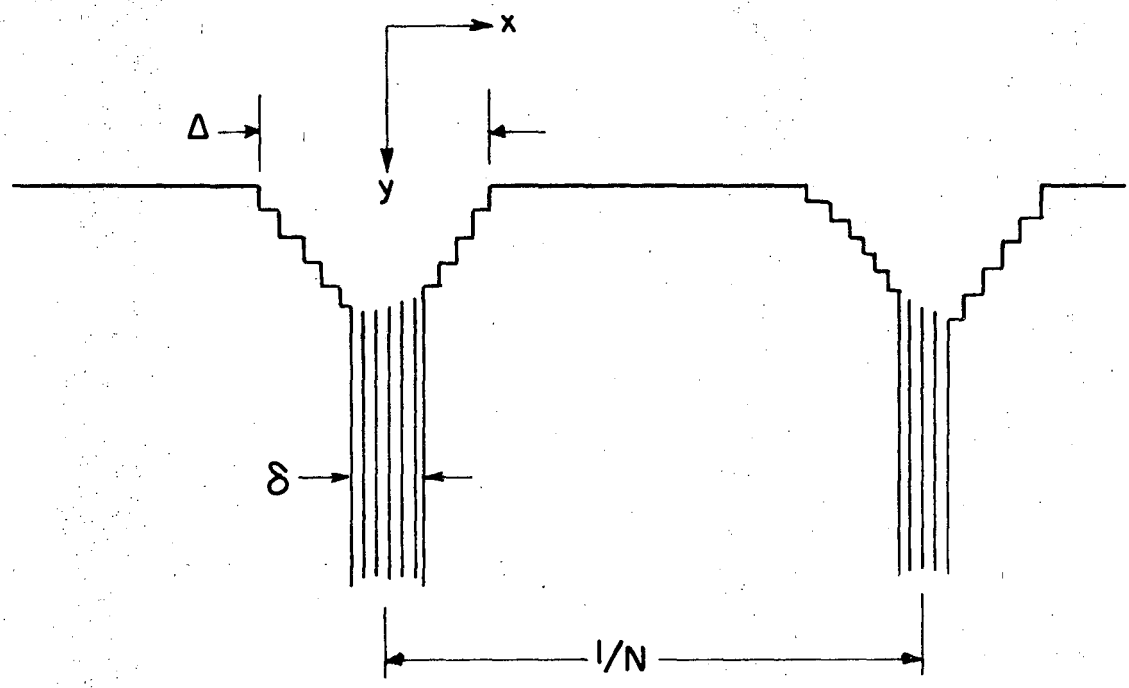

XBL717-6998

Fig. 58 Geometry for the prism plane "grain boundary" reaction model.

proceeding from molecular oxygen to adsorbed oxygen atoms to adsorbed CO would not be discernable from the present measurements and will not be considered at this time but may be easily added later). The adsorbed CO may desorb or diffuse into the graphite via the high diffusivity renucleation region. A surface mass balance on the concentration of adsorbed CO, n, (per unit area of active surface) may be written as,

$$\frac{dn}{dt} = 2\eta I_o\, g(t) - kn + \frac{\delta}{\Delta} D_1 \left(\frac{\partial C_1}{\partial y}\right)\Bigg|_{y=0} \quad . \tag{87}$$

Each molecule of oxygen can form 2 adsorbed CO with a probability η. $I_o\, g(t)$ is the modulated beam flux and k is the desorption rate constant. The last term accounts for diffusion loss via the high diffusivity renucleation region. D_1 is the diffusion coefficient for CO and C_1 is the concentration of CO in the high diffusivity region. The effectiveness of diffusion loss is reduced by the factor δ/Δ (a funneling effect).

The surface concentration n is related to the bulk concentration C_1 (just under the surface) by,

$$C_1\,(0,t) = H\, n(t) \tag{88}$$

where H is the solubility.

Diffusion in the renucleation region is governed by[82] (Grain boundary diffusion),

$$\frac{\partial C_1}{\partial t}(y,t) = D_1 \frac{\partial^2 C_1}{\partial y^2}(y,t) + \frac{2}{\delta} D_2 \left(\frac{\partial C_2}{\partial x}(y,t)\right)\Bigg|_{x=0} \quad . \tag{89}$$

Variation of C_1 across the renucleation region is neglected.

The lateral loss from the renucleation region into the uniformly deposited graphite (characterized by a diffusion coefficient D_2) is described by,

$$\frac{\partial C_2}{\partial t}(x,y,t,) = D_2 \frac{\partial^2 C_2}{\partial x^2}(x,y,t) \tag{90}$$

subject to

$$C_2(0,y,t) = C_1(y,t). \tag{91}$$

The diffusion equations will be solved subject to the boundary conditions,

$$\left(\frac{\partial C_2}{\partial x}\right)\Bigg|_{x\to\infty} = 0 \tag{92}$$

$$C_1(y,t)\Big|_{y\to\infty} = 0 \tag{93}$$

Eqs. (92) and (93) represent the assumption that the modulation of the concentrations C_1, C_2 damps out quickly as one proceeds down along the grain boundary or laterally into the grain. With respect to the propagation of the modulation of C_1 and C_2, the solid appears to be of infinite extent.

The linear equations (87), (89), and (90) are solved for the response to the first Fourier component of the modulated beam flux by substituting,

$$n(t) = n_1^* e^{j\omega t}$$

$$g_1(t) = g_1 e^{j\omega t}$$

$$C_1(y,t) = [C_1(y)]_1^* e^{j\omega t}$$

$$C_2(x,y,t) = [C_2(x,y)]_1^* e^{j\omega t}$$

The modulation frequency is ω (rad/sec). The asterisks (*) indicate complex quantities and the subscripts 1 designate the first Fourier coefficients.

Performing the substitutions we obtain,

$$[C_2(x,y)]_1^* = [C_1(y)]_1^* \, e^{-\sqrt{j\omega/D_2}\;x} \tag{94}$$

$$[C_1(y)]_1^* = H\, n_1^* \, e^{-\sqrt{j\omega/D_1 + 2/\delta\; D_2/D_1 \sqrt{j\omega/D_2}}\;y} \tag{95}$$

$$\varepsilon\, e^{-j\phi} = \frac{k\, n_1^*\, N\Delta}{I_o\, g_1} = \frac{2\eta\;\; N\Delta}{1 + j\,\frac{\omega}{k} + D_1\,\frac{H}{k}\,\frac{\delta}{\Delta}\sqrt{j\,\frac{\omega}{D_1} + \frac{2}{\delta}\,\frac{D_2}{D_1}\sqrt{j\,\frac{\omega}{D_2}}}} \tag{96}$$

The term $k\, n_1^*\, N\Delta$ is the first Fourier component of product emission per unit area of surface upon which the first Fourier of modulated beam flux $(I_o\, g_1)$ falls.

The condition of prime interest occurs when the very last term in the demoninator of Eq. (96) is dominant. Under this condition of strong double diffusion control, the reaction product vector becomes,

$$\varepsilon\, e^{-j\phi} \approx \frac{2\eta\;\; N\Delta\; e^{-j\pi/8}}{\frac{H}{k}\,\frac{\delta}{\Delta}\sqrt{\frac{2\; D_1\; D_2}{\delta}\sqrt{\frac{\omega}{D_2}}}} \tag{97}$$

The apparent reaction probability varies as $\omega^{-1/4}$ and the reaction phase lag has a constant value of 22 1/2°. Of course, in this limit the denominator of Eq. (96) is much greater than 1 and the signal is highly demodulated.

Equation (97) predicts that demodulation should separate the apparent reaction probabilities measured at 16 and 200 Hz by a factor $(200/16)^{1/4} = 1.9$. The curves of Fig. (49) are in fair agreement with this prediction.

Hysteresis effects can be incorporated in the double diffusion model by variation of the width Δ of the active surface area at each

renucleation region. Burn-off carried out at different temperatures establishes different proportions of active surface described by Δ. Reaction at low temperature provides a wide etch of the surface and a large value of Δ. At higher temperatures surface healing occurs shrinking Δ toward δ (the width of the renucleation region). The reactivity of a prism plane sample has been measured with the molecular beam impinging parallel and trasverse to the laminations. No difference in reactivity was measured suggesting that the reaction etch of the surface does not produce deep valleys with steep sides which would shield (shadow) some surface from direct "illumination" by the transverse beam.

A related topic grain boundary grooving has received considerable attention,[83] but the grain boundary groove widens with time at a rate which increases with temperature. This apparent contradiction may be reconciled by noting that a reactive surface consists of atoms dangling by only a few bonds--atoms on the corner of ridges would be reactive. The reactive bands of width Δ are then valleys with sloping sides that are neither too flat nor too steep. Surface migration which leads to grain boundary grooving tends to smooth the irregularities which would otherwise be reactive. The sharp corner between the free surface and a grain boundary is transformed to a smooth grooved grain boundary by transfering atoms from the corner to smooth humps running parallel on each side of the groove. The profile is like that of a plowed furrow, or more in keeping with the delicate balances involved--the profile of a seagull. For the graphite reaction, oxidation roughens the surface increasing Δ, but at high temperatures surface migration works to smooth the surface and reduce Δ.

Hysteresis in the apparent reaction probability (ε) may be described as follows. Proceeding from a low temperature where a steady Δ was

obtained to a higher temperature, one initially finds Δ in excess of the stable value at the new temperature and an excessively high value of reactivity is observed until the surface is able to adjust Δ to a stable value at the new temperature. Upon decreasing temperature a reverse behavior is observed. Initially Δ would be lower than the steady value thereby depressing the reactivity, but gradually burn-off would establish the steady value of Δ at the new lower temperature. The slow variation of Δ (slow, <u>observable</u> hysteresis) permits Δ to be taken as constant in Eq. (87).

Hysteresis was also exhibited in the reaction phase lag. The phase lag on the heating curve lay below the phase on the cooling curve. Equation (97) does not provide an explanation for the phase hysteresis, and neither does the complete expression Eq. (96). This is not entirely unexpected. The reaction phase lag is particularly sensitive to small details of the reaction model. (It may be recalled that the relatively complex basal plane reaction model staisfied all experimental data except the phase lag data at low temperature.)

What is needed (in both cases) is an additional reaction branch which need produce only a very small fraction, ι, of the total CO. This component of CO must be without diffusional demodulation and have a low phase angle. The CO produced with a low phase angle could arise from reaction which occurs via an immobile adsorption complex (thereby preventing diffusion loss). The apparent reaction vector for this process might be,

$$\varepsilon_\iota \, e^{-j\phi_\iota} = \frac{2\,\eta_\iota}{(1 + \omega/k)}$$

where formation of immobile CO is proportional to a sticking probability η_ι. The CO desorbs at a rate proportional to k. The small fraction

of CO which is desorbed by this branch would be a negligible perturbation to the surface mass balance, Eq. (87). The ι fraction of CO production must also be subject to hysteresis similar to the diffusion controlled fraction. The required hysteresis could be provided by varying η_ι, and a strong hysteresis in η_ι is desired.

The total apparent reaction vector would be the vector sum of the CO produced by the "diffusional" and "direct" branches. Fig. 59 shows the reaction product vectors for the double diffusion component of the CO product (as given by Eq. (96)) and the contribution of the CO produced by the "direct" branch discussed above (reaction product vector given by Eq. (98)). What appears in Fig. 59 to be a rather large fraction of CO production via the direct route is exaggerated due to the large demodulation which is incurred by the diffusional branch--as the modulation frequency is reduced, the length of the vectors at 22 1/2° in Fig. 59 would increase as $\omega^{-1/4}$, while the vectors laying on the in-phase (0°) axis would be unaffected by frequency.

From the basal plane studies, we would expect that the reactivity of both components would be higher on the heating branch than on the cooling branch, inasmuch as the excess reactive sites generated by low temperature oxidation persist during much of the heating branch. Since both the diffusional and the direct contributions to the CO product depend upon active sites available to initinate the reaction, the amplitude of both reaction product vectors should be larger on heatup than upon cool-down. This hysteresis in the amplitudes of each component is shown in Fig. 59. The phase angles of each component (22 1/2° for the diffusional component and 0° for the direct component) are not affected by heating or cooling.

By judicious selection of the magnitudes of each component and the

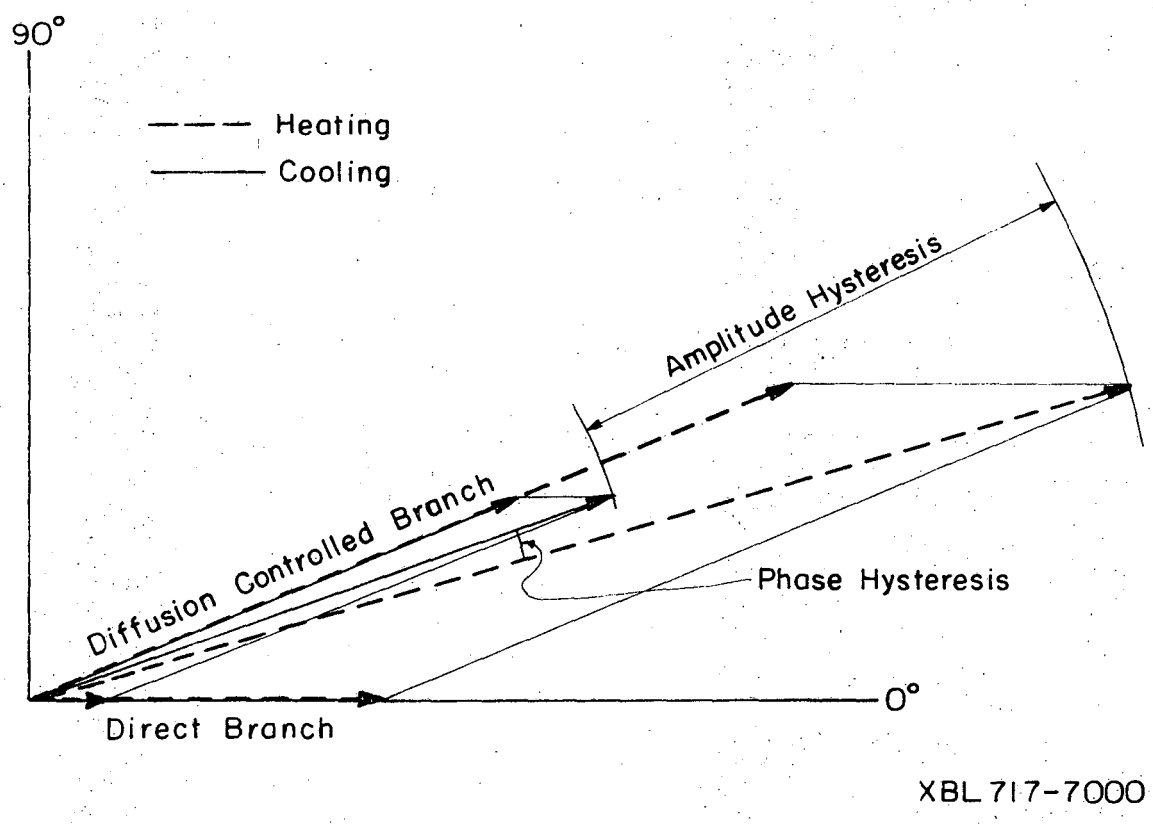

Fig. 59 Vector sum of the "diffusional" and "direct" components of CO producted by prism plane oxidation.

extent of amplitude hysteresis in each, the observed vector sum can be made to reflect the qualitative features of the observed amplitude and phase hysteresis.

Actually, only hysteresis in the direct component appears to be absolutely essential to explain both the amplitude and phase hysteresis. Lengthy quantitative comparisons with more experimental data might determine if Δ could remain constant. An in-situ analysis of the surface of the reacting target would be very informative in this regard.

At 200 Hz the double diffusion character may be turning somewhat toward ordinary (i.e. "single") diffusion (due to increasing importance of the first term in the square root of Eq. (96) compared to the second term) giving a slightly greater phase angle. Alternatively, the phase lag due to the desorption process (ω/k term) may be becoming significant. Whatever the case may be, the cooling curve phase lag is greater than 22 1/2° but the hysteresis of the direct branch acts to swing the heating curve phase lag below 22 1/2°.

The frequency scans (Figs. 53 and 54) show that at high frequency the double diffusion process is relinquishing control to a more extreme process which effects a stronger demodulation of the reaction signal. Increasing significance of ordinary bulk diffusion (the first term in the square root of Eq. (96)) or the ω/k desorption term in Eq. (96) could be responsible for the higher demodulation and increasing phase lag. Alternatively, the increased demodulation and phase lag might be due to other processes not present in the elementary double diffusion model, such as the direct CO production discussed previously.

At high temperatures the phase appears to be increasing with temperature (exceeding 22 1/2°) without showing hysteresis. Possibly bulk diffusion from the surface directly into the graphite (avoiding the

intermediary of the grain boundaries) is becoming important. This "single" diffusion loss mechanism is not provided in this model.

Unfortunately, more extextensive data is not available. Suitable modulated beam reaction kinetic data would permit determination of k and the other parameters of the model. Of course, the individual parameters D_1, D_2, H, δ, Δ, N, and η would not be determined but only their functional groups as present in the model. Extra information would be required to determine each of the system parameters.

Some estimate of N and Δ might be made from a careful analysis of the micrograph of the reacted surface, and an estimate of δ could be obtained from a consideration of X-ray data and the bulk density. From Fig. 46 one might estimate $N \approx 10^4$ cm^{-1} and $\Delta \approx 5 \times 10^{-5}$ cm. The density is 2.17 gr/cm^3 and X-ray data showed a "c" spacing of 3.41 Å. There are 3×10^7 basal layers per centimeter of "c" axis, so a renucleation region 60 layers wide ($\delta = 2 \times 10^{-6}$ cm) could account for the 2% deviation from theoretical density (2.26 gr/cm^3) due to excessively spaced planes (the renucleation region).

Based on the reaction model, the apparent lack of prism plane reactivity is seen to be simply due to demodulation of the reaction signal as a result of diffusion into the sample. The basal plane reaction was not controlled by bulk diffusion processes and exhibited somewhat larger apparent reaction probabilities than the prism plane. Although the modulated beam technique provides information about the reaction process, DC reaction rates can only be obtained by extrapolation using the reaction model developed with the aid of the AC experiments.

D. Room Temperature Reaction

At the beginning of each run, before heating the target, the reactant oxygen beam scattered from the target was monitored to establish the reactant reference signal. The purity of the beam was also checked by observing the signals at mass numbers 28 and 44 (CO and CO_2). Typically a small signal, out of phase with the signal at mass 32 (O_2), was observed. Impurity in the beam would be detected at nearly the same phase as the signal due to the scattered oxygen (as was verified by checking the krypton impurity scattered from the target). The mass 28 and 44 signals from an O_2 beam scattered from the room temperature target had been delayed by some "surface residence time" and were therefore the result of a "room temperature reaction."

Possibly CO and CO_2 impurities in the oxygen beam could be interacting with the target and their scattering (reemission) could be delayed. However, the liquid nitrogen cooled cold traps are very effective in condensing CO_2 and none should be present in the O_2 beam. Furthermore, the beam composition was checked with the beam monitor spectrometer which failed to reveal mass 28 and 44 contaminants. Indeed, it appears that the oxygen beam was reacting at room temperature with the clean pyrolytic graphite surface.

Reactions must proceed with a probability of better than 10^{-5} to be detected with this apparatus. Nevertheless even with a low 10^{-5} reaction probability, oxidation at atmospheric pressure would remove 1000 atomic layers per second or roughly 1 mm per hour. Of course, the conditions existing in the ultra high vacuum environment are considerably different from the conditions in the open air. Indeed, a block of graphite sitting idly on the table does not suffer the dramatic burn up that would be extrapolated from the measurements obtained in

the modecular beam reaction apparatus. Apparently, a protective surface is established by species adsorbed from the atmosphere.

Small amounts of room temperature reactivity were routinely observed, but after many experiments have been performed on one sample, it began to exhibit a rather fantastic 10^{-3} apparent reaction probability at room temperature. This very high reactivity was unquestionably not due to beam impurities and sparked considerable interest and concern. The sample was removed from the vacuum system for investigation.

A crack (slot) roughly 20 microns wide had developed across the sample parallel to the basal planes, probably as a result of thermal cycling (Fig. 46). Perhaps the crack had exposed reactive atoms. On the other hand, perhaps some catalytic effect was assisting the high vacuum room temperature oxidation. It was known that tungsten was vapor deposited on the back of the target by the electron beam heater, and tungsten has been found to catalyze graphite oxidation.[22]

Both sides of the target were given X-ray fluorescence analysis which indicated about 100 parts per million (volume concentration, atomic) of tungsten. Unfortunately, the X-ray fluorescence technique could not clearly distinguish between tungsten on the front or rear faces of the rather thin sample.

About 1 mg of material was scraped from the front face of the target for a neutron activation analysis which revealed tungsten contamination at about 6 parts per million (atomic). This tungsten concentration although quite small[22] was 3 orders of magnitude higher than in the as-received samples.

E. Mixed Isotope Reaction

The reasonably high CO_2 reaction probability obtained on the prism plane sample encouraged us to obtain some heavy oxygen (O_2^{18-18}) to use with normal O_2^{16-16} in a probe of the mechanism for CO_2 formation similar to the experiments of Walker et al.[33,34] We seek to determine whether (1) CO_2 is formed by reaction with both atoms of a given O_2 molecule or (2) CO_2 is formed by reaction with any two adsorbed oxygen atoms which may arise from different adsorbing O_2 molecules. In the most elementary terms, process (1) could be abstraction of a carbon atom by an O_2 molecule. Process (2) would point to dissociative adsorption of an O_2 molecule yielding two adsorbed oxygen atoms, O_{ads}, of which at least one is free to migrate about the surface until it encounters another O_{ads} (fixed or mobile) with which it reacts forming CO_2. Experimentally, a beam of oxygen containing both O_2^{16-16} and O_2^{18-18} molecules will be reacted with the prism plane pyroltyic graphite and the production of CO_2 of mass numbers 44, 46, 48 will be monitored. If no mass 46 (CO_2^{16-18}) is produced, process (1) will be indicated. Process (2) implies that CO_2^{16-18} will be produced.

Walker's group studied the production of CO_2 from oxidation of graphon at 500°C in an oxygen background of ca 10^{-2} torr by monitoring the concentrations of product(s) and reactant(s) mass spectrometrically. The consumption of reactant O_2 and the build-up of product CO_2 were obtained at 5 minute intervals. After very carefully determining that no serious complications from secondary reactions were occurring (e.g. exchange of O atoms between CO_2^{16-16} and CO_2^{18-18} which ultimately creates CO_2^{16-18}), a mixture of O_2^{16-16} and O_2^{18-18} was reacted with the graphon and from the first data at 5 minutes into the experiment it was apparent that an equilibrium mixture of CO_2^{16-16}, CO_2^{16-18}, and

CO_2^{18-18} was being produced. Only for times on the order of 30 minutes would the exchange among product CO_2 yield such an equilibrium mixture. They therefore concluded that CO_2 was a primary reaction product produced from dissociated oxygen.

The modulated beam system, by design, precludes the possibility of observing products produced by a secondary reaction on the surface or in the gas phase. Consequently, a modulated beam experiment reacting a mixture of O_2^{16-16}--O_2^{18-18} with pyrolytic graphite seems attractive. Of course, the poor utilization of the total beam source efflux means that we will waste a great deal of O_2^{18-18}. Nevertheless, a 1 liter flask containing 1/2 liter (STP) of O_2^{18-18} was obtained from Oak Ridge National Laboratory (for $1000) with the following assay:

Batch 1806/Assay 7563

Species	Per Cent
O^{18}	99.2
O^{17}	0.2
O^{16}	0.6
Ar	0.1
N_2	<1
$CO_2^{(18-18)}$	0.3

The large CO_2 impurity will be removed by the inlet system cold trap and the other impurties (Ar, N_2) do not show up at mass numbers of interest in this experiment--44, 46, 48.

Samples of the prism plane target had been scraped from the face for activation analysis. The surface was consequently restored, by a two week burn-off, to an oxidative etched condition which exhibited the same reactivity found previously (not enhanced by tungsten).

O_2^{18-18} from its glass flask was bled through a variable leak valve into the inlet system where it was mixed with O_2^{16-16} bled through a separate leak valve. The gas mixture then passed through the inlet cold trap to the source tube. The cold trap did indeed remove the CO_2^{18-18} impurity. Impurity in the oxygen beam will be detected at nearly zero phase lag with respect to the scattered oxygen beam. For the initial mixed beam composition (roughly 40 - 60) the following reactant and "background" signals were found at room temperature:

Mass	Signal (μv)	Phase
32	21500	0°
34	102	0°
36	31500	0°
44	(0.3μv random "noise")	(0°)
46	0.35 ± 0.08	23°
48	0.27 ± 0.08	48°

The mass 34 impurity would be expected to be O_2^{16-18} from the ordinary natural oxygen (O_2^{16-16}--99.52°, O_2^{16-18}--0.41%, O_2^{16-17}--0.07%) which supplied the O_2^{16-16}. The precision of signal measurements at mass numbers 46, 48 in contrast to that at mass number 44 reflects the absence (at least initially) of a CO_2 background of these "rare" isotopes. The mass number 44 "signal" is essentially noise due to a high background concentration of CO_2^{16-16}. However, the definite phase of the background signals at mass numbers 46,48 again suggests that some reaction may be occurring at room temperature. No subtraction of any "background" signal will be applied to the signals measured at reaction temperature.

A reaction temperature of 1450°K was selected for this experiment to give the best signal-to-noise ratio (trading high reactivity at high temperatures for reduced electrical noise from the electron beam heater at low temperatures). A low modulation frequency (16 Hz) was used to

help minimize demodulation of the desired signal.

The charge of O_2^{18-18} in the small flask would be significantly depleted during the run resulting in a variation of the beam composition and beam intensity. Consequently, the time for each "reading" was noted in order to correct for this decay in the O_2^{18-18} pressure. A four fold decrease in O_2^{18-18} signal was observed over the entire 3 hour run (also 5% decrease in O_2^{16-16}) and was interpolated assuming an exponential pressure decay (section III-B). Designating the O_2^{18-18} (mass 36) fraction as x and the O_2^{16-16} (mass 32) fraction as (1-x) we determine x at any time by the ratio of 36 and 32 signals (effective at that time) as,

$$\frac{x}{1 - x} = \frac{S_{36}}{S_{32}}$$

The mass 34 (O_2^{16-18}) fraction was approximated as 0.004(1 - x). From the value of x at any time the distribution of CO_2 among the mass numbers 44, 46, 48 may be claculated for the two extreme cases of <u>total mixing</u> and <u>no mixing</u>.

Mass	Mixing	No Mixing
44	$(1 - x)^2$	$(1 - x)$
46	$2x(1 - x)$	$0.004(1 - x)$
48	x^2	x

The "no mixing" contribution to mass 46 comes from oxidation by O_2^{16-18} (mass 34) in the O_2^{16-16} gas.

The following table gives the CO_2 signals obtained at mass numbers 44, 46, 48 and the value of x and source pressure in effect at the time of each reading. Also shown are the theoretical mass fractions corresponding to complete isotope mixing and no mixing. The CO_2 signals at each mass (44, 46, 48) were found to have a large 20 - 30 phase lag.

Mass	x	Press. (torr)	Signal	Mixed	Unmixed
44	.55	4.3	4.9 ± 3.4 μv	.20	.45
46	.47	3.7	1.12 ± 0.2 μv	.50	.002
48	.37	3.0	1.25 ± 0.4 μv	.14	.37

The mass 44 signal is proportional to the probability of producing CO_2^{44} and the source pressure. (The reaction was found to be first order.) Similar statements apply to mass numbers 46, 48. The same proportionality constant is assumed for each of 44, 46, 48 neglecting slight variation of spectrometer response to the different isotopes. Significant experimental results are the ratios,

$$\frac{S_{46}}{S_{44}} = \frac{1.12 \pm 0.2}{4.9 \pm 3.4} \; \frac{4.3}{3.7} \text{ , etc .,}$$

which may be compared to the theoretical ratios corresponding to complete or nil mixing. The experimental ratios (with probable error bars) are illustrated in Fig. 60 along with the mixing predictions. The results clearly show that <u>some</u> CO_2^{16-18} is produced but not so much as is expected for complete isotopic mixing. Why are these findings at odds with the results of Walker's investigations which revealed complete mixing?

It is proposed that the unusually clean conditions existing in high vacuum make possible the direct reaction of an oxygen molecule with graphite to form CO_2 containing both oxygen atoms of the incident molecule. No isotopic exchange occurs by this process.

Additionally, some CO_2 could be made from dissociated oxygen. This CO_2 would be isotopically mixed. The reaction mechanism for producing CO proposed direct dissociation of O_2 and formation of adsorbed CO. Possibly not all adsorbing dissociated oxygen would be

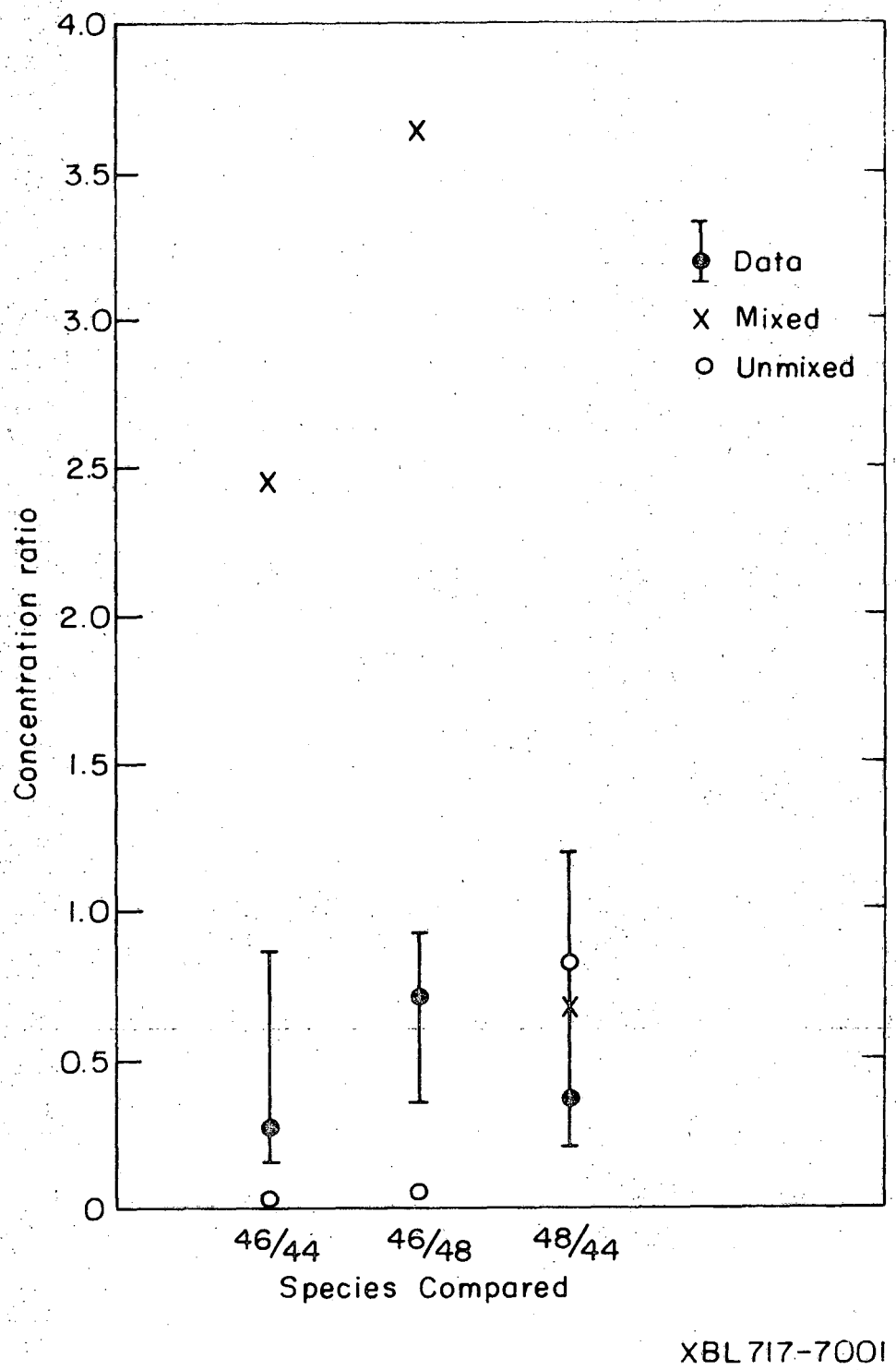

Fig. 60 Mixed oxygen isotope experiment--intensity concentration ratios comparing different CO_2 isotopes.

bound as CO--some oxygen may be adsorbed in atomic form. Reaction of this atomic oxygen with O_a + C or adsorbed CO would lead to an equilibrium isotopic mixture.

The 20-30° phase lag characteristic of double diffusion was observed for CO_2, consequently the CO_2 formed by either process must be subject to solution diffusion into the sample.

Neither the apparent reaction probability nor the reaction phase lag showed appreciable hysteresis with temperature cycling. Apparently the sites which led to CO_2 production directly from molecular oxygen (the major, unmixed portion) do not undergo readjustement at different temperatures.

Reaction to produce an isotopic mixture of CO_2 is inherently bimolecular and would result in non linear kinetics. However, the reaction was found to be first order with respect to variation in beam intensity providing an additional indication that oxygen molecules are directly involved in production of the major portion of the CO_2.

F. Annealed Prism Plane Pyrolytic Graphite

Samples of annealed pyrolytic graphite with a prismatic front face were subjected to oxidation study. From the previous observations on annealed basal plane samples, it was expected that the reactivity would be lower than for as-deposited prism plane pyroltyic graphite. What a great surprise it was to find that the annealed prism plane sample was more reactive--exceeding the apparent reaction probability of the as-deposited material by an order of magnitude!

Despite the high apparent reactivity, the annealed graphite exhibits the same hysteresis behavior for CO and gives nearly the same CO/CO_2 ratio (~10/1). The reaction is first order at 1450°K. With a high apparent reaction probability, the "cleaner" signals have permitted

quicker experimenting and the symmetrical details of hysteresis found by Duval[79] have been duplicated. Proceeding from a lower to a higher temperature results initially in a higher reaction signal while reducing temperature gives initially a lower reaction signal.

The reaction phase data may throw some light on the difference in apparent reactivity. Both samples were given a temperature scan at 16 Hz modulation frequency and 4 torr source pressure. The as-deposited specimen exhibited a fairly flat reaction phase lag between 20-30° independent of temperature. The annealed specimen generally had a lower phase lag (~10°) and the phase lag was less at high temperatures, ranging from 28° to 6° as temperature was increased from 1200°K to 2000°K. The reduction of the phase lag with increasing temperature is more like that of a chemically controlled surface reaction.

In terms of the double diffusion model presented earlier, the higher apparent reactivity of an annealed target is expected. Annealing produces a more uniform structure of higher density. Referring to Eq. (96), shrinking δ, the thickness of the renucleation regions, would reduce diffusion into the graphite thereby reducing diffusional demodulation. The remaining demodulation would be due to the "chemical control" of the desorption rate constant, k.

Although the size of disoriented regions would be reduced by annealing, the density of disturbed regions, N, may be unaffected. Removal of a renucleation boundary requires mutual ordering of the layers on each side of the boundary, but shrinking the size of the renucleation boundary region may be accomplished gradually by repositioning one atom at a time.

When N remains nearly constant as δ shrinks, the diffusional demodulation is reduced, and the apparent reaction probability rises toward,

0 0 0 0 3 6 0 3 4 1 6

$$\varepsilon\, e^{-j\phi} = \frac{2N\,\Delta\eta}{(1 + j\omega/k)} \tag{99}$$

which exhibits demodulation only due to the desorption process.

VI. QUASI-EQUILIBRIUM ANALYSIS OF REACTION RATES

Without assuming a detailed kinetic model, expressions for the rate of a gas-solid reaction may be formulated on the assumption that quasi-equilibrium conditions exist at gas-solid interfaces even when the temperature and chemical composition of the gas phase differ from equilibrium values. The following discussion follows that of Stickney and Batty[84] using equilibrium considerations, i.e., thermodynamics, the principle of detailed balance, kinetic theory for gas impingement rate, and the statistical mechanics of perfect gases. A generalized transmission or equilibration probability (commonly known as the sticking probability), the only adjustable parameter, prevents direct comparison with experiment.

The impingement rate Z_i of species i of mass m_i having a partial pressure p_i in a system at temperature T is given by kinetic theory as,

$$Z_i = p_i(2\pi m_i kT)^{-1/2} \tag{100}$$

A distinguishable fraction ζ_i of species i are assumed to equilibrate with the surface (adsorb). The remaining fraction $(1 - \zeta_i)$ rebound elastically.

According to detailed balance arguments, the adsorption rate $\zeta_i Z_i$ must be balanced in <u>equilibrium</u> by a desorption rate R_i of species i from the adsorbed phase. Furthermore, the adsorption-desorption rates must balance in detail for each angle and velocity increment.

For the non-equilibrium experiment, one writes a surface mass balance for each chemical <u>element</u>. Then one determines the set of equilibrium conditions (partial pressures) for the system which would give the same adsorption rate for each element. The desorption rate of

reaction products fromthe adsorbate phase in this equilibrium situation is assumed equal to the desorption rate under the experimental conditions.

For species that are equilibrated in times short relative to residence times in the adsorbate, the adsorbate state will depend on adsorption rates of the elements and will be independent of the molecular state in which they were brought to the surface (except for effects of molecular structure on ζ). Exceptional cases would occur for (i) slow equilibration or (ii) reaction mechanisms that require a certain molecular species to be supplied directly from the gas phase (Rideal-Eley mechanism).

The technique is applied to the molecular oxygen--graphite system as follows:

A surface balance on the <u>element</u> oxygen gives,

$$2\,\zeta_{O_2} Z_{O_2} = 2\,R_{CO_2} + R_{CO} + R_O + 2\,R_{O_2} \quad , \tag{101}$$

where $2\zeta_{O_2} Z_{O_2}$ is the rate of surface equilibration (adsorption) of oxygen atoms fed by a molecular impingement rate Z_{O_2}, and the R_i's are the emission rates of possible products.

By thermodynamics we may express the equilibrium constants for the possible reactions in terms of partial pressures. For the reaction

$$C + 1/2\ O_2(g) = CO(g) \quad ,$$

we have at equilibrium,

$$K_{p_{CO}} = p_{CO}(p_{O_2})^{-1/2} = \exp -(\Delta H^\circ_{CO} - T\Delta S_{CO})/RT. \tag{102}$$

Similar expressions may be obtained for the reactions,

$$C + O_2(g) = CO_2(g) \quad ,$$

$$K_{p_{CO_2}} = p_{CO_2}/p_{O_2} = \exp -(\Delta H^\circ_{CO_2} - T\Delta S_{CO_2})/RT$$

$$1/2\ O_2(g) = O(g) \tag{103}$$

and

$$K_{p_O} = p_O(p_{O_2})^{-1/2} = \exp -(\Delta H^\circ_O - T\Delta S_O)/RT \quad . \tag{104}$$

These equilibrium partial pressures are assumed to be related to the non-equilibrium desorption rates, R_i's, by,

$$R_i = \zeta_i Z_i = \zeta_i p_i\ (2\pi m_i kT)^{-1/2} \tag{105}$$

Due to lack of more specific information, the ζ_i of the products are assumed equal to one.

Using Eq. (105), the Eqs. (102), (103) and (104) may be rewritten in terms of R_i's. The resulting equations and Eq. (101) constitute a set in four unknowns R_{CO}, R_{CO_2}, R_O, and R_{O_2} which may be solved to yield the reaction probabilities, $R_{CO}/2\zeta_{O_2} Z_{O_2}$, etc.

The results are shown in Fig. 61 after Stickney and Batty.[84] By this analysis, CO is seen to be the dominant product above 700°K and exhibits first order kinetics in this range. Above 850°K, CO_2 is less than 10^{-5} as common as CO. Oxygen atom emission or recombination is negligible up to 3000°K.

The quasi-equilibrium analysis does not consider the nature of the reactive surface, but the surface condition was found to be a significant factor in pyrolytic graphite oxidation. This analysis predicts a negligible production of CO_2, whereas CO_2 was typically 10% as prevalent as CO in the molecular beam system measurements.

0 0 0 0 3 6 0 5 4 1 8

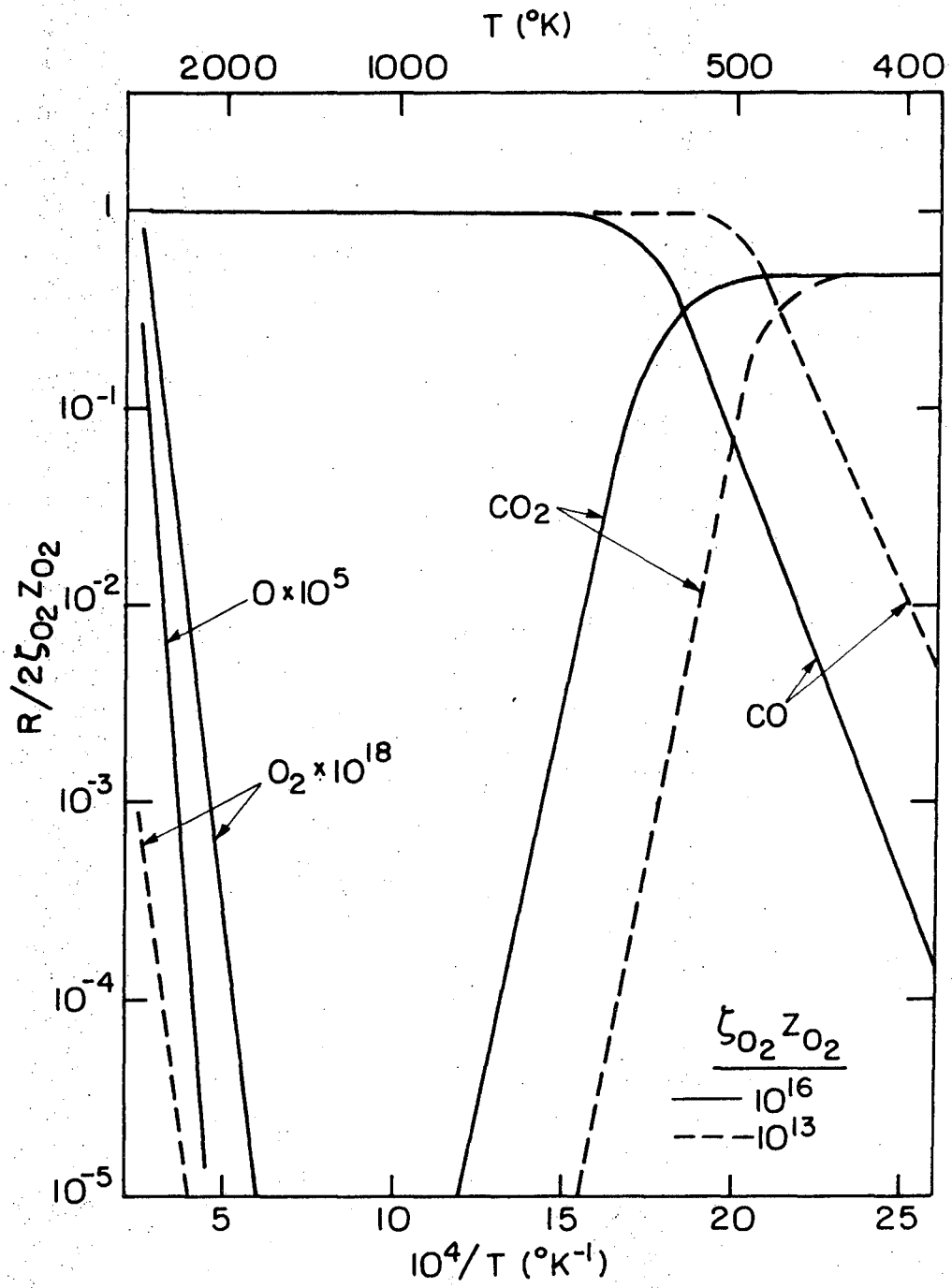

XBL717-7002

Fig. 61 Quasi-Equilibrium Analysis--theoretical evaporation rates of the volatile species formed in the chemical reaction of gaseous O_2 with solid carbon.

VII. CONCLUSION

Analytical methods for dealing with reactions proceeding via several branches, with one or more series steps, or involving bulk solution-diffusion were developed.

The modulated molecular beam reaction study was able to separate the contributions to the oxidation reaction from the elementary processes of surface migration, bulk diffusion, and desorption. The values of kinetic parameters controlling these mechanisims were evaluated. This is important information about the elementary processes, some of which is impossible to obtain by conventional steady state kinetic techniques.

The surface migration step in the basal plane reaction served only to delay the overall reaction forming CO. As only a delaying step, it certainly would not be observed in steady state kinetic experiments or continuous oxidation. However, at sufficiently high surface concentrations, the migrating O atoms may recombine to form O_2 before reacting with a type B site to form CO. Under these conditions, gassification of the graphite would be reduced due to the surface migration step. The modulated beam technique was able to observe the surface migration step before it became rate determining.

The bulk diffusion (double diffusion) step in the prism plane reaction mechanism was not rate determining, but was clearly indicated by the modulated beam experiments. The high apparent reactivity of the annealed prism plane sample vis-a-vis the as-deposited sample suggested that the oxidation reaction proceeds <u>on</u> the surface. Diffusion of product CO into and out of the bulk provided significant demodulation of the AC signal from the as-deposited sample. If some species (other than oxygen) were found to react <u>within</u> the graphite, then information on the (double) bulk diffusion process would have greater importance.

The surface diffusion and double diffusion steps above had no effect on the oxidation rate. They only served to demodulate the AC reaction signal. The distinction between the true (DC) and the apparent (AC) reaction probability is, in a sense, painfully clear. Only when the AC technique is used under conditions yielding zero phase lag are the two reaction probabilities equal. Extrapolating an apparent (AC) reaction probability to the true (DC, low frequency limit) reaction probability requires that the complete reaction mechanism be known.

Application of AC apparent reaction probabilities to engineering design must be approached with caution. Nevertheless, an understanding of the mechanistic details of reactions is highly desirable as a guide to research and development of materials with improved properties.

The literature on carbon oxidation appears to be in a state of great disorder. Carbon samples with vastly different crystallinity have been studied using a myriad of techniques with reactant gas pressures from 10^{-7} torr to nearly atmospheric pressure and at temperatures from room temperature to nearly 3000°K. The work is relatively spotty and there is a dramatic lack of overlap of the conditions and techniques employed by different investigators. Even within a given laboratory, different techniques lead to different conclusions.[30,31,32,37] Although the different results could be due to a disparity of proficiency and/or available support for different investigators, it seems more likely due to the complexities of the oxidation processes. Indeed, as more information is obtained, the different pieces are found to fit the whole puzzle and even link observations which had seemed to be in total conflict. For example, the inability to observe oxygen chemisorption on basal surfaces by LEED[38,39] is easily understood in terms of the vertical sides of etch pits observed by Hennig.[15]

In this work on the basal surface, dissociative adsorption leading to both mobile and immobile adsorbed species was observed. This may help to resolve the apparent conflict between several different adsorption experiments performed by Walker et al.[30,31,32,37]

The multi-site mechanism proposed to explain some adsorption experiments[35,36] is similar to the multi-branch reaction mechanism which was considered for the prism plane reaction. The latter, however, was also explained by the double diffusion mechanism.

The entire puzzle is not yet complete.

0 0 0 0 3 6 0 0 4 2 0

ACKNOWLEDGMENTS

This work has been supported by the United States Atomic Energy Commission through the Lawerence Berkeley Laboratory and by a three year fellowship administered by Oak Ridge Associated Universities through the "Special Fellowships in Nuclear Science and Engineering" program.

I would like to thank Professor Donald R. Olander of the Department of Nuclear Engineering, University of California for providing a stimulating problem as well as the noncoercive guidance and direct assistance which led to its solution and this thesis.

A special thanks to Professor Stanley G. Prussin of the Nuclear Engineering Department for performing the neutron activation analysis of the graphite samples and deciphering the results.

The swift typing and the dedication to perfection of Jean Wolslegel is appreciated.

APPENDIX I

Final Expressions of Basal Plane Model Calculation

The six constants $(a, b, c)_{ON,\ OFF}$ may be expressed in terms of the dimensionless parameters, $\xi = \sigma I_o/k_d$, $\gamma = k/k_d$, $\theta = \pi k/\omega$, $\tau = \pi k_d/\omega$:

$$a_{ON} = \frac{\xi}{1+\xi}\left[\frac{1 - e^{-\tau}}{e^{-\tau} - e^{(1+\xi)\tau}}\right] \tag{I-1}$$

$$a_{OFF} = \frac{\xi}{1+\xi}\left[\frac{1 - e^{(1+\xi)\tau}}{e^{-\tau} - e^{(1+\xi)\tau}}\right] \tag{I-2}$$

$$c_{ON} = \frac{\xi}{\gamma(1+\xi)}\left[\frac{e^{-\theta} - 1}{e^{\theta} - e^{-\theta}}\right] + \frac{a_{ON}\,\xi}{1+\xi-\gamma}\left[\frac{e^{-\theta} - e^{(1+\xi)\tau}}{e^{\theta} - e^{-\theta}}\right] \tag{I-3}$$

$$c_{OFF} = \frac{\xi}{\gamma(1+\xi)}\left[\frac{e^{\theta} - 1}{e^{\theta} - e^{-\theta}}\right] + \frac{a_{ON}\,\xi}{1+\xi-\gamma}\left[\frac{e^{\theta} - e^{(1+\xi)\tau}}{e^{\theta} - e^{-\theta}}\right] \tag{I-4}$$

$$b_{ON} = \frac{\xi}{1+\xi}\left[\frac{e^{-\tau} - 1}{e^{\tau} - e^{-\tau}}\right] + \frac{a_{ON}\,\gamma}{1+\xi-\gamma}\left[\frac{e^{-\tau} - e^{(1+\xi)\tau}}{e^{-\tau} - e^{\tau}}\right]$$
$$+ c_{ON}\frac{\gamma}{1-\gamma}\left[\frac{e^{-\tau} - e^{\theta}}{e^{\tau} - e^{-\tau}}\right] + c_{OFF}\frac{\gamma}{1-\gamma}\left[\frac{e^{-\tau} - e^{-\theta}}{e^{-\tau} - e^{\tau}}\right] \tag{I-5}$$

$$b_{OFF} = \frac{\xi}{1+\xi}\left[\frac{e^{\tau} - 1}{e^{\tau} - e^{-\tau}}\right] - a_{ON}\frac{\gamma}{1+\xi-\gamma}\left[\frac{e^{\tau} - e^{(1+\xi)\tau}}{e^{\tau} - e^{-\tau}}\right]$$
$$+ c_{ON}\frac{\gamma}{1-\gamma}\left[\frac{e^{\tau} - e^{\theta}}{e^{\tau} - e^{-\tau}}\right] - c_{OFF}\frac{\gamma}{1-\gamma}\left[\frac{e^{\tau} - e^{-\theta}}{e^{\tau} - e^{-\tau}}\right] \tag{I-6}$$

The sine and cosine intergrals S and C are:

$$S = \frac{-4}{\pi}\frac{\xi}{1+\xi}$$

$$-a_{ON}\frac{\pi}{\tau^2}\frac{1+\xi-2\gamma}{1+\xi-\gamma}\left[\frac{1+e^{(1+\xi)\tau}}{(1+\xi)^2+(\frac{\pi}{\tau})^2}\right] + a_{OFF}\frac{\pi}{\tau^2}\left[\frac{1+e^{-\tau}}{1+(\frac{\pi}{\tau})^2}\right]$$

$$-b_{ON}\frac{\pi}{\tau^2}\left[\frac{1+e^{\tau}}{1+(\frac{\pi}{\tau})^2}\right] + b_{OFF}\frac{\pi}{\tau^2}\left[\frac{1+e^{-\tau}}{1+(\frac{\pi}{\tau})^2}\right]$$

$$-c_{ON}\frac{\pi}{\theta^2}\frac{\gamma}{1-\gamma}\left[\frac{1+e^{-\theta}}{1+(\frac{\pi}{\theta})^2}\right] + c_{OFF}\frac{\pi}{\theta^2}\frac{\gamma}{1-\gamma}\left[\frac{1+e^{-\theta}}{1+(\frac{\pi}{\theta})^2}\right] \qquad \text{(I-7)}$$

$$C = -a_{ON}\frac{(1+\xi-2\gamma)}{\tau(1+\xi-\gamma)}\left[\frac{1+e^{(1+\xi)\tau}}{(1+\xi)^2+(\frac{\pi}{\tau})^2}\right] + a_{OFF}\frac{1}{\tau}\left[\frac{1+e^{-\tau}}{1+(\frac{\pi}{\tau})^2}\right]$$

$$-b_{ON}\frac{1}{\tau}\left[\frac{1+e^{\tau}}{1+(\frac{\pi}{\tau})^2}\right] + b_{OFF}\frac{1}{\tau}\left[\frac{1+e^{-\tau}}{1+(\frac{\pi}{\tau})^2}\right]$$

$$-c_{ON}\frac{1}{\theta}\frac{\gamma}{1-\gamma}\left[\frac{1+e^{\theta}}{1+(\frac{\pi}{\theta})^2}\right] + c_{OFF}\frac{1}{\theta}\frac{\gamma}{1-\gamma}\left[\frac{1+e^{-\theta}}{1+(\frac{\pi}{\theta})^2}\right] \qquad \text{(I-8)}$$

APPENDIX II

The transit time of ions in the mass spectrometer can also modify the response of the detection system. Molecules coasting through the ionizer region (faraday cage) are converted to ions. The faraday cage is maintained at a potential V and is a distance L_1 from the zero potential entrance apperature of the four pole mass filter. The ions are accelerated over the path length L_1 (~1 cm) as they acquire "ion energy" qV while they are extracted and sent to the quadrupole mass filter. There is no axial field in the quadrupole mass filter, and the extracted ions drift through the length of the filter L_2 (~18 cm, 7 inches) to the first dynode of the electron multiplier. The time required for acceleration and axial drift will be considered. Only a delay time or an equivalent phase lag will be calculated. There is no first order dispersion effect with respect to transverse molecular (or ion) energy and, consequently, there is no amplitude attenuation.

<u>Acceleration time</u>

Consider a singly charged ion of mass M accelerating over a distance L_1 through a voltage V. The time t_a required is determined from:

$$L_1 = 1/2 \frac{qV}{M L_1} t_a^2 \qquad \text{II-1}$$

The time delay is:

$$t_a = L_1 \sqrt{\frac{2 M}{q V}} = 1.4 L_1 \sqrt{\frac{M}{V}} \ (\mu \text{ sec}) \qquad \text{II-2}$$

L_1 (cm), M (amu), V (volts). For L_1 = 1 cm and 15 volt ion energy for oxygen ions (M = 32), we have,

$$t_a = 2.2 \ \mu \text{ sec} \quad .$$

At 1500 Hz this corresponds to a phase lag of 1.2°.

This is a "worst case" quantity. After leaving the faraday cage, the ions are strongly accelerated by a 100 volt focus apperature. Then, they are decelerated to the "ion energy" qV at the mass filter entrance apperature. Therefore, the ions travel from the faraday cage to the entrance apperature faster than they would have if they had only been accelerated by the potential V over that length.

Drift time

Consider a molecule (ion) of mass M and energy qV traveling a distance L_2. The drift time required is given by:

$$t_d = L_2 / \sqrt{2\ qV/M} = 0.72\ L_2 \sqrt{M/V}\ (\mu\ \text{sec}) \qquad \text{II-3}$$

L_2 (cm), M (amu), V (volts). For L_2 = 18 cm and 15 volt oxygen ions, we have:

$$t_d = 20\ \mu\ \text{sec} \quad .$$

At 1500 Hz this corresponds to a phase lag of 10.8°.

These ion flight phase lags are relatively small compared to the molecule transit phase lags or the phase lag due to the complex impedance. As with the other phase corrections it is the net correction between reactant and product signals that is significant and, of course, this difference is even smaller. Ion flight phase lag corrections were not applied to the data obtained in this work. In detailed studies the correction may be required--particulary if heavy species (ions) are involved.

REFERENCES

1. H. P. Boehm, and R. W. Coughlin, Carbon 2, 1 (1964).

2. J. M. Thomas and E. E. G. Hughes, Carbon 1, 209 (1964).

3. S. Ergun, Carbon 6, 141 (1968).

4. Data Sheet, PG (Pyrolytic Graphite) High Temperature Materials, Inc.; Lowell, Mass. 01852.

5. R. F. Strickland-Constable, Trans. of the Faraday Soc. 40, 333 (1944).

6. X. Duval, J. de Chimie Physique 47, 339 (1950).

7. F. Boulangier, X. Duval, and M. Letort, Proc. of the Third Conf. on Carbon, (Pergamon Press, 1959) p. 257.

8. L. Meyer, J. de Chimie Physique 47, 328 (1950).

9. R. F. Strickland-Constable, J. de Chimie Physique 47, 322 (1950).

10. J. Nagle, and R. F. Strickland-Constable, Proc. of the Fifth Conf. on Carbon, Vol. 1, (Pergamon Press, 1962) p. 154.

11. J. R. Walls, and R. F. Strickland-Constable, Carbon 1, 333 (1964).

12. G. Blyholder, J. S. Binford, and H. Eyring, J. Phys. Chem. 62, 263 (1958).

13. W. S. Horton, Proc. of the Fifth Conf. on Carbon, Vol. 2, (Pergamon Press, 1963) p. 233.

14. D. E. Rosner, and H. D. Allendorf, AIAA Journal 6, 650 (1968).

15. G. R. Hennig, Proc. of the Fourth Conf, on Carbon, (Pergamon Press, (1960) p. 145.

16. G. R. Hennig, Proc. of the Fifth Conf. on Carbon, Vol. 1, (Pergamon Press, 1962) p. 143.

17. G. R. Hennig, and M. A. Kanter, Fourth Int. Symp. on the Reactivity of Solids, Amsterdam (1960) p. 648, J. H. deBoer, ed.

18. J. M. Thomas, Carbon 7, 359 (1968).

19. J. M. Thomas, Chemistry and Physics of Carbon, Vol. 1, (Marcel Dekker Inc., New York, 1965) p. 121, Phillip L. Walker, Jr., ed.

20. J. M. Thomas, and E. E. G. Hughes, Carbon 1, 209 (1964).

21. H. Harker, Proc. of the Fourth Conf. on Carbon, (Pergamon Press, 1960) p.125.

22. E. A. Heintz, and W. E. Parker, Carbon 4, 473 (1966).

23. H. Amariglio, and X. Duval, Carbon 4, 323 (1966).

24. C. Roscoe, Carbon 6, 365 (1968).

25. H. Hering, S. Keraudy, F. M. Lang, and S. May, Proc. of the Fourth Conf. on Carbon, (Pergamon Press, 1960) p. 115.

26. B. L. Tonge, Proc. of the Fourth Conf. on Carbon, (Pergamon Press, 1960) p. 87.

27. M. Menster, and S. Ergun, Carbon 5, 331 (1967).

28. B. R. Puri, Carbon 4, 391 (1966).

29. L. Bonnetain, X. Duval, and M. Letort, Proc. of the Fourth Conf. on Carbon, (Pergamon Press, 1960) p. 107.

30. P. J. Hart, F. J. Vastola, and P. L. Walker, Jr., Carbon 5, 363 (1967).

31. N. R. Laine, F. J. Vastola, and P. L. Walker, Jr., Proc. of the Fifth Conf. on Carbon, Vol. 2, (Pergamon Press, 1963) p. 211.

32. R. O. Lussow, F. J. Vastola, and P. L. Walker, Jr., Carbon 5, 591 (1967).

33. F. J. Vastola, P. J. Hart, and P. L. Walker, Jr., Carbon 2, 65 (1964).

34. P. L. Walker, Jr., F. J. Vastola, and P. J. Hart, Fundamentals of Gas-Surface Interactions (Academic Press, 1967) p. 307, H. Saltzburg and J. N. Smith, Jr., eds.

35. R. C. Bansal, F. J. Vastola, and P. L. Walker, Jr., Carbon 8, 443 (1970).

36. R. Phillips, F. J. Vastola, and P. L. Walker, Jr., Carbon 8, 197 (1970).

37. P. L. Walker, Jr., L. G. Austin, and J. J. Tietjen, Chemistry and Physics of Carbon, Vol. 1, (Marcel Dekker, New York, 1965) p. 327, Phillip L. Walker, Jr., ed.

38. J. J. Lander, and J. Morrison, J. of Appl. Phys. 35, 3593 (1964).

39. D. Gerard, Commissariat a L'Energie Atomique, Report CEA-3841 (1969).

40. T. Evans, and C. Phaal, Proc. of the Fifth Conf. on Carbon, Vol. 1, (Pergamon Press, 1962) p. 147.

41. R. A. Krakowski, and D. R. Olander, J. Chem. Phys. 49, 5027 (1968).

42. R. T. Brackman, and W. L. Fite, J. Chem Phys. 34, 1572 (1961).

43. J. N. Smith, and W. L. Fite, J. Chem Phys. 37, 898 (1962).

44. J. D. McKinley, J. Chem. Phys. 40, 120 (1964).

45. J. Anderson, and M. Boudart, J. Catalysis 13, 216 (1964).

46. R. N. Coltharp, J. T. Scott, and E. E. Muschlitz, Jr., Proc. of the Fourth Intern. Materials Symp., (Wiley, 1969) pp. 66-1 to 66-5, G. A. Somorjai, ed.

47. R. J. Madix, and J. A. Schwarz, Surface Science 24, 264 (1971).

48. R. P. Merrill, Catalysis Reviews 4, 115 (1970).

49. K. J. Laidler, Chemical Kinetics, (McGraw-Hill, 1965) p. 4.

50. D. R. Olander, Proc. of the Fourth Intern. Materials Symp., (Wiley, 1969) pp. 45-1 to 45-50, G. A. Somorjai, ed.

51. J. A. Schwarz, Ph.D. thesis, Stanford University, (1969).

52. N. Balabanian, Fundamentals of Circuit Theory, Allyn and Bacon, 1962) Ch. 4.

53. B. McCarroll, J. Chem. Phys. 46, 863 (1967).

54. J. C. Batty, and R. E. Stickney, J. Chem. Phys., 51, 4475 (1969).

55. H. Saltzburg, J. N. Smith, R. L. Palmer, Proc. of the Fourth Intern. Materials Symp. (Wiley, 1969) pp. 42-1 to 42-22, G. A. Somorjai, ed.

56. R. J. Madix, R. Parks, A Susu, and J. Schwarz, Surface Science 24, 288 (1971).

57. H. Harrison, D. G. Hummer, and W. L. Fite, J. Chem, Phys. 41, 2567 (1964).

58. J. A. Schwarz, and R. J. Madix, J. Catalysis 12, 140 (1968).

59. W. J. Siekhaus, R. H. Jones, and D. R. Olander, J. Appl. Phys. 41, 4392 (1970).

60. H. S. Carslaw, and J. C. Jaeger, Conduction of Heat in Solids, (Oxford, Clarendon Press, 1959), pp. 64-70.

61. G. W. Greenwood, A. J. Foreman, and D. E. Rimmer, J. of Nuclear Mat'ls. 4, 305 (1959).

62. P. W. Tamm, and L. D. Schmidt, J. Chem. Phys. 51, 5352 (1969).

63. L. A. West, E. I. Kozak, and G. A. Somorjai, J. Vac. Sci, and Tech. 8, 430 (1971).

64. R. P. Merrill, and D. L. Smith, Surface Sci. 21. 203 (1970).

65. E. D. Morris, and H. S. Johnston, Rev. Sci. Instr. 39, 620 (1968).

66. F. M. Wachi, and D. E. Gilmartin, Carbon 8, 141 (1970).

67. N. F. Ramsey, Molecular Beams, (Oxford Univ. Press, London, 1963) pp. 11-50.

68. A. Kantrowitz and J. Grey, Rev. Sci. Inst. 22, 328 (1951).

69. J. B. Anderson, R. P. Andres, and J. B. Fenn, Adv. in Atomic and Molecular Phys. 1, 345 (1965).

70. R. H. Jones, D. R. Olander, and V. R. Kruger, J. Appl. Phys. 40, 4641 (1969), Part I of series.

7. D. R. Olander, J. Appl. Phys. 40, 4650 (1969), Part II.

72. D. R. Olander, and V. R. Kruger, J. Appl. Phys. 41, 2769 (1970). Part III.

73. D. R. Olander, R. H. Jones, and W. J. Siekhaus, J. Appl. Phys. 41, 4388 (1970), Part IV.

74. D. R. Olander, and R. H. Jones, Entropie 30, 42 (1969).

75. J. A. Giordmaine, and T. C. Wang, J. Appl. Phys. 31, 463 (1960).

76. G. M. Fryer, Trans. Faraday Soc. 293A, 329 (1966).

77. G. R. Hanes, J. Appl. Phys. 31, 2171 (1960).

78. M. Sibulkin, and W. H. Gallaher, AIAA J. 1, 1452 (1963).

79. X. Duval, Ann. de Chimie 10, 903 (1955).

80. H. W. Bode, Network Analysis and Feedback Amplifier Design, (Van Nostrand, New York, 1945). Ch. 14, p. 313.

81. N. F. Graves, A. W. Moore, and S. L. Strong, "Structure, Properties and Applications of Highly Oriented Graphite", Union Carbide Corp. Cleveland, Ohio, 44101.

82. P. G. Shewmon, Diffusion in Solids, (McGraw-Hill, 1963) p. 167.

83. P. G. Shewmon, loc. cit., pp. 179-184.

84. J. C. Batty, and R. E. Stickney, J. Chem. Phys. 51, 4475 (1969).

0 0 0 0 3 6 0 0 4 2 3

LEGAL NOTICE

This report was prepared as an account of work sponsored by the United States Government. Neither the United States nor the United States Atomic Energy Commission, nor any of their employees, nor any of their contractors, subcontractors, or their employees, makes any warranty, express or implied, or assumes any legal liability or responsibility for the accuracy, completeness or usefulness of any information, apparatus, product or process disclosed, or represents that its use would not infringe privately owned rights.

TECHNICAL INFORMATION DIVISION
LAWRENCE BERKELEY LABORATORY
UNIVERSITY OF CALIFORNIA
BERKELEY, CALIFORNIA 94720